UNIVERSITÀ DEGLI STUDI DI SALERNO

University of Salerno

Department of Chemistry and Biology "A. Zambelli"

XXXII Doctoral Cycle in Chemistry

Ph.D. thesis:

Solid state dynamic behaviour of organic molecules

Supervisor:

Prof. C. Tedesco

Co-supervisor:

Prof. F. De Riccardis

Coordinator:

Prof. R. Zanasi

Ph.D. student:

Giovanni Pierri

Matr.: **8800100023**

Academic year 2018/2019

Table of contents

ABBREVIATIONS

DFT: Density functional theory

DSC: Differential scanning calorimetry

$\boldsymbol{E}_{\mathbf{Coul}}$: Coulombic energy

$\boldsymbol{E}_{\mathbf{Disp}}$: Dispersion energy

$\boldsymbol{E}_{\mathbf{Pol}}$: Polarization energy

$\boldsymbol{E}_{\mathbf{Rep}}$: Repulsion energy

$\boldsymbol{E}_{\mathbf{Tot}}$: Total intermolecular interaction energy

GUI: Graphical user interface

HATU: 1-[Bis(dimethylamino)methylene]-1H-1,2,3-triazolo[4,5-b]pyridinium 3-oxid hexafluorophosphate

HF: Hartree-Fock

HSM: Hot-stage microscopy

iPrOH: Isopropyl alcohol

$\boldsymbol{N}_{\mathbf{4\text{-}Cl}}$**pe**: *N*-[2-(4-chlorophenyl)ethyl]glycine

***N*ae**: *N*-(2-aminoethyl)glycine

***N*amy**: *N*-(pentyl)glycine

***N*ce**: *N*-(2-carboxyethyl)glycine

***N*hex**: *N*-(hexyl)glycine

***N*me**: *N*-(methoxyethyl)glycine

***N*pa**: *N*-(propargyl)glycine

***N*pe**: *N*-(phenylethyl)glycine

OXTB: oxitropium bromide

RMSD: Root-mean-square deviation

SCSC: Single-crystal-to-single-crystal

SCXRD: Single crystal X-ray diffraction

VT-SCXRD: Variable temperature single crystal X-ray diffraction

VT-XRPD: Variable temperature X-ray powder diffraction

TGA: Thermal gravimetric analysis

XRPD: X-ray powder diffraction

CHAPTER I

INTRODUCTION

1.1 Crystal engineering

On December 29th, 1959, at the annual meeting of the American Physical Society, Richard P. Feynman declared "I can hardly doubt that when we have some control of the arrangement of things on a small scale, we will get an enormously greater range of possible properties that substances can have, and of different things that we can do." With these words, Feynman introduced the main purpose of crystal engineering: the control of the molecular assembly in the solid state.[1]

The term crystal engineering was introduced for the first time by Schmidt in 1971 in his work on photodimerization in the solid state.[2] But we have to wait until 1989 to get a modern and useful way to define the crystal engineering. In particular, Desiraju, who has actively contributed to the development of this fascinating field, defined the crystal engineering as the understanding of intermolecular interactions in the solid state and the use of this knowledge to design new solids with specific physical and chemical properties.[3]

The crystal engineering evolution goes through the first solid-state reactions in the 70s and 80s, *e.g.* the several works published by Schimdt[2] and Cohen,[4a,b] to the increasing understanding of the importance of the intermolecular interactions in the 90s. During the last 50 years, the control of the solid state assembly was used in any sort of field: pharmaceutical, cosmetics, non-linear optics, environmental science *etc*. Since the properties of a material are strictly related to the solid state assembly, the possibility to predict or, even better, to control how the molecules interact in the solid state represents the ultimate goal of the crystal engineering.[5]

[1] D. Braga, F. Grepioni, L. Maini and S. d'Agostino, *IUCrJ,* 2017, **4**, 369-379.
[2] G. M. J. Schmidt, *Pure Appl. Chem.*, 1971, **27**, 647-678.
[3] G. R. Desiraju*, Crystal Engineering: The design of Organic Solids,* Elsevier Scientific Publisher*,* Amsterdam and New York, 1989.
[4] a) M. D. Cohen and G. M. J. J. Schmidt, *J. Chem. Soc.,* 1964, 1996-2000; b) M. D. Cohen, Z Ludmer, J. M. Thomas and J. O. Williams, *Proc. R. Soc. London A,* 1971, **324**, 459-468.
[5] G. R. Desiraju, *J. Am. Chem. Soc.,* 2013, **135**, 9952-9967.

Unfortunately, since the formation of a crystal is related to a large number of events and variables, which most of the time are unpredictable, the control on the formation of a desired solid state assembly can be difficult to achieve. In particular, the design of crystals of purely organic molecules is still limited.

Effective crystal engineering is limited by the wide range of different forces that determine molecular interactions and ultimately the crystallization mechanism.[6] Small changes in the crystallization process may have a huge impact in the solid state assembly. In particular, the use of different solvents and/or changes of the environmental conditions like temperature, external humidity, pressure, can induce the formation of different type of polymorphs.

1.2 Supramolecular chemistry

Crystal engineering may be regarded as an application of supramolecular chemistry.

The best way to define the supramolecular chemistry is by using the words of one of the fathers of this chemistry field, Jean-Marie Lehn. The Nobel laureate defined the supramolecular chemistry as the "chemistry beyond the molecules".[7] The purpose of supramolecular chemistry is to create complex "supermolecules" using smaller building block which interacts through different non-covalent bonds.[8] These interactions are weaker than covalent bonds and include the force of attraction, like H-bonds, van der Walls forces, dipole-dipole interactions *etc*, and repulsion.

The supramolecular chemistry allows the creation of an infinite number of non-covalent supramolecular structures with tunable properties. One of the most used building blocks in supramolecular chemistry are macrocycles like calixarenes,[9] crown ethers,[10] cyclodextrins[11] and cyclic peptoids.[12] These compounds can be used as antibiotics,[13] drugs,[14] catalyst[15] *etc*.

One of the most fascinating concepts advanced by supramolecular chemistry is molecular self-assembly. In particular, molecules can organize themselves in a defined arrangement directed through non-covalent interactions. The molecular self-assembly mimics the construction of

[6] R. Dubey, M. S. Pavan, T. N. Guru Row and G. R. Desiraju, *IUCrJ*, 2014, **1**, 8-18.
[7] J. M. Lehn, *Supramolecular Chemistry, Concepts and Perspectives*, VCH, Weinmein, 1995.
[8] J. W. Steed, D. R. Turner and K. Wallace, *Core Concepts in Supramolecular Chemistry and Nanochemistry*, John Wiley & Sons, West Sussex, 2007.
[9] C. D. Gutsche, *Calixarenes*, Royal Society of Chemistry, Cambridge, 1989.
[10] C.J. Pedersen, *J. Am. Chem. Soc.*, 1967, **89**, 7017-7036.
[11] T. Wimmer, *Cyclodextrins*, Wiley-VCH Verlag GmbH & Co. KGaA, Weinheim, 2012.
[12] S. B. Y. Shin, B. Yoo, L. J. Todaro and K. Kirshenbaum, *J. Am. Chem. Soc.*, 2007, **129**, 3218-3225.
[13] A. Luther, C. Bisang and D. Obrecht, *Bioorg. Med. Chem.*, 2018, **26**, 2850-2858.
[14] E. Marsault and M. L. Peterson, *J. Med. Chem.*, 2011, **54**, 1961-2004.
[15] C. Deraedt and D. Astruc, *Coord. Chem. Rev.,* 2016, **324**, 106-122.

macromolecular assemblies in living organisms where a small number of building blocks can create an enormous amount of complex systems that are able to receive and exchange information through weak interactions.

Since the crystallization is based on specific non-covalent interactions between molecules it is a clear example of molecular recognition from the nucleation step through the crystal growth.

1.3 Non-covalent interactions

A covalent bond is created when two subsystems with unfilled electronic shells start to overlap and the electron density between them increases. The best overlap can be obtained when the distance between the two systems is below 2 Å. On the contrary, non-covalent interactions can exist at much greater distances (sometimes at more than 10 Å), do not involve electron sharing[16] but, they have enormous importance in molecular assembly. Molecular assembly is a process by which randomly distributed molecules arrange into ordered structures due to their non-covalent interactions like hydrogen bonding, halogen bonding, van der Waals force, aromatic interactions, hydrophobic effect, etc....

1.3.1 Hydrogen bond

The hydrogen bond is one of the most documented non-covalent interaction and plays a crucial role in determining the shape and functions of biological molecules.[17] By definition, an X-H···A interaction is called "hydrogen bond" if X-H acts as a proton donor to A, the acceptor. The donor may be a more electronegative atom or group than the hydrogen and the A may be another electronegative atom bearing a lone pair of electrons, for example, oxygen, nitrogen or fluorine. Moreover, considering the acid/base properties of X-H and A, a hydrogen bond can be inferred as a proton transfer reaction from X-H to A.[18] The energy of the hydrogen bond varies between 4 to 120 kJ/mol and depends on the geometry of the interaction and the nature of the donor/acceptor atoms. In addition to the importance of the distance between the H atom and the acceptor, which should be around 2.4-3.1 Å, another important parameter is the angle value X-H···A. In particular, the closer is the value to 180° more favourable is the interactions. In the case of oxygen atoms as donor or acceptor, the minimum distance observed is 1.2 Å. H-bonds are not only pure electrostatic

[16] P. Hobza and K. Müller-Dethlefs, *Non-covalent Interactions: Theory and Experiment*, RSC Publishing, Cambridge, 2010.
[17] S. J. Grabowski, *Chem. Rev.,* 2011, **111**, 2597-2625.
[18] T. Steiner, *Angew. Chem. Int. Ed.,* 2002, **41**, 48-76.

interaction, but involves a complicated mechanism. Indeed, the electron density delocalized from the lone pair orbital of proton acceptor atom to the anti-bond orbitals of the proton donor molecule has partially suggested the covalent-like feature of the H-bond.[19]

Crystallography represents one of the best tools to investigate the H-bond, but other techniques like IR and NMR spectroscopy could be also very useful. Indeed, the formation of an H-bond leads to a redshift in the infrared X-H stretching frequency and strong hydrogen bonds are revealed by a downfield shift in the ^{1}H NMR spectrum.

A very impressive example of how hydrogen bonds are important in crystal engineering are the cyclic peptides nanotubes, obtained for the first time by Ghadiri *et al*. in 1993.[20] The cyclic peptides were characterized by an alternation of D- and L- amino acids in order to obtain a ring-shaped flat conformation of the backbone. In this way, all the side chains lie perpendicular to the backbone plane. In this conformation, the cyclic peptides can stack one on top of the other interacting by means of the intermolecular hydrogen bond. Recently, Chalmers *et al.*[21] reported an example of cyclic D/L peptide, *cyclo*[(Asp-$_D$-Leu-Lys-$_D$-Leu)$_2$] that can form in the solid state antiparallel nanotubes thanks to CO···HN hydrogen bonds between the backbone carbonyl oxygen atom and the hydrogen atom attached to the backbone nitrogen atom (Figure 1.1).

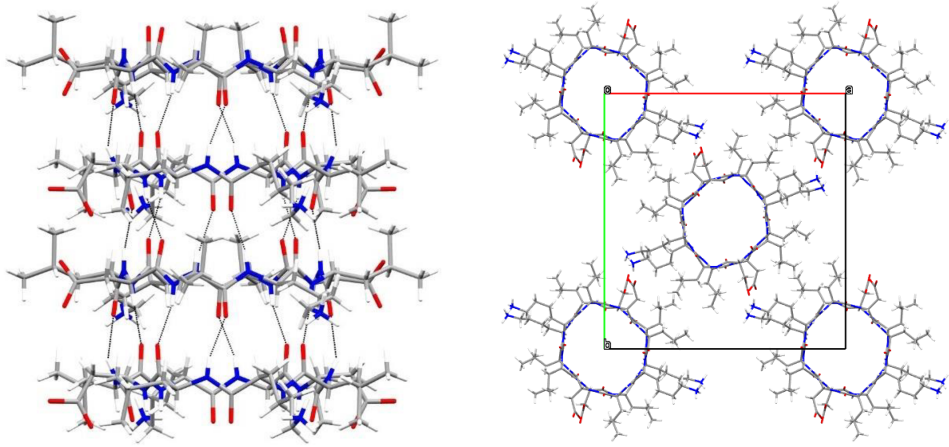

(a) (b)

Figure 1.1 (a) Example of hydrogen bonds in the cyclic peptide nanotube of *cyclo*[(Asp-$_D$-Leu-Lys-$_D$-Leu)$_2$] (CCDC number 1520676). (b) Crystal packing of the cyclic peptide nanotubes viewed along the *c* axis.

[19] Z. Zhang, D. Li, W. Jiang and Z. Wang, Adv. Phys. X, 2018, **3**, 1428915.
[20] M. R. Ghadiri, J. R. Granja, R. A. Milligan, D. E. McRee and N. Khazanovich, *Nature*, 1993, **366**, 324-327.
[21] M. R. Silk, J. Newman, J. C. Ratcliffe, J. F. White, T. Caradoc-Davies, J. R. Price, S. Perrier, P. E. Thompson and D. K. Chalmers, *Chem. Commun.,* 2017, **53**, 6613-6616.

1.3.2 Halogen bond

Recently, great attention has been given to the halogen bond. When a halogen atom is involved in the formation of a covalent bond, there is a region of higher electron density orthogonal to the covalent bond, and a region of lower electron density (σ-hole) where the potential is frequently positive. This electrophilic region associated with a halogen atom can form attractive interactions with electron-rich sites.[22] The International Union of Pure and Applied Chemistry defined the halogen bond as "evidence of an attractive interaction between an electrophilic region associated with a halogen atom and a nucleophilic region in another, or the same, molecular entity".[23]

Since the beginning of the exploration of this type of interaction, X-ray crystallography played a fundamental role in the identification of the interaction between halogen atom and electron donor species. Indeed, using X-ray diffraction it was possible to assess the halogen bond presence analysing the distance between the donor and acceptor atoms and the angle between the covalent and noncovalent bonds around the halogen atom.

The halogen bonds have been widely used in the past few years in the field of crystal engineering because they feature a stronger directionality with respect to the hydrogen bond. In a recent work, the halogen bond has been used to promote a [2+2] photodimerization in the solid state.[24] In particular, the authors use halogen bond as a template to assemble *trans*-1,2-bis(4-iodotetra-fluorophenyl)ethene in order to promote the photodimerization of two stilbene molecules to generate *rctt*-1,2,3,4-tetrakis(4-iodo-2,3,5,6-tetrafluoro-phenyl)cyclobutene after exposure to a broadband UV radiation for a period of 20 hours. To orient *trans*-1,2-bis(4-iodotetra-fluorophenyl)ethene in a correct geometry, the authors co-crystallize the olefin with 1,8-di(4-pyridyl)naphthalene. In the crystal structure, the double bonds are separated by 3.68 Å, which satisfies the criteria of Schmidt for a photodimerization reaction (Figure 1.2).

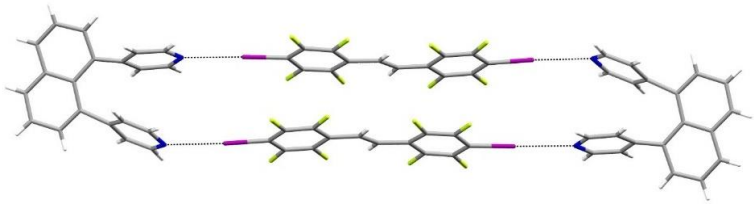

(a)

[22] G. Cavallo, P. Metrangolo, R. Milani, T. Pilati, A. Priimagi, G. Resnati and G. Terraneo, *Chem. Rev.,* 2016, **116**, 2478-2601.
[23] G. R. Desiraju, P. S. Ho, L. Kloo, A. C. Legon, R. Marquardt, P. Metrangolo, P. Politzer, G. Resnati and K. Rissanen, *Pure Appl. Chem.*, 2013, **85**, 1711-1713.
[24] M. A. Sinnwell and L. R. MacGillivray, *Angew. Chem. Int. Ed.*, 2016, **55**, 3477-3480.

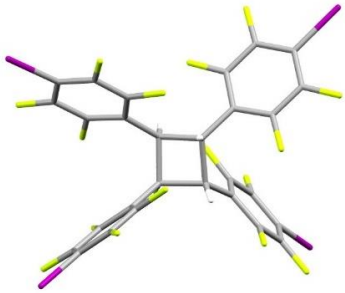

(b)

Figure 1.2 (a) X-ray crystal structure of co-crystal of *trans*-1,2-bis(4-iodotetra-fluorophenyl)ethene and 1,8-di(4-pyridyl)naphthalene (CCDC number 1436472). The halogen bond facilitates the face-to-face arrangement. (b) X-ray crystal structure of *rctt*-1,2,3,4-tetrakis(4-iodo-2,3,5,6-tetrafluoro-phenyl)cyclobutene (CCDC number 1436473).

1.3.3 Van der Waals interactions

Van der Waals interactions are weak interactions (0.4-4 kJ/mol) formed by two permanent or transient dipoles (dipole-dipole interactions or dipole-induced dipole interactions). This type of interaction is caused when a shift in the electron density is generated, creating an anisotropic distribution of the charge around the nucleus. In this way, the nearby atom can be attracted or repelled. The interaction depends on the distance between the two atoms following the Lennard-Jones equation (Eq. 1):

$$V(r) = 4\varepsilon\left[\left(\frac{\sigma}{r}\right)^{12} - \left(\frac{\sigma}{r}\right)^{6}\right] \quad 1$$

where σ is the diameter of the sphere approximating the atom, r is the distance and ε is the dielectric constant. In particular, the term r^{12} describe the repulsive term due to the overlapping electron orbitals at a short distance, while r^{6} is the attractive long-range term.

Dispersion forces, or London dispersion forces, are the weakest components of the van der Waals forces.[25] Generally, atoms or molecules of nonpolar substances show a symmetric distribution on the electron charge but, sometimes, it could happen that this distribution is not symmetric inducing the formation of an instantaneous dipole. When this happens, this fluctuation of the electron charge induces a redistribution of the electronic cloud in other atoms and the electron motions become correlated. The strength of the London forces depends on the polarizability of the atom or of the

[25] F. London, *Trans. Faraday Soc.,* 1937, **33**, 8b-26.

molecule and decreases as $-r^{-6}$. The interaction energy can be approximated using the London formula (Eq. 2):

$$V_{12} = -\frac{3}{2}\frac{I_1 I_2}{I_1 + I_2}\frac{\alpha_1 \alpha_2}{r^6} \qquad 2$$

where I is the ionization energy of each molecule, α is the polarizability, r is the distance between molecules.

1.3.4 π-π interactions

π-π interactions are weak forces generated between molecules with π-system such as benzene and are characterized by different geometries: parallel stacked, parallel displaced, edge-to-face and T-shaped (Figure 1.3). There is still a great debate about the nature of π-π interactions. Hunter and Sanders[26] noted that the electron density on aromatic rings creates a quadrupole moment, where a partial positive charge is generated around the periphery, while a partial negative charge is present above aromatic faces, generating interaction between aromatic rings, which is purely related to van der Waals forces. This model predicts that the parallel stacked geometry should be strengthened with the introduction of an electron-withdrawing substituent while the introduction of an electron-donating substituent should weaken the interaction.

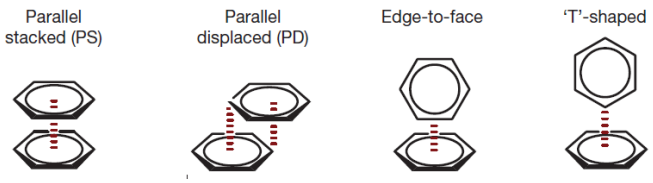

Figure 1.3 Different π-π interactions geometries.

Recently, an *ab initio* study showed that the introduction of any substituent should increase the strength of the interaction. Starting with this observation, Houk and Wheeler[27] suggested that the substituent effect on benzene dimer is related to a direct interaction of the substituent with the aromatic ring and for this reason, the π-system is not involved. In particular, they have demonstrated that the interaction energy between benzene and mono-substituted benzene (X-phe) correlate with the *meta* Hammett parameter and replacing the substituted benzene ring with a hydrogen atom (X-

[26] C. A. Hunter and J. K. M. Sanders, *J. Am. Chem. Soc.,* 1990, **112**, 5525-5534.
[27] S. E. Wheeler and K. N. Houk, *J. Am. Chem. Soc.*, 2008, **130**, 10854-10855.

H) an identical correlation has been obtained, suggesting that the aromatic ring is not involved in the interaction.

The π-system are involved also in other types of interactions like cation-π, anion-π and polar-π.

Recently, a new attractive force, the CH-π interaction, has been shown to have a significative role in a variety of chemical phenomena.[28] It was demonstrated by *ab initio* MO calculation that the energy of a typical CH-π interaction comes from dispersion force, while the electrostatic, polarization and charge transfer contributions play a less important role.[29] The interaction energy is strictly related to the nature of the molecular fragment. Generally, stronger is the proton donating ability of the C-H group, larger is the stabilizing effect.[30] The CH-π interaction has been used in many fields like supramolecular chemistry, chiral discrimination, solid state reactions, polymer science e*tc*.

An elegant example of how CH-π interaction can influence the molecular organization in the solid state is given by Sozzani's work. [31] In particular, they have demonstrated that Tris-(*o*-phenylenedioxy)spirocyclotriphosphazene (TPP) can form an adduct with polyethylene (PE) and assemble to form nanostructured material with an hexagonal lattice. Using multinuclear solid-state NMR, it was possible to underline the role of the CH-π interactions in the formation of the polymer nanostructured material (Figure 1.4).

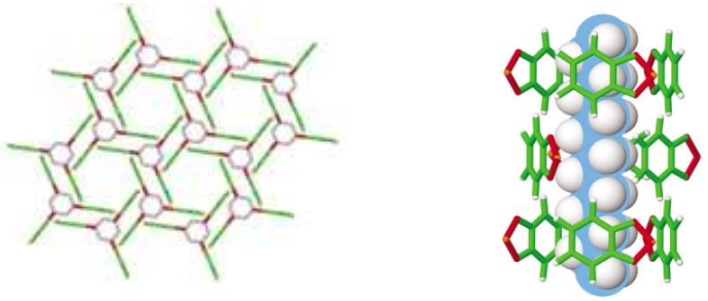

(a) (b)

Figure 1.4 (a) Hexagonal arrangement of TPP molecules. (b) Nanochannels of TPP and PE guest molecules.

[28] M. Nishio, M. Hirota and Y. Umezawa, *The CH/π Interaction. Evidence, Nature, and Consequences*, Wiley, New York, 1998.
[29] S. Sakaki, K. Kato, T. Miyazaki, Y. Musashi, K. Ohkubo, H. Ihara and C. Hirayama, *J. Chem. Soc., Faraday Trans.*, 1993, **89**, 659-664.
[30] M. Nishio, *Phys. Chem. Chem. Phys.*, 2011, **13**, 13873-13900.
[31] P. Sozzani, A. Comotti, S. Bracco and R. Simonutti, *Chem. Commun.*, 2004, **40**, 768-769.

1.3.5 Hydrophobic effect

In the solid state, another fundamental aspect that we must consider is the hydrophobic effect that can be explained as the tendency of non-polar substances to aggregate in solution in order to banish their solvating water molecules. The attractive interaction is due to enthalpic and entropic effects. In particular, nonpolar molecular surfaces tend to interact with other nonpolar molecules banishing the water molecules from the interacting surface. Generally, when water molecules surround a nonpolar solute, they establish new interactions to compensate for the weaker interactions between solute and water molecules. Therefore, the water molecules around the solute are more ordered given a negative entropy of dissolution. When two nonpolar molecules interact, they reduce their nonpolar area exposed to the solvent, reducing the amount of structured water and determining a favourable entropy of association. In the crystal engineering is widely used to the enclosure of non-polar guest molecules within, for example, cyclodextrin cavities.[32]

1.4 Dynamic behaviour in the solid state

The Nobel prize winner Lavoslav Ruzička declared "Ein Kristall ist ein chemischer Friedhof" (A crystal is a chemical graveyard). Indeed, when we talk about crystals, we imagine a solid material where all the components are highly ordered and "frozen" in their specific positions.

Nothing could be further from the truth! Understanding dynamic in the solid state offers the potential application in different fields like gas adsorption and separation, sensing, gas storage, smart materials.

By definition, a single-crystal-to-single-crystal (SCSC) transformation is a structural response to an external stimulus, such as temperature variation, light, pressure or the presence of solvents, of particular crystalline materials. During this transformation, the crystal integrity is retained.

In the next paragraphs, a brief introduction to the dynamic behaviour in the solid state will be given with the hope to convince the readers that crystals are more interesting than a graveyard.

1.4.1 Solid state photochemistry

Thanks to solid state photochemistry it is possible to synthesize different types of organic compounds with a green chemistry approach. In particular, photochemical reactions in crystals are generated due to the absorption of photons by the organic molecules.

[32] A. Bom, M. Bradley, K. Cameron, J. K. Clark, J. van Egmond, H. Feilden, E. J. MacLean, A. W. Muir, R. Palin, D. C. Rees and M.-Q. Zhang, *Angew. Chem. Int. Ed.*, 2002, **41**, 265-270.

The first example of dynamic behaviour in the solid state is given by the [2+2] photodimerization performed in the solid state using cinnamic acids molecules.[2] For these compounds, the crystalline matrix provides an extraordinary spatial control on the initiation and progress of the solid state reaction. Indeed, the cinnamic acids do not undergo dimerization in solution. In 1980, Nakanishi and collaborators demonstrated that the [2+2] photodimerization is compatible with the SCSC transition.[33a,b] This discovery confirmed that transformations of covalent bonds in the solid state are possible and it is the first evidence of an SCSC transformation. More recently, it was demonstrated that it is possible to induce a [4+4] dimerization using different anthracene derivatives molecules.[34]

1.4.2 Dynamic behaviour induced by thermal treatment

The simplest way to obtain a dynamic behaviour in the solid state is to expose crystals or powder to a thermal treatment, in this way it is possible to induce a rearrangement of the molecules in the crystal and promote the formation of another polymorph.

Unfortunately, during the thermal treatment, the molecular rearrangements can induce tension and shear, which can increase the crystal mosaicity or, in an extreme case, can induce the crystal "crack".[35]

Many strategies have been developed in order to avoid this side effect and recently, MacGillivray and co-workers[36] have demonstrated that the co-crystallization offers the opportunities to modify thermal properties of solids. The authors, using a co-crystallization procedure, were able to modify the thermal properties of crystals based on azo group favouring the pedal motion, which usually is quite rare in the single-component crystal. The authors prepared a co-crystal of 4-phenylazopyridine and 4,6-dichlororesorcinol in a ratio 2:1 where the three components assemblies alternate head-up, tail-up along the *b* axis. While the single crystal of the 4-phenylazopyridine does not show a dynamic behaviour, the co-crystal manifests a pedal motion involving the azo group (Figure 1.5). In particular, in the co-crystal is possible to obtain a twist of the pyridine and benzene ring and a pedal motion resulted in the formation of two new C-H···N hydrogen bonds. Moreover, the SCSC is correlated

[33] a) W. Jones, H. Nakanishi, C. R. Theocharis and J. M. Thomas, *J. Chem. Soc., Chem. Commun.,* 1980, 610-611 b) H. Nakanishi, W. Jones, J. M. Thomas, M. B. Hursthouse and M. Motevalli, *J. Chem. Soc., Chem. Commun.,* 1980, 611-612.
[34] I. Zouev, Den-Ke Cao, T. V. Sreevidya, M. Telzhensky, M. Botoshanskya and M. Kaftory, *CrystEngComm*, 2011, **13**, 4376-4381.
[35] J.-P. Zhang, P.-Q. Liao, H.-L. Zhou, R.-B. Lin and X.-M. Chen*, Chem. Soc. Rev.*, 2014, **43**, 5789-5814.
[36] K. M. Hutchins, R. H. Groeneman, E. W. Reinheimer, D. C. Swensona and L. R. MacGillivray, *Chem. Sci.*, 2015, **6**, 4717-4722.

also to a positive thermal expansion along with the *a* and *c* axis and a negative thermal expansion along the *b* axis.

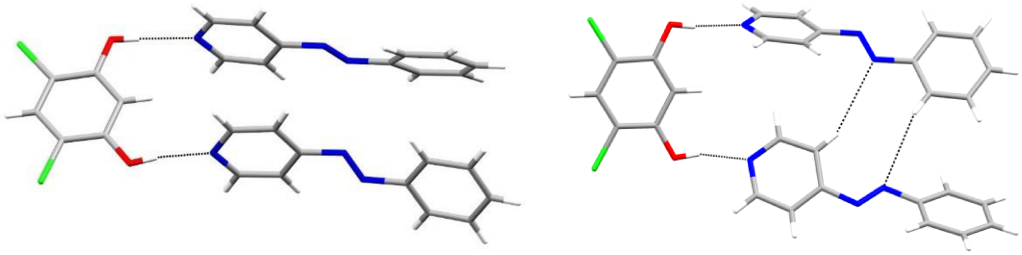

(a) (b)

Figure 1.5 (a) Face-to-face interactions of 2 azo groups at 290 K (CCDC number 1026675). (b) After the thermal treatment at 250 K (CCDC number 1026673), the benzene rings of the 2 azo groups molecules underwent to an approximate 30° twist, the pyridine of the azo group on top to a 64° twist and the pyridine of the azo group at the bottom to a 14° twist. These movements allow the formation of C-H···N hydrogen bonds.

One of the most fascinating effects of the dynamic behaviour in the solid state is related to the thermosalient effect or also known as "jumping crystal". This phenomenon can be explained as a large and anisotropic change in the unit cell volume causing the crystals to jump.[37] The first example of a jumping crystal is given by Etter[38] who was investigating on a phase transformation in a palladium compound induced by a thermal treatment. She noticed that, depending on the way the crystals were heated up, some crystal flew off the hot stage. But the first detailed study on this interesting phenomenon was carried on by Naumov in 2010.[37] In his work, Naumov focused on the molecular explanation of the phenomenon of the oxitropium bromide (OXTB) jumping crystals, which was already published in 1994.[39] In the previous work, only the crystal structure of the polymorph OXTB-A was determined, while for the high temperature polymorph (OXTB-B) only the unit cell parameters were known. After obtaining the structure of OXTB-B, it was possible to investigate the molecular mechanism, which induces the crystal jumping with a variety of different technique, like thermal, spectroscopic, microscopic and structural methods.

Crystals which undergo a thermal treatment can jump, bend, twist, rotate but in some cases, they can also walk.[40] Crystals of N-[[4-*p*-dimethylaminophenylazo]benzoyl]-1-phenylethylamine can

[37] Ž. Skoko, S. Zamir, P. Naumov and J. Bernstein, *J. Am. Chem. Soc.*, 2010, **132**, 14191-14202.
[38] M. C. Etter and A. R. Siedle, *J. Am. Chem. Soc.*, 1983, **105**, 641-643.
[39] S. Zamir, J. Bernstein and D. J. Greenwood, *Mol. Cryst. Liq. Cryst.*, 1994, **242**, 193-200.
[40] T. Taniguchi, H.Sugiyama, H. Uekusa, M. Shiro, T. Asahi and H. Koshima, *Nat. Commun.*, 2018, **9**, 538.

undergo an SCSC transformation and, during this event in the crystals start to slowly "walk" along the long *b* axis. This movement is due to the bending of the crystal caused by the molecular rearrangement: in the β-crystal phase (low temperature polymorph) the main interactions are NH···O between the two conformers A and B, while in the γ-phase (high temperature polymorph) the conformational change of benzene rings of conformers A and B allows the molecules to push away surrounding molecules along the *c* axis and to condense along the *b* axis inducing the crystal movement.

1.4.3 Solvent induced dynamic behaviour

Porous molecular solids are a class of compounds that possess intrinsic or extrinsic voids which are accessible to solvent and/or gas molecules. Intrinsic porosity is a characteristic of molecular solid, which already have guest-accessible cavities that preclude close-packing, while extrinsic porosity consists of interstitial spaces between host molecules caused by packing defects.[41]

Interestingly, some porous materials can reversibly change their structure in response to solvent removal or exchange. An elegant example is given by the Atwood's work[42] on crystals of *p*-Bu^t-calix[4]arene. This compound crystallizes in the monoclinic system and the calixarene molecules form two bilayers. Interestingly, this crystal form does not show the presence of voids. Soaking a crystal in vinyl bromide it was possible to induce an SCSC transformation and obtained a new solvatomorph characterized by the presence of vinyl bromide with a ratio of 1:1 with the host molecule. The incorporation of the vinyl bromide into the calixarene lattice does not induce a change in the bilayer packing motif, but it is possible to notice only a translation along the [210] direction. As the crystal is not characterized by voids, the authors suggested that the formation of the solvatomorph is the result of a complicated cooperative process, where the host molecules can transfer the guest inside the crystal without forming continuous channels. This is a clear example of a non-porous molecular compound that can transform to host-guest compounds upon exposure to selected gas or vapours.

Gas molecules can also induce a solid state transformation. Recently, porous organic cages gained a lot of attention because of their capability to absorb different gas[43] and exhibit stimuli-responsive dynamic sorption behaviour and reversible structure transformation.

[41] L. J. Barbour, *Chem. Commun.*, 2006, 1163-1168.
[42] J. L. Atwood, L. J. Barbour, A. Jerga and B. L. Schottel, *Science*, 2002, **298**, 1000-1002.
[43] T. Mitra, X. Wu, R. Clowes, J. T. A. Jones, K. E. Jelfs, D. J. Adams, A. Trewin, J. Bacsa, A. Steiner and A. I. Cooper, *Chem. Eur. J.*, 2011, **17**, 10235-10240.

Recently, a new type of soft porous organic cage (NKPOC-1) has been studied.[44] NKPOC-1 can absorb CO_2 showing a breathing behaviour: crystals of NKPOC-1 can switch from a closed nonporous phase (α) to two porous open phases (β and γ). The β-phase is characterized by the presence of guest molecules located in cavities between the layers, while the γ phase shows the presence of guest molecules both between and within the cage (Figure 1.6).

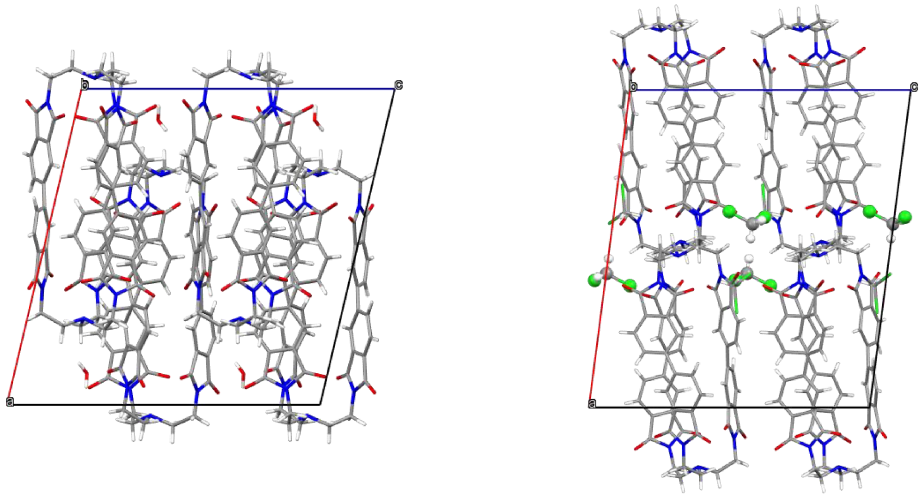

(a) (b)

Figure 1.6 (a) α- and (b) β-phase of NKPOC-1 (CCDC numbers 1904744-1904745, respectively). The β-phase shows the presence of dichloromethane as a guest molecule. The γ-phase crystal structure is not reported by the authors.

1.4.4 Mechanochemistry

Mechanochemistry is an emerging tool for molecular synthesis by using only mechanical action, conducted by grinding or milling, which has the advantage to be rapid, clean, and environmentally friendly and, often, solvent-free. According to IUPAC, a mechanochemical reaction is a "Chemical reaction that is induced by the direct absorption of mechanical energy". The reaction mechanism can be described in three phases: 1) diffusion of reactants through a mobile phase, 2) nucleation and growth of the products, 3) exposing of fresh reactant which can react to form a new product.[45]

[44] Z. Wang, N. Sikdar, S.-Q. Wang, X. Li, M. Yu, X.-H. Bu, Z. Chang, X. Zou, Y. Chen, P. Cheng, K. Yu, M. J. Zaworotko and Z. Zhang, *J. Am. Chem. Soc.*, 2019, **141**, 9408-9414.
[45] G. Kaupp, *CrystEngComm*, 2003, **5**, 117-133.

Metal-organic frameworks (MOFs),[46] a recent class of compounds which can be used in different fields like gas separation, gas storage, catalysis, as drug delivery system, can be synthesized with mechanochemistry procedure. Recently, it was demonstrated that using a mechanochemistry approach, it is possible to synthesize MOFs with a very high microporosity.[47]

Mechanical treatment of molecular solids is a quite common procedure in the industry. For example, pharmaceutical solids can be subjected to grinding that can induce polymorphic transition. This transition can be undesirable, if this event determines the deterioration of the compound properties, or desirable if it improves, for example, bioavailability.[48] The possibility to control the result of the mechanical action on pharmaceutical compounds is extremely important and for this reason, it is fundamental to understand the mechanism of the processes induced by grinding.[49]

1.5 Peptoids and cyclic peptoids

α-peptoids, or *N*-substituted glycine, are peptidomimetic compounds, which differ from peptide since the side chain is attached to the nitrogen atom (Figure 1.7), the peptoid unit is achiral and the tertiary amide bond can undergo a *cis*/*trans* isomerization.[50] These small changes have a tremendous impact on the physical properties of peptoids.

(a) (b)

Figure 1.7 Structure of generic peptide (a) and peptoid (b).

In particular, the side chain attached to the nitrogen atom guarantees the possibility to use a great variety of primary and secondary amines[51] and the *cis*/*trans* isomerization allows the side chains to

[46] O. M. Yaghi, G. Li and H. Li, *Nature*, 1995, **378**, 703-706.
[47] A. M. Fidelli, B. Karadeniz, A. J. Howarth, I. Huskić, L. S. Germann, I. Halasz, M. Etter, S.-Y. Moon, R. E. Dinnebier, V. Stilinović, O. K. Farha, T. Friščić and K. Užarević, *Chem. Commun.*, 2018, **54**, 6999-7002.
[48] J. Bernstein, *Polymorphism in Molecular Crystals*, Oxford University Press Inc., New York, 2002.
[49] T. N. Drebushchak, A. A. Ogienkoc and E. V. Boldyreva, *CrystEngComm*, 2011, **13**, 4405-4410.
[50] R. N. Zuckermann, *Biopolymers*, 2011, **96**, 545-555.
[51] J. Sun and R. N. Zuckermann, *ACS Nano*, 2013, **7**, 4715-4732.

control structure of peptoids.[52] Interesting, the abiotic character of these molecules guarantees protection from proteolytic degradation, offering a wide variety of biological applications.

Peptoid can be synthesised with different approaches. The first example was given by Bartlett and co-workers who synthesised the monomer in solution and then achieved the oligomerization on solid-phase.[53] Another approach consists of a two-step assembly of the monomer unit on solid-phase from two submonomers, the bromoacetic acid and the primary amine.[54]

Since the first studies on peptoids, the scientists have tried to obtain specific secondary structures but, because of the backbone flexibility, they are not well defined. Many studies have confirmed that a helical secondary structure can be obtained by using chiral side chains.[55] Successively, it was demonstrated that the side chain length, the presence of aromatic or aliphatic residues and the steric features of the side chain can influence the helix conformation.

Peptoids have found application in catalysis, sensors of ion and small molecules, as cellular transporter and medical imaging.[56]

To gain rigidity, peptoids can be cyclized obtaining cyclic peptoids.[12] After the synthesis on linear peptoid, the cyclization can be easily achieved using a common coupling agent which induce the head-to-tail condensation reaction. The cyclization reactions make cyclic peptoids even more resistant to proteolysis. It was demonstrated using SCXRD[57] and NMR analysis that cyclic peptoids show a sequence of *cis* and *trans* conformation of amide bond which depends on the number of residues and the complexation with a metal ion (Table 1.1).

Different strategies can be followed to obtain more rigid cyclic peptoids. The first one consists of cyclized short oligomers. Indeed, tetrameric cyclic peptoids are characterized by a structure, which is the same in the solid state and solution.[58] A second strategy involves the use of metal coordination or the introduction of sterically bulky and chiral side chains.[59]

---

[52] E. J. Robertson, A. Battigelli, C. Proulx, R. V. Mannige, T. K. Haxton, L. Yun, S. Whitelam and R. N. Zuckermann, *Acc. Chem. Res.*, 2016, **49**, 379-389.
[53] R. J. Simon, R. S. Kania, R. N. Zuckermann, V. D. Huebner, D. A. Jewell, S. Banville, S. Ng, L. Wang, S. Rosenberg, C. K. Marlowe, D. C. Spellmeyer, R. Tan, A. D. Frankel, D. V. Santi, F. E. Cohen and P. A. Bartlett, *Proc. Natl. Acad. Sci.*, 1992**, 82**, 9367- 9371.
[54] R. N. Zuckermann, J. M. Kerr, S. B. H. Kent and W. H. Moost, *J. Am. Chem. Soc.*, 1992**, 114**, 10646-10647.
[55] P. Armand, K. Kirshenbaum, A. Falicov, R. L. Dunbrack Jr, K. A. Dill, R. N. Zuckermann and F. E. Cohen, *Fold Des.*, 1997, **2**, 369-375.
[56] A. S. Culf, *Biopolymers*, 2019, **110**, e23285.
[57] C. Tedesco, L. Erra. I. Izzo and F. De Riccardis, *CrystEngComm*, 2014, **16**, 3667-3687.
[58] N. Maulucci, I. Izzo, G. Bifulco, A. Aliberti, C. De Cola, D. Comegna, C. Gaeta, A. Napolitano, C. Pizza, C. Tedesco, D. Flot, and F. De Riccardis, *Chem. Commun.*, 2008, 3927–3929.
[59] A. D'Amato, G. Pierri, C. Tedesco, G. Della Sala, I. Izzo, C. Costabile and F. De Riccardis, *J. Org. Chem.*, 2019, **84**, 10911-10928.

Cyclic peptoids found application in many heterogeneous fields. These biomimetic compounds can be used as cytotoxic molecules,[60] antimicrobical agents,[61a,b] membrane ion carrier[62] and protein binding agent.[63] In the pure chemistry field, cyclic peptoids are used as a phase-transfer catalyst.[64]

Table 1.1 Sequence of *cis* (*c*) and *trans* (*t*) conformation of amide groups in the X-ray molecular structures of cyclic peptoids.

Number of residues	Sequence
3	*ccc*
4	*ctct*
5	*ccctt*
6	*cctcct*
6 – metal complex	All-*trans*
7	*ccccttt*
8	*ccttcctt*
8 – metal complex	All-*trans*
	ctctctct
9	*ccctcccct*
10	*ccttcccctt*

1.5.1 Cyclic peptoids in the solid state

Cyclic peptoids, for their peculiar properties, are useful building blocks for the construction of supramolecular architectures with novel chemical properties. For example, cyclic hexapeptoid conformation can mimic reverse turn in proteins (Figure 1.8).

[60] A. D'Amato, R. Volpe, M. C. Vaccaro, S. Terracciano, I. Bruno, M. Tosolini, C. Tedesco, G. Pierri, P. Tecilla, C. Costabile, G. Della Sala, I. Izzo and F. De Riccardis, *J. Org. Chem.*, 2017, **82**, 8848-8863.
[61] a) M. L. Huang, S. B. Y. Shin, M. A. Benson, V. J. Torres and K. Kirshenbaum, *ChemMedChem*, 2012, **7**, 114-22; b) K. Andreev, M. W. Martynowycz, A. Ivankin, M. L. Huang, I. Kuzmenko, M. Meron, B. Lin, K. Kirshenbaum and D. Gidalevitz, Langmuir, 2016, **32**, 12905-12913.
[62] R. Schettini, C. Costabile, G. Della Sala, J. Buirey, M. Tosolini, P. Tecilla, M. C. Vaccaro, I. Bruno, F. De Riccardis and I. Izzo, *Org. Biomol. Chem.*, 2018, **16**, 6708-6717.
[63] S. Park and Y. Kwon, *ACS Comb. Sci.*, 2015**, 17**, 196-201.
[64] R. Schettini, F. De Riccardis, G. Della Sala and I. Izzo*, J. Org. Chem.*, 2016, **81**, 2494-2505.

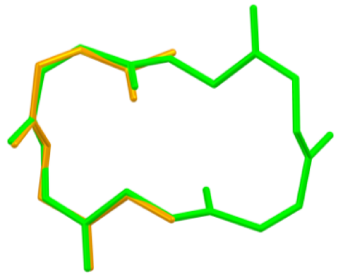

Figure 1.8 Superimposition of peptoid backbone atoms of a cyclic hexapeptoid (green) and an ideal type I β-turn (yellow). RMSD 0.142 Å.

The lack of amide protons prevents the formation of NH···OC hydrogen bonds, which are fundamental in the assembly of peptides and proteins. In cyclic peptoids, these interactions are substituted by inter-annular CH_2···OC hydrogen bonds (backbone-to-backbone interactions)[65] which can induce a face-to-face (Figure 1.9) or a side-by-side arrangement (Figure 1.10). Moreover, in the side-by-side arrangement, it is possible to recognize a side-by-side arrangement along the long side or the short side of the peptoid backbone.

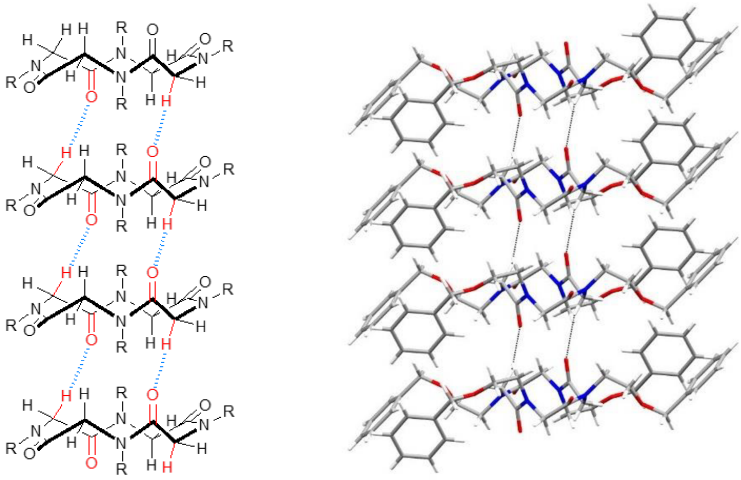

(a) (b)

Figure 1.9 (a) Network of CO···HC interactions which induces a face-to-face arrangement. (b) Example of a face-to-face arrangement in a cyclic tetrapeptoid *N*-benzyloxyethyl glycine (CCDC number 685415).

[65] D. R. Greer, M. A. Stolberg, J. Kundu, R. K. Spencer, T. Pascal, D. Prendergast, N. P. Balsara and R. N. Zuckermann, *J. Am. Chem. Soc.*, 2018, **140**, 827-833.

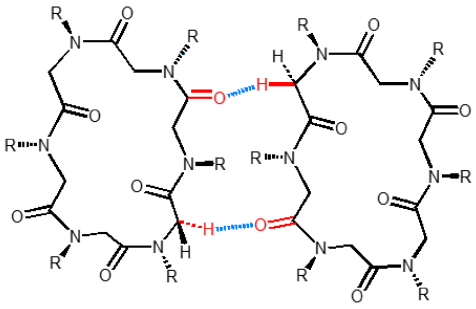

(a)

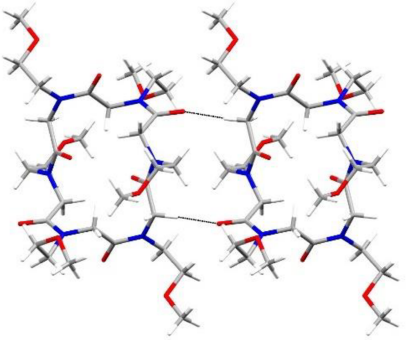

(b)

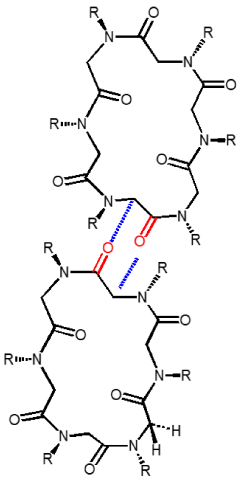

(c)

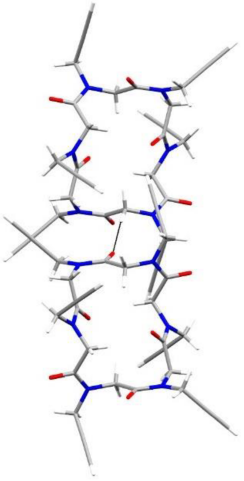

(d)

Figure 1.10 Network of CO···HC interactions which induces a side-by-side arrangement along the long side of the backbone (a) and a side-by-side arrangement along the short side of the backbone (c). (b) Example of side-by-side arrangement along the long side in a cyclic hexapeptoid *N*-methoxyethyl glycine (CCDC number 897774). (d) Example of side-by-side arrangement along the short side in a cyclic hexapeptoid *N*-propargyl glycine (CCDC number 1491786).

Different combinations of side chains and ring size lead to a variety of solid state assemblies such as columns, tubes or layers.

The columnar architecture is obtained when cyclic peptoids align one on top of the other but the space between the macrocycles is not enough to host the guest molecules. Thus, if guest molecules

are present, they usually occupy the space between the columns forming channel or cavities. It is widely known that columnar arrangement can be induced by, for example, methoxyethyl and propargyl side chains, which act as pillars extending vertically with respect to the macrocycle plane (Figure 1.11).[66]

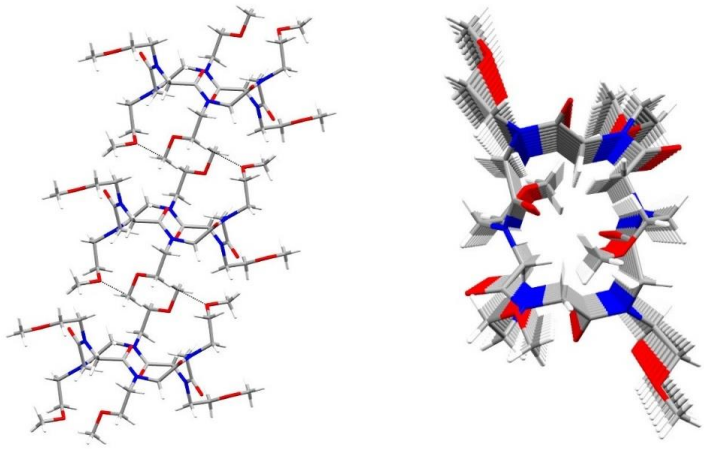

Figure 1.11 Example of the columnar arrangement mediated by side chain-to-side chain interactions in a cyclic hexapeptoid *N*-methoxyethyl glycine (CCDC number 897774).

Other two typical solid state arrangements of cyclic peptoids are tubes and layers.[67] The tubular architecture is obtained when the macrocycles align one on top of the other forming cavities where the guest molecules are located (Figure 1.12). The layer arrangement often involves side-by-side interactions that can be backbone-to-side chain or backbone-to-backbone (Figure 1.13).

[66] C. Tedesco, E. Macedi, A. Meli, G. Pierri, G. Della Sala, C. Drathen, A. N. Fitch, G. B. M. Vaughan, I. Izzo and F. De Riccardis, *Acta Crystallogr., Sect. B: Struct. Sci., Cryst. Eng. Mater.*, 2017, **73**, 399-412.
[67] C. Tedesco, A. Meli, E. Macedi, V. Iuliano, A. G. Ricciardulli, F. De Riccardis, G. B. M. Vaughan, V. J. Smith, L. J. Barbour and I. Izzo, *CrystEngComm*, 2016,**18**, 8838-8848.

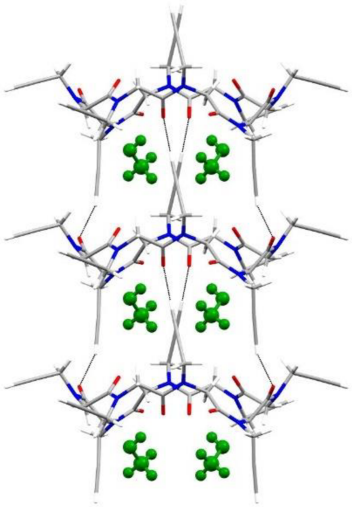

Figure 1.12 Example of tubular arrangement mediated by backbone-to-side chain interaction of a cyclic octapeptoid *N*-propargyl glycine (CCDC number 1491788). Methanol guest molecules are depicted in green. The interactions between the macrocycle and guest molecules are not reported.

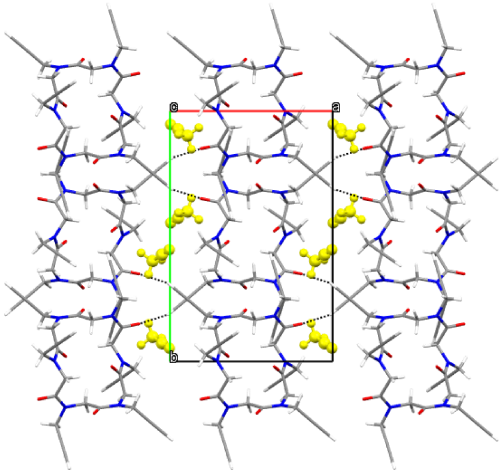

Figure 1.13 Example of layer arrangement mediated by backbone-to-side chain interaction of a cyclic hexapeptoid *N*-propargyl glycine (CCDC number 1491786). Acetonitrile guest molecules are depicted in yellow. The interactions between the macrocycle and guest molecules are not reported.

With the aim to understand and control the solid state assembly of the cyclic peptoids, the role of the side chain in the crystal packing was deeply investigated.

Recently, we have demonstrated that the substitution of two *N*-propargyl side chains in a cyclic octapeptoid full propargylated, with two *N*-methoxyethyl side chains, can improve the solid state stability forming permanent 1D porosity.[68] Indeed, while crystals of cyclic octapeptoid *N*-propargyl glycine tend to fade after the loss of the guest molecules, removing the solvent molecules in crystals of *cyclo*-[(*N*pa)$_3$(*N*me)]$_2$ induces the formation of the apohost structure without destroying the crystal. In this fascinating example, the methoxyethyl side chains act as an H-bond acceptor by tightening as wall ties the host framework.

Beyond the nature and/or the length of the side chains, the size of the macrocycle is another important variable that can have an active role in the determination of the solid state assembly of the cyclic peptoids. Recently, it was demonstrated that using the same side chains but varying the macrocycle size, it is possible to obtain different solid state assembly. In particular, considering two cyclic peptoids decorated with propargyl side chains but characterized by a different ring size, two different solid state arrangements have been obtained: the cyclic hexapeptoid shows a layer arrangement with the guest molecules localized between the macrocyclic layers (Figure 1.12), while cyclic octapeptoid forms nanotubes where the guest molecules occupy the voids inside the peptoid nanotube (Figure 1.13).[67]

1.6 Screening of organic crystals with interesting dynamic behaviour

Since the purpose of this Ph.D. project is to identify dynamic behaviour in the solid state, it was necessary to solve the structure of several different organic compounds (not only peptoids) in order to identify the most interesting for our studies. The screening was necessary since, at state of the art, it is not possible to predict a dynamic behaviour in the solid state *a priori* knowing only the chemical formula or the crystal packing.

In particular, during these 3 years, different class of compounds were characterized by means of SCXRD analysis: phthalides, isoindolinones, multi-heteroatomic cyclic compounds and peraza-macrocycles. Unfortunately, except for a specific 3,3-disubstituted isoindolinone, it was not possible to highlight any dynamic behaviour for these compounds.

Phthalides are aromatic butyrolactones compounds, widely distributed in nature, which can be used in medicinal chemistry[69] and as a useful building block for the synthesis of pharmaceutical

[68] C. Tedesco, R. Schettini, V. Iuliano, G. Pierri, A. N. Fitch, F. De Riccardis and I. Izzo, *Cryst. Growth Des.*, 2019, **19**, 125-133.
[69] R. Karmakar, P. Pahari and D. Mal, *Chem. Rev.*, 2014, **114**, 6213-6284.

compounds.[70a,b,c] For this class of compounds, five crystals structure were determined and reported in two different papers.[71a,b] In particular, in the first case the crystal structure of two different 3,3-disubstituted phthalides obtained via arylogous Michael reaction of 3-aryl have been determined,[71a] while in the second case the crystal structure of three different 3-monosubstituted phthalides obtained by a highly diastereoselective arylogous Michael reaction using mild reaction conditions have been characterized.[71b] In these two works, the X-ray single crystal diffraction analysis was fundamental to define the stereochemistry of the reaction products.

X-ray single crystal analysis was performed also on a 3,3-disubstituted isoindolinone obtained by the reaction of 2-acetylbenzonitriles with dimethyl malonate.[72] More recently, it was proposed a new procedure for the synthesis of the 2-cyanobenzophenones that can be used in the synthesis of a 3,3-disubstituted isoindoline.[73] In both cases, the X-ray diffraction analysis confirms the formation of a tetrasubstituted carbon.

Thanks to the X-ray diffraction analysis, it was possible to prove the formation of a new class of multi-heteroatomic cyclic compounds containing the N,S-acetal functionality by an asymmetric cascade reaction of thiols and 2-cyano-N-tosylbenzylidenimine.[74] The X-ray diffraction analysis proved undoubtedly the presence of an imine group.

In recent work, we proposed a new synthetic approach for the synthesis of peraza-macrocycles. This important class of compound are usually synthesized via alkylation of polyaza-cycloalkanes by ring-opening of epoxides or by Eschweiler-Clarke methylation. Unfortunately, these two approaches have a limitation on the side chain diversity. With our approach, it is possible to install the desired side chains on a cyclic peptoid and then a reduction of the tertiary amide groups determines the formation of the peraza-macrocycle.[75] The X-ray diffraction analysis allowed us to confirm the

[70] a) D. Mal, K. Ghosh and S. Jana, Org. Lett., 2015, 17, 5800-5803; b) J. N. N. Eildal, J. Andersen, A. S. Kristensen, A. M. Jørgensen, B. Bang-Andersen, M. Jørgensen and K. Strømgaard, *J. Med. Chem.* 2008, **51**, 3045-3048, c) K. Rathwell and M. A. Brimble, *Synthesis*, 2007, **15**, 643-662.

[71] a) M. Sicignano, A. Dentoni Litta, R. Schettini, F. De Riccardis, G. Pierri, C. Tedesco, I. Izzo and G. Della Sala, *Org. Lett.*, 2017, **19**, 4383-4386; b) M. Sicignano, R. Schettini, L. Sica, G. Pierri, F. De Riccardis, I. Izzo, B. Maity, Y. Minenkov, L. Cavallo and G. Della Sala, *Chem. Eur. J.*, 2019, **25**, 7131-7141.

[72] A. Di Mola, M. Di Martino, V. Capaccio, G. Pierri, L. Palombi, C. Tedesco and A. Massa, *Eur. J. Org. Chem.*, 2018, 1699-1708.

[73] A. Di Mola, A. Macchia, C. Tedesco, G. Pierri, L. Palombi, R. Filosa and A. Massa, *ChemistrySelect*, 2019, **4**, 4820-4826.

[74] V. Capaccio, A. Capobianco, A. Stanzione, G. Pierri, C. Tedesco, A. Di Mola, A. Massa and L. Palombi, *Adv. Synth. Catal*,. 2017, **359**, 2874-2880.

[75] R. Schettini, A. D'Amato, G. Pierri, C. Tedesco, G. Della Sala, O. Motta, I. Izzo and F. De Riccardis, *Org. Lett.*, 2019, **21**, 7365-7369

formation of the desired compound and describe the complexation properties of the peraza-macrocycles.

1.7 Aim of the thesis

Since molecules within a crystal interact mainly by means of weak interactions, even small changes in the environmental condition could cause dramatic consequences on the crystal packing and, most of the time, induce the loss of crystallinity of the compound. Thus, the principal goal of this thesis is the understanding of how organic crystals are able to adapt and modify their crystal packing in response to external stimuli like thermal treatment, exposure to different gases or solvents.

To reach this ambitious goal, we have widely used X-ray diffraction analysis. Thanks to this fascinating and powerful technique, it is possible to characterize the organic compounds and their solid state assembly. Furthermore, performing single crystal and powder X-ray diffraction analysis in non-ambient conditions, it is possible to have unequivocal proof of the structural changes in the solid state assembly of the studied compounds and monitor all the crystal packing changes.

Moreover, to fully understand how molecules interact in crystals, different computational method, like PIXEL and the energy framework analysis, have been used. Thanks to these two tools, it is possible to obtain intermolecular energy values which are fundamental to figure out what are the main interactions in the studied organic crystals. Furthermore, comparing the energy values of two different crystal forms related by an SCSC transformation, it is possible to directly correlate the "old" and the "new" crystal packing and highlight the formation or the loss of interactions.

Moreover, crystal structure changes will be investigated also by means of differential scanning calorimetry (DSC) and thermal gravimetric analysis (TGA). The combination of these two thermoanalytical techniques, combined with the X-ray diffraction analysis, offers additional information to better understand the dynamic behaviour in the solid state.

Two different class of compounds are investigated: cyclic peptoids and a 3,3-disubstituted isoindolinone. The first class of compounds was chosen since it was widely demonstrated that cyclic peptoids can respond to external stimuli and form porous crystal structures. In particular, we studied:

- an hexacyclic peptoid decorated with four propargyl and two methoxyethyl side chains (compound **1**), which exhibits an SCSC transformation from an acetonitrile solvate crystal form (form 1A) to an anhydrous crystal form (form 1B). In particular, we decided to investigate how polymorphs and solvatomorphs respond to external stimuli;
- an hexacyclic peptoid decorated with four methoxyethyl and two propargyl side chains (compound **2**) characterized by an unusual number of polymorphs and solvatomorphs;

- two cyclic hexapeptoids decorated with alkyl side chains (compound **3** and compound **4**) to highlight the role of the side chains in the solid state assembly;
- a 3,3-disubstituted isoindolinone (compound **5**), which crystallize as a toluene solvate, where the guest molecules appear to strongly interact with the host.

CHAPTER II

Cyclo-[(*N*me-*N*pa$_2$)$_2$]

In this chapter, a description of the results obtained working with *cyclo*-[(*N*me-*N*pa$_2$)$_2$] (**1**) (Figure 2.1) will be given.

In particular, the first paragraph is dedicated to a brief description of the compound and its behaviour in the solid state. Then the energetic aspect of an SCSC transformation regarding a crystal form of this compound is deeply investigated in the second paragraph. The last paragraph is entirely dedicated to its X-ray powder diffraction analysis. In particular, a detailed discussion about the thermal behaviour and gas absorption properties of the compound are given.

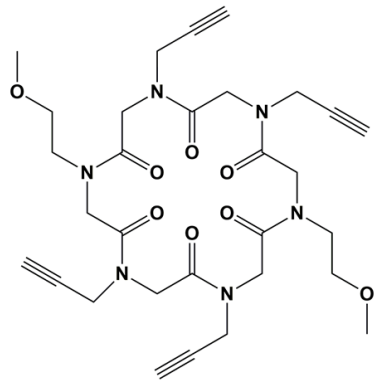

Figure 2.1 *Cyclo*-[(*N*me-*N*pa$_2$)$_2$] (**1**). *N*me = *N*-(methoxyethyl)glycine, *N*pa = *N*-(propargyl)glycine.

2.1 Compound 1

Compound **1** has been synthesised following the standard procedure: the linear precursor has been synthesized using the sub-monomer approach[54] and then cyclized under high dilution condition with 1-[Bis(dimethylamino)methylene]-1H-1,2,3-triazolo[4,5-b]pyridinium 3-oxid hexafluorophosphate (HATU) as the coupling agent.

2.1.1 CH-π zipper

Crystals of compound **1** can be obtained dissolving the cyclic peptoid in hot acetonitrile, obtaining an acetonitrile solvate crystal form (form 1A) with a ratio of 1:2 between the cyclic peptoid and acetonitrile molecules.[76] This crystal form possesses a crystallographic inversion centre and a distorted *cctcct* conformation of the peptoid backbone. Moreover, form 1A shows two methoxyethyl and two propargyl side chains which point vertically with respect to the macrocycle plane, while two propargyl side chains extend horizontally. The cyclic peptoids align along the shortest *c* axis by means of CO···HC interactions (Figure 2.2) involving the oxygen atom of the backbone and the terminal hydrogen atom of the vertical propargyl side chain. The solvent molecules are located into the void between columns forming channel parallel to the *c* axis.

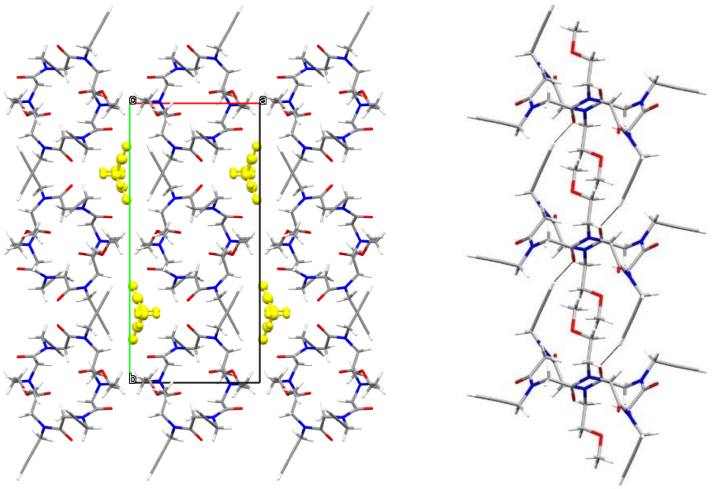

(a) (b)

Figure 2.2 (a) Crystal packing of form 1A (CCDC number 1431223) viewed along the shortest *c* axis. Acetonitrile molecules are depicted in yellow (b) Columnar arrangement of the cyclic peptoid molecules in form 1A.

Differential scanning calorimetry (DSC) and thermal gravimetric analysis (TGA) demonstrated that acetonitrile molecules are released when crystals are heated from 30 to 85° C and hot-stage microscopy (HSM) shows that the loss of the guest molecules does not affect the shape of the crystals. X-ray single crystal diffraction analysis (SCXRD) revealed that after the thermal treatment and the

[76] A. Meli, E. Macedi, F. De Riccardis, V. J. Smith, L. J. Barbour, I. Izzo and C. Tedesco, *Angew. Chem. Int. Ed.*, 2016, **55**, 4679-4682.

loss of solvents, a solvent-free crystal form has been obtained (form 1B). This new crystal form shows two independent molecules in the asymmetric unit (Figure 2.3), type A and type B molecules, and half of the cyclic peptoid molecules adopt a new conformation in order to better occupy the space left behind by the guest molecules. In particular, the two vertical propargyl side chains move horizontally with respect to the macrocyclic plane with a variation of 113° and the molecules align on top of the other by means of CH···O interactions involving the methoxyethyl side chains and the oxygen atoms of the backbone.

Soaking experiments have demonstrated that the crystals of form 1B can adsorb acetonitrile and transform into the form 1A promoting a reversible SCSC transformation.

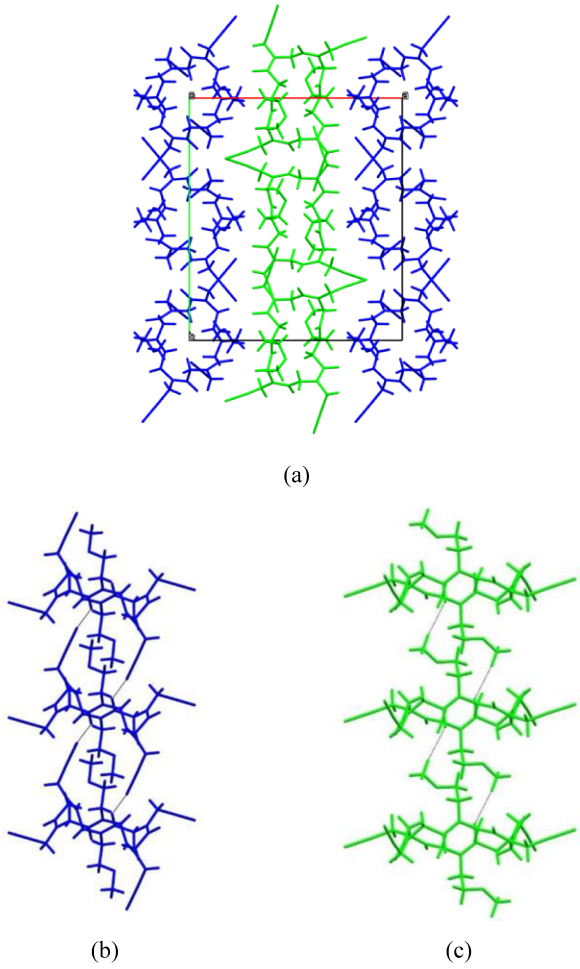

Figure 2.3 (a) Crystal packing of form 1B (CCDC number 1431224) viewed along the shortest *c* axis. Type A molecules are depicted in blue, while type B molecules in green. Columnar arrangement of type A (b) and type B molecules (c).

The dynamic behaviour can be explained as a synchronized motion and the propargyl side chain movement allows the formation of CH-π interactions between methylene H atoms and propargyl triple bond of adjacent columns, forming a CH-π zipper (Figure 2.4). The CH-π zipper can be closed or open: when the crystals release the solvent molecules the propargyl side chains rotate by 113° and close the zipper, with the guest uptake the propargyl side chains return to their starting position facilitating the solvent absorption.

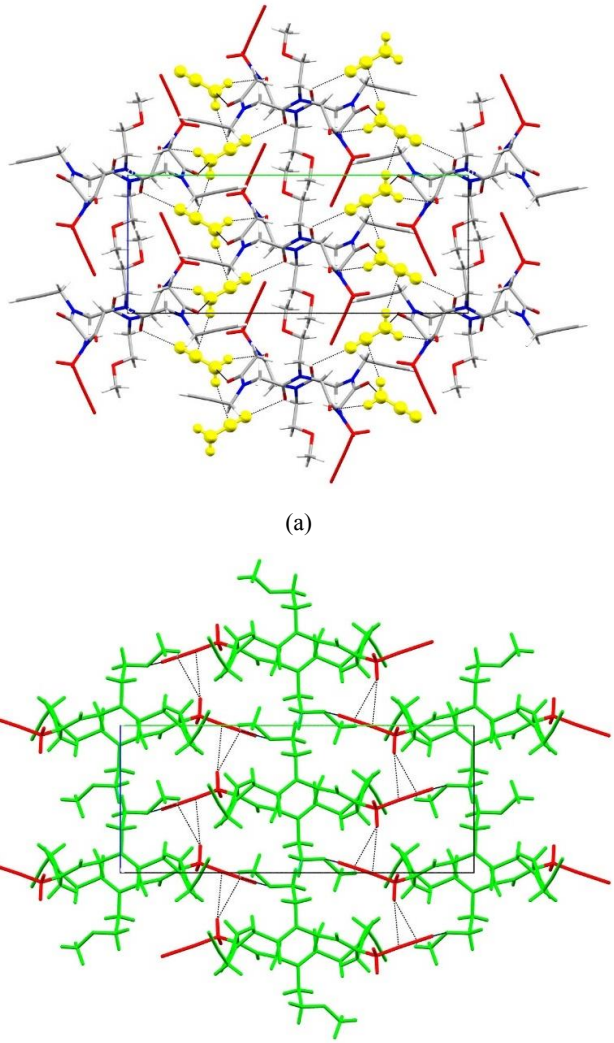

(a)

(b)

Figure 2.4 Comparison between the open (a) and closed (b) CH-π zipper. The acetonitrile guest molecules are depicted in yellow and the propargyl side chains which move during the transformation are depicted in red.

2.1.2 Solvatomorphic behaviour of compound 1

Changing the crystallization solvent, it is possible to obtain different crystal forms of compound **1** (Figure 2.5).[77] In particular, two different crystal forms can be obtained using a different mixture of solvents: the form 1C using acetonitrile/water and the methanol solvate form 1D using acetonitrile/methanol solution. Notably, these two crystal forms exhibit differences in the solid state assembly and in the macrocycle conformation. In the form 1C both propargyl side chains show a *trans* conformation, while the form 1D the methoxyethyl side chain corresponds to the *trans* conformation.

Another difference is related to the solid state assembly. In particular, in the form 1C, it is possible to recognize a layered arrangement in the *ab* plane guaranteed by backbone-to-side chain $CO\cdots H_2C$ interactions involving the methoxyethyl and propargyl side chains. In the form 1D, the main motif is related to the columnar arrangement along the short axis provided by backbone-to-side chain interactions involving the *cis* propargyl side chains acting as a pillar.

In the form 1D, the methanol molecules occupy the cavities between the columns and are bonded to the macrocycle by means of H-bonds involving the *cis* carbonyl oxygen atom. Exposing a crystal of form 1D to the open air, it is possible to exchange the methanol molecules with water molecules obtaining the water solvate crystal form 1E which is isostructural with form 1D. The water molecules occupy the cavities previously occupied by methanol molecules and are bonded to the *cis* carbonyl oxygen atom. Interestingly, an anhydrous form 1F can be obtained removing the guest molecules performing an *in situ* VT-SCXRD experiment (Figure 2.6). This new form shows the presence of voids and despite this aspect, the columnar arrangement is still intact highlighting the robustness of the cyclic peptoid framework.

[77] E. Macedi, A. Meli, F. De Riccardis, P. Rossi, V. J. Smith, L. J. Barbour, I. Izzo and C. Tedesco, *CrystEngComm*, 2017, **19**, 4704-4708.

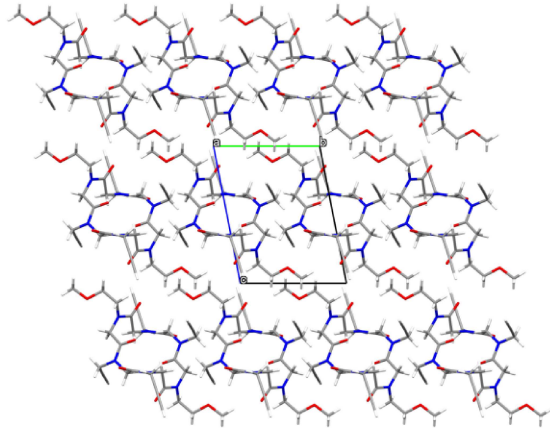

(a)

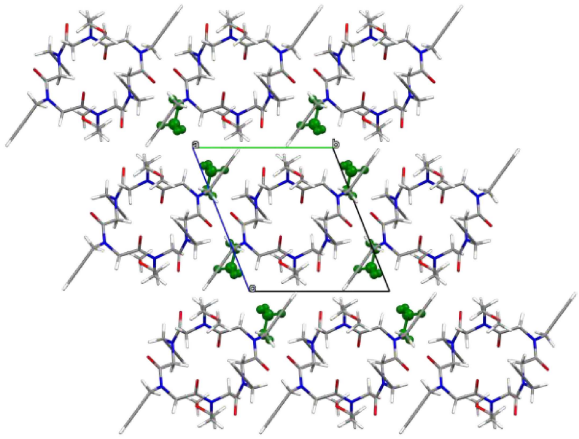

(b)

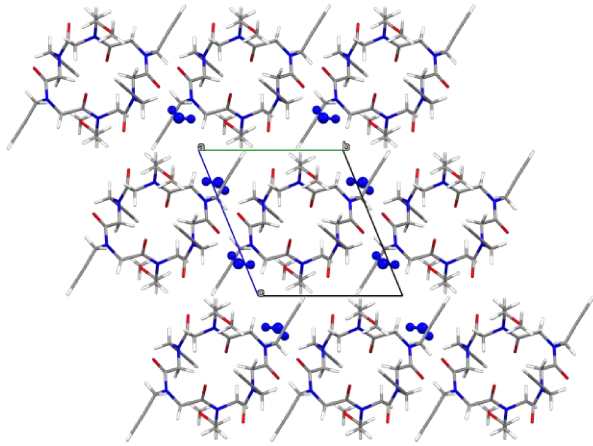

(c)

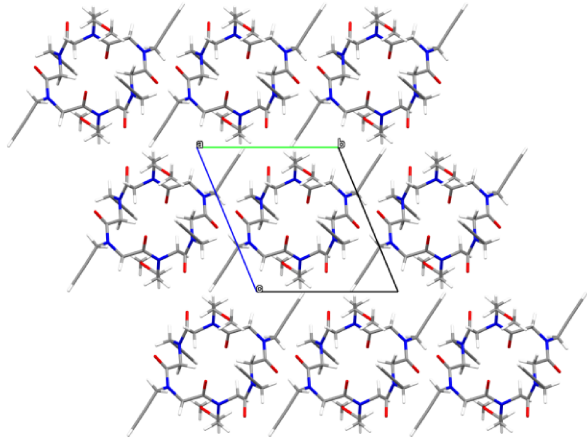

(d)

Figure 2.5 Crystal packing of form 1C (a), 1D (b), 1E (c) and 1F (d) viewed along the shortest axis. In the form 1D, the methanol guest molecules are depicted in green, in form 1E the water guest molecules are depicted in blue. (CCDC numbers 1545931-1545934).

These studies confirm the conformational flexibility of the cyclic peptoids and the peculiar absorption properties (Figure 2.6). Notably, in the crystal form 1D and 1E the guest molecules interact with a specific backbone oxygen atom, which acts as a binding site.

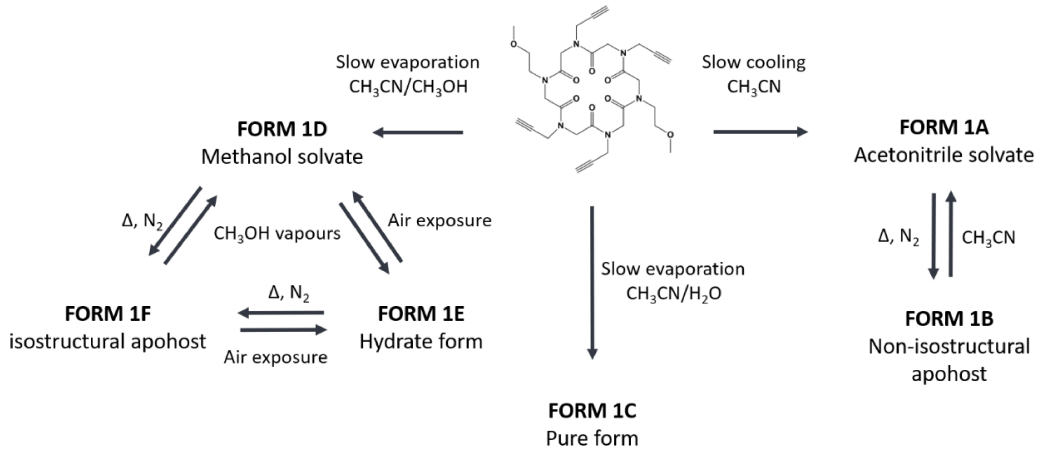

Figure 2.6 Schematic representation of the different crystal forms that can be obtained changing the crystallization solvents or the environmental conditions.

It is interesting to notice that the absorption and desorption mechanism is different between the different crystal forms. Indeed, in the crystal form 1A the release of the guest molecules causes a dramatic change in the solid state assembly of the cyclic peptoids, while in the form 1D and 1E the release of the guest molecules induces the formation of an isostructural apohost structure with stable cavities.

2.2 Energetic aspects of the SCSC transformation

A solid state transformation is a fascinating phenomenon which gained a lot of attention in the last few years, as can be deduced by the increase in the number of publications. To better understand the mechanism of the transformation and the reason for the molecular rearrangement in the solid state, is fundamental to study the energetic aspect of the transformation.

Using different tools like CLP-PIXEL,[78a,b,c] energy frameworks analysis,[79a,b] Hirshfeld surfaces[80] and DFT periodic calculations performed using the CRYSTAL14 software[81a,b], it was possible to deeply investigate the reversible SCSC transformation of compound **1**.[76]

[78] a) A. Gavezzotti, *New J. Chem.*, 2011, **35**, 1360-368; b) A. Gavezzotti, *J. Phys. Chem. B*, 2003, **107**, 2344-2353; c) A. Gavezzotti, *J. Phys. Chem. B*, 2002, **106**, 4145-4154.
[79] a) M.J. Turner, S.P. Thomas, M.W. Shi, D. Jayatilaka and M.A. Spackman, *Chem. Commun.*, 2015, **51** ,3735-3738; b) C.F. Mackenzie, P.R. Spackman, D. Jayatilaka and M.A. Spackman, *IUCrJ*, 2017, **4** ,575-587.
[80] J.J. McKinnon, M.A. Spackman and A.S. Mitchell, *Acta Cryst. B*, 2004, **60** ,627-668.
[81] a) R. Dovesi, R. Orlando, A. Erba, C. M. Zicovich-Wilson, B. Civalleri, S. Casassa, L. Maschio, M. Ferrabone, M. De La Pierre, P. D'Arco, Y. Noel, M. Causa, M. Rerat and B. Kirtman.

2.2.1 DFT periodic calculations

The energy values of the transformation have been defined using the developer version of the software CRYSTAL14. Since the peptoidic system is characterized by many atoms, we decided to perform all the calculation using HF-3c method (Hartree-Fock) with a MINIX basis set. Thus, it was possible to drastically reduce the computational time obtaining good results as well. Full optimization of the crystal structures, included the unit cell parameters, has been performed at Γ point at room temperature (Table 2.1).

The HF-3C method was developed to fill the gap between existing semiempirical methods and Density Functional Theory (DFT) in terms of cost-accuracy ratio. The meaning of "3C" is related to the 3 corrections applied to the method: dispersion, basis set superimposition error (BSSE) and short-ranged basis set incomplete errors (SRB). [82] The calculation of the electronic energy is performed with a standard HF treatment. The MINIX basis set consists of different sets of basis functions for different groups of atoms: valence scaled minimal basis set MINIS and the split valence double-zeta basis sets SV, SVP and def2-SV(P).

To evaluate the results of the optimization, the structures of the macrocycle obtained with SCXRD analysis were superimposed with the structures obtained after the optimization, showing only small differences (Figure 2.7).

Table 2.1 Unit cell parameters of the form 1A and 1B obtained after the optimization. The calculations have been performed at Γ point using HF-3c method and MINIX basis set.

	Form 1A	**Form 1A HF-3c**	**Form 1B**	**Form 1B HF-3c**
***a* (Å)**	9.773	9.822 (+0.50%)	17.887	18.040 (+0.86%)
***b* (Å)**	20.961	21.245 (+1.35%)	20.335	20.476 (+0.69%)
***c* (Å)**	8.5	8.610 (+1.29%)	8.4716	8.546 (+0.88%)
***β* (°)**	90.990	91.982 (+1.09%)	93.160	92.895 (-0.28%)
***V* (Å^3)**	1740.98	1795.52 (+3.13%)	3076.71	3152.55 (+2.46%)

Int. J. Quantum Chem., 2014, **114**, 1287-1317, b) R. Dovesi, V. R. Saunders, C. Roetti, R. Orlando, C. M. Zicovich-Wilson, F. Pascale, B. Civalleri, K. Doll, N. M. Harrison, I. J. Bush, P. D'Arco, M. Llunell, M. Causà and Y. Noël, CRYSTAL14 User's Manual (University of Torino, Torino, 2014).

[82] R. Sure and S. Grimme, *J. Comput. Chem.*, 2013, **34**, 1672-1685.

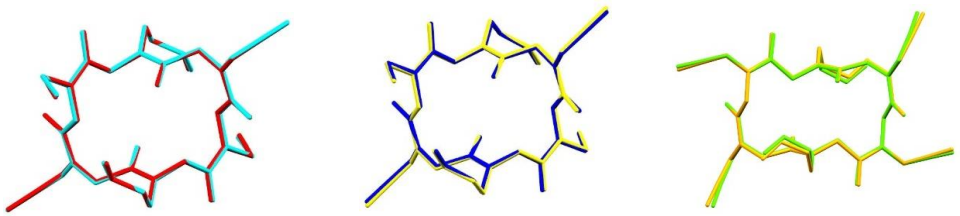

(a) (b) (c)

Figure 2.7 (a) Superimposition of the crystal structure of form 1A (red) and the structure obtained after the optimization (cyan). RMSD 0.066 Å. (b) Superimposition of type A molecule of the form 1B (blue) and the type A molecule obtained after the optimization (yellow). RMSD 0.074 Å. (c) Superimposition of type B molecule of the form 1B (blue) and the type B molecule obtained after the optimization (orange). RMSD 0.145 Å. Hydrogen atoms have been omitted for clarity.

As we expected, the transformation of the form 1B to the form 1A is energetically favoured (ΔE_1= -193.9 kJ/mol). Since the energy values obtained using CRYSTAL14 are given in kJ/mol, it was necessary to halve the energy value calculated for the form 1B, since it possesses two independent molecules in the asymmetric unit. Using this expedient, it was possible to make comparable the energy values of the form 1B and the form 1A (Figure 2.8, Eq. 3). The energy associated with the acetonitrile molecules was calculated considering the molecules in the gas phase.

$$\Delta E_1 = E_{form\,1A} - \left[\left(\frac{E_{form\,1B}}{2}\right) + (4 * \mathrm{CH_3CN})\right] \quad 3$$

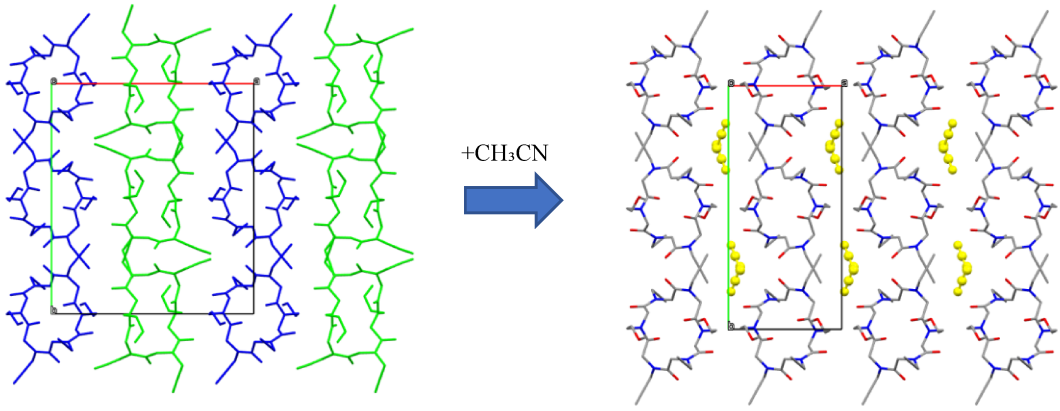

Figure 2.8 Transformation of the form 1B to the acetonitrile solvate crystal form 1A. Hydrogen atoms have been omitted for clarity.

When the form 1A releases the acetonitrile molecules, the resulting crystal forms, without any rearrangements, shows voids which occupy the 4.4% of unit cell volume (Figure 2.9). As expected, the loss of solvent is a non-favoured process ($\Delta E_2 = 218.8$ kJ/mol). To calculate the energy associated with the loss of solvent, the acetonitrile molecules have been virtually removed and the resulting structure (form 1A*) has been optimized.

$$\Delta E_2 = \left[(4 * \mathrm{CH_3CN}) + E_{form\ 1A*}\right] - E_{form\ 1A} \qquad 4$$

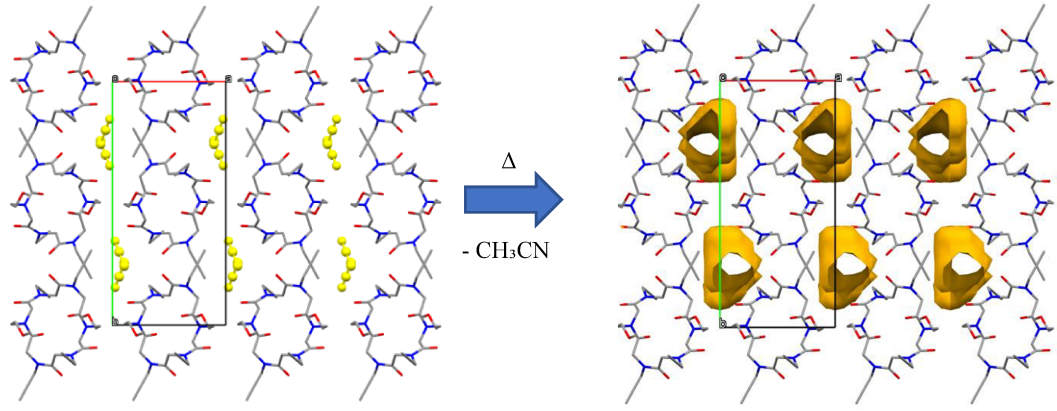

Figure 2.9 The loss of acetonitrile molecules induces the formation of voids which are thermodynamically unfavored. Hydrogen atoms have been omitted for clarity.

Considering the high positive energy value calculated in the previous equation, the loss of acetonitrile is, of course, a not favoured process from the energy point of view.

What makes possible the SCSC transformation is the conformational flexibility of the cyclic peptoids. Indeed, thanks to the conformational change in a row of cyclic peptoids it is possible to fill the voids left behind by the acetonitrile molecules and induce the formation of a much more stable crystal form (Figure 2.10). This event is energetically favoured (ΔE_3 = -24.9 kJ/mol, Eq. 5). Also in this case, it was necessary to halve the energy value calculated for the form 1B.

$$\Delta E_3 = \left[\left(\frac{E_{form\ 1B}}{2}\right) - E_{form\ 1A}\ *\right] \quad 5$$

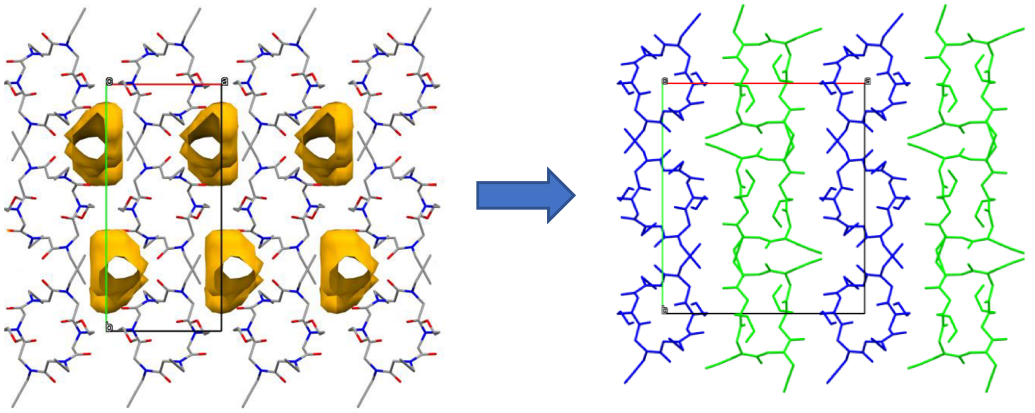

Figure 2.10 The conformational change of the cyclic peptoid allows the formation of the form 1B. Hydrogen atoms have been omitted for clarity.

In a very simple way, it was also possible to calculate the cohesive energy (ΔE^c) related to the formation of the form 1B. To obtain such value, the molecule type A and type B of the form 1B have been optimized in the gas phase using HF-3c MINIX basis set. After obtaining the two energy values, the mean value was calculated (E_{mean}) and the ΔE^c (-218.3 kJ/mol) has been calculated with the following equation (Eq.6):

$$\Delta E^c = \left[\left(\frac{E_{form\ 1B}}{4}\right) - E_{mean}\right] \quad 6$$

2.2.2 Intermolecular potential energies

To better understand the effects that conformational change has on crystal packing, we exploited Hirshfeld surface analysis and lattice energy calculations, also augmented by energy frameworks analysis.

The energy framework analysis, combined with the PIXEL calculation, is a useful tool to describe in a very straightforward way the intermolecular interaction energies governing the crystal packing. Energy framework calculations with CE-B3LYP/6-31G(d, p) and Hirshfeld surface analysis have been performed using the software CrystalExplorer 17.5,[83] while the lattice energy calculation was performed using CLP-PIXEL package.[78] In this dissertation, for all the calculations, the lengths of X-H bonds are normalized using standard X-H distances.[84] Thus, reported X-H distances and X···H contacts refer to the recalculated structures and are not equal to those calculated from the original cif files.

In Table 2.2 and 2.3 are reported the intermolecular distances (Å), angles (°) and interaction energies (kJ/mol) in the host framework of form 1A and 1B.

As already mentioned in the previous paragraph, form 1A is characterized by a columnar arrangement (motif I; Figure 2.11 a) involving the vertical *cis* propargyl side chain and the carbonyl oxygen atom of the backbone (C10-H10···O1 = 2.08 Å; O1···H10-C10 = 161.6°). Moreover, it is possible to recognize a CH-π interaction between the methylene atom of the *trans* methoxyethyl side chain and the triple bond of the *cis* vertical propargyl (C14-H14B···C10≡ = 2.71 Å; C10≡···H14B-C14 = 120.2°). The importance of these interactions can be deduced analysing the Hirshfeld surface (Figure 2.11 b). Indeed, the interaction between the propargyl side chain and the oxygen atom of the backbone is highlighted with a big intense red spot, which means that the interaction is very strong. In addition, also the CH-π interaction is showed as a small red spot.

[83] M. J. Turner, J. J. McKinnon, S. K. Wolff, D. J. Grimwood, P. R. Spackman, D. Jayatilaka and M. A. Spackman, *CrystalExplorer17*. University of Western Australia, 2017.
[84] F. H. Allen, D. G. Watson, L. Brammer, A. G. Orpen and R. Taylor, *International Tables for Crystallography Vol. C: Mathematical, Physical and Chemical Tables 3rd ed.*; Prince, E., Ed.; Kluwer Academic, Dordrecht, The Netherlands, 2004.

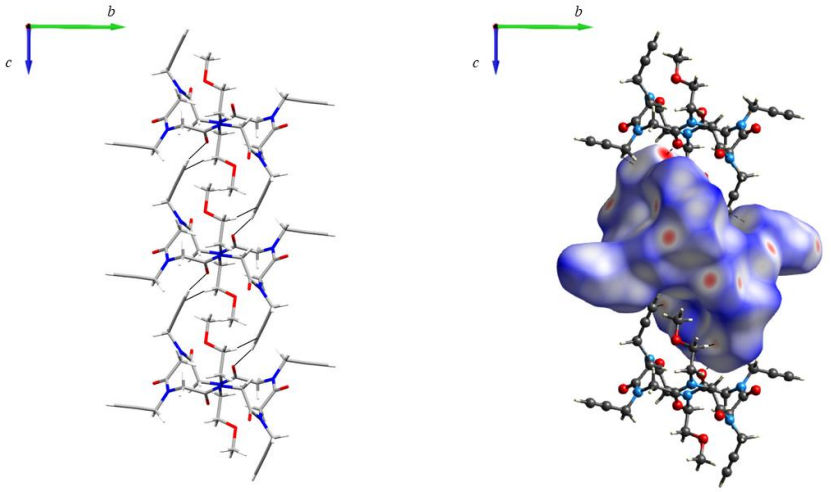

(a) (b)

Figure 2.11 (a) Motif I of the form 1A. (b) Hirshfeld surface mapped with d_{norm} of motif I.

The macrocycle molecules align along the *a* axis (motif II; Figure 2.12 a) by means of CH···OC interactions involving the carbonyl oxygen atom and the hydrogen atom of the *trans* methoxyethyl side chain (C13-H13B···O3 = 2.27 Å; O3···H13B-C13 = 141.2°). This side-by-side interaction is evident in the Hirshfeld surface (Figure 2.12 b).

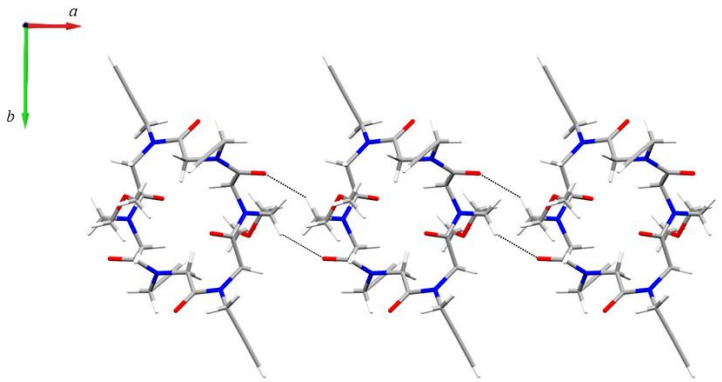

(a)

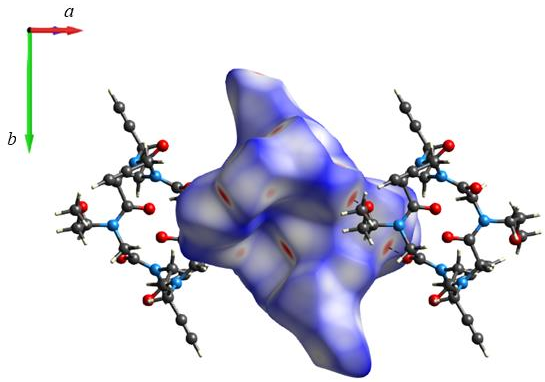

(b)

Figure 2.12 (a) Motif II of the form 1A. (b) Hirshfeld surface mapped with d_{norm} of motif II.

In motif III the cyclic peptoids align along the unit cell diagonal by means of CH···OC interactions (Figure 2.13 a). In particular, it is possible to notice a backbone-to-side chain interaction involving the *cis* propargyl side chain (C8-H8A···O2 = 2.33 Å; O2···H8A-C8 = 138.4°) and side chain-to-side chain interaction, which involves the *trans* methoxyethyl side chain and the equatorial *cis* propargyl side chain (C5-H5···O4 = 2.38 Å; O4···H5-C5 = 129.7°). Analysing the Hirshfeld surface (Figure 2.13 b), it is possible to notice that the two types of interactions are characterized by two small red spots indicating that the interactions are not so strong.

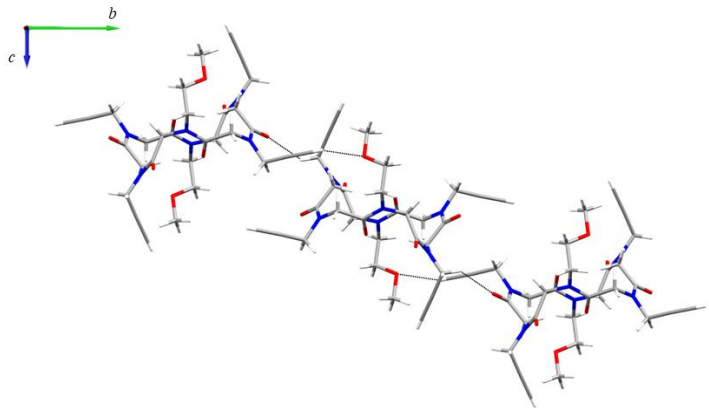

(a)

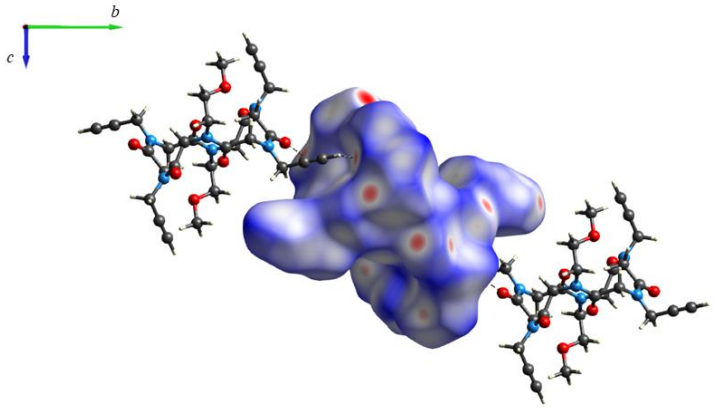

(b)

Figure 2.13 (a) Motif III of the form 1A. (b) Hirshfeld surface mapped with d_{norm} of motif III.

Acetonitrile molecules occupy the voids between the cyclic peptoid columns, forming channels parallel to *c* axis. The guest molecules are linked together by means of CH-π interactions. Acetonitrile molecules interact with macrocycle by means of the methyl hydrogen atom and backbone oxygen atoms (C17-H17C···O3 = 2.36 Å; O3···H17C-C17 = 141.8°; C17-H17B···O2 = 2.60 Å; O3···H17C-C17 = 150.2°) and the nitrogen atom of the acetonitrile molecule and the methylene hydrogen atom of the *trans* methoxyethyl side chain (C13-H13A···N4 = 2.64 Å; N4···H13A-C13 = 124.3°). In Figure 2.14 are reported the motif I-S and II-S. The interactions between the guest molecules and the macrocycle are quite weak. Indeed, the Hirshfeld surface highlight only a small red spot related to the interaction between the hydrogen atom H17C and O3. The other interactions are characterized by white spots.

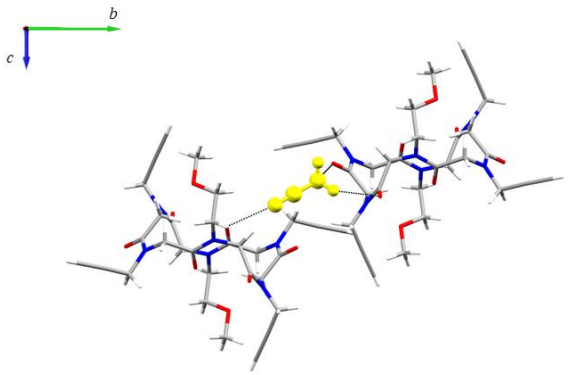

(a)

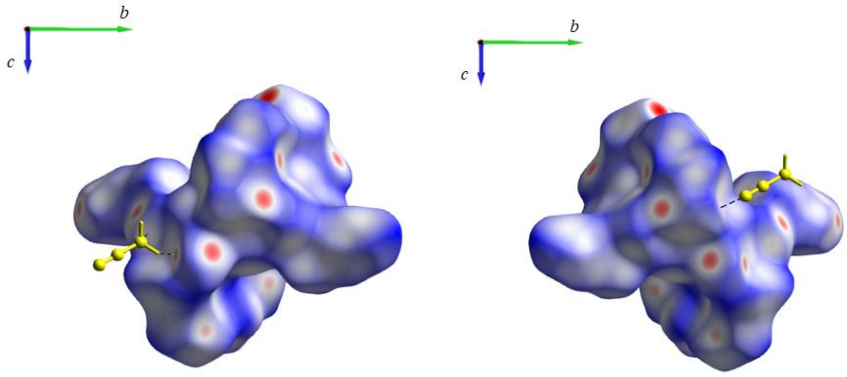

(a) (c)

Figure 2.14 (a) Motif I-S and II-S of the crystal form 1A. Hirshfeld surface mapped with d_{norm} of motif I-S (b) and II-S (c).

Table 2.2 List of intermolecular distances (Å), angles (°) and interaction energies (kJ/mol) in the framework of form 1A. The motifs which describe the interactions between host and guest molecules are indicated with an "S". Energy values are reported in kJ/mol.

Motif	D-H···A	H···A (Å)	D-H···A (°)	Symm. Op.	Centroid Distance (Å)	E_{Coul}	E_{Pol}	E_{Disp}	E_{Rep}	E_{Tot}
I	C10-H10···O1	2.08	161.6	x, y, -1 +z	8.500	-78.0	-30.5	-96.5	111.6	-93.6
	C14-H14B···C10≡	2.71	120.2	x, y, 1 +z						
II	C13-H13B···O3	2.27	141.2	-1+x, y, z	9.773	-30.4	-15.5	-35.9	40.8	-41.0
				1+x, y, z						
III	C8-H8A···O2	2.33	138.4	1-x, -1/2+y, 1/2 -z	11.309	-23.1	-9.1	-35.4	32.7	-35.0
	C5-H5···O4	2.38	129.7							
				1-x, 1/2+y, 1/2-z		-22.9	-9.0	-34.8	32.6	-34.2
				1-x, -1/2+y, 3/2-z						
				1-x, 1/2+y, 3/2-z						
I-S	C13-H13A···N4	2.64	124.3	x, y, z	6.626	-13.1	-4.8	-11.7	11.5	-18.1
II-S	C17-H17C···O3	2.36	141.8	1+x, y, z	7.559	-10.2	-3.7	-10.9	8.9	-15.8
	C17-H17B···O2	2.60	150.2							

Since the form 1B is characterized by the presence of two independent molecules in the asymmetric unit, we will take into accounts the interactions between type A and type A molecules, then the interactions between type B and type B molecules and, finally, the interactions between type A and type B molecules.

Type A molecules show a conformation very similar to the cyclic peptoid of the form 1A, therefore also the solid state assembly is identical. The main motif is characterized by a columnar arrangement of the cyclic peptoids along the shortest *c* axis (Figure 2.15 a). The main interaction is a CH···OC interaction involving the hydrogen atom of the vertical propargyl side chain and the oxygen atom of the backbone (C10B-H10B···O1B = 2.03 Å; O3···H17C-C17 = 167.5°). A CH-π interaction is established between the hydrogen atom of the *trans* methoxyethyl side chain and the triple bond of the vertical *cis* propargyl side chain (C15B-H15F···C9B≡ = 2.76 Å; C9B≡···H15F-C15B = 155.2°). By inspecting the Hirshfeld surface (Figure 2.15 b), the interaction that determines the columnar assembly is highlighted by a big red spot.

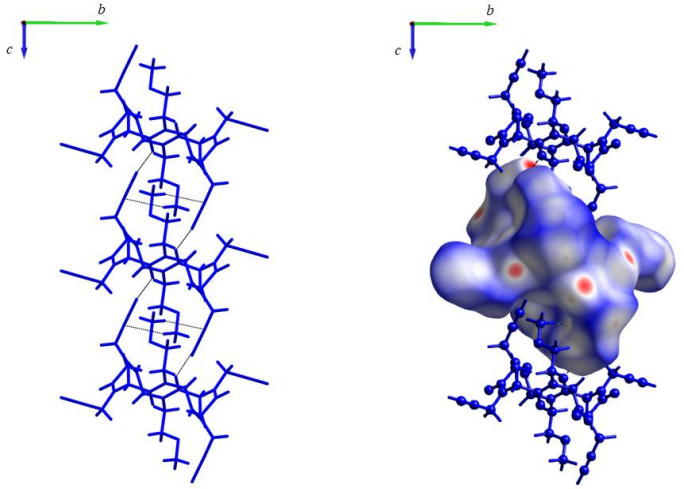

(a) (b)

Figure 2.15 (a) Motif I A-A of the form 1B. (b) Hirshfeld surface mapped with d_{norm} of motif I A-A.

In motif II, type A molecules align along the unit cell diagonal by means of CH···OC interactions (Figure 2.16 a) which involve the *cis* propargyl side chain and the carbonyl oxygen atom (C8B-H8D···O2B = 2.24 Å; O2B···H8D-C8B = 138.5°) and the *trans* methoxyethyl side chain and the equatorial *cis* propargyl side chain (C5B-H5B···O4B = 2.56 Å; O4···H5-C5 = 112.9°). Although this assembly is the same as the motif I the form 1A, comparing the Hirshfeld surface of motif I A-

A and motif I, it is possible to appreciate that in motif I A-A the spots are smaller and light red (Figure 2.16 b).

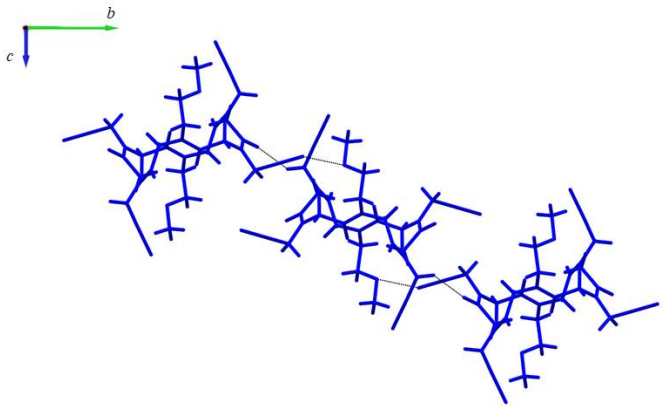

(a)

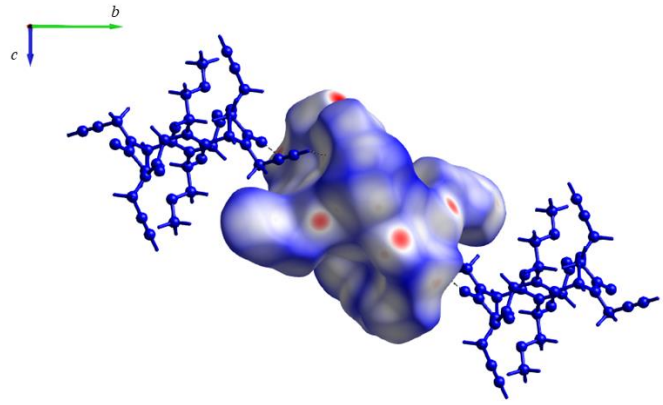

(b)

Figure 2.16 (a) Motif II A-A of the form 1B. (b) Hirshfeld surface mapped with d_{norm} of motif II A-A.

The conformational change has a tremendous impact on the crystal packing. In particular, the columnar arrangement is not anymore the main motif in the arrangement of type B molecules and energy values of the intermolecular interactions is considerably lower than the values of the columnar arrangement in the form 1A or in the type A molecules of the form 1B.

In motif I B-B (Figure 2.17), the cyclic peptoids molecules align along unit cell diagonal. The interactions involve the *cis* propargyl side chain and the *trans* methoxyethyl side chain (C10A-H10A···O4A = 2.24 Å; O2B···H8D-C8B = 126.7°) and a backbone-to-backbone interaction (C7A-H7B···O2A = 2.13 Å; O2A···H7B-C7A = 169.9°). Moreover, the *cis* propargyl which rotates by

113°, interacts with the methylene hydrogen atom of the other propargyl side chain by means of CH-π interactions. This rotation induces the closing of the CH-π zipper. The Hirshfeld surface shows that only backbone-to-backbone interaction is very strong. Indeed, this interaction is characterized by an intense red spot, while the other two interactions show a light red and a white spot.

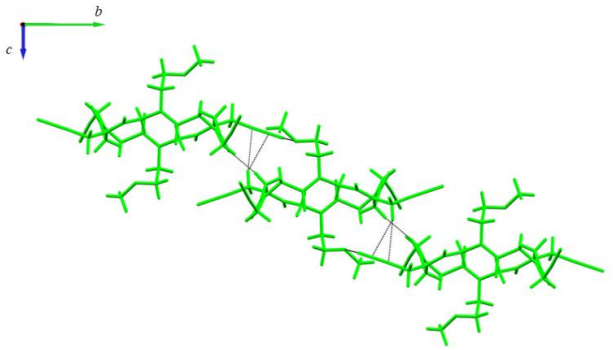

(a)

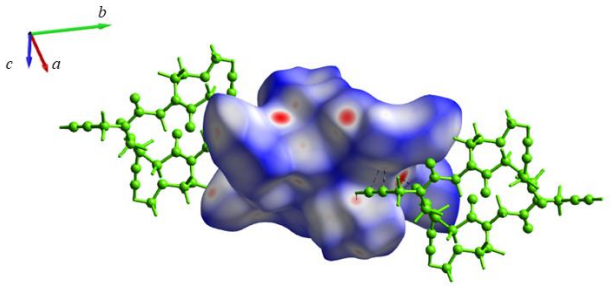

(b)

Figure 2.17 Motif I B-B of the form 1B. (b) Hirshfeld surface mapped with d_{norm} of motif I B-B.

The columnar arrangement (motif II B-B, Figure 2.18 a) is assured by CH···OC interaction between the methylene hydrogen atom of the *trans* methoxyethyl side chain and the oxygen atom of the backbone (C15A-H15A···O1A = 2.47 Å; O1A···H15A-C15A = 171.4°).

Comparing the red spots indicating the columnar arrangement of type B molecules (Figure 2.18 b) with the spots related to the same motif in the form 1A and in form 1B type A molecule, it is clear that the columnar arrangement in type B molecules is less efficient.

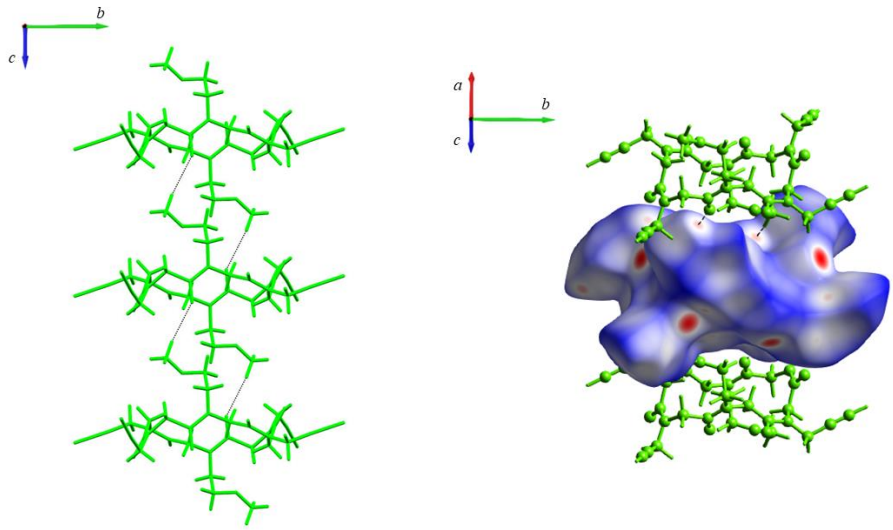

(a) (b)

Figure 2.18 Motif II B-B of the form 1B. (b) Hirshfeld surface mapped with d_{norm} of motif II B-B.

The two different conformers align along the *a* axis (Figure 2.19 a) and interact by means of a large number of contacts involving:

- the hydrogen atom of the *cis* propargyl side chain of the type B molecule and the carbonyl oxygen atom of the backbone of the type A molecule (C5A-H5A···O2B = 2.60 Å; O2B···H5A-C5A = 118.1°);
- the methylene hydrogen atom of the backbone of the type A molecule and the carbonyl oxygen atom of the backbone of the type B molecule (C2A-H2B···O3B = 2.16 Å; O3B···H2B-C2A = 151.1°);
- the hydrogen atom of *trans* methoxyethyl side chain of the type B molecule and the carbonyl oxygen atom of the backbone of the type A molecule (C13A-H13B···O3B = 2.50 Å; O3B···H13B-C13A = 137.1°);
- the hydrogen atom of the *trans* methoxyethyl side chain of the type A molecule and the oxygen atom of the backbone of the type B molecule (C13B-H13D···O3A = 2.54 Å; O3A···H13D-C13B = 135.8°);
- the methylene hydrogen atom of the backbone of the type A molecule and the oxygen atom of the backbone of the type B molecule (C2B-H2D···O3A = 2.23 Å; O3A···H2D-C2B = 154.6°);

- CH-π interaction between the *cis* propargyl side chain of the type B molecule and the triple bond of the *cis* propargyl side chain (C8A-H8A···C5B≡ = 2.73 Å; C5B···H8A-C8A = 130.8°);
- The methylene hydrogen atom of the *trans* methoxyethyl side chain of the type A molecule and the double bond of the carbonyl group of the type B molecule (C13B-H13D···C1A = 2.72 Å; C1A···H13D-C13B = 144.5°).

The Hirshfeld surface (Figure 2.19 b) gives us an idea of how strong the interactions between the two different conformers are. In addition to the big red spot related to the backbone-to-backbone interactions, it is possible to notice numerous light red and white spots related to other weaker interactions between the two molecules.

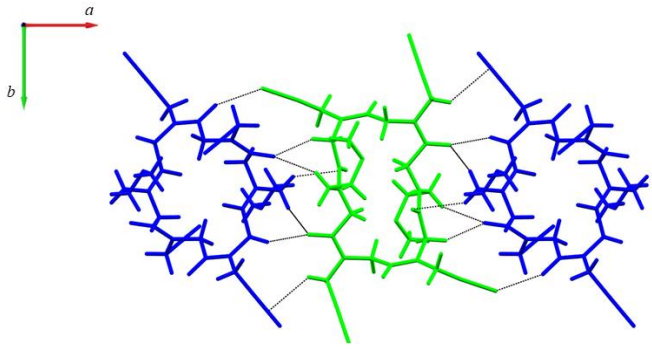

(a)

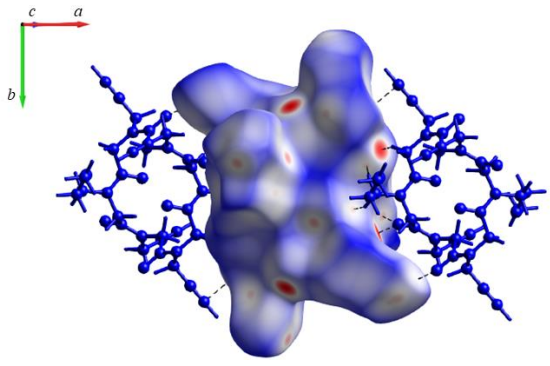

(b)

Figure 2.19 (a) Motif I A-B. (b) Hirshfeld surface mapped with d_{norm} of motif I A-B.

Table 2.3 List of intermolecular distances (Å), angles (°) and interaction energies (kJ/mol) in the framework of form 1B. Energy values are reported in kJ/mol.

Motif	D-H···A	H···A (Å)	D-H···A (°)	Symm. Op.	Centroid Distance (Å)	E_{Coul}	E_{Pol}	E_{Disp}	E_{Rep}	E_{Tot}
I A-A	C10B-H10B···O1B	2.03	167.5	x, y, -1 +z x, y, 1 +z	8.472	-78.9	-31.6	-94.7	112.1	-93.1
II A-A	C8B-H8D···O2B C5B-H5B···O4B	2.24 2.56	138.5 112.9	-x, 1/2+y, 1/2-z -x, -1/2+y, 1/2-z -x, -1/2+y, 3/2-z -x, 1/2+y, 3/2-z	11.015	-20.9	-8.5	-35.7	33.9	-31.2
I B-B	C7A-H7B···O2A C10A-H10A···O4A C8A-H8B···C9A≡C10A	2.13 2.24 2.71, 2.78	169.9 126.7 163.9, 141.1	1-x, -1/2+y, 1/2-z 1-x, -1/2+y, 3/2-z 1-x, 1/2+y, 1/2-z 1-x, 1/2+y, 3/2-z	11.015	-32.9	-15.4	-53.7	49.8	-52.2
II B-B	C15A-H15A···O1A	2.47	171.4	x, y, -1+z x, y, 1+z	8.472	-31.7	-9.8	-47.9	38.8	-50.7
I A-B	C5A-H5A···O2B C2A-H2B···O3B C13A-H13B···O3B C13B-H13D···O3A C2B-H2D···O3A C8A-H8A···C5B≡ C13B-H13D···C1A	2.60 2.16 2.50 2.54 2.23 2.73 2.72	118.1 151.1 137.1 135.8 154.6 130.8 144.5	x, y, z 1+x, y, z -1+x, y, z	8.944	-56.9	-21.2	-61.1	69.2	-70.0

Numbers are numbers! In order to visualize and better understand the crystal packing, a useful tool is the energy frameworks analysis, which combines the calculation of the intermolecular interaction energies with a graphical representation of their magnitude. The relative strength of the crystal packing along a particular direction will be represented as a cylinder. Larger are the cylinders, stronger is the intermolecular interaction energies! In this very simple but efficient way, it is possible to visualize the supramolecular architecture of molecular crystal structures.

As already described, the main motif that characterizes the form 1A crystal packing is the columnar arrangement. This observation is further corroborated by the energy frameworks analysis. Indeed, analysing Figure 2.20 a it is possible to clearly visualize the importance of this motif in the crystal packing. Comparing the diameter of the cylinders related to the columnar arrangement to the cylinders that indicate the relative strength of motif II and III (Figure 2.20 b), it is clear that the columnar arrangement is the dominant motif in the crystal packing of form 1A.

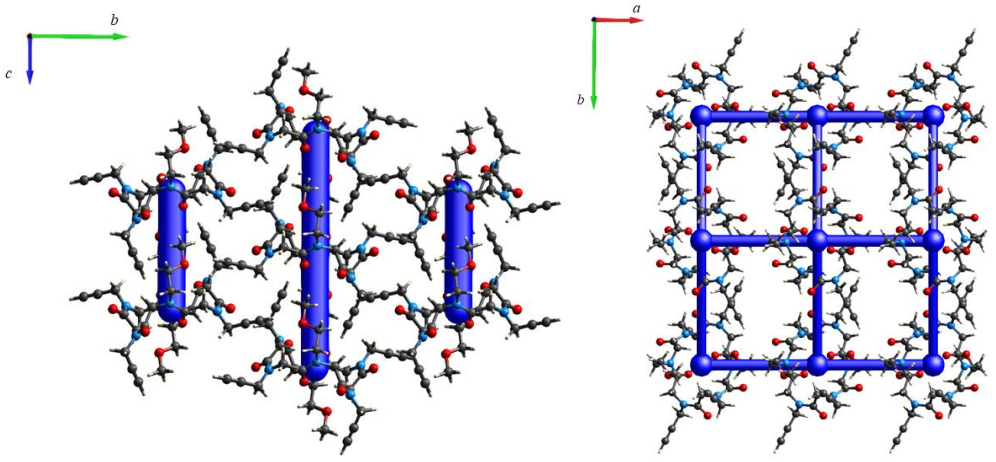

(a) (b)

Figure 2.20 Energy frameworks of form 1A. To highlight the columnar arrangement (a), the cylinders related to the other motifs have been omitted. (b) The energy frameworks related to motif II and III are almost identical. Acetonitrile molecules have been omitted for clarity.

The dramatic conformational change induces a dramatic change in the solid state assembly. This event can be easily noted analysing the energy frameworks of type A and type B molecules. The main difference is related to the columnar arrangement: while the type A molecules present the same columnar arrangement of motif I in form 1A, the type B molecules are characterized by a less efficient columnar arrangement. The columnar arrangement in the form 1A and in the type A molecules is guaranteed by the vertical propargyl side chain. But, after the transition, this side chain

undergoes a rotation and the propargyl moves to the equatorial plane with respect to the cyclic peptoid backbone. For this reason, the columnar arrangement is guaranteed by the *trans* methoxyethyl side chain that points vertically with respect to the macrocycle plane. Thanks to the Hirshfeld surface analysis, it was possible to observe that the methoxyethyl side chains cannot establish a strong interaction with the cyclic peptoids above and below, defining a weaker columnar arrangement.

All these observations are supported by the energy frameworks analysis (Figure 2.21 a,b). Indeed, the diameter of the cylinders related to the columnar arrangement of type A molecules is much bigger than the cylinders related to type B molecules.

Though the columnar arrangement is less favoured, the type B molecules show a better arrangement along the unit cell diagonal (motif I B-B) as can be seen by the energy frameworks and the energy values calculated using PIXEL. Interestingly, this motif is guaranteed, in addition to the side chain-to-side chain and backbone-to-backbone interactions, by the CH-π interaction between the propargyl that rotates and the propargyl side chain of a cyclic peptoid below.

Thus, the conformational change does not guarantee the formation of an efficient columnar assembly, which is replaced by more efficient side-by-side interactions. Analysing the energy framework results, in type B molecules is evident that there is no predominant arrangement and the alignment along the unit cell diagonal and the side-by-side arrangement are characterized by the same relative energy.

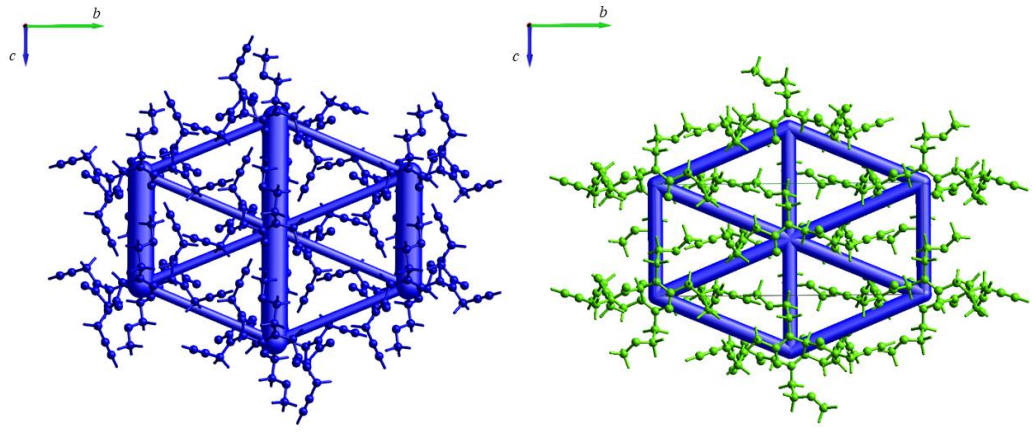

(a) (b)

Figure 2.21 Comparison between the energy framework of type A molecule (a) and type B (b) molecule of form 1B.

The reason for the SCSC transformation is in the interaction between the different conformers. Indeed, a closer look at the interaction between type A and type B molecule and to the energy frameworks showing the interaction between them, allows us to explain what happens after the transformation (Figure 2.22).

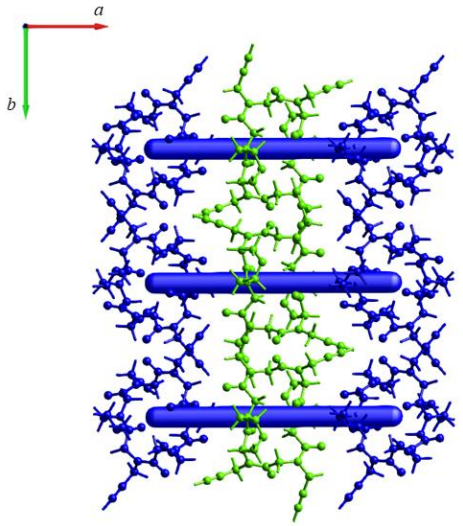

Figure 2.22 Energy frameworks of motif I A-B.

The loss of acetonitrile induces the formation of voids. Since the voids are thermodynamically unstable, a row of cyclic peptoids undergoes a conformational change in order to better occupy the voids left behind by the guest molecules. Despite the type B molecules show a less efficient columnar arrangement (-52.2 kJ/mol respect to the -93.6 kJ/mol of form 1A), the conformational change allows the formation of stronger assembly along the unit cell diagonal of the type B molecules and a better side-by-side interactions between the two conformers (-70.0 kJ/mol respect to the -41.0 kJ/mol of form 1A). These new interactions, which directly involve the rotation of the propargyl side chain, can replace the role of the acetonitrile molecules in the crystal packing.

The uptake of acetonitrile causes a less efficient side-by-side interaction, but the presence of the guest molecules compensates for this effect.

In conclusion, the SCSC transformation of form 1A to Form 1B is guaranteed by the conformational change of cyclic peptoid. Indeed, thanks to this event the cyclic peptoid molecules can better occupy the space left behind by the loss of solvents and, moreover, can establish better interactions with the other conformer. The conformational change and the rotation of the propargyl

side chain makes possible the formation of new interactions between the two different conformers guaranteeing a better side-by-side arrangement.

2.3 X-ray powder diffraction analysis of compound 1

The solid state behaviour of compound **1** was also deeply investigated using X-ray powder diffraction (XRPD) analysis.

In particular, two types of experiments have been performed: variable temperature analysis and gas absorption experiment.

2.3.1 Variable temperature X-ray powder diffraction

Two different VT-XRPD experiments were performed on two different powder samples of compound **1**. The two samples were synthesized with the same experimental procedure in two different moments.

The first sample was analysed at Europeans Synchrotron Radiation Facility (ESRF, Grenoble, France), beamline ID22. In particular, the powder has been obtained by grinding a few milligrams of crystals of compound **1** obtained by dissolving compound **1** in hot acetonitrile in an agate mortar.

The powder is characterized by the presence of three or more phases. By carefully analysing the sample, it was possible to identify form 1E or 1F (since the two crystal forms are isostructural, the powder patterns are very similar) and the form 1A. Unfortunately, not all the phases were identified, and it was not possible to perform a Rietveld refinement.

After the sample evaluation at room temperature, a variable temperature experiment has been performed. In particular, the sample was heated up to 473 K and then measured again at room temperature (Figure 2.23). The powder patterns were collected at 333 K, 343 K, 373 K, 398 K, 423 K, 448 K, 473 K and 298 K.

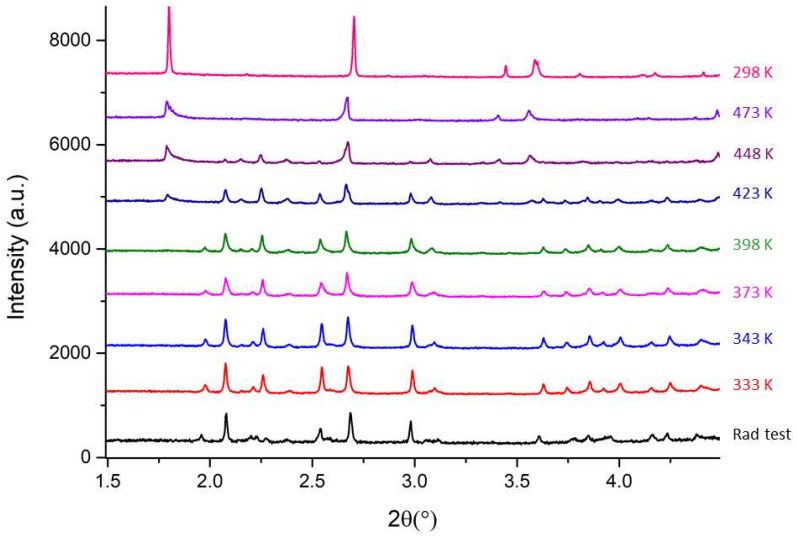

Figure 2.23 Powder patterns obtained during the variable temperature experiments performed at ESRF.

As can be noted in Figure 2.23, during the experiment something happens to the sample. At 423 K a new peak at 1.80° starts to appear. When the temperature reaches the 448 K the peaks related to the starting phases slowly start to disappear and, finally, at 473 K only one phase is present. Comparing the starting powder pattern to the last one, the small number of peaks in the pattern collected after the variable temperature experiment, suggests that it was possible to obtain only one unknown phase from a multiphase sample.

Another powder sample of compound **1** obtained after the synthesis procedure, was analysed with a laboratory diffractometer at the Max Planck Institute for Solid State Research (Stuttgart, Germany). In this case, the starting sample is a monophasic sample containing only the form 1B (Figure 2.24). On this sample, a variable temperature experiment was performed (Figure 2.25 a). Surprisingly, the final phase obtained after the thermal treatment is the same obtained at the ESRF (Figure 2.25 b).

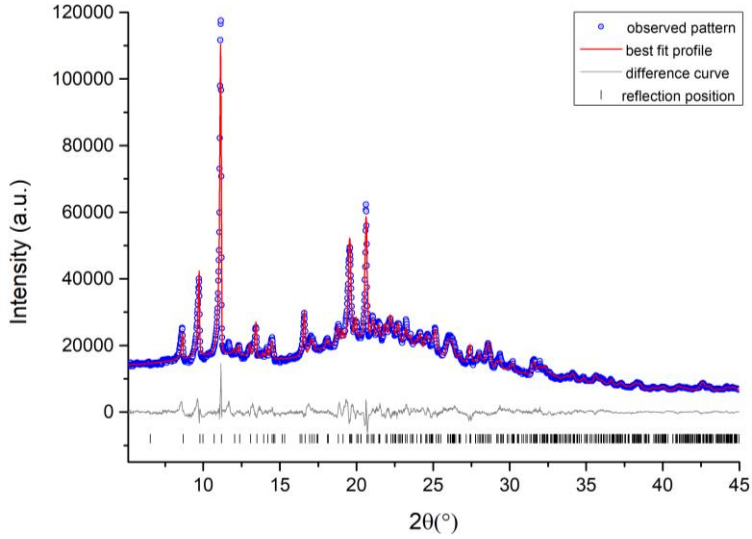

Figure 2.24 Rietveld refinement results for powder pattern obtained at 298 K at MPI. In the figure are shown the observed pattern (circles), the best Rietveld fit profiles (line), the difference curve between the observed and the calculated profiles (below) and the Bragg positions of the form 1B phase (vertical ticks).

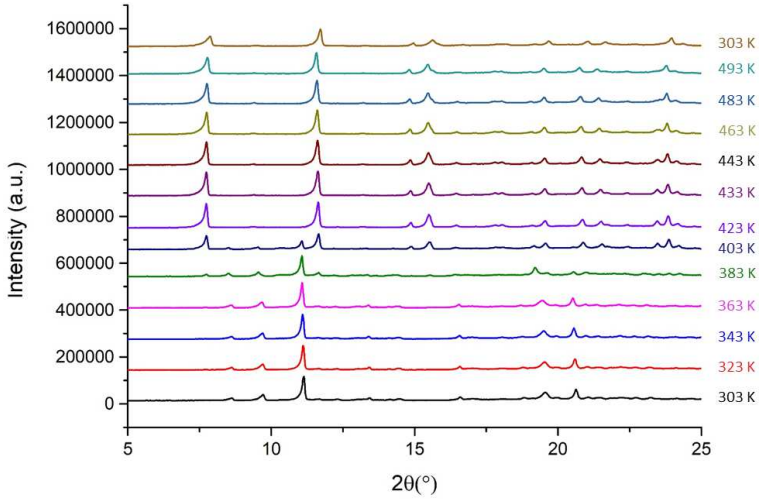

(a)

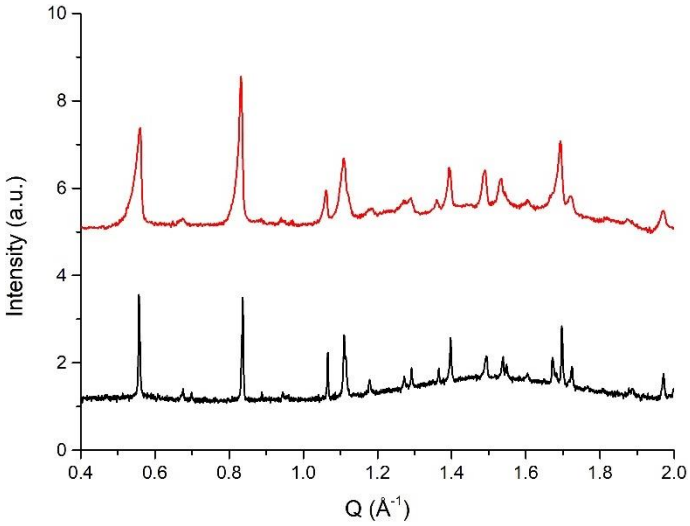

(b)

Figure 2.25 (a) Powder patterns obtained during the variable temperature experiments with laboratory equipment. (b) Comparison between the powder patterns obtained after the thermal treatment at the ESRF (black) and at the MPI (red). To compare the powder pattern collected at different wavelengths, the plot is reported in Q ($Å^{-1}$).

At this point, we tried to solve the structure of the unknown phase using the data obtained at the ESRF since the data quality of the experiments is better than the data quality of the laboratory experiment.

The first step for the structure solution is the identification of the unit cell parameters of the new phase. The indexing procedure was performed using the software McMaille[85] implemented in EXPO2014[86]. The unit cell parameters are reported in Table 2.4. The Pawley fit, performed using TOPAS V6,[87] confirms that the sample obtained after the thermal treatment contains only one phase (Figure 2.26).

In Table 2.5 are reported the final indices of the Pawley fit and Rietveld refinement performed in this chapter.

[85] A. Le Bail, *Powder Diffraction*, 2004, **19**, 249-254.
[86] A. Altomare, C. Cuocci, C. Giacovazzo, A. Moliterni, R. Rizzi, N. Corriero and A. Falcicchio, *J. Appl. Cryst.*, 2013, **46**, 1231-1235.
[87] Topas (version 6.0), General profile and structure analysis software for powder diffraction data, Bruker AXS, Karlsruhe (Germany) 2017.

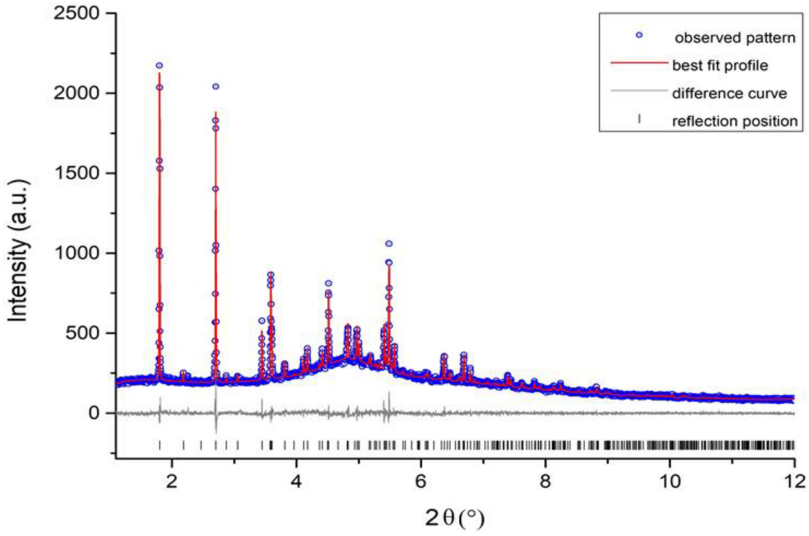

Figure 2.26 Pawley fit of the sample obtained at 298 K. Final unit cell parameters are reported in Table 2.4.

Interestingly, the unit cell obtained is very similar to the unit cell of a crystal form of a cyclic hexapeptoid decorated with five propargyl and one methoxyethyl side chains previously characterized in our research group (Figure 2.27).

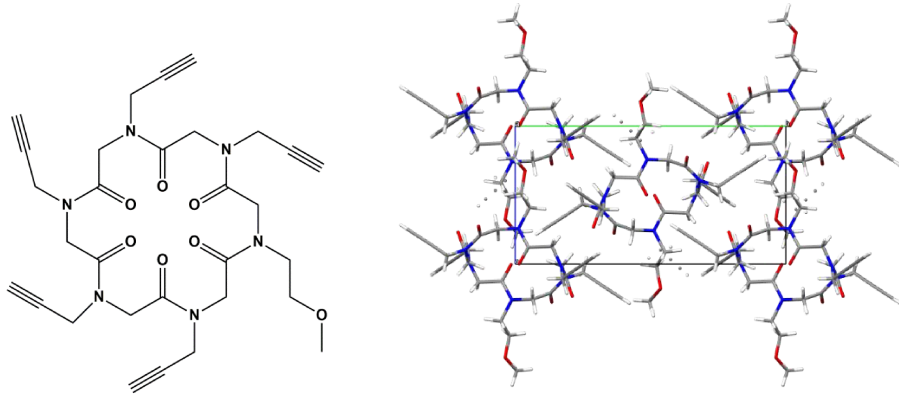

(a) (b)

Figure 2.27 (a) Schematic representation of *cyclo*-[*N*pa$_5$*N*me]. (b) Crystal packing viewed along the *a* axis.

Table 2.4 Unit cell parameters of the new crystal form and *cyclo*-[*N*pa$_5$*N*me].

	***a* (Å)**	***b* (Å)**	***c* (Å)**	***α* (°)**	***β* (°)**	***γ* (°)**	***V* (Å^3)**	**Space group**
New phase	11.7016	16.4751	8.7483	90	105.429	90	1625.8	$P2_1/c$
New phase Pawley	11.6904(5)	16.4737(4)	8.7531(3)	90	105.504(3)	90	1624.4 (1)	$P2_1/c$
Cyclo-[(*N*pa)$_5$(*N*me)]	10.9504(8)	17.0244(10)	8.9112(6)	90	102.730(3)	90	1620.43(19)	$P2_1/c$

Cyclo-[(*N*pa)$_5$(*N*me)] does not possess a molecular inversion centre, but the space group is centrosymmetric and the cyclic peptoid molecules are located on an inversion centre. Therefore, the crystal structure shows positional disorder of the methoxyethyl side chain which can occupy two different positions with the same probability.

Since the difference between compound **1** and *cyclo*-[*N*pa$_5$*N*me] is related to the presence/absence of a methoxyethyl side chain, the structure of the *cyclo*-[*N*pa$_5$*N*me] was used for the simulated annealing.

Using as starting structure the crystal form of *cyclo*-[*N*pa$_5$*N*me], it was built a model of compound **1**. Thus, the *trans* propargyl side chain was substituted by a methoxyethyl side chain. With this simple but very effective way, we obtained a model that can be easily used in the simulated annealing.

The simulated annealing was performed using TOPAS V6.

Table 2.5 Final indices of the Rietveld refinements and Pawley fit reported in this paragraph.

	Rietveld 303 K (Lab data)	**Pawley fit back 303 K (ESRF)**	**Rietveld simulated annealing**
R_p fitted (%)	3.27	3.17	3.76
R_{wp} fitted (%)	4.36	4.18	5.21

The space group of the high temperature phase is $P2_1/c$. In this space group, the molecules centre of mass is usually localised on the crystallographic inversion centres. This information was crucial to solve the structure.

Indeed, a rigid body of the molecule has been defined with the centre of mass located on the special position (0, 0, 0), which corresponds to an inversion centre. In this way, it was possible to

construct the entire molecule using only half of the atoms (the whole molecule will be generated by the inversion).

Since the molecule must be localised on the inversion centre with coordinates (0,0,0), during the simulated annealing, the translation was keep fixed and only the rotational parameters were refined. Furthermore, the torsion angles of the side chains were refined too.

The final result is showed in Figure 2.28.

Since the structure was obtained by powder diffraction experiment, it seems to be too ambitious the deep study of the crystal packing. For this reason, we decided to report only the most characterizing aspects of the crystal packing of this new crystal form without performing energetic studies about the intermolecular interactions.

Compared to the form 1B, this new crystal form shows one molecule in the asymmetric unit and the space group after the transformation does not change. Analysing the unit cell parameters, it is clear that the two unit cells are not so different. Indeed, the *c* axis does not change, the *a* axis of form 1B and *b* axis of high temperature crystal form are quite similar and *b* axis in form 1B is double with respect to the *a* axis of the high temperature phase. The main reason why this happens is related to the presence of only one molecule in the asymmetric unit in the high temperature phase. Taking into account the volume of the two crystal forms, halving the unit cell volume of form 1B, is evident an increasing of the volume mainly caused by the increase of the temperature (+5.30%).

Regarding the crystal packing, the main motif is characterized by a side-by-side interaction along the short side of the cyclic peptoid. In this arrangement are involved the oxygen atom of the backbone and the methylene hydrogen atom of the backbone (C7-H6···O2 = 2.12 Å; O2···H6-C7 = 154.9°; C2-H3···O2 = 2.24 Å; O2···H3-C2 = 151.9°) Å and the terminal hydrogen atom of the propargyl side chain and the oxygen atom of the backbone (C10-H14···O1 = 1.79 Å; O1···H14-C10 = 174.1°). This motif induces the formation of a layer of cyclic peptoids. Moreover, an interesting CH-π interaction is established between the *cis* propargyl side chain and the terminal methylene hydrogen atom of the trans propargyl side chain. The interacting molecules are related by the screw axis along the *b* axis.

Moreover, cyclic peptoids align along the *a* axis by means of backbone-to-side chain interactions involving the *cis* propargyl side chain and the *trans* methoxyethyl side chain and the oxygen atom of the backbone (C5-H11···O3 = 2.55 Å; O3···H11-C5 = 118.6°; C15-H20···O3= 2.59 Å; O3···H20-C15 = 144.7°).

Interestingly, this new crystal form does not show any columnar arrangement and all the side chains are in equatorial position with respect to the macrocycle plane.

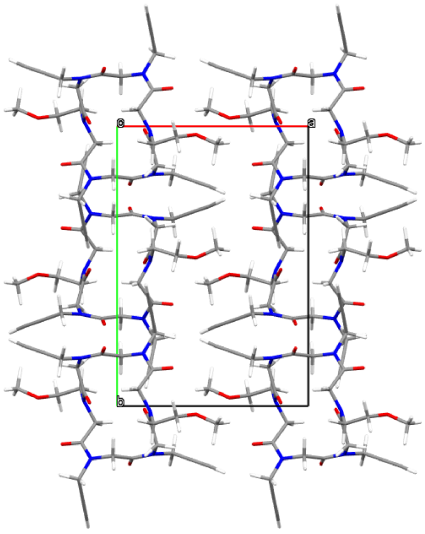

(a)

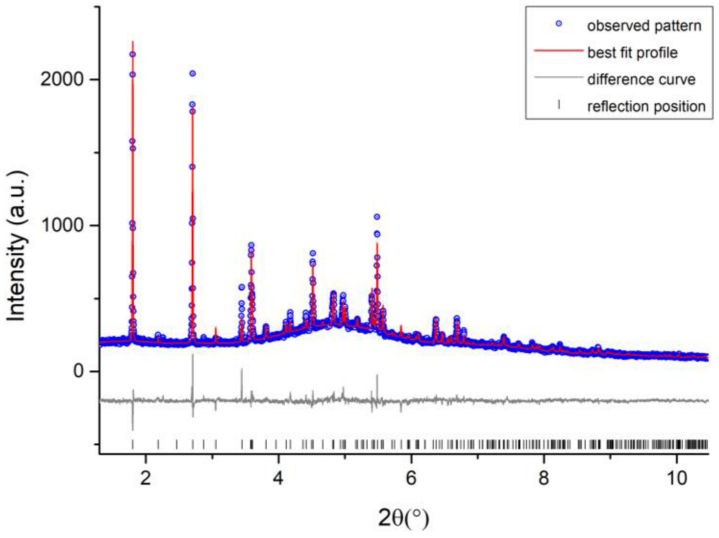

(b)

Figure 2.28 (a) Crystal packing viewed along the *c* axis of the crystal structure obtained after the simulated annealing. (b) Rietveld refinement results for powder pattern obtained at 298 K at ESRF. In the figure are shown the observed pattern (circles), the best Rietveld fit profiles (line), the difference curve between the observed and the calculated profiles (below) and Bragg positions of the new high temperature (HT) form1B phase (vertical ticks).

2.3.2 Gas absorption experiment

It was demonstrated how the conformational flexibility of compound **1** is fundamental for the solvatomorphic behaviour in the solid state.[77] Furthermore, the presence of a specific recognition site, the carbonyl oxygen atom of the backbone that can act as an acceptor of hydrogen bonds, facilitate the interactions with specific solvents.

Considering all these particular aspects of the cyclic peptoids, we investigate more thoroughly the absorption properties of compound **1** exposing a powder sample to different gases.

To facilitate the interpretation of the results and the understanding of the absorption phenomenon, it was important to use a powder sample containing only one characterized phase.

For this reason, we evaluated the absorption properties of a powder sample containing only the form 1F. This crystal form is perfect for this type of experiment. Indeed, it possesses voids that can be filled by different solvents, the host frameworks remain intact after the absorption and desorption of the guest molecules and it was demonstrated in a previous work[77] that the carbonyl oxygen atom of the backbone can act as recognition site.

Two different samples consisting of the only crystal form 1F were exposed to two different gases, propyne and CO_2, and the absorption process was followed by means of X-ray powder diffraction analysis. Propyne has been chosen because of its triple bond that can favour the formation of CH-π interactions with the propargyl side chains and can act as donor-acceptor of H-bond. On the other hand, CO_2 has been investigated for its role in biological mechanisms as well as its abundance in living systems. Compounds which can adsorb CO_2 gained more and more interest in recent years because the increasing concentration of CO_2 in the atmosphere, caused by human activity, is one of the main reasons for global warming. Moreover, CO_2 represents a system completely different respect the propyne gas and the other solvents, which can be adsorbed by compound **1**. Indeed, it can act only as H-bond acceptor.

The first powder sample (powder sample 1) was measured at the ESRF, beamline ID22. The powder was obtained by grinding in an agate mortar, crystals of **1** obtained by slow evaporation of acetonitrile. The sample was analyzed at room temperature to characterize the starting crystalline phase. To be sure that no water molecules were present into the voids, the sample was heated up to 343 K. The Rietveld refinement (Figure 2.29), performed using the software TOPAS V6, confirms the presence of just one anhydrous phase, the form 1F. Final indices are reported in Table 2.6. Since the two experiments on the two different samples were performed using two different wavelengths, herein we decided to report al the powder diffraction plots in Q ($Å^{-1}$).

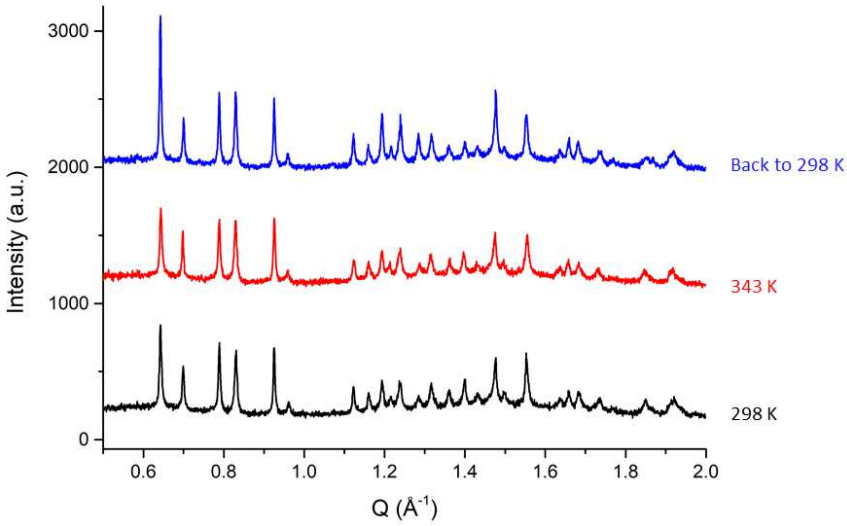

(a)

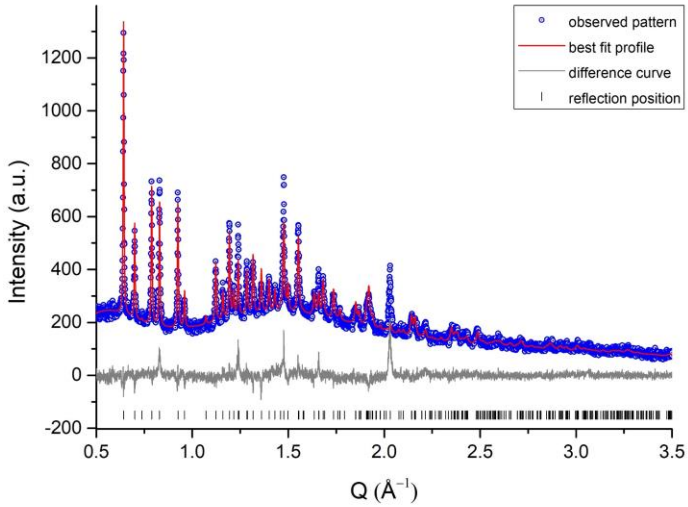

(b)

Figure 2.29 (a) Powder patterns collected during the thermal treatment of powder sample 1. (b) Rietveld refinement results for powder pattern obtained at 298 K after the thermal treatment. In the figure are shown the observed pattern (circles), the best Rietveld fit profiles (line), the difference curve between the observed and the calculated profiles (below) and the Bragg positions of the form 1F phase (vertical ticks).

The sample was exposed to a pressure of propyne of 5 bar and the diffraction patterns have been collected after 1, 4 and 7 hours of exposure. As can be noted in Figure 2.30, the XRPD pattern

collected after 7 hours is different with respect to the starting one. By carefully selecting the new peaks, it was possible to index the new phase. Performing a Pawley fit using TOPAS V6, we have confirmed the presence of two phases: form 1F and form 1G (Table 2.6). Interestingly, the form 1G shows a unit cell very similar to the desolvated form but with a larger volume (Table 2.7). We can use the unit cell expansion as the signature of gas absorption. Moreover, it was possible to remove the propyne gas with an evacuation procedure and a thermal treatment at 343 K.

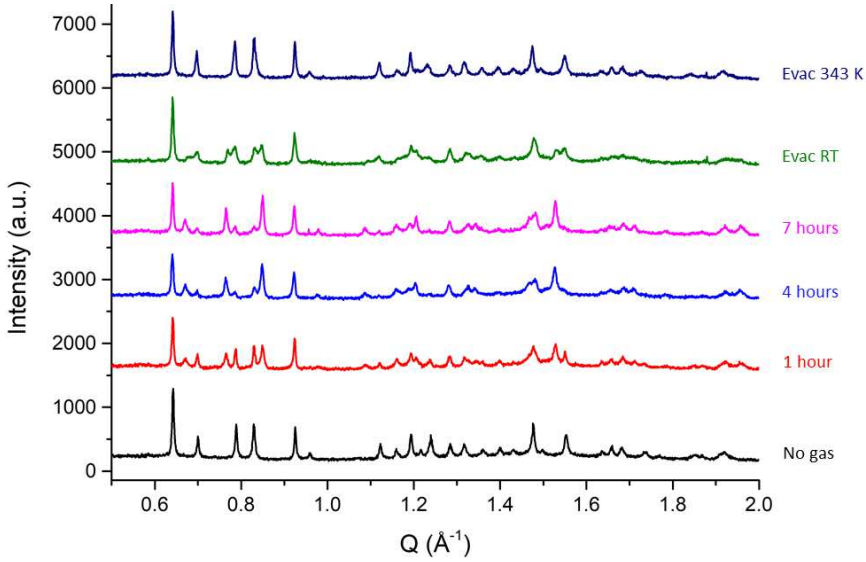

Figure 2.30 Comparison of XRPD patterns obtained at different gas exposure times at 5 bar.

Using the software TOPAS V6 it was possible to perform a simulated annealing procedure in order to obtain the right position of propyne molecule in the unit cell and, with a rigid body model, optimize the side chains position (Rietveld refinement result is showed in Figure 2.31 a; Table 2.6). In the crystal form obtained (Figure 2.31 b), the propyne molecules occupy the cavities between the columns and interact with the cyclic peptoids by means of a CH···O interaction (CO···HC = 1.75 Å; O···H-C = 151.9°) with a refined occupancy of 0.52. It is interesting to notice that the oxygen atom involved in the interaction is the same oxygen atom that we have already demonstrated can act as H-bond binding/recognition site. The presence of propyne gas does not influence the crystal packing of cyclic peptoid molecules. Indeed, the columnar arrangement remains intact. Virtually removing the propyne molecules, the structure without propyne gas shows voids of 44.3 $Å^3$ (5.2% of unit cell volume).

In Figure 2.32 is reported the superimposition of the form 1F and 1G.

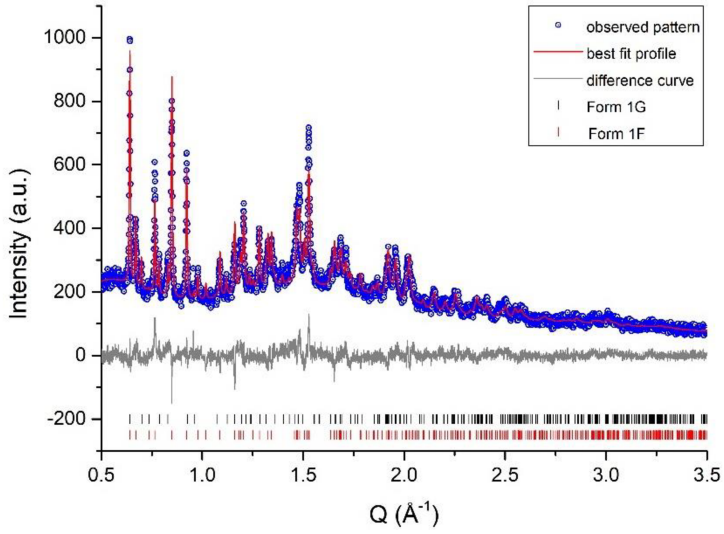

(a)

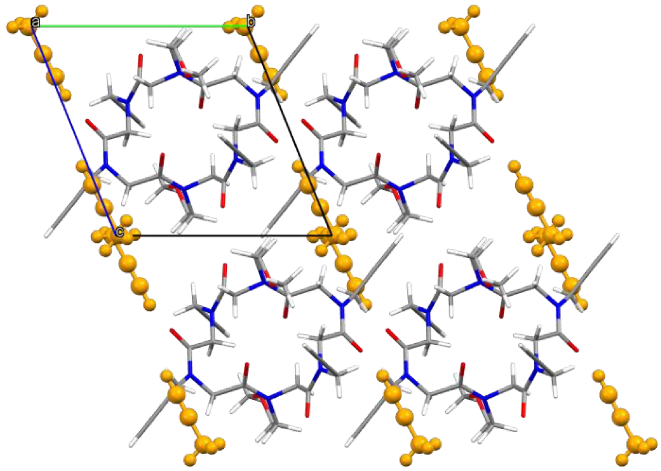

(b)

Figure 2.31 (a) Scattered X-ray intensities of powder sample 1 after 7 hours of exposure to a pressure of 5 bar of propyne as a function of diffraction angle 2θ. In the figure are shown the observed pattern (circles), the best Rietveld fit profiles (line), the difference curve between the observed and the calculated profiles (below) and the Bragg positions of the form 1F and 1G phases (vertical ticks). (b) Crystal packing of the crystal form 1G. Propyne molecules are depicted in orange. View along the *a* axis.

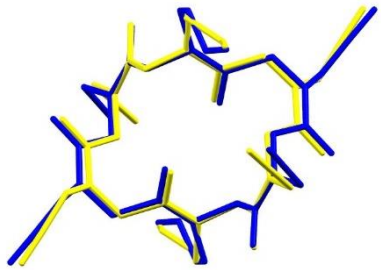

Figure 2.32 Molecule overlay of the structure of the form 1F (yellow) and form 1G (blue). RMSD 0.323 Å.

The powder sample 2 was obtained by grinding in an agate mortar crystals of compound **1** obtained by slow evaporation of a solution of acetonitrile/water. A room temperature XRPD measurement performed on the sample using a laboratory diffractometer confirmed the presence of the form 1F. Also in this case, to be sure that no water molecules are localized into the channels, a thermal treatment has been performed (Figure 2.33 a) and a Rietveld refinement at the end of the thermal treatment has been executed (Rietveld refinement result is showed in Figure 2.33 b; Table 2.6). After that, the powder sample 2 was exposed to a pressure of 1, 2, 3, 5 and 10 bar of CO_2 and the gas absorption was followed by collecting the powder patterns every 10 minutes for 4 hours. In Figure 2.34 are showed the powder patterns after 4 hours of exposure. Also in this case, the plot is reported in Q ($Å^{-1}$).

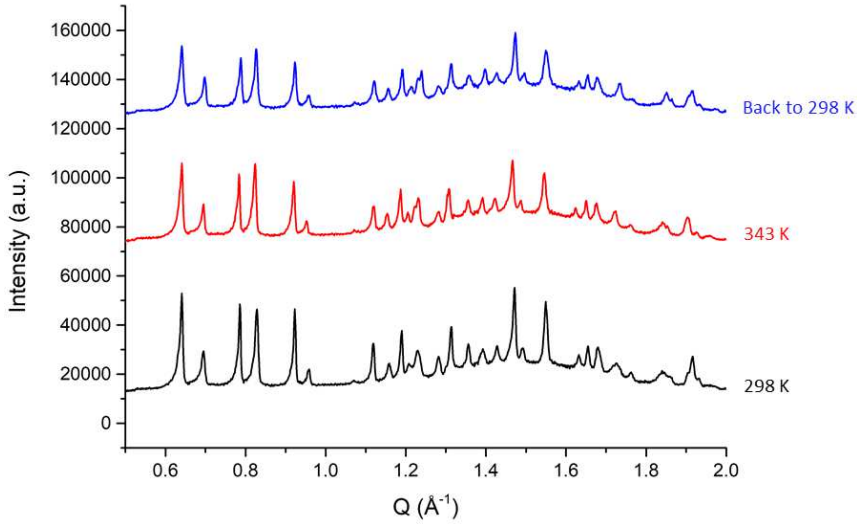

(a)

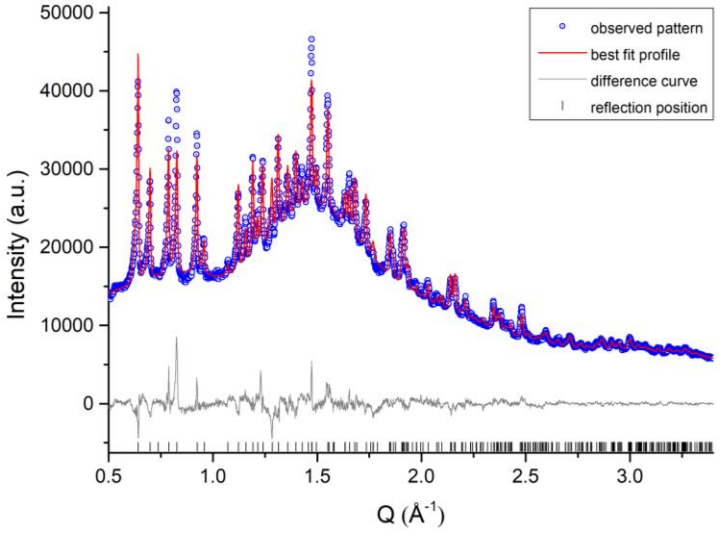

(b)

Figure 2.33 (a) Powder patterns collected during the thermal treatment of powder sample 2. (b) Rietveld refinement results for powder pattern obtained at 298 K after the thermal treatment. In the figure are shown the observed pattern (circles), the best Rietveld fit profiles (line), the difference curve between the observed and the calculated profiles (below) and the Bragg positions of the form 1F phase (vertical ticks).

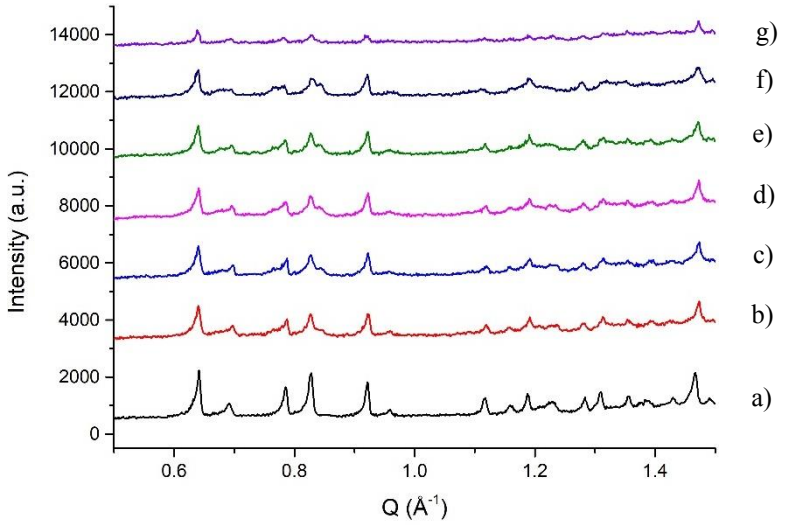

Figure 2.34 Comparison of XRPD patterns obtained at different gas exposure times. a) pattern collected before the gas exposure, b) pattern obtained at 1 bar after 4 hours of exposure, c) pattern obtained at 2 bar after 4 hours of exposure, d) pattern obtained at 3 bar after 4 hours of exposure, e) pattern obtained at 5 bar after 4

hours of exposure, f) pattern obtained at 10 bar after 4 hours of exposure, g) pattern obtained at room temperature after the evacuation.

It is possible to notice the formation of new peaks which testifies the absorption of CO_2 (unit cell values are reported in Table 2.7). By selecting the new peaks, it was possible to index the new phase and with a Pawley fit we confirmed the presence of two phases: the form 1B and the form 1H (crystal form with CO_2). Using TOPAS V6, it was possible to localize the CO_2 molecules with a simulated annealing procedure and, with a rigid body model, refine the side chains position (Rietveld refinement result is showed in Figure 2.35 a; Table 2.6). The CO_2 molecules occupy the voids between columns and interact with cyclic peptoid molecules by means of CH···O interactions (Figure 2.35 b) and show a refined occupancy of 0.32. In particular, the atoms involved in the interactions are the hydrogen atom H15C of the *trans* methoxyethyl side chain and oxygen atom O5 of the CO_2 molecule (CO···HC = 2.31 Å; O···H-C = 172.0°) and hydrogen atom H7B of the backbone and oxygen atom O6 of the CO_2 molecule (CO···HC = 2.14 Å; O···H-C = 143.4°). Virtually removing the CO_2 molecules, the structure without CO_2 gas shows voids of 29.11 $Å^3$ (3.4% of unit cell volume).

In Figure 2.36 is reported the superimposition of the form 1F and 1H.

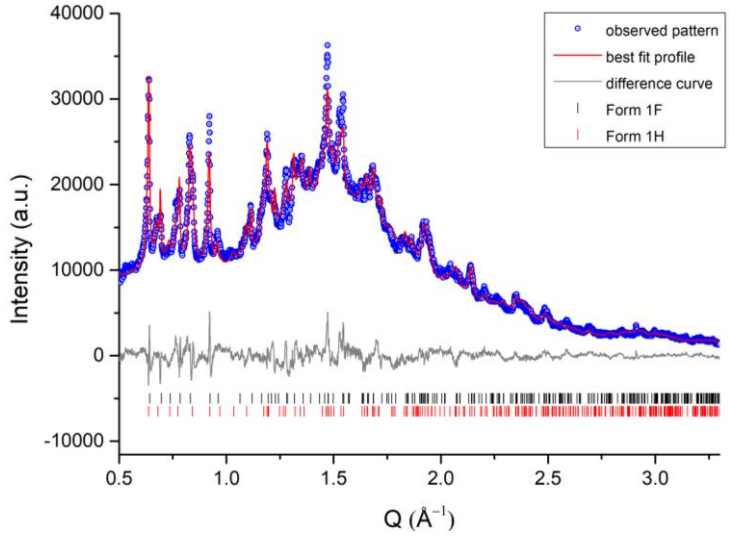

(a)

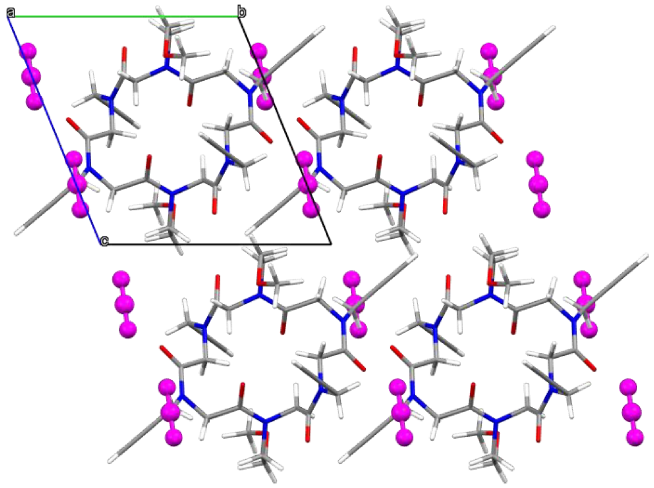

(b)

Figure 2.35 (a) Scattered X-ray intensities of powder sample 2 after 4 hours of exposition to a pressure of 10 bar of CO2 as a function of diffraction angle 2θ. In the figure are shown the observed pattern (circles), the best Rietveld fit profiles (line), the difference curve between the observed and the calculated profiles (below) and the Bragg positions of the form 1F and 1H phases (vertical ticks). (b) Crystal packing of the crystal form 1H. CO_2 molecules are depicted in purple. View along the *a* axis.

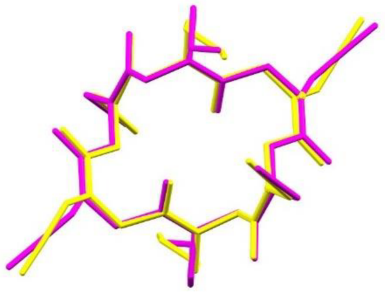

Figure 2.36 Molecule overlay of the structure of the form 1F (yellow) and form 1H (magenta). RMSD 0.365 Å.

Table 2.6 Final indices of the Rietveld refinements reported in this paragraph.

	Rietveld 298 K (ESRF)	Rietveld propyne (ESRF)	Rietveld 298 K (MPI)	Rietveld CO_2 (MPI)
R_p fitted (%)	5.93	6.09	2.68	2.87
R_{wp} fitted (%)	8.07	7.65	3.72	3.70

Table 2.7 Comparison between the cell parameters of the form 1F, form 1G at 5 bar after 7 hours of exposure and form 1H at 10 bar after 4 hours of exposure.

Crystal form	*a* (Å)	*b* (Å)	*c* (Å)	*α* (°)	*β* (°)	*γ* (°)	*V* (Å^3)
Form 1F	8.5875(8)	10.3508(8)	10.6762(8)	67.884(7)	86.630(7)	68.351(8)	813.60(13)
Form 1G	8.6528(9)	10.6392(13)	10.5967(12)	67.684(8)	85.220(8)	71.776(6)	856.50(18)
Form 1H	8.653(3)	10.592(4)	10.670(4)	67.69(3)	85.95(3)	70.28(3)	849.8(6)

To evaluate the quality of the models obtained after the simulated annealing, both structures have been optimized* using the self-consistent charge density-functional tight-binding (DFTB) method as implemented in the DFTB+ software package,[88a,b] holding fixed the experimental crystalline lattice constants in presence of periodic boundary conditions (PBC). The DFTB-D3 formalism[89] has been used to take into account the van der Waals interaction in the crystalline phase.[90]

The superimposition of the structures of form 1G obtained after the simulated annealing and the optimization shows that the main differences between the two models are related to the position of the side chain due to their flexibility (Figure 2.37). The optimized propyne molecules establish the same CH···O involving the acetylenic hydrogen (CO···HC = 1.91 Å; O···H-C = 156.6°).

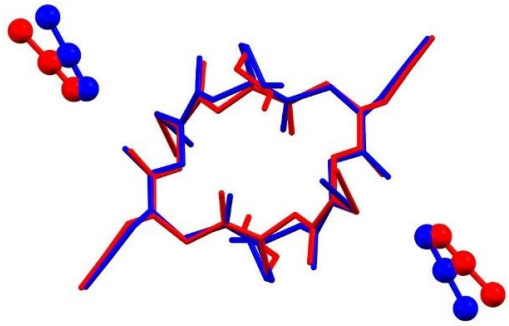

Figure 2.37 Molecule overlay of the structure of the form 1G obtained with simulated annealing (blue) and after the optimization (red). Propyne molecules are depicted in ball and stick style.

* Optimization performed by Dr Alessandro Landi

[88] (a) M. Elstner, D. Porezag, G. Jungnickel, J. Elsner, M. Haugk, T. Frauenheim, S. Suhai and G. Seifert, *Phys. Rev. B: Condens. Matter Mater. Phys.*, 1998, **58**, 7260-7268; (b) G. Seifert and J.-O. Joswig, *WIREs Comput. Mol. Sci.*, 2012, **2**, 456-465.

[89] S. Grimme, J. Antony, S. Ehrlich and H. Krieg, *J. Chem. Phys.*, 2010, **132**, 154104.

[90] A. Landi and A. Troisi, *J. Phys. Chem. C*, 2018, **122**, 18336-18345.

The same optimization procedure has been done of the form 1B crystal form. Also in this case, the main difference between the two models are related to the side chain position (Figure 2.38). The CO_2 molecules rotate of almost 90° respect to the position of the CO_2 molecules obtained after the simulated annealing and interact with the cyclic peptoids molecules by means of CH···O interactions. The atoms involved in the interaction are the oxygen atom of CO_2 and the H8B hydrogen of the *cis* propargyl side chain (CO···HC = 2.20 Å; O···H-C = 145.5°) and the H7B hydrogen atom of the backbone and the oxygen atom of the CO_2 molecule (CO···HC = 2.23 Å; O···H-C = 130.2°).

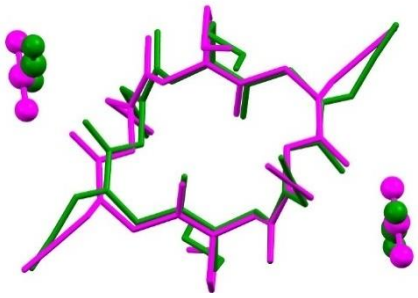

Figure 2.38 Molecule overlay of the structure of the form 1H obtained with simulated annealing (magenta) and after the optimization (green). CO_2 molecules are depicted in ball and stick style.

2.4 Experimental section

2.4.1 Single crystal X-ray data collection, structure solution and refinement

X-ray single crystal data for crystal form 1A and 1B were collected at 100 K using an Oxford Cryosystems Cryostream 700+ cryostat with a Bruker Smart diffractometer at University of Stellenbosch equipped with an APEXII CCD detector using Mo*K*α radiation (λ = 0.71073 Å). Both crystals were mounted on a cryoloop with paratone oil. Data reduction was performed with the crystallographic package APEX[91] and the structures were solved by direct methods using the program SHELXS[92a,b] and refined by means of full-matrix least-squares based on F^2 using the program SHELXL97.[93] The software X-Seed[94] was used as GUI.

[91] APEX Data Reduction Software, v 6.45; Bruker AXS Inc., Madison, WI, 2003.
[92] a) SADABS, Version 2.05; Bruker AXS Inc., Madison, WI, 2002; b) R. H. Blessing, *Acta Crystallogr., Sect. A: Found. Crystallogr.*, 1995, **51**, 33-38.
[93] G. M. Sheldrick, *Acta Crystallogr., Sect. A: Found. Crystallogr.*, 2008, **64**, 112-122.
[94] L. J. Barbour, *J. Supramol. Chem.*, 2001, **1**, 189-191.

Crystals of the form 1C and 1D were selected and mounted on a MiTeGen microloop with paratone oil. Data collection was performed at 100 K using an Oxford Cryosystems Cryostream 700 for temperature control with a Rigaku AFC7S diffractometer at University of Salerno equipped with a Mercury2 CCD detector using graphite monochromated Mo*K*α radiation (λ = 0.71073 Å). Data reduction was performed with the crystallographic package CrystalClear.[95] Data were corrected for Lorentz, polarization and absorption.

For the from 1E, the data were collected at 100 K on a Bruker DUO Quasar diffractometer equipped with an APEX-II CCD area-detector and an Oxford Cryosystems Cryostream 700Plus for temperature control. The radiation was produced from a Mo*K*α (λ = 0.71073 Å) Incoatec IμS microsource fitted with a multilayer monochromator. Data reduction was performed with the crystallographic package APEX.[91] Data collection on the crystal of form 1F was measured at 100 K using an Oxford Diffraction Excalibur diffractometer with Mo*K*α radiation (λ = 0.71073 Å). Data collection was performed with the program CrysAlis CCD,[96] the data reduction was carried out with the program CrysAlis RED[97] and absorption correction was performed with the program ABSPACK in CrysAlis RED.[97]

The crystal structures of form 1C, 1D, 1E and 1F were solved by direct methods using the program SIR2014[98] and refined by means of full-matrix least-squares based on F^2 using the program SHELXL.[99] *OLEX*2[100] and X-Seed[94] were used as GUI.

Crystallographic data and refinement information are reported in Table 2.8. ORTEP diagrams were drawn using *OLEX*2[100] (Figure 2.39).

[95] CrystalClear, Crystal Structure Analysis Package, Rigaku-Molecular Structure Corp.
[96] CrysAlis CCD, Version 1.171.29.2 (release 20.01. CrysAlis171 .NET); Oxford Diffraction Ltd.: Oxfordshire, U.K., 2006.
[97] CrysAlis RED, Version 1.171.29.2 (release 20.01. CrysAlis171 .NET); Oxford Diffraction Ltd.: Oxfordshire, U.K., 2006.
[98] M. C. Burla, R. Caliandro, B. Carrozzini, G. L. Cascarano, C. Cuocci, C. Giacovazzo, M. Mallamo, A. Mazzone and G. Polidori, *J. Appl. Cryst.,* 2015, **48**, 306-309.
[99] G. M. Sheldrick, *Acta Cryst.*, 2015, **C71**, 3-8.
[100] O. V. Dolomanov, L. J. Bourhis, R. J. Gildea, J. A. K. Howard and H. Puschmann, *J. Appl. Cryst.*, 2009, **42**, 339-341.

Table 2.8 Crystallographic data for crystal form 1A, 1B, 1C, 1D, 1E and 1F.

	Form 1A	**Form 1B**	**Form 1C**	**Form 1D**	**Form 1E**	**Form 1F**
T (K)	100	100	296	100	100	100
Formula	$C_{30}H_{38}N_6O_8 \cdot 2\ CH_3CN$	$C_{30}H_{38}N_6O_8$	$C_{30}H_{38}N_6O_8$	$C_{30}H_{38}N_6O_8 \cdot 2CH_3OH$	$C_{30}H_{38}N_6O_8 \cdot 1.16H_2O$	$C_{30}H_{38}N_6O_8$
Formula weight	692.77	610.66	610.66	667.06	628.68	610.66
System	Monoclinic	Monoclinic	Triclinic	Triclinic	Triclinic	Triclinic
Space group	$P\,2_1/c$	$P\,2_1/c$	$P\,\bar{1}$	$P\,\bar{1}$	$P\,\bar{1}$	$P\,\bar{1}$
***a* (Å)**	9.773(5)	17.887(3)	8.814(3)	8.5007(14)	8.5852(15)	8.5875(8)
***b* (Å)**	20.961(10)	20.335(3)	9.0944(18)	10.396(11)	10.492(17)	10.3508(8)
***c* (Å)**	8.500(4)	8.4716(12)	10.982(4)	10.910(17)	10.556(2)	10.6762(8)
***α* (°)**	90	90	78.86(2)	67.863(11)	68.110(9)	67.884(7)
***β* (°)**	90.990(7)	93.160(2)	87.55(3)	84.552(15)	86.318(10)	86.630(7)
***γ* (°)**	90	90	66.35(2)	71.048(13)	67.035(9)	68.351(8)
***V* (Å^3)**	1740.9(14)	3076.7(8)	790.6(4)	844.3(2)	808.8(3)	813.60(13)
Z	2	4	1	1	1	1
***Dx* (g cm^{-3})**	1.322	1.318	1.283	1.327	1.297	1.246
λ (Å)	0.71073	0.71073	0.71073	0.71073	0.71073	0.71073
***μ* (mm^{-1})**	0.096	0.097	0.094	0.099	0.097	0.092
F_{000}	736.0	1296.0	324.0	360.0	336.0	324.0
R1 (I > 2σI)	0.0465(2958)	0.0495(5005)	0.0762(1454)	0.0700(2055)	0.0582(1780)	0.0492(2051)
$_wR_2$	0.1173(3594)	0.1148(7060)	0.256(3541)	0.1966(3798)	0.1560(3240)	0.1099(3081)
N. of param.	226	397	200	218	212	199
N. of relections	3594	7060	3541	3798	3240	3081
GooF	1.057	1.013	0.986	0.993	0.925	1.020
ρ_{min}, ρ_{max} (eÅ^{-3})	-0.26, 0.27	-0.24, 0.27	-0.22, 0.33	-0.32, 0.33	-0.28, 0.25	-0.21, 0.23

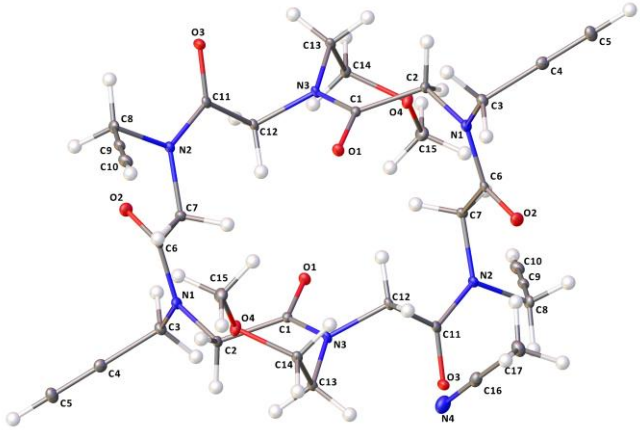
O3
C13
C14
C5
C4
N3
C2
C11
C1
C3
C8
C12
O4
N1
C9
N2
O1
C15
C10
C6
O2
C7
O2
C7
C6
C10
C9
C15
O1
N2
N1
C12
C8
O4
C1
C11
C3
N3
C2
C14
O3
C17
C4
C13
C16
C5
N4

(a)

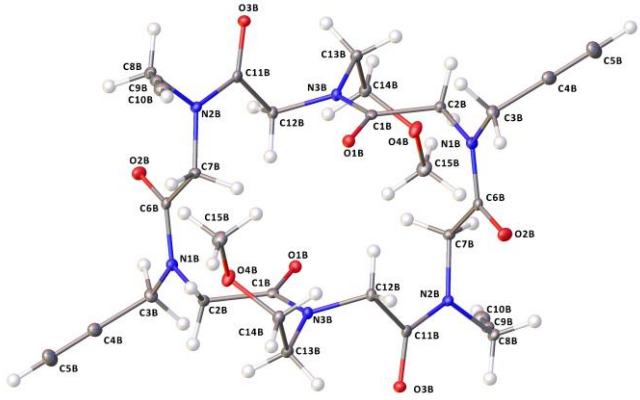
O3B
C8B
C11B
C13B
C5B
C9B
C10B
N3B
C14B
C4B
N2B
C12B
C2B
C3B
C1B
O1B
O4B
N1B
O2B
C7B
C15B
C6B
C6B
O2B
C15B
C7B
N1B
O4B
O1B
C1B
C12B
N2B
C3B
C2B
N3B
C10B
C9B
C4B
C14B
C11B
C8B
C5B
C13B
O3B

(b)

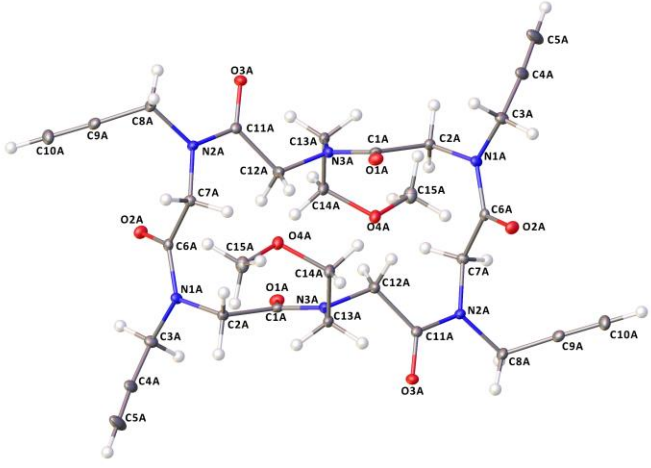
C5A
O3A
C4A
C8A
C11A
C3A
C9A
C13A
C1A
C2A
C10A
N2A
N3A
O1A
N1A
C12A
C15A
C7A
C14A
C6A
O2A
O4A
O2A
C6A
C15A
O4A
C7A
C14A
C12A
N1A
O1A
N3A
N2A
C3A
C2A
C1A
C13A
C11A
C10A
C9A
C8A
C4A
O3A
C5A

(c)

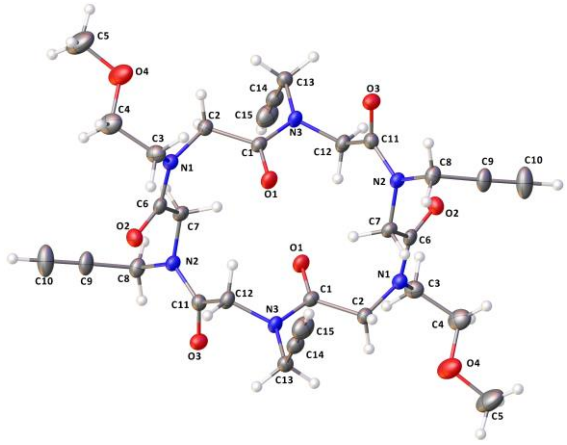
C5
O4
C4
C3
N1
C6
O2
C7
C10
C9
C8
N2
C14
C13
C15
N3
C2
C1
O1
C12
C11
O3
O3
O2
C7
C6
N1
C3
C4
O4
C5

(d)

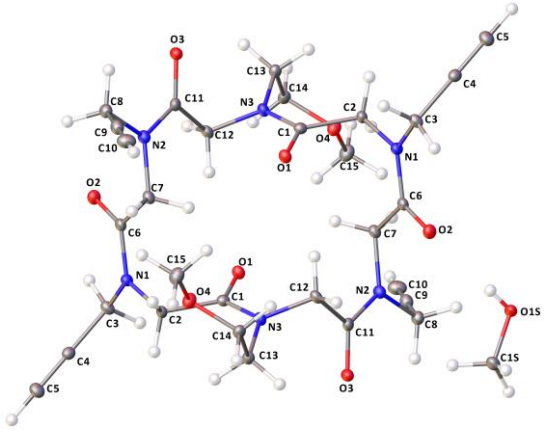
O3
C13
C14
C5
C4
C8
C11
N3
C2
C3
C9
C10
N2
C12
C1
O4
N1
O1
C15
O2
C7
C6
C6
C7
O2
C15
O1
N1
C12
N2
C10
C9
O4
C1
C3
C2
C14
N3
C11
C8
O1S
C4
C13
C1S
C5
O3

(e)

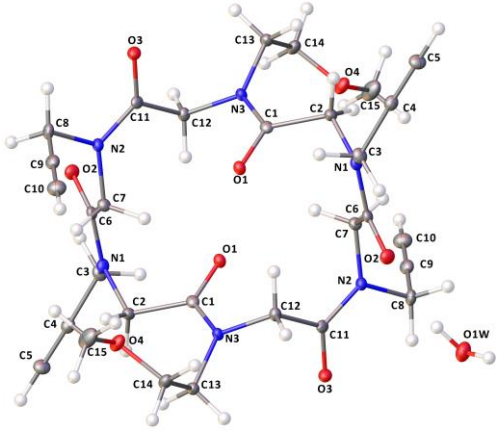
C13
C14
O3
O4
C5
C11
N3
C1
C2
C15
C4
C12
C8
N2
C3
C9
O2
N1
O1
C10
C7
C6
C6
C7
C10
O1
O2
C9
C3
N1
N2
C8
C2
C1
C12
C4
C11
O1W
C5
O4
N3
C15
C14
C13
O3

(f)

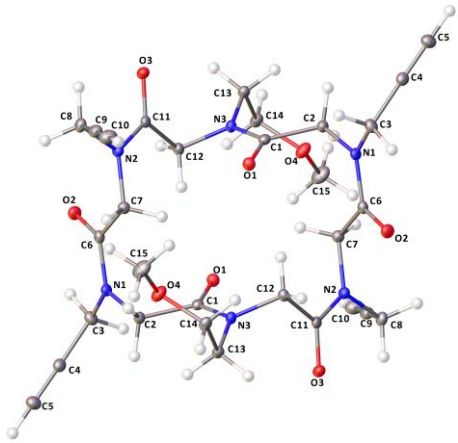

(g)

Figure 2.39 ORTEP diagrams for crystal form 1A (a), 1B type A molecule (b), 1B type B molecules (c), 1C (d), 1D (e), 1E (f) and 1F (g). Atom types: C grey, O red, H white, N blue. Ellipsoids are drawn at 20% probability level.

2.4.2 Powder diffraction experiment

The variable temperature and gas absorption experiment on powder sample of compound **1** were performed at the European Synchrotron Radiation Facility (ESRF) in Grenoble at the beamline ID22. A glass capillary of 0.5 mm was filled with powder and analysed using a wavelength of 0.35437 Å from an insertion device source with a double-crystal Si(111) monochromator and data were collected using the multianalyser stage. The patterns were collected in a 2θ range from 0° to 25.9° and raw data were rebinned into steps of 0.002° 2θ. The temperature was controlled using an Oxford Cryostream cold nitrogen gas blower. For the variable temperature experiments, the sample was heated up with a rate of 2 K/min and from 298 K to 473 K. At each temperature, a powder diffraction pattern was collected after a delay time of 15 minutes in order to guarantee the thermal equilibration of the sample.

The propyne gas pressure was applied by using the gas rig system.[101] The gas cell was mounted on a heavy-duty goniometer head mounted coaxially with the axis of the diffractometer and rocked during the measurements in order to improve randomisation of the orientations of the individual crystallites. Data were collected at 298 K.

[101] A. H. Hill, *J. Appl. Cryst.,* 2013, **46**, 570-572.

The particular gas rig system allows to reach a pressure of 100 bar and to work under vacuum. This is possible thanks to the six pneumatic valves connected to a 1/4 inch Swagelok VCR parts to form a rigid system. It is possible to load the desired gas pressure into the central body of the rig and then release it into the capillary.

Laboratory X-ray powder diffraction experiment was performed at the Max Planck Institute for Solid State Research using a Stadi P-Diffraktometer (Stoe), Cu*K*α radiation from a primary Ge(111)-Johann-type monochromator and three Mythen 1 K detectors (Dectris). For the variable temperature experiments, data were collected in a 2θ range from 2.0° to 115.0° measuring the sample for a total scan time of 2 hours. The temperature was controlled by an Oxford Cryostream device (Oxford Cryostream 500). The sample was heated up with a rate of 2 K/min from 303 K to 473 K, with an increment of 20 K until 413 K and then the increment was 10 K until 473 K. At each temperature, a powder diffraction pattern was collected after a delay time of 15 minutes in order to guarantee the thermal equilibration of the sample. For the gas experiment with CO_2, the experiment was performed using a microreactor connected to a pumping station (T-Station 75 Turbomolecular), which allow us to introduce a desired gas pressure inside the capillary. Initially, it was applied pressure of 1 bar of CO_2, collecting a powder pattern every ten minutes for 4 hours with a total scan time of 5 minutes. The same procedure was repeated with a pressure of 2, 3, 5 and 10 bar. At 10 bar, we left the sample at this pressure for 4 hours and then a powder patter was collected with a total scan time of 2 hours. In Figure 2.40 are reported the powder patterns collected at the different gas pressure.

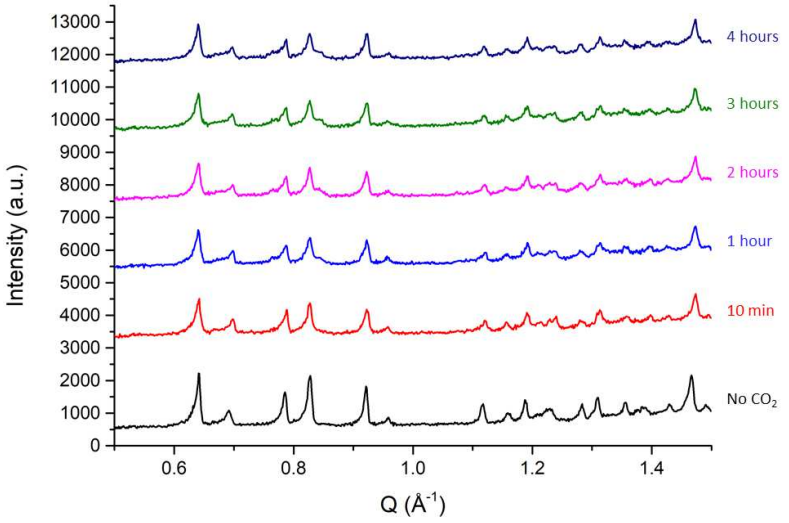

(a)

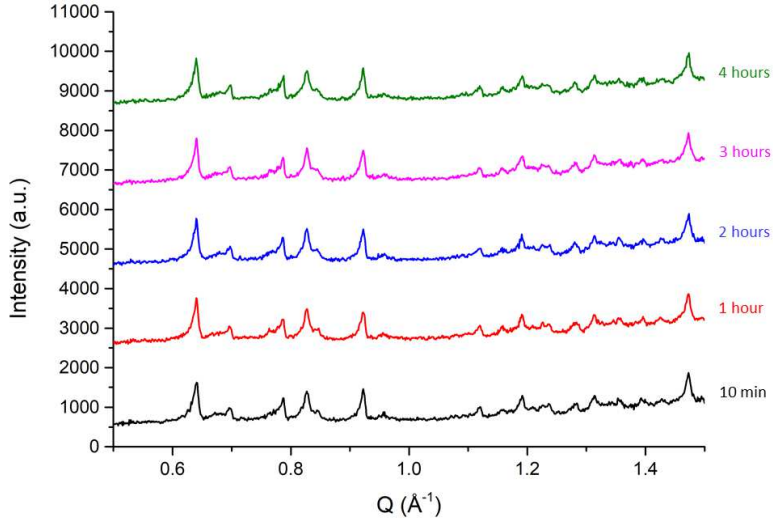
11000
10000
9000
8000
7000
6000
5000
4000
3000
2000
1000
0
Intensity (a.u.)
0.6
0.8
1.0
1.2
1.4
Q (Å-1)
4 hours
3 hours
2 hours
1 hour
10 min

(b)

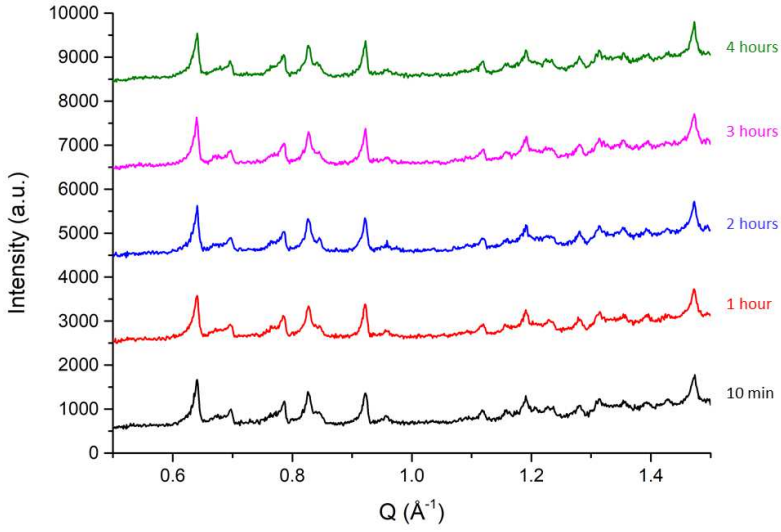
10000
9000
8000
7000
6000
5000
4000
3000
2000
1000
0
Intensity (a.u.)
0.6
0.8
1.0
1.2
1.4
Q (Å-1)
4 hours
3 hours
2 hours
1 hour
10 min

(c)

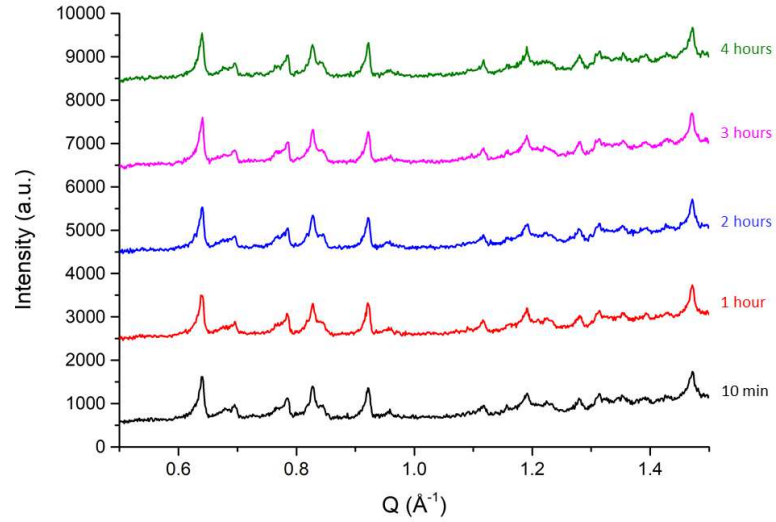

(d)

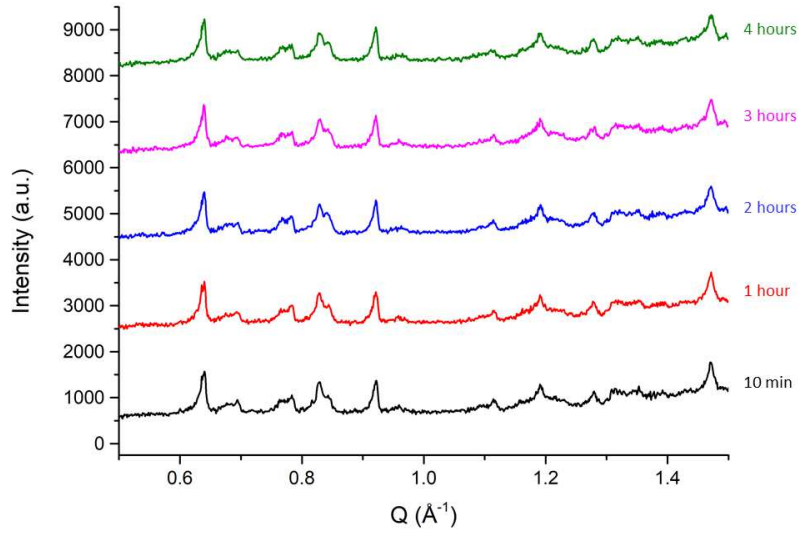

(e)

Figure 2.40 Comparison between the XRPD patterns collected at a pressure of CO_2 of 1 (a), 2 (b), 3 (c), 5 (d) and 10 (e) bar.

2.4.3 X-ray powder diffraction data analysis

The indexing of the powder pattern collected after the thermal treatment at the ESRF was performed using McMaille[85] software implemented in EXPO2014.[86] After the peak hunting

procedure, the 2θ peak positions are used with the intensities to build a pseudo powder pattern, which is compared to the patterns calculated using the cell parameters proposed by a Monte Carlo search process. At the end of the procedure, the unit cell with the highest McM20 has been selected. After the unit cell search, thanks to the evaluation of the systematic absences of reflection, the $P2_1/c$ space group was selected.

With a Pawley refinement, the peak profile was determined using and the background was determined using Chebyshev polynomial of 10^{th} order.

The crystal structure was solved using the global optimization method of simulated annealing.[102] The entire molecule was constructed using rigid bodies in z-matrix notation. As already mentioned in the previous paragraph, a dummy atom with coordinates (0, 0, 0) was used to position the cyclic peptoid on an inversion centre and with this expedient, it was possible to keep fixed the translation parameter and refine only the rotation. The torsion angles C2-N1-C3-C4, C7-N2-C8-C9, C13-N3-C12-C11, C12-N3-C13-C14, N3-C13-C14-O4 and C13-C14-O4-C15 were refined fixing the range of values that the torsion angles could have. The thermal factors of all the atoms were refined and the final value obtained is 3.57.

After the simulated annealing procedure, a Rietveld refined has been performed.

Concerning the gas absorption experiment, Rietveld refinements were performed using TOPAS V6.

The indexing of the form 1G was performed using DICVOL[103] by selecting the peaks at the following 2θ values: 2.073, 2.168, 2.472, 2.746, 2.984, 3.160, 3.512, 3.749, 3.897, 4.144, 4.290, 4.344, 4.792, 4.938, 5.344, 5.450, 5.537, 6.212, 6.330, 6.532. The final figures of merit are M_{20}= 11.3 and F_{20}= 102.4.

The localization of the gas molecules via simulated annealing and the rigid body Rietveld refinement were accomplished using the program TOPAS V6.

Since we were not able to obtain a pure sample containing only the form 1G at the end of the experiment, the simulated annealing and the Rietveld refinement were performed considering the presence of the form 1F. In particular, before simulated annealing, a Pawley refinement using the unit cell of the new phase was performed in order to obtain the best profile function. After that, all the parameters were fixed, and we carried on the simulated annealing procedure.

A propyne molecule model has been constructed with the following parameters:

- C1pr – C2pr distance = 1.458 Å;

[102] A. A. Coelho, *J. Appl. Cryst.*, 2000, **33**, 899-908.
[103] A. Boultif and D. Louer, *J. Appl. Cryst.*, 1991, **24**, 987-993.

- C2pr – C3pr distance = 1.279 Å;
- C1pr – C2pr – C3pr angle = 180.00 °;
- C–H distances = 1.089 Å.

The starting model for the simulated annealing is the structure obtained by SCXRD experiment (CCDC number 1545934). In order to take into account the possible reorganization of the side chains, rigid body models of the side chains has been created. In particular, the nitrogen atoms have been used as the first atom of the rigid body z-matrix and the coordinates of these atoms have been used as the translation parameter and not refined, while the rotation parameters have been refined for all the side chain. Moreover, rigid body refinements were performed considering as variable two torsion angles (C15-O4-C14-C13 and O4-C14-C13-N3) of the methoxyethyl side chains, the three rotation and three translation parameters without any constraints of the propyne molecule, one overall temperature factors for the cyclic peptoid atoms restraining the value between 1 and 5 while for the propyne molecule the thermal parameter has been fixed to 5, the profile and background parameters. The propyne position has been optimized by changing the rotation and translation parameters without any constraints, the occupancy has been refined as a free variable and the final value is 0.52.

The unit cell parameters of the new phase (form 1H) were identified performing a Pawley fit using the unit cell parameters of the form 1G.

Since we were not able to obtain a pure sample containing only the form 1G at the end of the experiment, the simulated annealing and the Rietveld refinement were performed considering the presence of the anhydrous form. In particular, before simulated annealing, a Pawley refinement using the unit cell of the new phase and a Rietveld refinement was performed in order to obtain the best profile function. After that, all the parameters were fixed, and we carried on the simulated annealing procedure.

For the CO_2 molecule, the same procedure has been performed. In particular, the CO_2 molecule model has been constructed with the following parameters:

- C16 – O5 and C16 – O6 = 1.160 Å;
- O5 – C16 –O6 angle = 180.00 °.0

Also in this case, the starting model for the simulated annealing, is the structure obtained by SCXRD experiment (CCDC number 1545934). In order to take into account the possible reorganization of the side chains, rigid body models of the side chains has been created. In particular, the nitrogen atoms have been used as the first atom of the rigid body z-matrix and the coordinates of these atoms have been used as the translation parameter and not refined, while the rotation parameters have been refined for all the side chain. Moreover, rigid body refinements were performed

considering as variable two torsion angles (C15-O4-C14-C13 and O4-C14-C13-N3) of the methoxyethyl side chains, the three rotation and three translation parameters without any constraints of the CO_2 molecule, one overall temperature factors for the cyclic peptoid atoms restraining the value between 1 and 7 while for the CO_2 molecule the thermal parameter has been fixed to 8, the profile and background parameters. The CO_2 position has been optimized by changing the rotation and translation parameters without any constraints, the occupancy has been refined as a free variable and the final value is 0.33.

CHAPTER III

Cyclo-[(*N*me$_2$-*N*pa)$_2$]

This chapter is dedicated to the description of the results obtained working with *cyclo*-[(*N*me$_2$-*N*pa)$_2$] (**2**) (Figure 3.1).

The first paragraph is dedicated to a brief description of all the crystal forms obtained working with compound **2**. Subsequently, an in-depth description of the crystalline packing of the form 2A, 2B, 2C and 2D are given. This description is necessary in order to fully understand the following paragraphs wherein the thermal studies on single crystals and powder sample of compound **2** are presented.

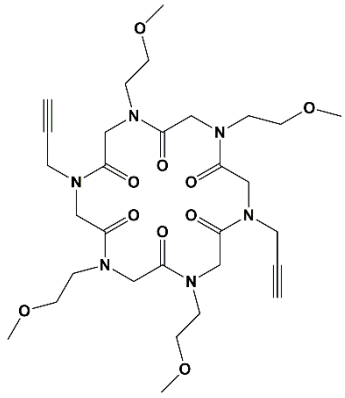

Figure 3.1 *Cyclo*-[(*N*me$_2$-*N*pa)$_2$] (**2**).

3.1 Compound 2

In the previous chapter, we have demonstrated that propargyl and methoxyethyl side chain can induce a columnar arrangement of peptoid macrocycles, acting as pillars when they extend vertically with respect to the macrocycle plane and interacting with backbone atoms of the cyclic peptoids below and above.

To deeper understand the role of propargyl and methoxyethyl side chains in the solid state assembly, compound **2** has been synthesized.

Synthesis has been performed following the standard procedure: the linear precursor has been synthesized using the sub-monomer approach[54] and then cyclized under high dilution condition with HATU as the coupling agent.

3.1.1 Solvatomorphism and polymorphism of compound 2

Compound **2** showed an even more interesting behaviour in the solid state than compound **1**.

In particular, it was possible to obtain a huge number of crystal forms changing the crystallization solvent, performing co-crystallization and changing the environmental conditions.

In Table 3.1 are reported the crystal forms obtained working with compound **2**, while in Table 3.2 are reported the unit cell parameters.[104]

Table 3.1 List of polymorphs, solvatomorphs and co-crystals of compound **2**.

Crystal form	mg of compound	Solvent	Crystallization Method	Crystal form
Form 2A	5	$CHCl_3$/iPrOH (2:1)	Slow evaporation	Hydrate
Form 2B	5	CH_3CN/H_2O (1:1) Or $CHCl_3$/iPrOH (2:1)	Slow evaporation	Monohydrate
Form 2C	5	Grinding with ethylene glycol and dissolving in $CHCl_3$/iPrOH (2:1)	Slow evaporation	Anhydrous
Form 2D	5	$CHCl_3$/ H_2O (1:1)	Slow evaporation	Anhydrous
Form 2E	5	$CHCl_3$	Slow evaporation	Anhydrous
Form 2F	5	CH_3CN	Slow cooling	Acetonitrile solvate
Form 2G	5	$CHCl_3$/Toluene (1:2)	Diffusion of toluene vapors in a solution of $CHCl_3$	Toluene solvate
Form 2H	5	$CHCl_3$/iPrOH (2:1) + Hydroquinone	Slow evaporation	Hydroquinone co-crystals
Form 2I	5	$CHCl_3$/iPrOH (2:1) + aniline	Slow evaporation	Aniline co-crystal

[104] G. Gallo, *Verso il controllo dell'assemblaggio allo stato solido di ciclopeptoidi*. Bachelor Thesis, Academic year 2013-2014.

Table 3.2 Unit cell parameters of the different crystal forms of compound **2**.

Crystal form	*a* (Å)	*b* (Å)	*c* (Å)	*α* (°)	*β* (°)	*γ* (°)	*V* (Å^3)	Space group
Form 2A	8.364(5)	9.580(5)	13.365(8)	94.129(8)	104.34(2)	96.239(19)	1025.9(10)	$P\bar{1}$
Form 2B	8.363(4)	9.394(4)	21.648(10)	78.362(5)	88.664(7)	83.547(5)	1655.1(13)	$P\bar{1}$
Form 2C	9.0367(17)	10.6221(18)	18.022(3)	90	102.661(4)	90	1687.9(5)	$P2_1/n$
Form 2D	8.577(2)	9.1796(16)	11.532(3)	77.088(13)	89.790(17)	68.335(14)	819.4(3)	$P\bar{1}$
Form 2E	9.0574(13)	9.5063(17)	10.821(2)	88.210(15)	79.493(13)	62.314(9)	809.7(3)	$P\bar{1}$
Form 2F	8.575(6)	9.743(6)	14.182(7)	75.11(6)	74.68(8)	82.69(8)	1102.2(11)	$P\bar{1}$
Form 2G	8.5340(10)	9.766(2)	14.045(2)	73.176(10)	76.699(12)	80.254(12)	1083.7(3)	$P\bar{1}$
Form 2H	8.445(4)	11.781(7)	11.911(6)	104.837(9)	94.616(8)	101.905(11)	1109.7(10)	$P\bar{1}$
Form 2I	9.6051(15)	13.730(2)	17.446(3)	76.088(11)	82.131(12)	75.417(10)	2160.5(6)	$P\bar{1}$

The different polymorphs show, of course, different crystal packing in the solid state. In particular, form 2A, 2B, 2I and 2J are characterized by a columnar arrangement, while the remaining crystal forms do not show this peculiar solid state assembly. Moreover, crystal form 2F and 2G are isostructural, despite they have been obtained using different crystallization conditions.

In Figures 3.2 are reported the crystal packing of the different crystal forms which are cited in this thesis. In the following paragraphs, an in-depth description of the crystal packing of the form 2A, 2B, 2C and 2D will be given. The other crystal forms have been cited in order to give to the readers an idea of the extreme flexibility of this compound in the solid state.

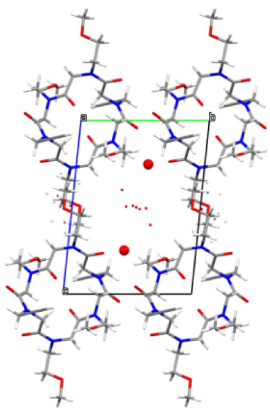

(a)

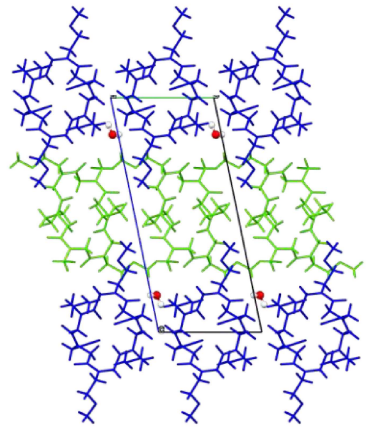

(b)

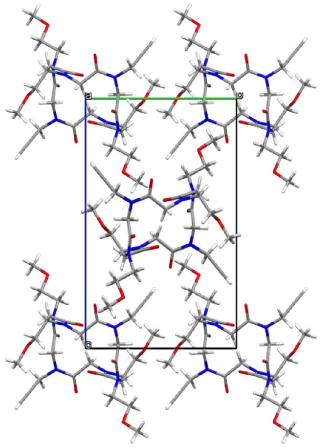

(c)

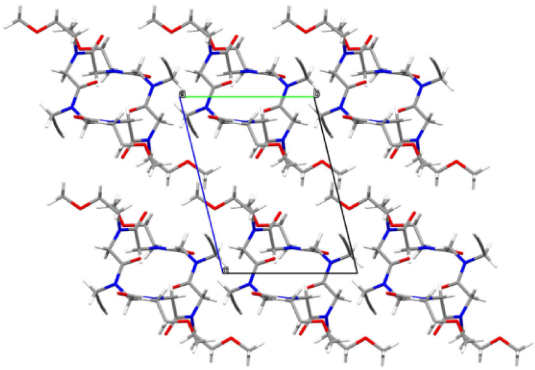

(d)

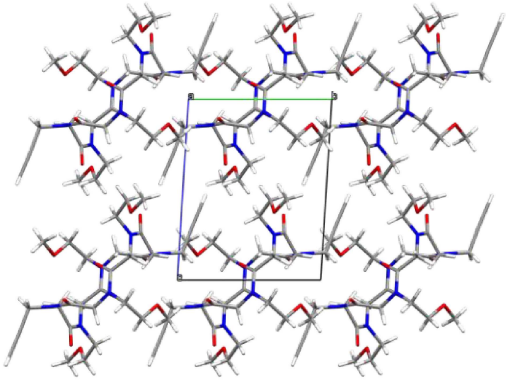

(e)

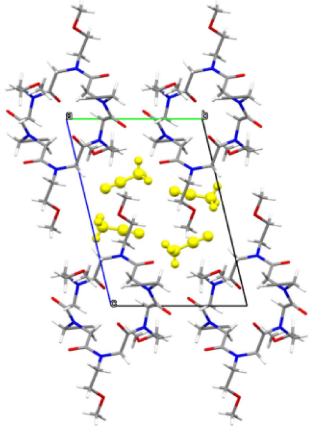

(f)

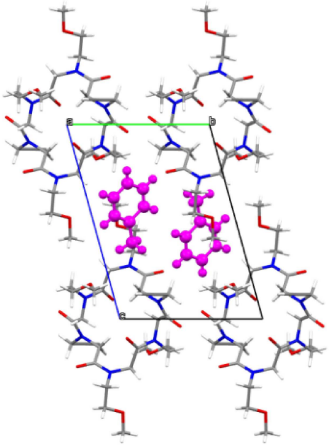

(g)

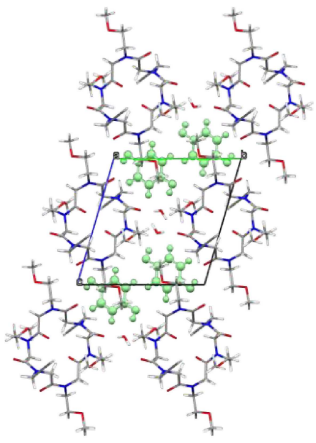

(h)

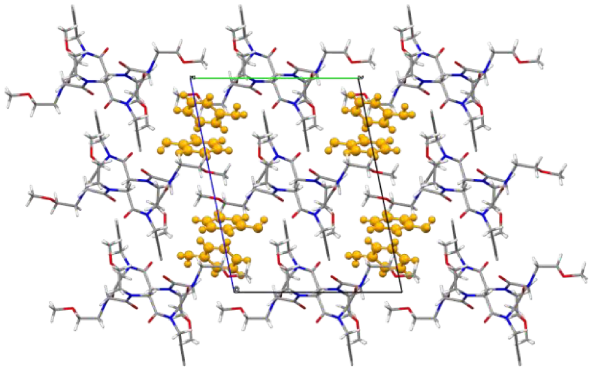

(i)

Figure 3.2 Crystal packing view along the *a* axis of form 2A (a), 2B (b), 2C (c), 2D (d), 2E (e), 2F (f), 2G (g), 2H (h) and 2I (i). Water molecules in form 2A and 2B are depicted in ball and stick style. Type A and type B molecules of form 2B are shown in blue and green, respectively. Acetonitrile molecules in form 2F are depicted in yellow, toluene molecules in form 2G are depicted in magenta, hydroquinone molecules in form 2H are depicted in light green and aniline molecules in form 2I are depicted in brown. (CCDC numbers form dorm 2B and 2C 1509155; 1509157, respectively)

To further underline how environmental conditions can have a profound impact on the crystallization process, herein we report a clear example of how two different purification procedures can determine the precipitation of powder of compound **2** containing the same phases but in different ratio.[66]

In particular, two different powder batches of compound **2** have been prepared following the same synthetic steps but slightly changing the purification procedure.[66]

Analysing the two powder batches at the ESRF, it was possible to notice that they contain different amount of the same crystal phases. In particular, powder sample 1 contains 85.3% of form 2B and 14.7% of form 2C (Figure 3.3), while the powder sample 2 contains 29.2 % of form 2B and 70.8 % of form 2C (Figure 3.4).

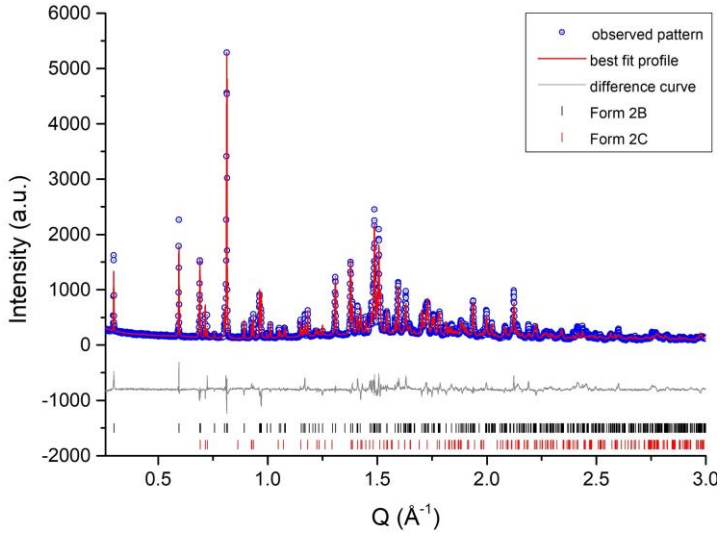

Figure 3.3 Rietveld refinement results for batch 1 at 100 K.

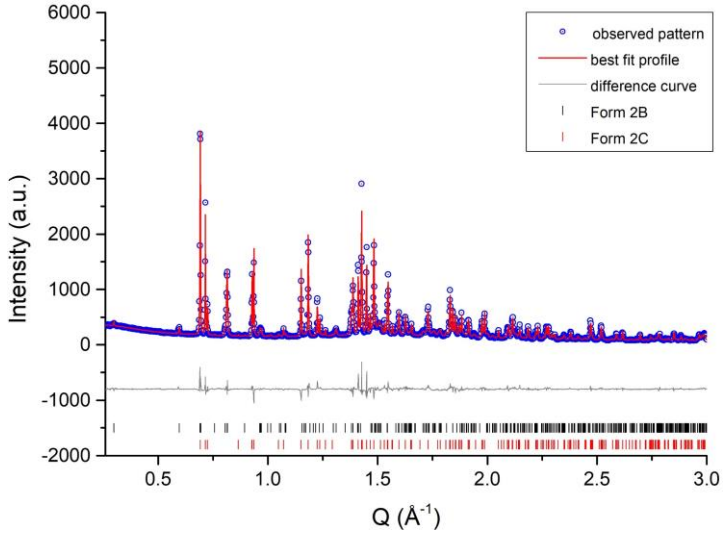

Figure 3.4 Rietveld refinement results for batch 2 at 100 K.

This simple example clearly demonstrates how even small changes in environmental conditions can have a tremendous impact on the crystallization and on the solid state packing of compound **2**.

3.2 Crystal packing analysis

This paragraph is dedicated to the accurate description of the crystal packing of the form 2A, 2B, 2C and 2D by means of PIXEL calculations, energy frameworks analysis and Hirshfeld surface analysis. All the crystal packing analysis on crystal forms 2A, 2B, 2C and 2D, was performed using crystal data reported in a previous thesis work.[104] The structure solution and refinement of form 2A were performed by me.

3.2.1 Form 2A

Form 2A can be obtained dissolving compound **2** with chloroform and then adding isopropanol in a 2:1 ratio. Using this condition, a porous crystal form is obtained. In particular, the water molecules occupy channels localized between the cyclic peptoids. As the water molecules do not establish any interaction with the macrocycles, except for water molecule indicated as O1W, they display thermal disorder. Thus, we decided to not refine their occupancy factor but to fix it. These parameters were chosen in relation to the thermal parameter values of each water molecules: the occupancy factors were fixed so that the thermal parameters do not exceed the value of 0.25.

This crystal form possesses a crystallographic inversion centre and a distorted *cctcct* conformation of the peptoid backbone and in particular, two *trans* methoxyethyl and two *cis* propargyl side chains point vertically with respect to the macrocycle plane, whereas the remaining *cis* methoxyethyl side chains extend horizontally.

The *cis* methoxyethyl side chain shows positional disorder. In particular, the atoms can occupy two possible positions with refined occupancy factor 0.68(3) and 0.32(3). Thus, restraints on anisotropic displacement parameters were applied to disordered group atoms.

In Table 3.3 are reported the intermolecular distances (Å), angles (°) and interaction energies (kJ/mol) in the host framework of form 2A.

Since the water molecules localized inside the channels are disordered and it was not possible to define their specific position, except for water molecules O1W, all the calculations have been performed virtually removing the water molecules, obtaining an “empty” structure. This decision does not influence the quality and reliability of the results.

The columnar arrangement along the shortest *a* axis is the main motif of the crystal packing of form 2A (Figure 3.5 a). As already demonstrated in the previous chapter and in different published papers,[66] the vertical propargyl side chains act as pillar allowing the disposition of the cyclic peptoids one on top of the other. The main interaction is represented by a CO···HC hydrogen bond involving

the *cis* propargyl side chain and the oxygen atom of the backbone (C5-H5···O2 = 1.97 Å; O2···H5-C5 = 165.6°). The Hirshfeld surface analysis (Figure 3.5 b) highlights the importance of the interaction between the propargyl side chain and the carbonyl oxygen atom.

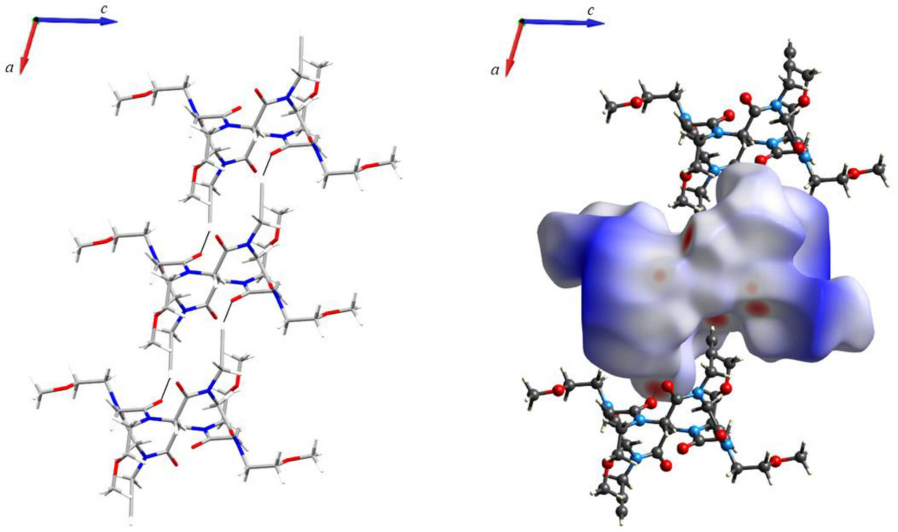

(a) (b)

Figure 3.5 (a) Motif I of the form 2A. (b) Hirshfeld surface mapped with d_{norm} of motif I.

The second motif is represented by a side-by-side interaction along the *b* axis (Figure 3.6 a). The fundamental interaction is associated with the hydrogen bond between the methylene hydrogen atom of the *trans* methoxyethyl side chain and the backbone oxygen atom (C8-H8A···O3 = 2.43 Å; O3···H8A-C8 = 144.3°). Also the water molecules play a key role in this particular motif acting as a bridge between the two macrocycles (Figure 3.6 a, c). The hydrogen bond between the water molecules involves the oxygen atom of the backbone O3 (motif I A-W, O1W-H2AW···O3 = 1.99 Å; O3···H2AW-O1W = 158.2°) and O1 (motif II A-W, O1W-H1AW···O1 = 1.98 Å; O1···H1AW-O1W = 141.7°).

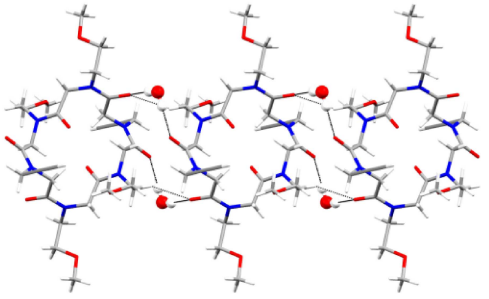

(a)

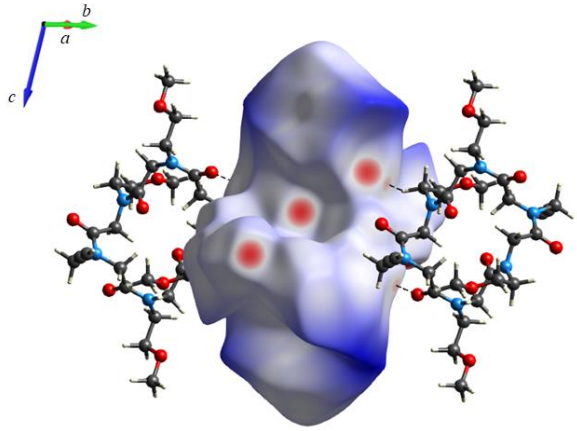

(b)

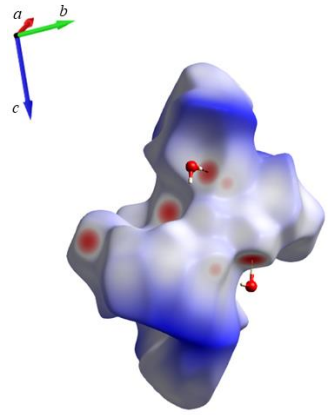

(c)

Figure 3.6 (a) Motif II of the form 2A. Moreover, the interactions between the cyclic peptoids and water molecules are shown too. (b) Hirshfeld surface mapped with d_{norm} of motif II. (c) Hirshfeld surface mapped with d_{norm} of the interactions between the host and guest molecules (motif I A-W and II A-W).

The last motif (motif III, Figure 3.7 a) is represented by the alignment of the cyclic peptoids along the *c* axis. Interestingly, it was not possible to highlight any strong interaction in this particular arrangement, as can be also noted by a carefully studying of the Hirshfeld surface (Figure 3.7 b), and only C···H contacts between the *cis* methoxyethyl side chain and the hydrogen atom of the backbone are present. As mentioned above, the *cis* methoxyethyl side chain shows positional disorder. Since this side chain does not show any strong intermolecular interaction, it is free to move.

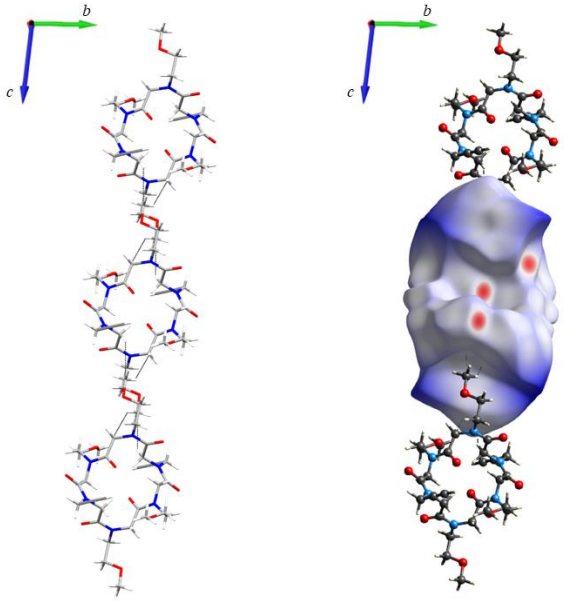

(a) (b)

Figure 3.7 (a) Motif III of the form 2A. (b) Hirshfeld surface mapped with d_{norm} of motif III.

It is interesting to notice that the more hydrophilic side chains (methoxyethyl) are directly exposed to the water molecules which are present into the channels, while the more hydrophobic side chains (propargyl) are "hidden" between the cyclic peptoid molecules (Figure 3.8).

Moreover, analysing the macrocycle backbone, it can be noted that it does not adopt a planar conformation (Figure 3.9, RMSD 0.662 Å). It is possible to give an explanation to this observation if we consider the importance of the propargyl side chain in the formation of the columnar arrangement. Indeed, thanks to this non-planar conformation, the CH···OC interaction between the propargyl and the oxygen atom of the backbone can be established.

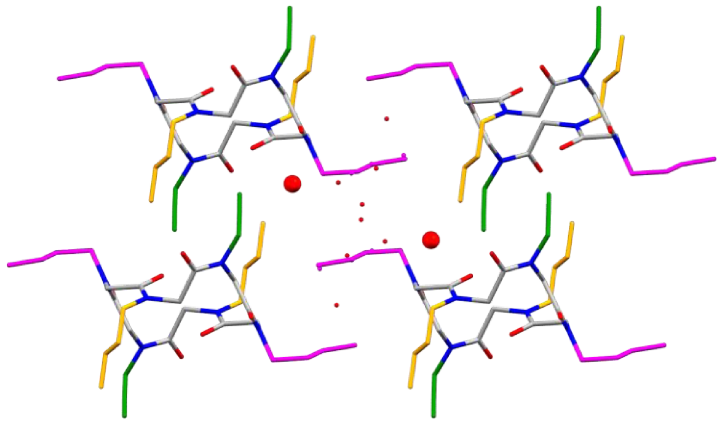

Figure 3.8 Side chains disposition of the form 2A: in magenta is represented the *cis* disordered side chain, in yellow the *trans* methoxyethyl side chain and in green the *cis* propargyl side chain. Water molecules O1W are represented in ball and stick while the other water molecules in capped and stick. Hydrogen atoms have been omitted for clarity.

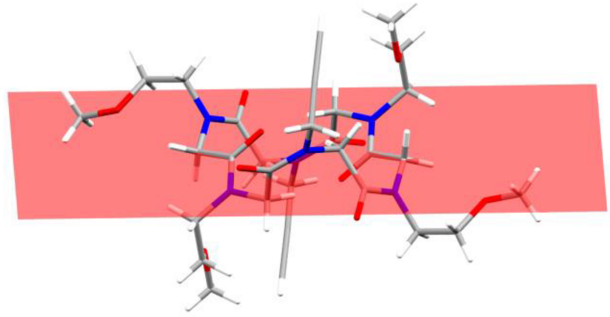

Figure 3.9 Regression plane of the macrocycle ring is shown in red.

Table 3.3 List of intermolecular distances (Å), angles (°) and interaction energies (kJ/mol) in the framework of form 2A. Energy values are reported in kJ/mol.

Motif	D-H···A	H···A (Å)	D-H···A (°)	Symm. Op.	Centroid Distance (Å)	E_{Coul}	E_{Pol}	E_{Disp}	E_{Rep}	E_{Tot}
I	C5-H5···O2	1.97	165.6	-1+x, y, z 1+x, y, z	8.332	-73.9	-29.0	-88.9	102.7	-89.2
II	C8-H8A···O3	2.43	144.3	x, -1+y, z x, 1+y, z	9.548	-33.5	-14.9	-51.9	42.6	-57.7
III	C···H contacts			x, y, -1+z x, y, 1+z	13.312	-8.0	-5.0	-50.4	31.0	-32.3
I A-W	O1W-H2AW···O3	1.99	158.2	x, -1+y, z x, 1+y, z	6.078	-32.4	-9.7	-10.5	23.1	-29.4
II A-W	O1W-H1AW···O1	1.98	141.7	x, y, z -x, -y, -z	6.084	-24.9	-14.1	-16.6	37.3	-18.2

3.2.2 Form 2B

Crystal of form 2B can be obtained in two different ways using different solvents: CH_3CN/H_2O (1:1) or $CHCl_3$/iPrOH (2:1). This crystal form is characterized by the presence of two crystallography independent molecules in the asymmetric (indicated as type A and type B molecules, reported blue and green, respectively) and two water molecules (Figure 3.1 b). This crystal form possesses a crystallographic inversion centre and a distorted *cctcct* conformation of the peptoid backbone.

Two *trans* methoxyethyl and two *cis* propargyl side chains point vertically with respect to the macrocycle plane, whereas the remaining *cis* methoxyethyl side chains extend horizontally.

The principal difference between the two different conformers is related to the backbone shape. In particular, type A molecules are characterized by a more "compact" and round shape while type B molecules present a more rectangular shape (Figure 3.10). Moreover, type B molecules show a deviation from the planarity less evident than the type A molecules (Figure 3.11 a,b). The RMSD values for the deviation from the planarity is 0.667 Å for type A molecule and 0.436 Å for type B molecule.

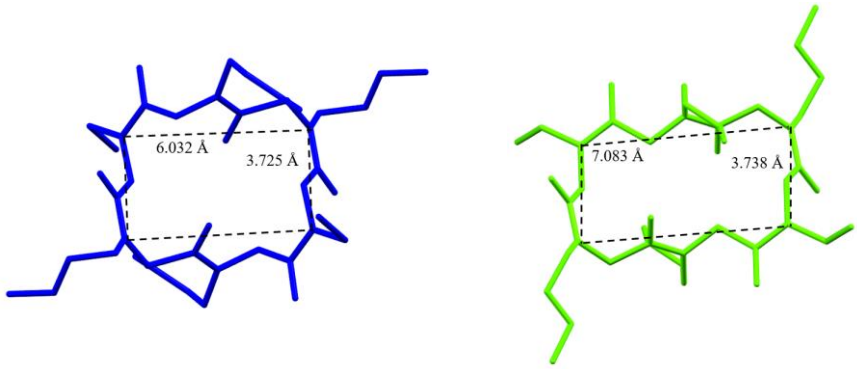

Figure 3.10 Comparison between type A (blue) and type B (green) shape molecules. Rectangular widths and lengths of the macrocycles are also reported. These values were calculated measuring the distance between the nitrogen atom at the corner of the ideal rectangle. Hydrogen atoms have been omitted for clarity.

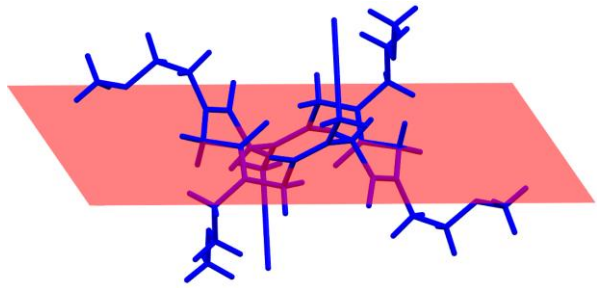

(a)

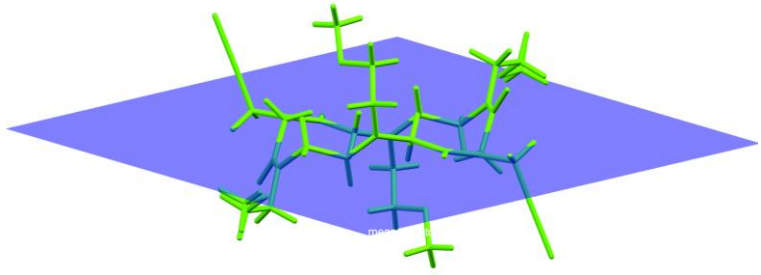

(b)

Figure 3.11 (a) Regression plane of the macrocycle ring of type A molecule is shown in red. (b) Regression plane of the macrocycle ring of type B molecule is shown in blue.

Interestingly, the two conformers are very similar to the conformers of form 1B of compound **1**. Indeed, the superimpositions of the peptoid backbone of the type A molecules of form 1B and 2B and the superimposition of type B molecules of form 1B and 2B, show a very good RMSD value

(Figure 3.12). This value is 0.114 Å for the superimposition of type A molecule of form 1B and type A molecule of form 2B, and 0.127 Å for the backbone superimposition of type B molecule of form 1B and type B molecule of form 2B.

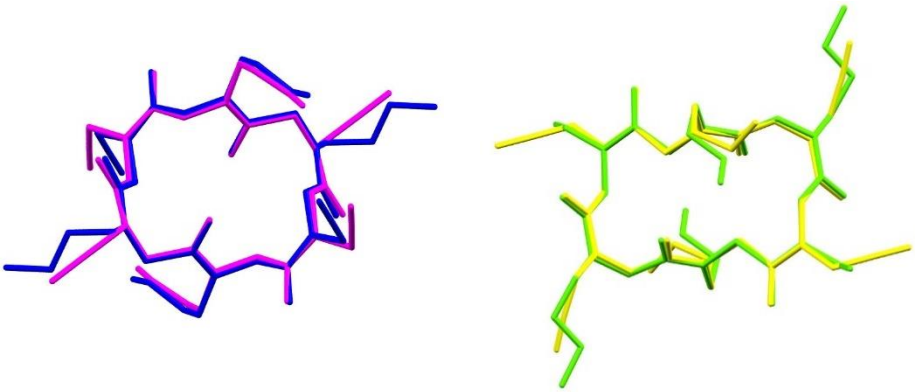

(a) (b)

Figure 3.12 (a) Backbone superimposition of type A molecule of form 1B (magenta) and type A molecule of form 2B (blue). (b) Backbone superimposition of type B molecule of form 1B (yellow) and type A molecule of form 2B (green).

As for crystal form 1B, the crystal packing of form 2B will be described taking into accounts the interactions between the same conformers (type A vs type A and type B vs type B) and then the interactions between the two different conformers.

In Table 3.4 are reported the intermolecular distances (Å), angles (°) and interaction energies (kJ/mol) in the host framework of form 2B.

In type A molecules, the strongest interactions are related to the motif I A-A, which correspond to the alignment of cyclic peptoid molecules along the shortest *a* axis forming columns (Figure 3.13 a). Columnar interactions in type A molecules consist of CO···HC hydrogen bonds involving the carbonyl oxygen atom of the backbone and the hydrogen atom of the *cis* propargyl side chains (C5A-H5A···O2A = 2.09 Å; O2A··· H5A- C5A = 150.1°). As can be noted by means of Hirshfeld surface analysis (Figure 3.13 b), two red spots highlight this type of interaction.

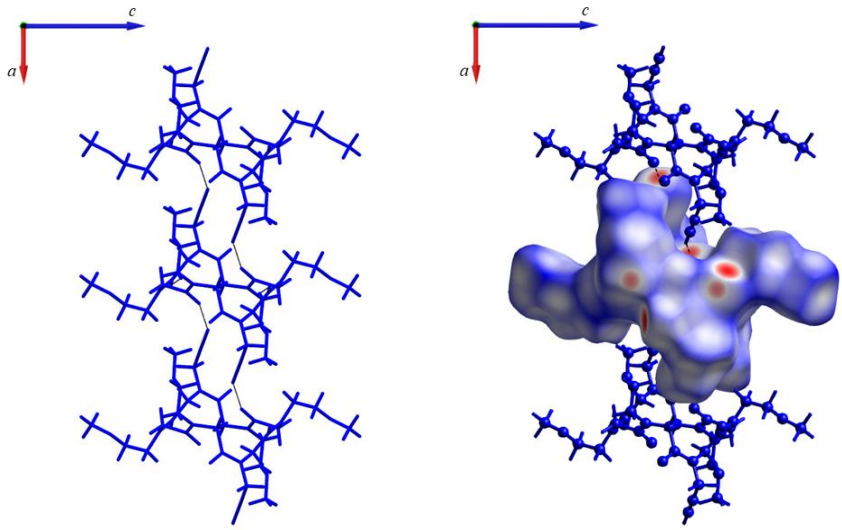

(a) (b)

Figure 3.13 (a) Motif I A-A of the form 2B. (b) Hirshfeld surface mapped with d_{norm} of motif I A-A. In the Hirshfeld surface are reported also the interactions with the water molecules.

Intercolumnar interactions in type A molecules, motif II A-A (Figure 3.14 a), occur along the *b* axis by means of CO···HC interactions between the carbonyl oxygen atom and the methylene hydrogen atom of the *trans* methoxyethyl side chain (C8A-H8A2···O3A = 2.27 Å; O3A···H8A2-C8A= 151.3°). This assembly is a side-by-side interaction (backbone-to-side chain). Furthermore, the cyclic peptoid molecules involved in motif II A-A are bridged together by water molecules as can be seen by the Hirshfeld surface analysis (motif I A-W and II-W, Figure 3.14 b). The interactions involve the carbonyl oxygen atoms of the backbone and the water molecules hydrogen atoms (O1W-H1W···O3A = 1.95 Å; O3A··· H1W-O1W = 164.8°; O1W-H2W···O1A = 1.88 Å; O1A··· H2W-O1W = 133.7°).

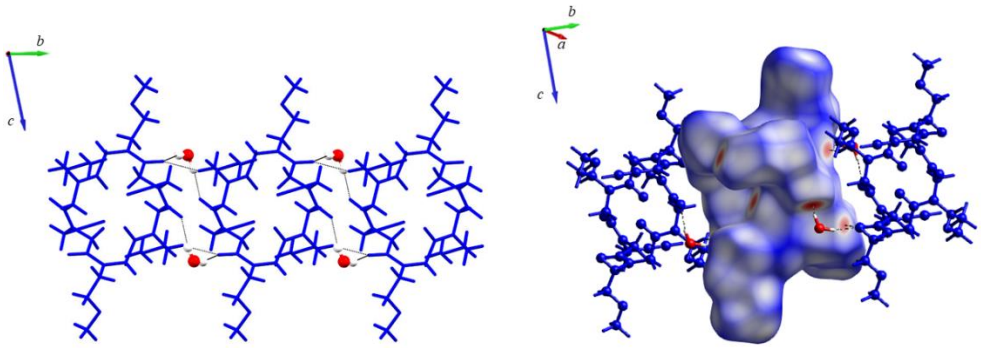

(a) (b)

Figure 3.14 (a) Motif II A-A, I A-W and II A-W of the form 2B. (b) Hirshfeld surface mapped with d_{norm} of motif II A-A, I A-W and II A-W of the form 2B.

The principal interactions in type B molecules of form 2B are related to a columnar arrangement where the cyclic peptoid molecules align along the shortest *a* axis (Figure 3.15 a,b). Intracolumnar interactions consist of CO···HC hydrogen bonds involving the carbonyl oxygen atoms and the terminal hydrogen atoms of the vertical *cis* propargyl side chain (C5-H5B···O3B = 2.16 Å; O3B···H5B-C5 = 170.4°).

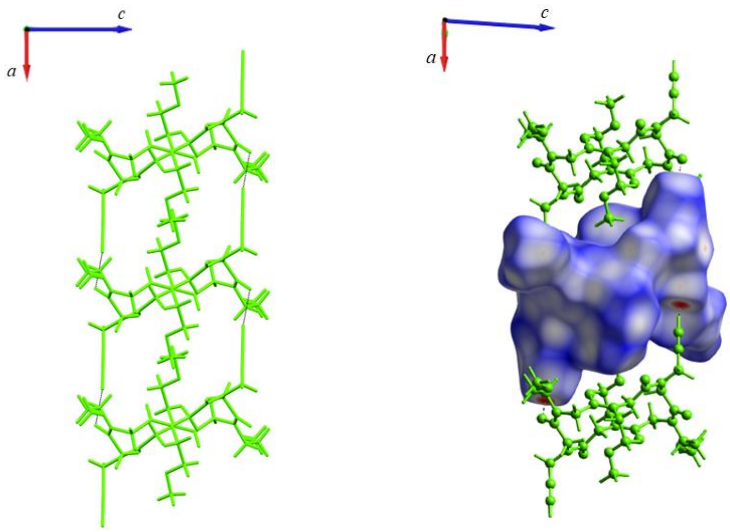

(a) (b)

Figure 3.15 (a) Motif I B-B of the form 2B. (b) Hirshfeld surface mapped with d_{norm} of motif I B-B.

Interactions between columns in type B molecules occur along the *b* axis (Figure 3.16 a). In particular, the main interactions are CO···HC involving the terminal methylene hydrogen atom of the *cis* methoxyethyl side chain and carbonyl oxygen atom of the backbone (C15B-H15D···O3B = 2.556Å; O3B···H15D-C15B = 127.5°) and the methylene hydrogen atom of the *trans* methoxyethyl side chain and carbonyl oxygen atom (C8B-H8B2···O1B = 2.57 Å; O1B···H8B2-C8B = 162.5°). Despite the energy value of motif II B-B is higher than the energy value of motif II A-A (-70.6 kJ/mol respect to -54.6 kJ/mol), in the Hirshfeld surface analysis (Figure 3.16 b) is not possible to recognize red spots related to the main interactions which characterize this motif.

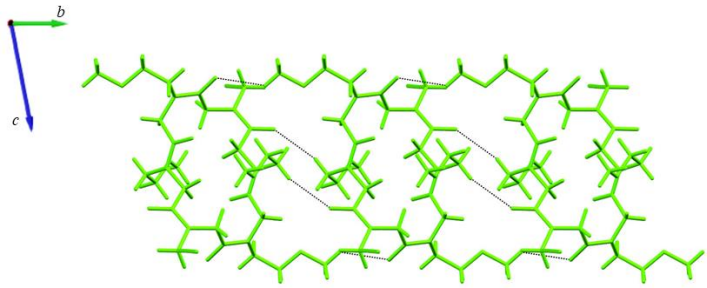

(a)

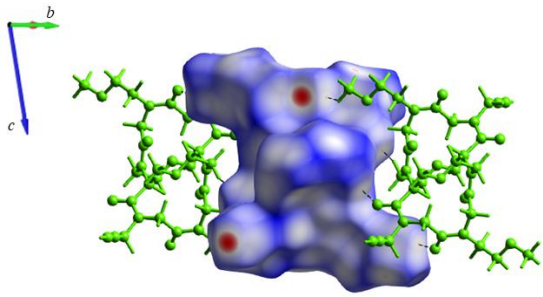

(b)

Figure 3.16 (a) Motif II B-B of the form 2B. (b) Hirshfeld surface mapped with d_{norm} of motif II B-B.

Interactions between the two different conformers are less energetically relevant than interactions among the same conformers. In particular, the motif I A-B (Figure 3.17 a) is characterized by a CO···HC interaction involving the methylene hydrogen atom of the *trans* methoxyethyl side chain and the backbone oxygen atom (C10A-H10C···O3B = 2.65 Å; O3B···H10C-C10A = 121.8°). Also in this case, analysing the Hirshfeld surface (Figure 3.17 b), is not possible to recognize any red spot related to this interaction.

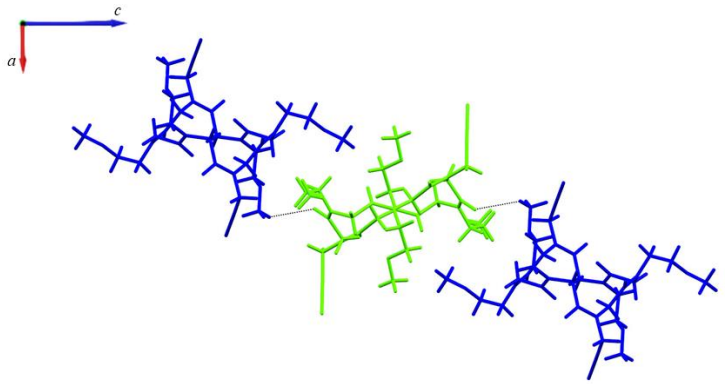

(a)

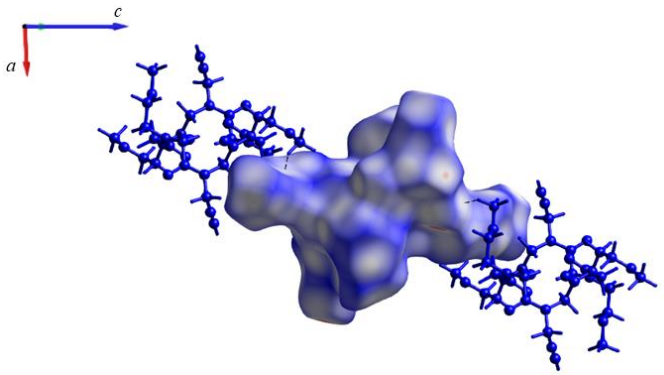

(b)

Figure 3.17 (a) Motif I A-B of the form 2B. (b) Hirshfeld surface mapped with d_{norm} of motif I A-B.

In motif II A-B (Figure 3.18 a,b), the main interaction is a CO···HC involving the oxygen atom of the methoxyethyl side chain and the methylene hydrogen atom of the backbone (C11B-H11C···O5A = 2.60 Å; O5A···H11C-C11B = 141.8°).

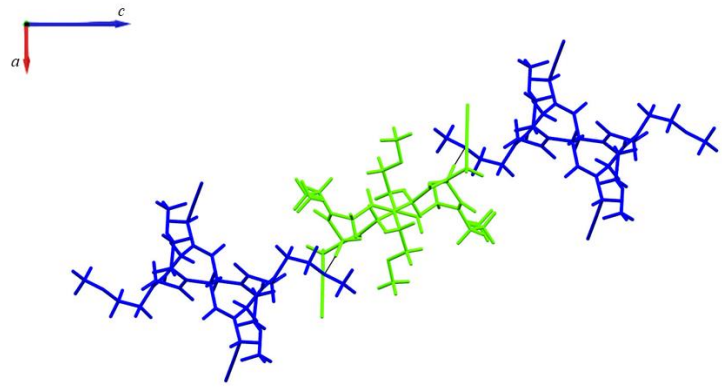

(a)

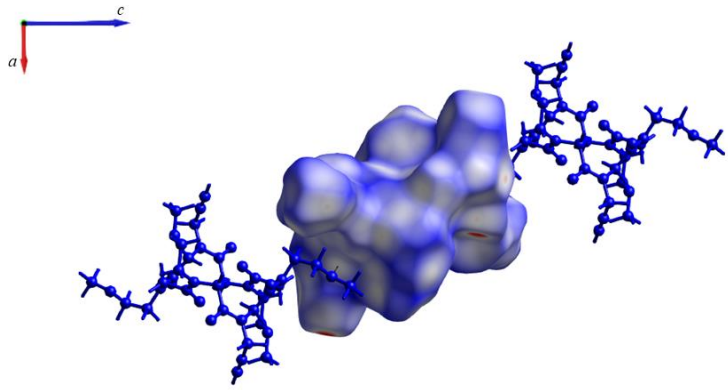

(b)

Figure 3.18 (a) Motif II A-B of the form 2B. (b) Hirshfeld surface mapped with d_{norm} of motif II A-B.

In conclusion, the main motifs in form 2B are the columnar arrangement of type A and type B molecules. Moreover, the type B molecules present also a more efficient side-by-side interactions respect to the type A molecules. The interactions between the two different conformers are less energetically important than the interactions between the same conformers.

Table 3.4 List of intermolecular distances (Å), angles (°) and interaction energies (kJ/mol) in the framework of form 2B.

Motif	D-H···A	H···A (Å)	D-H···A (°)	Symm. Op.	Centroid Distance (Å)	E_{Coul}	E_{Pol}	E_{Disp}	E_{Rep}	E_{Tot}
I A-A	C5A-H5A···O2A	2.09	150.1	-1+x, y, z 1+x, y, z	8.363	-59.9	-24.6	-88.3	85.9	-86.9
II A-A	C8A-H8A2···O3A	2.27	151.3	x,-1+y, z z, 1+y, z	9.394	-35.0	-16.0	-54.6	51.1	-54.6
I B-B	C5-H5B···O3B	2.16	170.4	-1+x y, z 1+x, y, z	8.636	-52.8	-17.9	-69.2	62.5	-77.5
II B-B	C15B-H15D···O3B C8B-H8B2···O1B	2.56 2.57	127.5 162.5	x, -1+y, z x, 1+y, z	9.394	-34.0	-13.4	-62.0	38.8	-70.6
I A-B	C10A-H10C···O3B	2.65	121.8	x, y, z 1+x, y, 1+z -1+x, y, -1+z	11.694	-13.4	-6.4	-47.7	27.0	-40.6
II A-B	C11B-H11C···O5A	2.60	141.8	x, y, 1+z 1+x, y, z -1+x, y, z x, y, -1+z	11.512	-13.2	-6.1	-49.9	32.1	-37.1
I A-W	O1W-H1W···O3A	1.95	164.8	x, -1+y, 1+z x, 1+y, -1+z	6.169	-33.6	--11.7	-12.4	27.7	-30.2
II A-W	O1W-H2W···O1A	1.88	133.7	x, y, 1+z x, y, -1+z	6.085	-38.6	-15.3	-14.4	38.5	-29.8

3.2.3 Form 2C

Crystal of form 2C can be obtained kneading compound **2** with ethylene glycol and then dissolving the powder in a solution of $CHCl_3$/iPrOH (2:1). This crystal form possesses a crystallographic inversion centre and a distorted *cctcct* conformation of the peptoid backbone.

An important difference between the form 2C and all other crystal forms is related to the space group. Indeed, while the majority of the obtained crystal forms have a triclinic unit cell with a $P\bar{1}$ space group, in this case, we have a monoclinic unit cell with a $P2_1/n$ space group.

As for the form 2B, also form 2C presents two *trans* methoxyethyl and two *cis* propargyl side chains which point vertically with respect to the macrocycle plane and the *cis* methoxyethyl side chains extend horizontally.

In Table 3.5 are reported the intermolecular distances (Å), angles (°) and interaction energies (kJ/mol) in the host framework of form 2C.

In the principal motif in form 2C (motif I, Figure 3.19 a) cyclic peptoid molecules align side-by-side along the shortest *a* axis by means of backbone-to-backbone and backbone-to-side chains interactions. The interacting atoms in the backbone-to-backbone interactions are the carbonyl oxygen atom of the backbone and the methylene atom of the backbone (C1-H1B···O3 = 2.34 Å; O3···H1B-C1 = 151.7°). The backbone-to-side chains interaction involve the hydrogen atom of the *trans* methoxyethyl side chain and the carbonyl oxygen atom (C8-H8B···O3 = 2.50 Å; O3···H8B-C8 = 109.7°).

Interestingly, the spots on the Hirshfeld surface (Figure 3.19 b) related to the motif I are not the most intense red spots. Indeed, the main interaction energies reported by PIXEL in motif I is the dispersion energy.

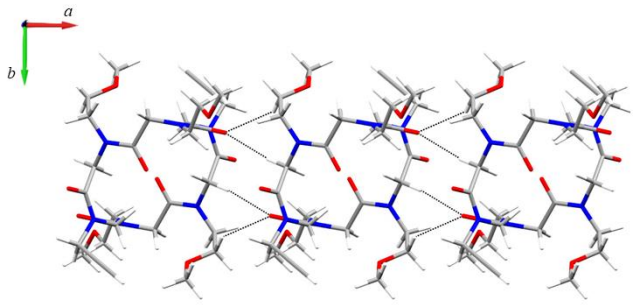

(a)

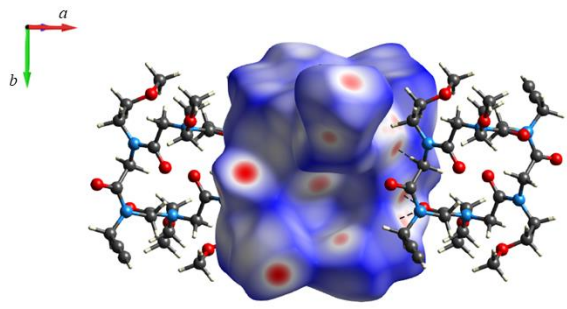

(b)

Figure 3.19 (a) Motif I of the form 2C. (b) Hirshfeld surface mapped with d_{norm} of motif I.

Motif II is made by molecules related by the screw axis, which interact by means of backbone-to-side chains interactions (Figure 3.20 a,b). In particular, the backbone oxygen atom interacts with

the terminal hydrogen atom of the *cis* propargyl side chain (C5-H5···O1 = 2.08 Å; O1···H5-C5 = 166.5°) and the methylene hydrogen atom of the *cis* methoxyethyl side chain (C14-H14B···O1 = 2.39 Å; O1···H14B-C14 = 153.3°).

Motif I defines a one-dimensional ribbon of cyclic peptoids along the *a* axis interlaced at *b* = 1/2 by the backbone-to-side chains interactions characterizing motif II.

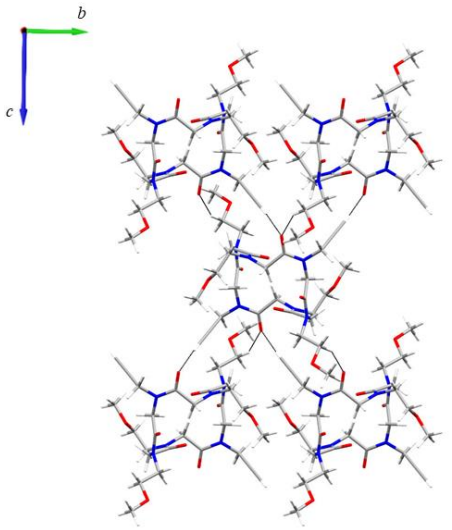

(a)

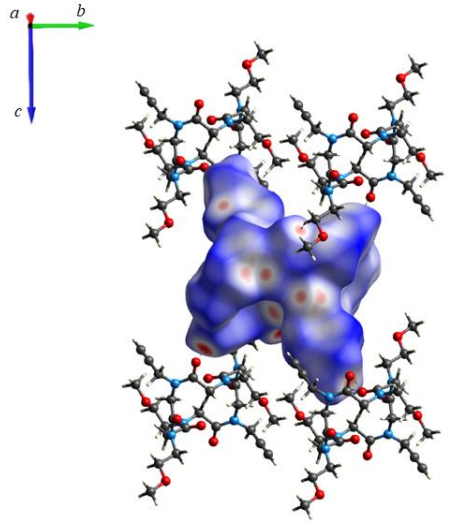

(b)

Figure 3.20 (a) Motif II of the form 2C. (b) Hirshfeld surface mapped with d_{norm} of motif II.

In motif III, cyclic peptoids align along the *b* axis (Figure 3.21 a) by means of very weak interactions like C···H contacts, which mostly involve the *trans* methoxyethyl side chain and the methylene hydrogen atom of the backbone (C10-H10C···C12 = 2.86 Å; C12···H10C-C10 = 138.9°; C11-H11B···C10 = 2.93 Å; C10···H11B-C11 = 134.6°). Thus, in the Hirshfeld surface analysis (Figure 3.21 b) no red spots related to this type of interactions are present, while in PIXEL calculation the main intermolecular energy between the macrocycles in motif III is the dispersion energy.

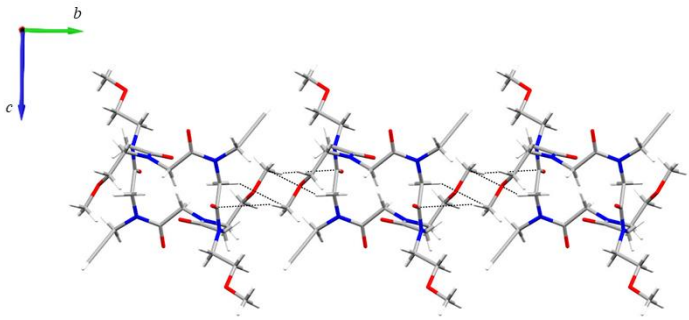

(a)

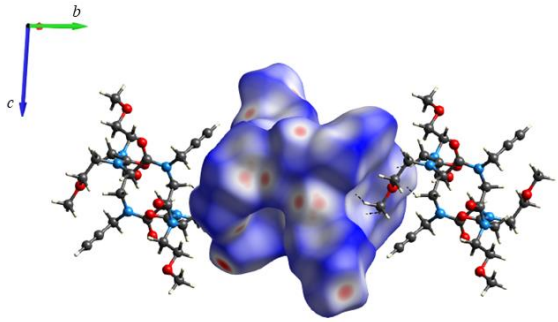

(b)

Figure 3.21 (a) Motif III of the form 2C. (b) Hirshfeld surface mapped with d_{norm} of motif III.

In motif IV (Figure 3.22 a,b), cyclic peptoids interact by means of CH···OC interactions involving the *cis* methoxyethyl and *trans* methoxyethyl side chains (C10-H10A···O5 = 2.37 Å; O5···H10A-C10 = 169.5°) hydrogen atom of the *cis* methoxyethyl side chain and a carbonyl oxygen atom (C15-H15A···O2 = 2.66 Å; O2···H15A-C15 = 91.9°).

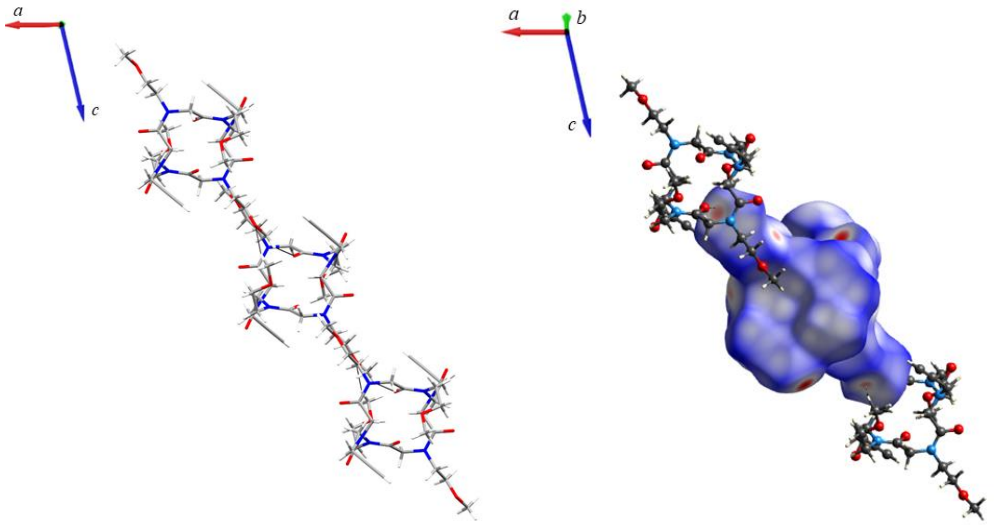

(a) (b)

Figure 3.22 (a) Motif IV of the form 2C. (b) Hirshfeld surface mapped with d_{norm} of motif IV.

In conclusion, in form 2C it is not possible to recognize a columnar arrangement and the main motif is represented by a side-by-side arrangement. Moreover, analysing the intermolecular interaction energies reported in Table 3.5, it is clear that the motifs are characterized by almost the same energy values and, considering the crystal packing of the other crystal forms, this is a peculiar aspect of form 2C.

In conclusion, it is possible to observe that cyclic peptoids form ribbons by means of backbone-to-backbone CH···OC interactions mimicking β-sheet secondary structures in proteins.

Table 3.5 List of intermolecular distances (Å), angles (°) and interaction energies (kJ/mol) in the framework of form 2C. Energy values are reported in kJ/mol.

Motif	D-H···A	H···A (Å)	D-H···A (°)	Symm. Op.	Centroid Distance (Å)	E_{Coul}	E_{Pol}	E_{Disp}	E_{Rep}	E_{Tot}
I	C1-H1B···O3	2.34	151.7	-1+x, y, z	9.037	-33.4	-20.9	-60.1	57.5	-56.9
	C8-H8B···O3	2.50	109.7	1+x, y, z						
II	C5-H5···O1	2.08	166.5	1/2-x, -1/2+y, -1/2-z	10.582	-43.1	-15.7	-38.2	45.5	-51.6
	C14-H14B···O1	2.39	153.3	1/2-x, 1/2+y, -1/2-z						
				3/2-x, -1/2+y, 1/2-z						
				3/2-x, 1/2+y, 1/2-z						
III	C10-H10C···C12	2.86	138.9	x, -1+y, z	10.622	-7.4	-7.4	-57.0	34.5	-37.3
	C11-H11B···C10	2.93	134.6	x, 1+y, z						
IV	C10-H10A···O5	2.37	169.5	1/2-x, 1/2+y, 1/2-z	12.152	-20.6	-8.4	-36.3	34.7	-30.6
	C15-H15A···O2	2.66	91.9	1/2-x, -1/2+y, 1/2-z						
				3/2-x, -1/2+y, -1/2-z						
				3/2-x, 1/2+y, -1/2-z						

3.2.4 Form 2D

Crystals of form 2D were obtained by slow evaporation of a solution of $CHCl_3$/ H_2O (1:1). This crystal form possesses a crystallographic inversion centre and a distorted *cctcct* conformation of the peptoid backbone.

The main difference which can be observed between the form 2D and all the other analysed crystal forms is related to the propargyl side chain. Indeed, in all the crystal forms that have been obtained using the different crystallization solvents, form 2D is the only one that shows the propargyl side chain in *trans* conformation. This aspect, which has a tremendous impact on the crystal packing of this crystal form, will be extensively described in the following paragraphs.

In Table 3.6 are reported the intermolecular distances (Å), angles (°) and interaction energies (kJ/mol) in the host framework of form 2D.

The principal interaction involves a side-by-side arrangement along the long side of the cyclic peptoid backbone creating a layer of cyclic peptoids along the *b* axis (Figure 3.23 a,b). The interacting atoms in the backbone-to-backbone interactions are the carbonyl oxygen atom of the backbone and the methylene hydrogen atom of the backbone (C1-H1A···O3 = 2.35 Å; O3···H1A-C1 = 136.5°). The backbone-to-side chains interaction involves the hydrogen atom of the *trans* propargyl side chain and the carbonyl oxygen atom (C3-H3A···O3 = 2.32 Å; O3···H3A-C3 = 176.6°).

If we compare the motif I of form 2D with the motif I of the form 2C, it is evident that the two motifs are very similar. The principal differences are related to the energy values, which in the form 2D is considerably higher than the motif I of form 2C (-81.7 kJ/mol vs -56.9 kJ/mol), and to the side chains which are involved in the interactions. Indeed, carefully studying this motif it is clear that the interactions are the same, but in the specific case of form 2C, a key role is played by the *trans* methoxyethyl side chains, while in form 2D the side chain involved is the *trans* propargyl side chain.

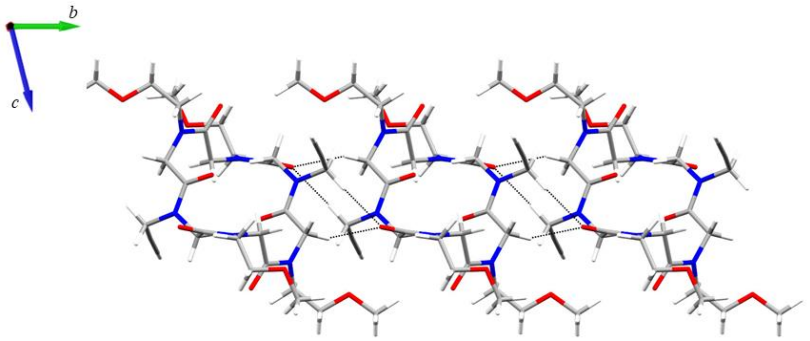

(a)

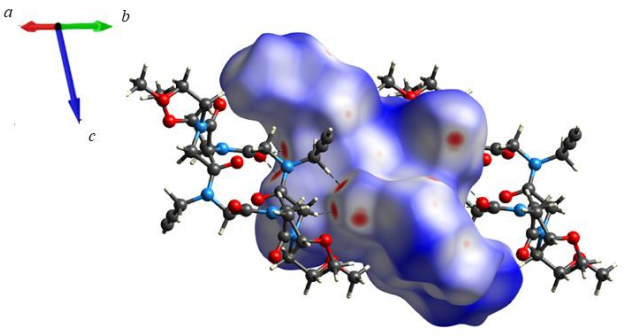

(b)

Figure 3.23 (a) Motif I of form 2D. (b) Hirshfeld surface mapped with d_{norm} of motif I.

Cyclic peptoids align along the shortest *c* axis forming a columnar-like arrangement (motif II, Figure 3.24 a). In this case, the *trans* propargyl side chain act as pillar linking together the macrocycles. The interaction involves the hydrogen atom of the propargyl side chain and the carbonyl oxygen atom of the backbone (C5-H5···O3 = 2.37 Å; O3···H5-C5 = 125.3°). By carefully analysing the Hirshfeld surface (Figure 3.24 b) it was possible to discover two more short contact favouring the motif II: a hydrogen bond between the oxygen atom of the *cis* methoxyethyl side chain and the methylene hydrogen atom of the *cis* methoxyethyl side chain (C8-H8A···O5 = 2.57 Å; O5···H8A-C8 = 156.3°) and a more interesting contact between the methylene hydrogen atom of the *cis* methoxyethyl side chain and carbonyl carbon atom the backbone (C13-H13A···C12 = 2.64 Å; C12···H13A-C13 = 156.0°). This contact is a CH-π interaction between the hydrogen atom and π-electrons of the C=O double bond.

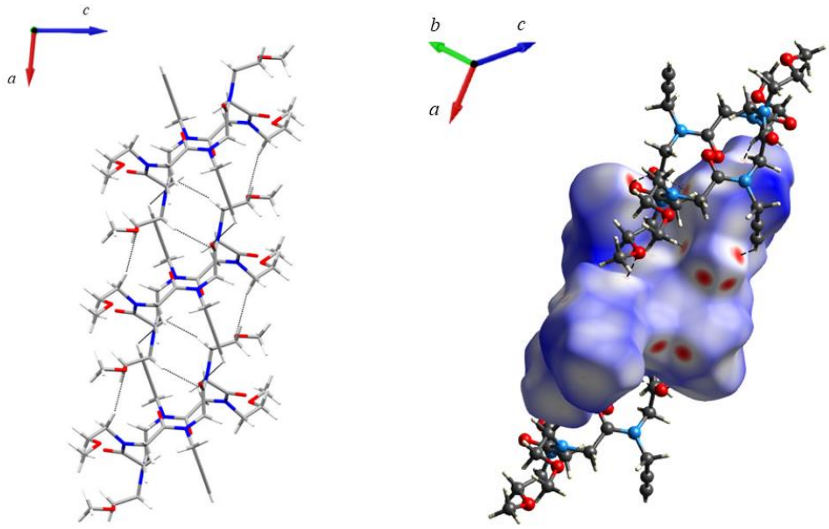

(a) (b)

Figure 3.24 (a) Motif II of the form 2D. (b) Hirshfeld surface mapped with d_{norm} of motif II.

Motif III (Figure 3.25 a) is defined by the alignment of the cyclic peptoids along the *ab* diagonal by means of CH···O interaction between the terminal hydrogen atom of the *trans* propargyl side chain and the oxygen atom of the *cis* methoxyethyl side chain (C5-H5···O4 = 2.70 Å; O4···H5-C5 = 153.4°) and a CH-π interaction between the methylene hydrogen atom of the backbone ant the triple bond of the *trans* propargyl side chain (C1-H1B···C5≡ = 2.75 Å; C5≡···H1B-C1 = 118.7°). The Hirshfeld surface analysis (Figure 3.25 b) points out that there are no strong interactions between

the cyclic peptoids. Indeed, the PIXEL calculation shows that the main intermolecular interaction energy is the dispersion energy.

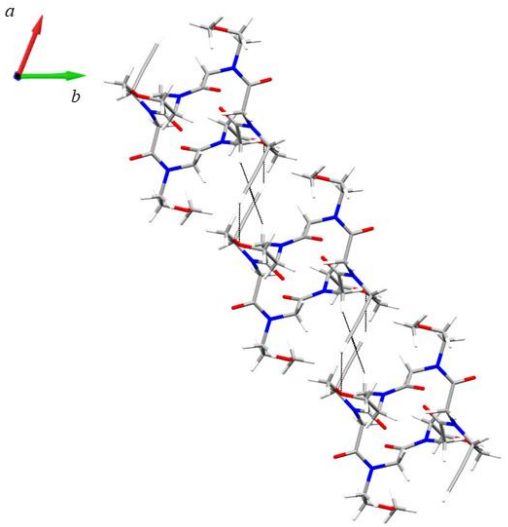

(a)

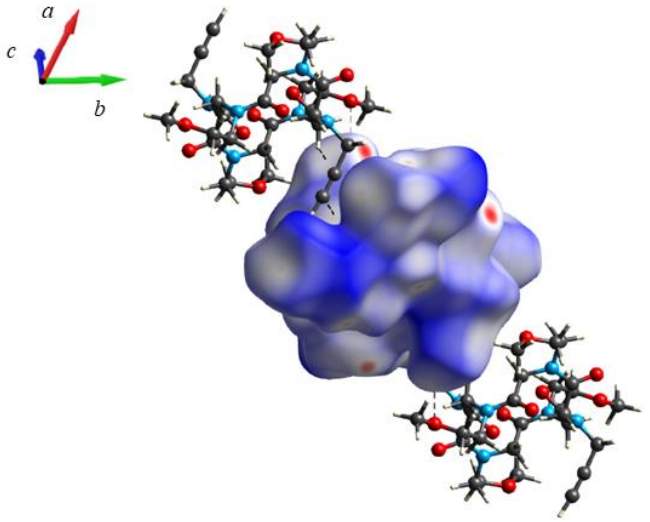

(b)

Figure 3.25 (a) Motif III of the form 2D. (b) Hirshfeld surface mapped with d_{norm} of motif III.

Cyclic peptoids align along the longest *c* axis forming the motif IV (Figure 3.26 a). The only interaction that can be visualised from the Hirshfeld surface analysis (Figure 3.26 b) is a CH···OC

interaction between the methylene hydrogen atom of the *cis* methoxyethyl side chain and the carbonyl oxygen atom of the backbone (C9-H9···O2 = 2.52 Å; O2···H9-C9 = 149.6°).

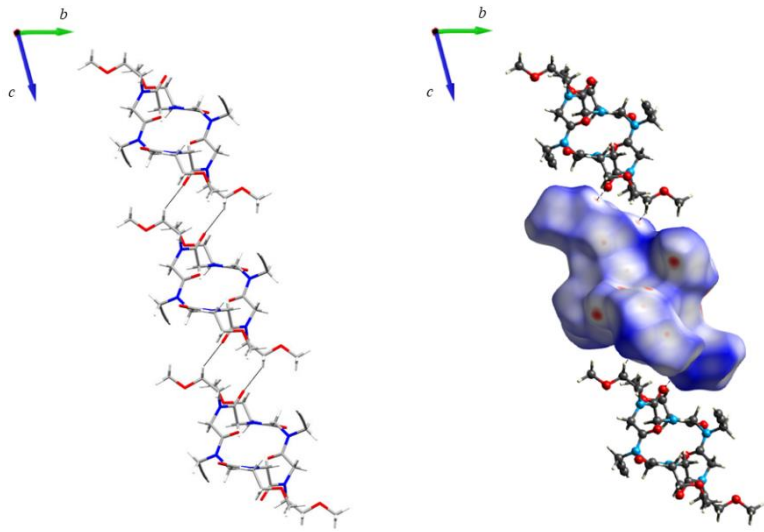

(a) (b)

Figure 3.26 (a) Motif IV of the form 2D. (b) Hirshfeld surface mapped with d_{norm} of motif IV.

The description of the crystal packing of form 2D highlights the importance of the *trans* propargyl side chain. In this conformation, it can establish a large number of interactions with the other cyclic peptoid molecules. Indeed, it is directly involved in motif I, II and III.

Table 3.6 List of intermolecular distances (Å), angles (°) and interaction energies (kJ/mol) in the framework of form 2D. Energy values are reported in kJ/mol.

Motif	D-H···A	H···A (Å)	D-H···A (°)	Symm. Op.	Centroid Distance (Å)	E_{Coul}	E_{Pol}	E_{Disp}	E_{Rep}	E_{Tot}
I	C3-H3A···O3	2.32	176.6	x, -1+y, z	9.180	-50.2	-24.2	-72.5	65.1	-81.7
	C1-H1A···O3	2.35	136.5	x, 1+y, z						
II	C5-H5···O3	2.37	125.3	-1+x, y, z	8.577	-52.8	-24.8	-95.2	96.9	-75.9
	C8-H8A···O5	2.57	156.3	1+x, y, z						
	C13-H13A···C12	2.64	156.0							
III	C5-H5···O4	2.70	153.4	-1+x, 1+y, z	9.985	-28.5	-9.8	-58.2	44.3	-52.1
	C1-H1B···C5≡	2.75	118.7	1+x, -1+y, z						
IV	C9-H9···O2	2.52	149.6	x, y, -1+z	11.532	-11.4	-5.1	-26.6	15.6	-27.5
				x, y, 1+z						

3.3 SCSC transformations

Usually, when organic porous crystals are left in the open air tend to fade. The main cause of this phenomenon is due to the loss of the solvent which, although weakly bound to the host molecules, is fundamental for the integrity of the crystal.

In the previous description of form 2A, it was mentioned that this crystal form presents channels between cyclic peptoid molecules full of water, which do not have any structural role in the crystal packing except for water molecules O1W.

Surprisingly, when crystals of form 2A were left in the open air an SCSC transformation happens and the form 2A evolves into form 2B. As in the SCSC transformation described in paragraph 2.1.1, also in this case, the transformation determines the formation of a crystal form which is characterized by two independent molecules in the asymmetric unit. Furthermore, the water molecule O1W acting as a bridge between the cyclic peptoids is still present, playing a key role in the crystal packing.

The conformational change is not the only event needed to explain the transformation of the form 2A to the form 2B.

Since there are several mechanisms that could explain what happens during the transition, we decided to describe the mechanism that provides the least number of changes and movement of the molecules within the crystal lattice.

Looking at the crystal packing of form 2B along the *a* axis (Figure 3.27) it is possible to recognize that the type A molecules do not show any significant change with respect to the cyclic peptoid molecules in the form 2A. To obtain type B molecules, a conformational change is needed. This change is quite similar to what happens after the transformation of the form 1A to the form 1B previously described. Indeed, the backbone superimposition of type B molecule of form 1B and 2B (Figure 3.12) clearly shows that there are no significant differences between them.

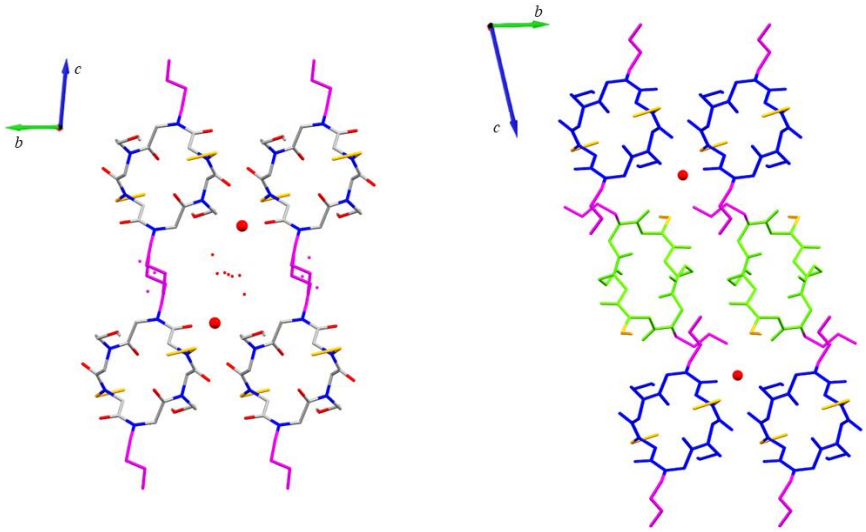

Figure 3.27 Transformation of the form 2A to the form 2B after the loss of water molecules inside the channel. In magenta are depicted the *cis* methoxyethyl side chains and in orange the *cis* propargyl side chains. Hydrogen atoms have been omitted for clarity.

Beyond the conformational change, something more interesting happens. Carefully looking at the crystal packing of form 2B along the *a* axis it is possible to recognize that the *cis* propargyl and methoxyethyl side chains in type B molecules point in the opposite direction with respect to the corresponding side chains of the molecules in crystal form 2A and in type A molecules of form 2B (Figure 3.27). To help the reader to easily visualize these small differences, in Figure 3.27 the *cis* propargyl side chains are reported in yellow, while the *cis* methoxyethyl side chains in magenta.

This difference can be explained if we consider that during the conformational change the *cis* side chains "flip". We have already demonstrated[76] that this type of side chain movement is "common" in the dynamic behaviour in the solid state of cyclic peptoid molecules. A clear example is reported in chapter II.

Of course, the presence of an inversion centre determines that in the other half of the molecules the side chains point in the "right" direction. But, despite this observation, we must consider the side chain flip because also applying the inversion symmetry operation, there will be always a row of cyclic peptoid molecules characterized by the *cis* side chains, which point in the opposite direction with respect to another row.

The side chain flipping is not the only "dramatic" movement that can be observed after the transformation. Indeed, the last difference that came out from studying the crystal packing of form 2B respect to the form 2A is related to the shift of the cyclic peptoid molecules of 1/2 along the *a*

axis (Figure 3.28). Thanks to the macrocycles shift along the *a* axis, the cyclic peptoids can occupy in a more efficient way the voids left behind by the guest removal.

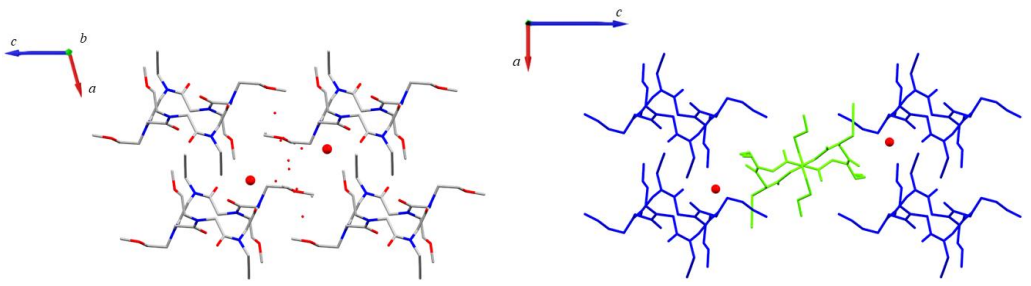

(a) (b)

Figure 3.28 View along the *b* axis of form 2A (a) and 2B (b). This figure clearly shows that type B molecules are shifted of 1/2 along the *a* axis. Hydrogen atoms have been omitted for clarity.

Since this SCSC transformation reminds the SCSC transformation described in the previous chapter, it seems to be very useful compare the energy results obtained for the two different crystal forms.

Analysing the energy values obtained using PIXEL (Table 3.4), it is clear that for type A and type B molecules the main motif is related to the columnar arrangement along the *a* axis. This is a peculiar aspect of form 2B. Indeed, the conformational change in type B molecules of the crystal form 1B induced by the loss of acetonitrile molecules determines a less efficient columnar arrangement favouring a stronger side-by-side arrangement.

In the specific case of form 2B, not only the conformational change does not induce a less efficient columnar arrangement of type B molecules but allows also a better side-by-side arrangement (motif II B-B), which is stronger than the equivalent side-by-side arrangement of type A molecules (motif II A-A).

Once again, after the loss of solvent molecules, the formation of a new conformer assures a better side-by-side arrangement of the cyclic peptoid.

Regarding the interactions between the two different conformers, a dramatic difference emerges when we compare the energy values of form 2B (Table 3.4) with the form 1B (Table 3.3). Indeed, in the SCSC transformation of compound **1**, the interactions between the two conformers are fundamental for the integrity of the crystal after the transformation. In the case of compound **2**, this type of interactions is not so important for crystal packing. The energy values are considerably lower than the energy values associated with the other motifs. This particular observation could explain

why the water molecule O1W is still present in the form 2B after the transformation. Thus, only the conformational change is not enough to ensure the integrity of the crystal.

The energy framework analysis, in a very efficient and simple way, gives us the opportunity to visualize the supramolecular assembly in form 2B and confirm what we tried to explain with words. Since the form 2A shows disordered water molecules inside the channels, we decided to not report the energy frameworks because during the calculation it is not possible to include the solvent molecules.

Comparing the frameworks of type A and type B molecules (Figure 3.29 a, b), it is clear that type B molecules can assembly in a more efficient way than the type A molecules and the main reason is related to the better side-by-side arrangement of the green molecules.

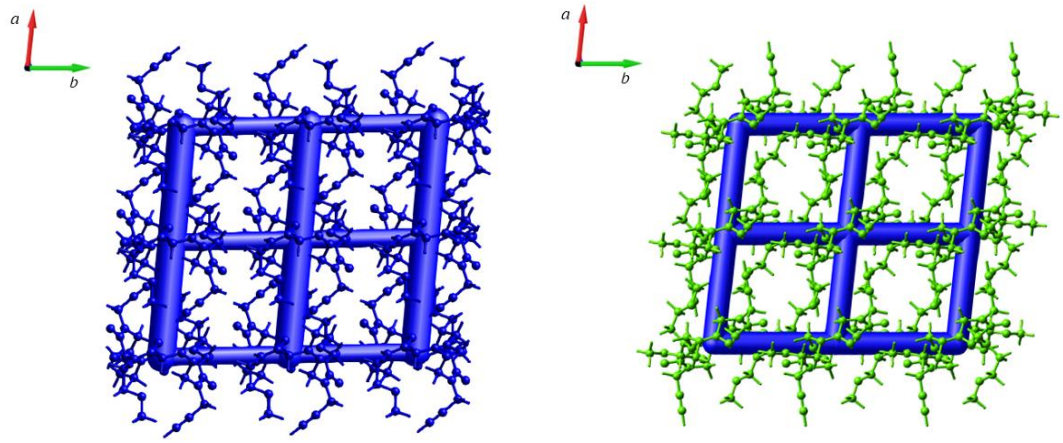

(a) (b)

Figure 3.29 Comparison between the energy framework of type A molecules (a) and type B (b) molecules of form 2B.

Observing the frameworks that illustrate the intermolecular interactions between the two different conformers (Figure 3.30), it is possible to notice that the interactions between the two conformers act as junctions which hold together the columns of type A and type B molecules.

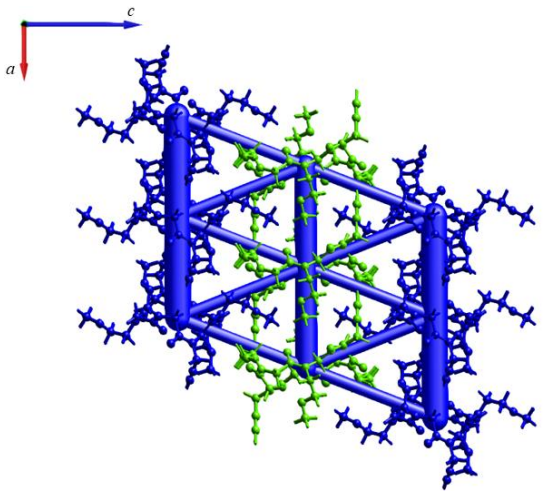

Figure 3.30 Energy frameworks of motif I A-B of the form 2B.

For the sake of knowledge, we decided to perform a variable temperature X-ray single crystal experiment on a crystal of the form 2B at the "Dipartimento di Scienze della Terra e Geoambientali" (University of Bari).

To confirm that the starting crystal form is the desired one, a data collection at RT was performed. After that, the crystal was heated up by step of 25 K until 453 K. At every single temperature step, a fast data collection was performed in order to obtain the unit cell values and monitor the possible phase transition (Table 3.7). In Figure 3.31 are reported two photos of the crystal obtained at RT and 398 K. As can be deduced from Figure 3.31, the crystal seems to be darker at 398 K.

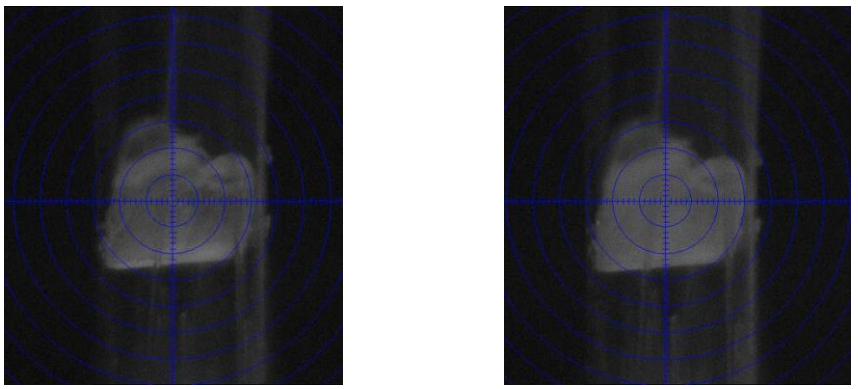

(a) (b)

Figure 3.31 Photos of the crystals at RT before the variable temperature experiment (a) and 398 K (b).

Table 3.7 Unit cell values obtained during the thermal treatment.

Temperature (k)	*a* (Å)	*b* (Å)	*c* (Å)	*α* (°)	*β* (°)	*γ* (°)
298	**8.4676(7)**	**9.4083(8)**	**21.6949(20)**	**78.740(5)**	**88.809()**	**84.004(5)**
323	8.50(2)	9.39(4)	21.64(8)	78.74(4)	88.78(11	83.77(7)
348	8.62(5)	9.47(5)	21.82(10)	78.84(5)	88.34(13)	83.43(10)
373	8.56(3)	9.39(3)	21.72(7)	78.74(4)	88.19(10)	83.47(6)
398	**8.6662(7)**	**20.8273(19)**	**9.5465(9)**	**90**	**96.73(6)**	**90**
413	8.72(3)	20.89(7)	9.56(3)	90	96.65(6)	90
423	8.64(4)	20.73(9)	9.46(4)	90	96.46(6)	90
433	8.56(4)	20.56(9)	9.38(4)	90	96.52(6)	90
438	8.55(5)	20.51(10)	9.37(4)	90	96.52(8)	90
443	8.60(4)	20.59(9)	9.40(4)	90	96.81(7)	90
448	8.61(5)	20.68(11)	9.47(5)	90	96.76(7)	90
453	8.78	21.14	9.60	90	90.13	90

As can be seen in Table 3.7, when the temperature reaches the 398 K the unit cell changes. Thus, a complete data collection was performed in order to obtain the crystal structure of this unknown phase.

Thanks to a new SCSC transformation, we obtained a new crystal form named form 2L. This crystal form possesses a crystallographic inversion centre and a distorted *cctcct* conformation of the peptoid backbone and presents two *trans* methoxyethyl and two *cis* propargyl side chains, which point vertically with respect to the macrocycle plane and the *cis* methoxyethyl side chains extend horizontally. The unit cell is monoclinic with a $P2_1/c$ space group.

The comparison between the form 2B and the form 2L is reported in Figure 3.32.

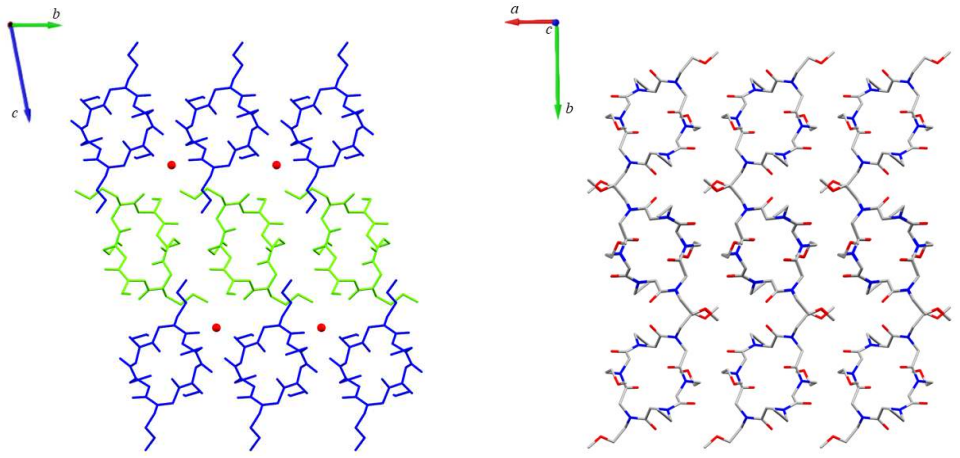

(a) (b)

Figure 3.32 Comparison between the crystal packing of form 2B viewed along the *a* axis (a) and 2L viewed along the *c* axis (b). Hydrogen atoms have been omitted for clarity.

The *cis* methoxyethyl side chain shows positional disorder. In particular, the atoms can occupy two possible positions with refined occupancy factor 0.53(3) and 0.47(3). Thus, restraints on anisotropic displacement parameters were applied to disordered group atoms.

In Table 3.8 are reported the intermolecular distances (Å), angles (°) and interaction energies (kJ/mol) in the host framework of form 2L.

Before the explanation of the possible events that characterize the SCSC transformation, a complete description of the crystal packing of the new crystal form will be presented.

The main motif of form 2L is the typical columnar arrangement of the cyclic peptoids along the shortest *c* axis (Figure 3.33 a). Columnar interactions in type A molecules consist of CO···HC hydrogen bonds involving the carbonyl oxygen atom and the terminal hydrogen atom of the vertical *cis* propargyl side chains (C5-H5···O2 = 2.34 Å; O2A··· H5A-C5A = 153.5°) and a CH-π interaction involving the methylene hydrogen atom of the vertical *trans* methoxyethyl side chain and the triple bond of the *cis* propargyl (C9-H9A···C5≡ = 2.68 Å; C5≡···H9A-C9 = 160.3°). Thanks to the Hirshfeld surface analysis (Figure 3.33 b) was possible to emphasize the importance of the CH-π interaction for the columnar arrangement.

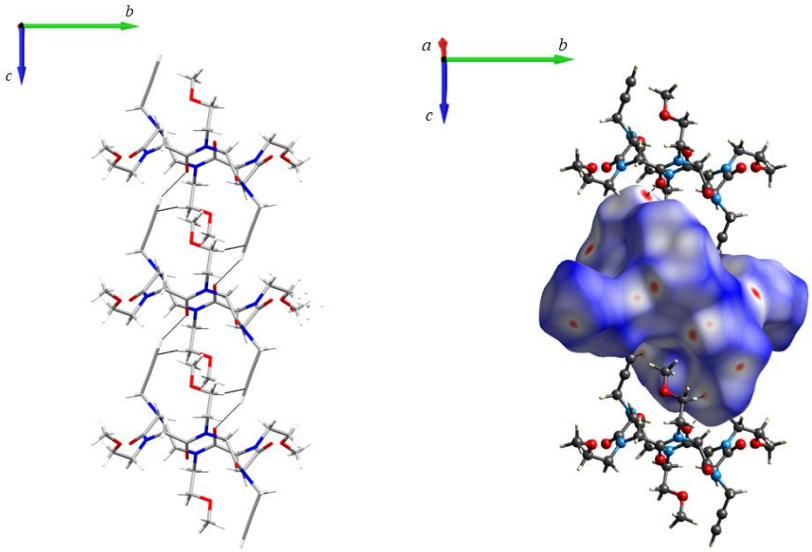

(a) (b)

Figure 3.33 (a) Motif I of the form 2L. (b) Hirshfeld surface mapped with d_{norm} of motif I.

The second motif is characterized by a side by side interaction along the *a* axis (Figure 3.34 a). This motif is realized by a backbone-to-side chain interaction involving the *trans* methoxyethyl side chain and the carbonyl oxygen atom of the backbone (C8-H8A···O1 = 2.42 Å; O1···H9A-C8 = 165.4°) and a backbone-to-backbone interaction, which involves the carbonyl oxygen atom and the methylene hydrogen atom of the backbone (C6-H6B···O1 = 2.53 Å; O1···H6B-C6 = 139.9°). Two small red spots on the Hirshfeld surface (Figure 3.34 b) clarify that the two interactions are less strong then the interactions characterizing the columnar arrangement.

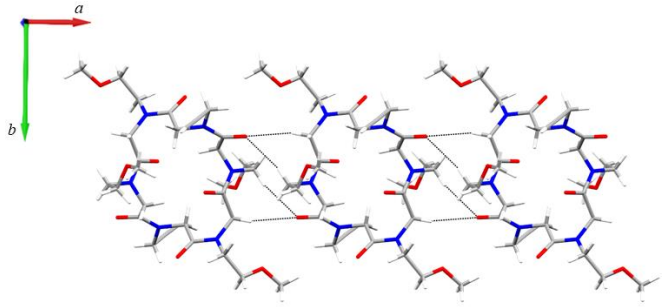

(a)

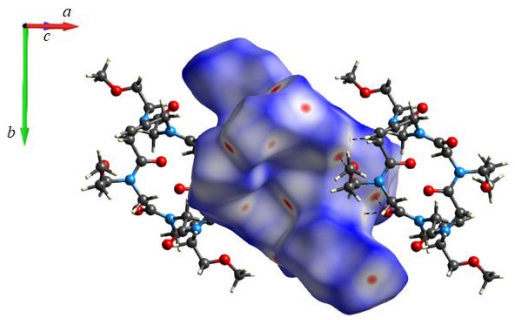

(b)

Figure 3.34 (a) Motif II of the form 2L. (b) Hirshfeld surface mapped with d_{norm} of motif II.

Motif III is characterized by the cyclic peptoid molecules which are related to the screw axis (Figure 3.35 a). Despite the centroid distances between the interacting molecules are the same, there are slight differences in the energy values. Since these differences are limited, we decided to consider them as a unique motif.

The principal interaction related to this motif is a CO···HC hydrogen bond, which involves the methylene hydrogen atom of the *cis* propargyl side chain and the carbonyl oxygen atom of the backbone (C3-H3B···O3 = 2.35 Å; O3···H3B-C3 = 131.7°). The Hirshfeld surface analysis (Figure 3.35 b) clearly testifies the strong interaction the cyclic peptoid related to the screw axis.

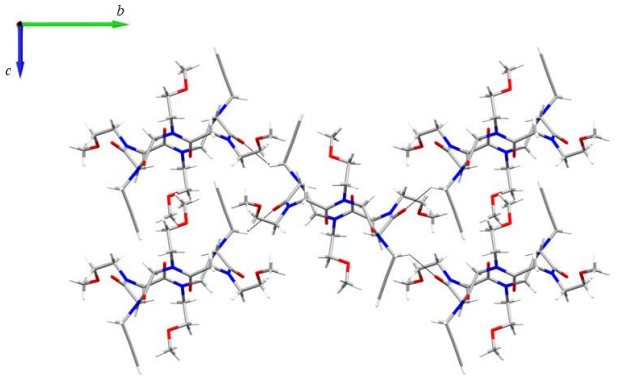

(a)

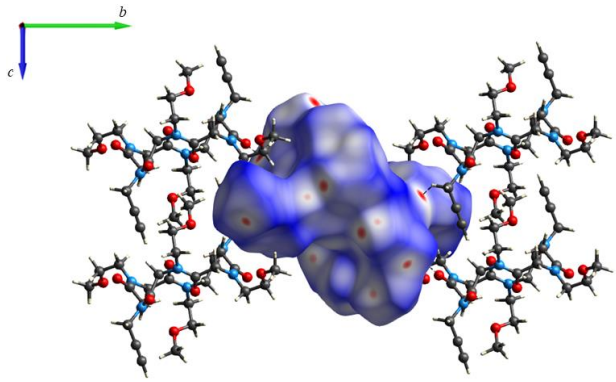

(b)

Figure 3.35 (a) Motif III of the form 2L. (b) Hirshfeld surface mapped with d_{norm} of motif III.

Table 3.8 List of intermolecular distances (Å), angles (°) and interaction energies (kJ/mol) in the framework of form 2L. Energy values are reported in kJ/mol.

Motif	D-H···A	H···A (Å)	D-H···A (°)	Symm. Op.	Centroid Distance (Å)	E_{Coul}	E_{Pol}	E_{Disp}	E_{Rep}	E_{Tot}
I	C5-H5···O2	2.34	153.5	x, y, -1+z	8.666	-56.0	-20.2	-78.3	66.4	-88.2
	C9-H9A···C5≡	2.68	160.3	x, y, 1+z						
II	C8-H8A···O1	2.42	165.4	-1+x, y, z	9.547	-27.0	-13.4	-39.5	24.6	-55.2
	C6-H6B···O1	2.53	139.9	1+x, y, z						
III	C3-H3B···O3	2.35	131.7	1-x, -1/2+y, 1/2-z	11.279	-9.0	-5.2	-34.6	17.6	-31.1
				1-x, -1/2+y, 3/2-z	11.279	-9.2	-5.2	-34.0	17.0	-31.4
				1-x, 1/2+y, 1/2-z	11.279	-9.0	-5.2	-34.6	17.6	-31.1
				1-x, 1/2+y, 3/2-z	11.279	-9.2	-5.2	-34.0	17.0	-31.4

At 398 K it is possible to force the loss of water molecules. We have demonstrated with Hirshfeld surface analysis and the energy frameworks that the water molecules are fundamental for the form 2B crystal packing. Thus, the loss of the water molecules has a tremendous impact on the crystal packing of the cyclic peptoids.

The most evident change is the conformational change of type B molecules. Indeed, the form 2L shows only one molecule in the asymmetric unit. Interestingly, the backbone superimposition of type A molecule of form 2B and form 2L (Figure 3.36) demonstrates that there are no significative differences between them (RMSD 0.152 Å). The main differences are related to the side chains

disposition. As expected, when we try to overlay the entire molecule, the RMSD value increase to 0.531 Å.

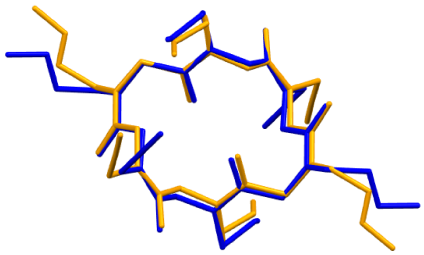

Figure 3.36 Backbone superimposition of type A molecule (Blue) of form 2B and form 2L (yellow). RMSD value 0.152 Å.

Beyond the conformational change, also a side chains flipping of the *cis* side chains must be considered. This change is very similar to what happens in the SCSC previously described.

For the sake of knowledge, we evaluate the energy in the gas phase of the different conformers, which characterized the different crystal forms of compound **2** (Table 3.11). Surprisingly, type B molecule of form 2B is the most stable conformer while type A molecule and form 2L are energetically very similar.

The reasons for the conformational change that led to a less stable conformer is related to crystal packing. As we have already demonstrated, the water molecules are fundamental for the crystal packing of the form 2B. When these water molecules are loss, something must happen to guarantee the integrity of the crystal and in this case, the conformational change to a less stable conformer allows the creation of the interactions that are fundamental for the crystal.

Recently, we have reported that in cyclic peptoids is possible to recognize a chirality related to the backbone "direction" (Figure 3.37).[105] Since the space group of form 2L imposes the presence of a glide plane, in the crystal we have two different conformational enantiomers (Figure 3.38 a).

If we draw an arrow following the directionality nitrogen-methyl-carbonyl atoms of the backbone, it is possible to define two different directions: clockwise or counterclockwise. Thanks to this simple representation it is possible to easily identify two different enantiomers. As already explained, because of the presence of the glide plane perpendicular to the *b* axis with a shift along the *c* axis, in the crystal of form 2L, we can have both enantiomers as can be seen in Figure 3.38 b.

[105] A. D'Amato, G. Pierri, C. Costabile, G. Della Sala, C. Tedesco, I. Izzo and F. De Riccardis, *Org. Lett.*, 2018, **20**, 640-643.

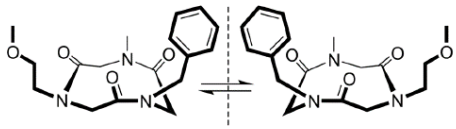

Figure 3.37 Example of enantiomorph cyclic peptoid.

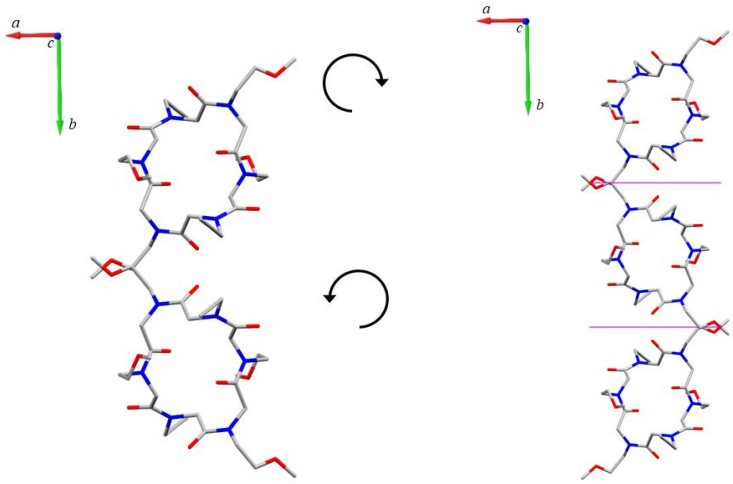

(a) (b)

Figure 3.38 (a) Representation of the different enantiomers in the crystal packing of form 2L. (b) Glide plane perpendicular to the *b* axis. The other symmetry elements and the hydrogen atoms have been omitted for clarity.

Also in this case, the mechanism of the transformation is very complicated and probably there are different ways to obtain the final result. As in the description for the SCSC transformation from the form 2A to the form 2B, also, in this case, we decided to describe the mechanism that provides the least number of changes and movement of the molecules within the crystal lattice.

For this reason, the simplest mechanism that allows us to describe the formation of two enantiomers is considering a rotation of 180° along the *b* axis.

Since the rotation does not change the interactions that can be generated between the same enantiomers, the reason for this dramatic event must be related to the interactions between the two different enantiomers.

Carefully looking at the interactions between the different enantiomers it is possible to notice a strong backbone-to-side chain interaction between the methylene hydrogen atom of the *cis* propargyl side chain and the carbonyl oxygen atom of the backbone. This strong interaction was previously

highlighted by the Hirshfeld surface analysis (Figure 3.35 b). Without the rotation and the resulting change of the chirality of the cyclic peptoid backbone, this interaction cannot be established.

The energy frameworks analysis clearly shows the fundamental role of the interactions between the different enantiomers in crystal packing (Figure 3.39). These interactions act as a tight junction between the cyclic peptoid columns, and a similar assembly can be recognized in form 2B involving the two different conformers. This observation can help us to further explain the presence of two different enantiomers in crystal form 2L: the conformational change would not allow the formation of these types of interaction but, thanks to the 180° rotation, the interactions between columns are preserved.

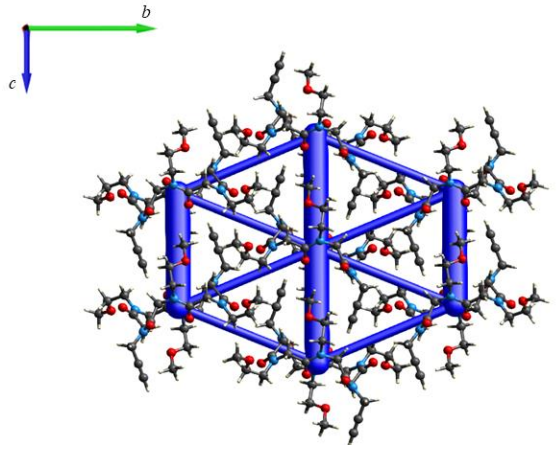

Figure 3.32 Energy framework of form 2L. In this representation are highlighted the columnar arrangement (motif I) and the arrangement between the two different enantiomers (motif III) along the unit cell diagonal. It is clear that they can act as a junction between columns.

In conclusion, crystals of the form 2A exposed to the open air lost the water molecules present inside the pores between the cyclic peptoid molecules. This loss induces a rearrangement of the molecules within the crystal lattice and determines the formation of a new crystal form, form 2B, by an SCSC transformation. This crystal form shows the presence of two independent molecules in the asymmetric unit. Type B molecules can be obtained considering a conformational change in a row of cyclic peptoids. This new conformer can establish better side-by-side interaction with the same conformers guaranteeing the integrity of the crystal after the loss of solvent molecules. Moreover, to obtain the new crystal forms side chains flipping and a shift of 1/2 along the *a* axis are necessary.

If a crystal of form 2B is heated up to 398 K, is possible to force the loss of the water molecules O1W that act as a bridge between two cyclic peptoid molecules inducing a dramatic change in the

new crystal form. The first evident change is the conformational change of type B molecules. Moreover, the transformation determines the formation of a crystal form characterized by a monoclinic unit cell and a $P2_1/c$ space group.

This space group show four symmetry elements: the identity (x, y, z), the inversion centre (-x, -y, -z), the screw axis parallel to the *b* direction (-x, 1/2+y, 1/2–z), glide plane *c* perpendicular to the *b* direction (x, 1/2-y, 1/2+ z). The presence of a glide plane induces the presence of two different enantiomers in the crystal. The simplest way to obtain this new enantiomer is by applying a 180° rotation along the *b* axis. Despite this event is so dramatic, the transformation is an SCSC transformation.

By using the PIXEL calculations, Hirshfeld surface analysis and energy frameworks we have demonstrated that the two different enantiomers can interact in a way that would not be possible without the rotation.

3.4 Variable temperature X-ray powder diffraction analysis

To investigate the thermal behaviour of compound **2**, powder sample 1 was exposed to a thermal treatment. In particular, the sample was heated up to 450 K, increasing the temperature by step of 50 K and collecting the powder pattern at each temperature value, and then cooled down to 100 K. The experiment was performed at the ESRF, at the beamline ID22 using a wavelength of 0.400067(2) Å.

The main aim of this study was to investigate what happens to a sample characterized by more than one phase when it is exposed to thermal treatment.

As already mentioned in the previous paragraph, the starting sample is characterized by two phases: form 2B and 2C with a ratio of 85.3 % and 14.7 % respectively.

In figure 3.40 are reported the powder patterns collected at different temperature.

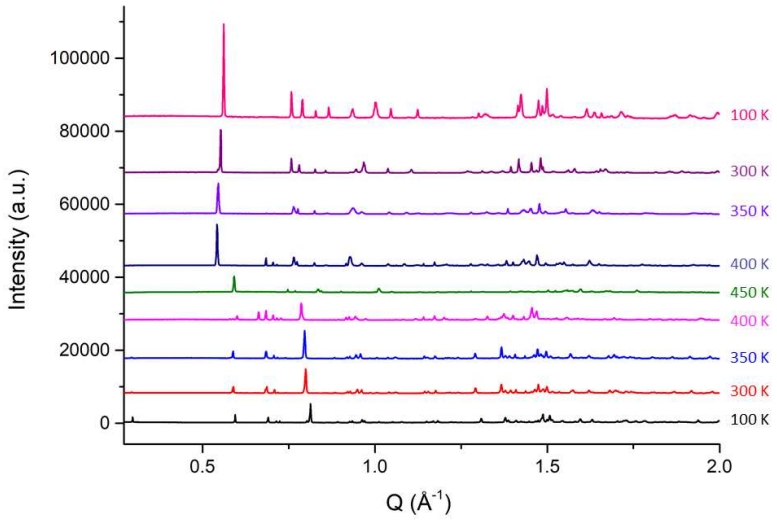

Figure 3.40 Powder patterns obtained during the variable temperature experiments.

As can be noted from Figure 3.40, at 400 K a new phase appears. From variable temperature X-ray single crystal experiment, we have demonstrated that at 398K the form 2B evolves into form 2L. Carefully performing a Rietveld refinement, it was possible to notice that using only form 2C and 2L some peaks at a low angle cannot be fitted. Adding the form 2B was possible to assign one peak to this crystal form but, unfortunately, one of the peaks remains unindexed. Concerning the form 2C, it seems that at this temperature this phase is stable. The final indices of the Rietveld refinement (Figure 3.41), included the percentage of each phase present into the powder sample, are reported in Table 3.9.

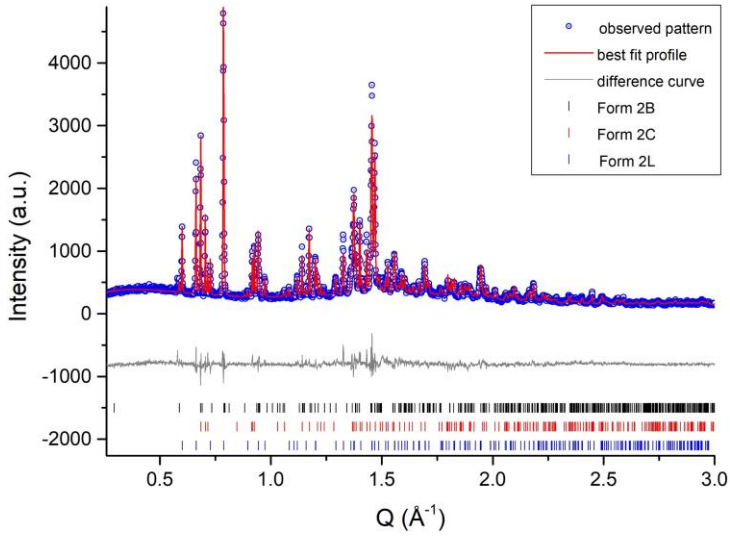

Figure 3.41 Scattered X-ray intensities of powder sample 1 after obtained at 400 K as a function of diffraction angle 2θ. In the figure are shown the observed pattern (circles), the best Rietveld fit profiles (line), the difference curve between the observed and the calculated profiles (below) and the Bragg positions of the form 2B, 2C and 2L phases (vertical ticks).

Finally, when the temperature reaches the 450 K the form 2B and form 2L completely disappears and the form 2D, previously characterized by X-ray single crystal diffraction, appears. At this temperature, the form 2C is still present. Performing a Rietveld refinement (Figure 3.42) it was possible to confirm the presence of two phases and their amounts. Final indices are reported in Table 3.9.

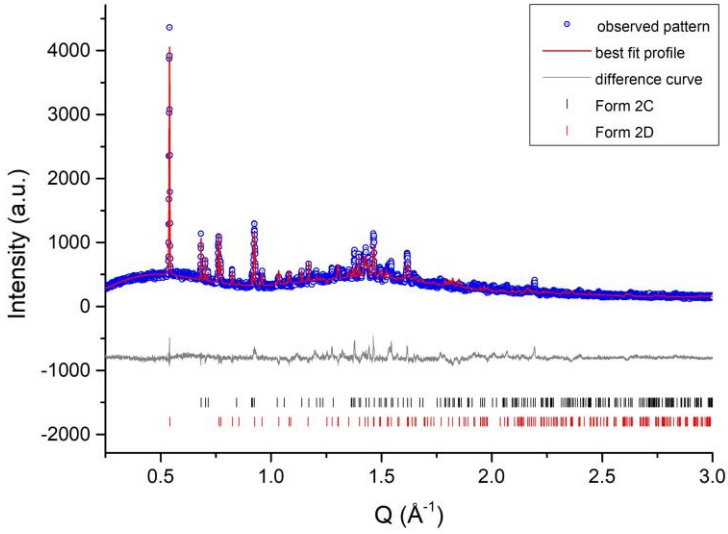

Figure 3.42 Scattered X-ray intensities of powder sample 1 after obtained at 450 K as a function of diffraction angle 2θ. In the figure are shown the observed pattern (circles), the best Rietveld fit profiles (line), the difference curve between the observed and the calculated profiles (below) and the Bragg positions of the form 2C and 2D phases (vertical ticks).

Decreasing the temperature to 100 K, a monophase powder sample was obtained. In particular, during the cooling procedure, the form 2C constantly decreased until the complete disappearing. At the end of the experiment only form 2D is present as confirmed by the Rietveld refinement (Figure 3.43). Final indices are reported in Table 3.9.

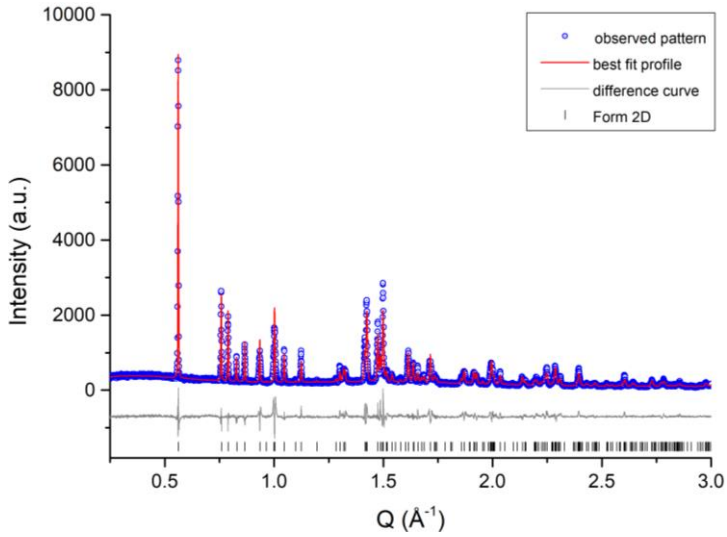

Figure 3.43 Scattered X-ray intensities of powder sample 1 after obtained at 100 K as a function of diffraction angle 2θ. In the figure are shown the observed pattern (circles), the best Rietveld fit profiles (line), the difference curve between the observed and the calculated profiles (below) and the Bragg positions of the form 2D phase (vertical ticks).

Table 3.9 Final indices of the Rietveld refinement performed at 100 K, 400 K, 450 K and back to 100 K.

Temperature (K)	R_p fitted (%)	R_{wp} fitted (%)	Form 2B (%)	Form 2C (%)	Form 2D (%)	Form 2L (%)
100	8.45	11.53	85.3	14.7	-	-
400	6.45	8.19	0.4	36.0	-	63.6
450	7.19	9.54	-	25.0	75.0	-
back to 100	9.24	12.48	-	-	100	-

The interesting aspect of the transition to the form 2D is associated with a *cis-trans* isomerization in the solid state. Indeed, as already mentioned in the previous paragraph, form 2D is the only crystal form showing the propargyl in *trans* conformation while the starting phase, form 2B and form 2C, are characterized by the methoxyethyl side chain in *trans*. This is a remarkable result since the *cis-trans* isomerization implies a drastic change in the crystal packing.

Concerning the backbone conformation, the backbone superimposition of the form 2D with the type A molecule of the form 2B, form 2C and form 2D evidence that no significant differences are present (Figure 3.44).

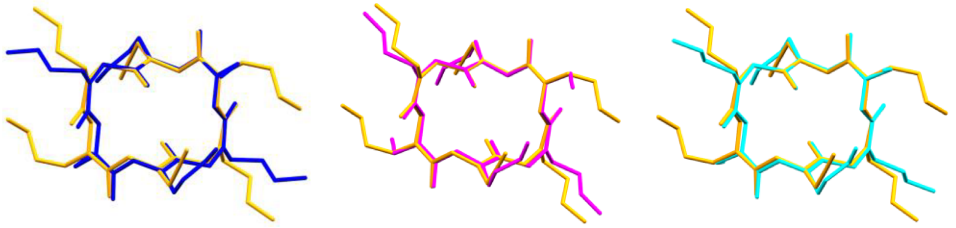

(a) (b) (c)

Figure 3.44 (a) Superimposition of the backbone of form 2D (orange) and the backbone of the type A molecule of the form 2B (blue). RMSD 0.090 Å. (b) Superimposition of the backbone of form 2D (orange) and the backbone of form 2C (magenta). RMSD 0.075 Å. (c) Superimposition of the backbone of form 2D (orange) and the backbone of the form 2L (cyan). RMSD 0.077 Å.

Building an ideal rectangle defined by the four nitrogen atoms at the corners, it is easy to notice that *trans* side chains are always located along the length of the rectangle while the *cis* side chains occupy the corners.

Considering the transformation of the form 2C and 2L to the form 2D, we have to take into account the shift of the propargyl side chain from the corner (*cis* conformation) to the length (*trans* conformation) of the rectangle. This event can be explained only if we consider a conformational change of the cyclic peptoid molecules, which does not induce a change of the backbone shape of the macrocycle.

To explain in a very simple way this conformational change, we can compare the cyclic peptoid to a gear. The conformational change allows only the shift of the propargyl side chain to the *trans* conformation without inducing any modification to the backbone shape (Figure 3.45).

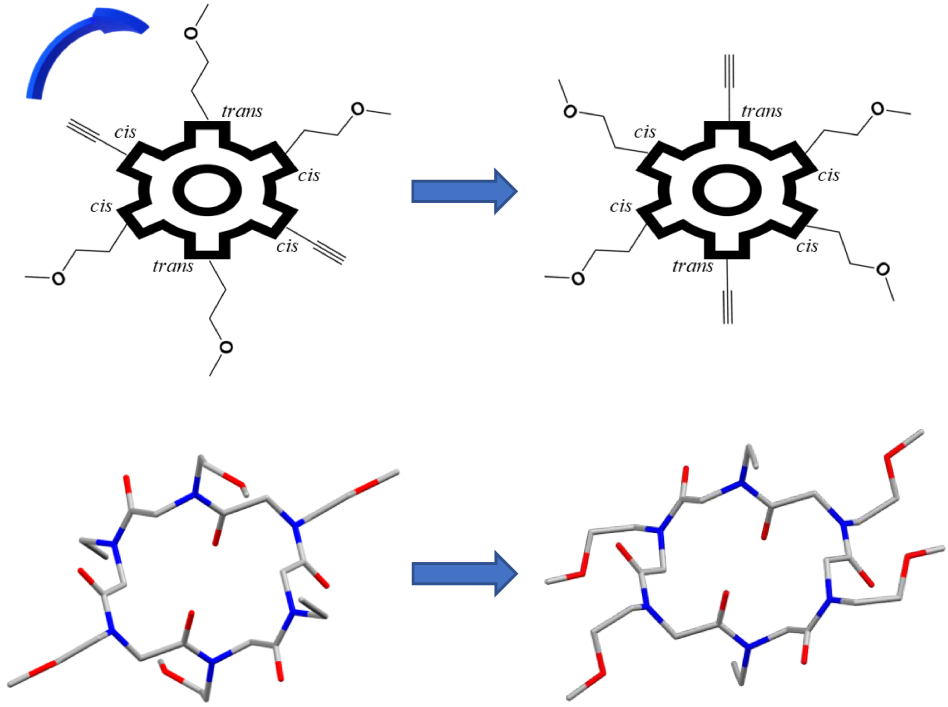

Figure 3.45 Comparison of the transformation of the form 2C to the form 2D to a gear. The gear rotation, which represents the cyclic peptoid conformational change, allows the *cis*/*trans* isomerization of the propargyl side chains without changing the backbone shape.

To explain the reason for the *cis*/*trans* isomerization, a closer look at the crystal packing is necessary (Table 3.10).

The energy values and packing coefficient reported in Table 3.10 were calculated by the CLP module. The reason for this choice is related to a limitation of the PIXEL software, which is not able to perform calculations when there are more than two molecules in the asymmetric unit.

In the case of form 2A, all the calculations were performed after the virtual removal of the water molecules inside the channel and, for this reason, it seems to be useless report the packing coefficient and the lattice energy since the model used for the calculation is far from the reality.

Table 3.10 Coefficient packing, and energy values of the different analysed crystal forms obtained using CLP. Energy values are reported in kJ/mol.

Crystal form	Packing coefficient	E_{Coul}	E_{Pol}	E_{Disp}	E_{Rep}	E_{Tot}
Form 2B	0.762	-58.3	-48.7	-157.0	103.1	-160.9
Form 2C	0.721	-92.9	-74.7	-270.0	228.2	-209.4
Form 2D	0.743	-79.4	-78.7	-292.4	190.8	-259.6
Form 2L	0.706	-66.0	-68.4	-233.6	129.0	-239.0

Moreover, a gas phase optimization was performed with Gaussian09,[106] using a polarized valence triple-zeta basis set (cc-pVTZ) and B97D3 method, a Grimme's modified functional, which includes the D3 empirical dispersion correction, in order to understand if the presence of the propargyl side chain in *trans* position determines the formation of a more stable conformer (Table 3.11). Surprisingly, form 2D is not the most stable form.

Table 3.11 Energy values differences of the different crystal forms.

Molecule	ΔE (kJ/mol)
Type B form 2B	0
Form 2A	+10.756
Type A form 2B	+10.756
Form 2L	+10.756
Form 2D	+20.289
Form 2C	+28.264

This particular result may appear unexpected, but we must consider that transformation happens in the solid state where molecules can interact with other molecules. Indeed, taking into account the results obtained using CLP (Table 3.10), it is possible to conclude that form 2D shows a better packing coefficient, second only to form 2B, which is characterized by the presence a water molecule, and lower lattice energy.

The *trans* propargyl side chains participate in three different motifs in form 2D, in particular to motif I, II and III. Comparing the energy frameworks of this crystal form to the frameworks of the form 2B and form 2C, reported in the previous paragraph, it is possible to underline that form 2D shows a more efficient packing.

[106] Gaussian 09, Revision D.01, M. J. Frisch *et al*., Gaussian, Inc., Wallingford CT, 2013.

The energy frameworks analysis clearly demonstrates the extremely efficient crystal packing of form 2D. In Figure 3.46, are reported the energy frameworks for motifs I, II and III. As can be easily deduced from the figure, all the three motifs are represented by cylinders with almost the same diameter indicating that the intermolecular energy related to the three motifs are the same.

We can deduce that when the propargyl side chains are in *trans* conformation, the interactions that can be formed are stronger.

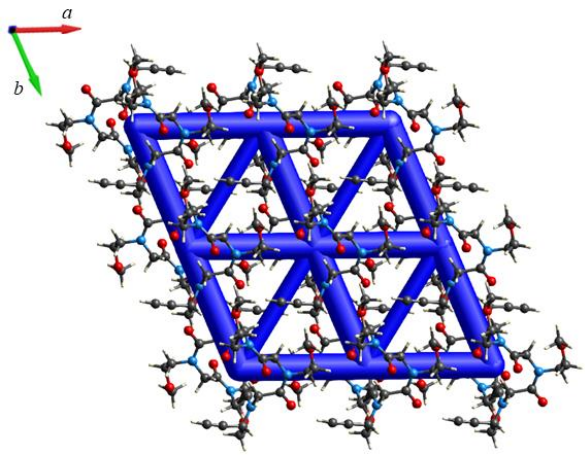

Figure 3.46 Energy frameworks of the form 2D of motif I, II and III.

During the variable temperature experiment, which confirms the SCSC transformation of the form 2B, the same crystal was heated up to 453 K, to understand if the *cis*/*trans* is compatible with an SCSC transformation. Unfortunately, when the temperature reaches the 453 K the crystal cracks (Figure 3.47 a). As can be seen in Figure 3.47 b, the sample diffracts like a powder sample instead of as a single crystal. The X-ray pattern was collected using a Gandolfi movement of the goniometric head (Figure 3.47 b).

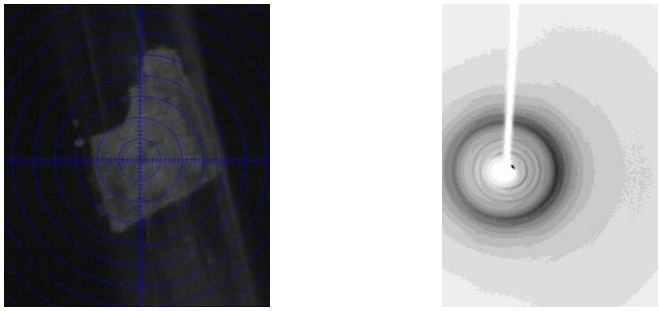

(a) (b)

Figure 3.47 (a) Photo of the crystal at 453 K. (b) X-ray pattern obtained analysing a single crystal of form 2B exposed to a temperature of 453 K.

The X-ray powder diffraction analysis clearly shows, as demonstrated also with the variable temperature SCXRD analysis, that the thermal treatment can induce the transition from the form 2B to the form 2L at 400 K. Moreover, increasing the temperature to 450 K it is possible to cause a new transformation and obtain the form 2D. At 450 K, the powder sample still contains the form 2C but, when we reduce the temperature to 100 K, it is possible to induce the transformation of the form 2C to the form 2D.

It is possible to explain why the transformation of the form 2C to the form 2D happens during the cooling down procedure considering that this transformation is kinetically slower than the transformation of the form 2L to the form 2D.

The most fascinating aspect of the transition is related to the *cis*/*trans* isomerization. Thanks to PIXEL calculations and energy frameworks analysis it was possible to demonstrate that the propargyl side chain in *trans* conformation is able to induce a more efficient crystal packing.

3.5 Thermal analysis and hot stage microscopy

On crystals of form 2A, 2B, 2C and 2D a DSC analysis was performed (Figure 3.48-3.51).

The DSC on form 2A shows a broad endothermic peak around 310 K followed by a small peak at 331 K. This event can be associated with the transformation of the form 2A to the form 2B. At 429 K an endothermic peak followed by an exothermic peak is present. In this case, we can explain these events considering the transformation from the form 2B to the form 2L. At 453 K another event can be seen which is associated with the transformation of the form 2L to the form 2D. Finally, at 472 K, an endothermic peak associated with the melting of form 2D can be seen.

Interestingly, the DSC analysis performed on crystals of form 2B shows different temperature associated with the transformation. But also in this case, we have the peaks related to the transformation from the form 2B to the form 2L (371 K) and from 2L to the form 2D (437 K). Finally, at 473 K it is possible to appreciate the exothermic peak associated with the melting of the compound.

The DSC shows that form 2C shows an endothermic peak at 454 K followed by an endothermic peak at 472 K. Concerning the DSC measurement performed on crystals of form 2D, the thermal analysis shows the presence of only one endothermic peak at 471 K. The results of the VT-XRPD analysis and DSC are perfectly consistent. Indeed, the endothermic peak at 454 K of the form 2C indicates the transition of this crystal form to the more stable form 2D. Moreover, the fusion peaks of the two experiment are very similar, indicating that form 2C evolves into form 2D which melts around the 471 K.

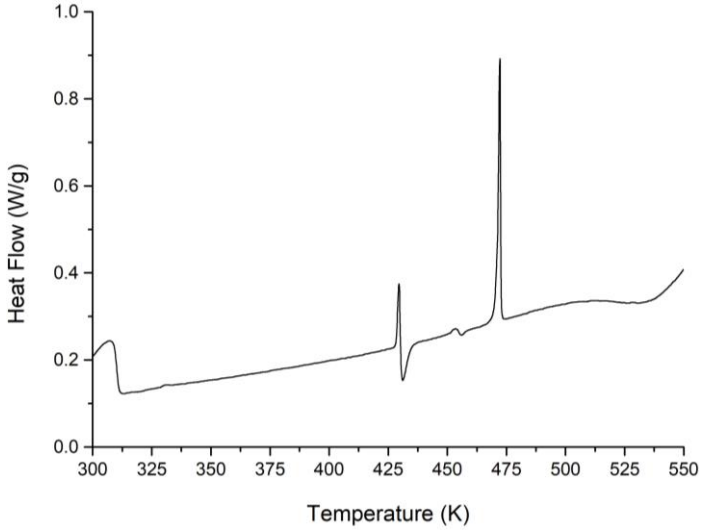

Figure 3.48 DSC measurement performed on crystals of the form 2A. The plot is reported with exo down.

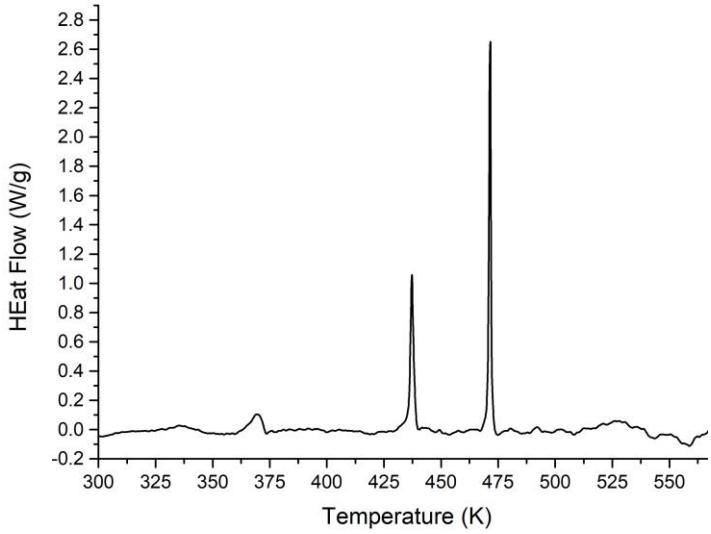

Figure 3.49 DSC measurement performed on crystals of the form 2B. The plot is reported with exo down.

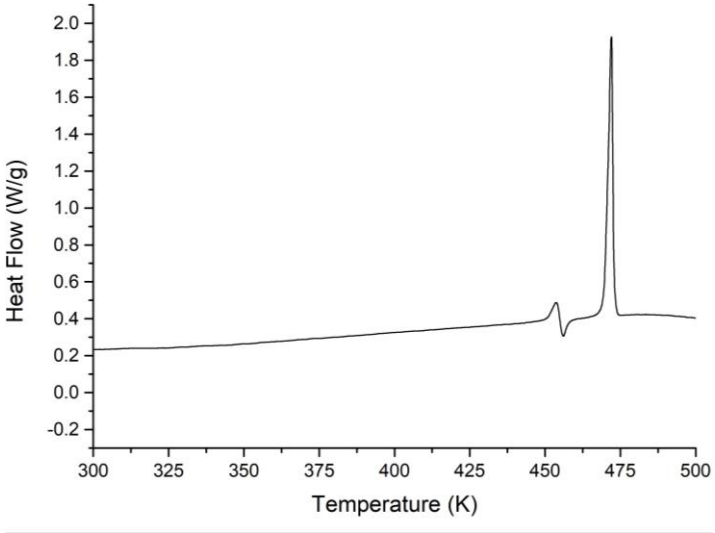

Figure 3.50 DSC measurement performed on crystals of the form 2C. The plot is reported with exo down.

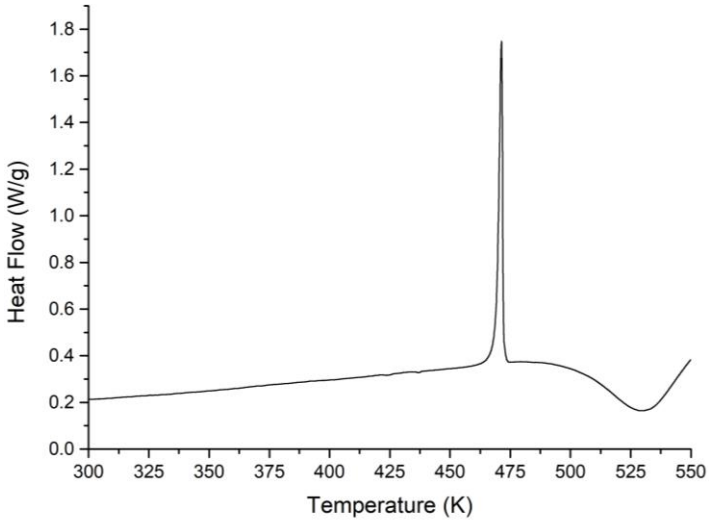

Figure 3.51 DSC measurement performed on crystals of the form 2D. The plot is reported with exo down.

Hot stage microscopy (HSM) analysis was performed on a crystal of form 2A heating up the crystal to 443 K at a rate of 2 K/min and then cooled down to the starting temperature with the same rate. The results obtained with this experiment further support the SCSC transformations (Figure 3.52).

Following the colour changes during the HSM experiment, it is possible to observe all the SCSC transformations. In particular, at 323 K (Figure 3.52 b) the crystal became lighter before becoming darker at 413 K (Figure 3.52 c). These first two colour changes are related to the transformation of the form 2A to the form 2B and then of the form 2B to the form 2L. At 443 K is possible to appreciate another colour change (Figure 3.52 d). Decreasing the temperature to 303 K, the crystal changes again becoming darker (Figure 3.52 e). These two last changes can be associated with the transformation to the form 2D.

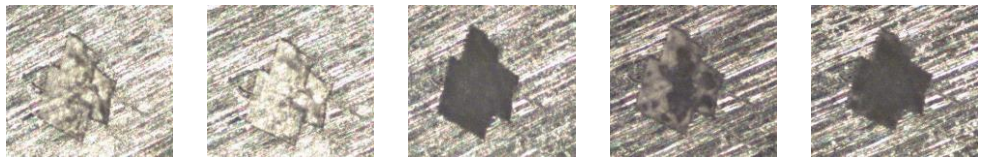

(a) (b) (c) (d) (e)

Figure 3.52 Hot stage microscopy snapshots at 303 K (a), 323 K (b), 413 K (c), 443 K (d) and back to 303 K (e).

3.6 Experimental section

3.6.1 Single crystal X-ray data collection, structure solution and refinement

Crystals of form 2A, 2C and 2D were selected and mounted on a MiTeGen microloop with paratone oil. Data collection was performed at 100 K with a Rigaku AFC7S diffractometer equipped with a Mercury2 CCD detector using graphite monochromated Mo*K*α radiation (λ = 0.71073 Å) and an Oxford Cryosystems Cryostream 700 for temperature control. Data reduction for the data collection of the form 2C and 2D were performed with the crystallographic package CrystalClear.[95] Data were corrected for Lorentz, polarization and absorption. For the form 2A, data reduction was performed with the crystallographic package CrysAlisPro 1.171.40.53.[107] The absorption correction was performed using spherical harmonics, implemented in SCALE3 ABSPACK scaling algorithm. Form 2A shows positional disorder on the *cis* methoxyethyl side chain. In particular, the atoms can occupy two possible positions with refined occupancy factor 0.68(3) and 0.32(3). Thus, restraints on anisotropic displacement parameters were applied to disordered group atoms.

Crystal data for the form 2B were collected at ESRF, beamline ID11. The crystal was mounted on a MiTeGen microloop and measured at 100 K. The chosen wavelength was 0.29520 Å. Data reduction was performed with the Bruker programs SMART, SAINT and SADABS.[108]

The variable temperature experiment on the crystal of the form 2B was performed at the Dipartimento di Scienze della Terra e Geoambientali (University of Bari). To keep the crystal in position during the measurement and avoid the use of glues or cement, the crystal was inserted in a glass capillary of 0.3 mm of diameter and sustained by quartz wool.

To control the temperature, it was used a heating system based on the Bruker FR559 heater, which allows using vertical air or gas flow to heat the sample. The system is mounted externally, above the crystal at a fixed angle, and it is characterized by a thermocouple placed at the exit of the gas flow. Temperature precision is ±2 K in the whole temperature range.

When the transformation happens, a complete data collection was performed with a Bruker-AXS SMART-APEX 2 equipped with a charge-coupled device (CCD) detector and graphite-monochromatized Mo*K*α (λ= 0.71073 Å). Data reduction was performed using the SAINT-Plus software.[109] Empirical absorption corrections were accomplished using SADABS.[110] Final unit-cell

[107] CrysAlis PRO (2014). Agilent, Agilent Technologies Ltd, Yarnton, Oxfordshire, England.
[108] Bruker (2012). SMART, SAINT, SADABS. Bruker AXS Inc., Madison, Wisconsin, USA.
[109] Bruker B (2008) APEX2, SAINT and TWINABS. AXS Inc., Madison, Wisconsin, USA.
[110] R. H. Blessing, *Acta Cryst A*, 1995, **51**, 33-38.

parameters were obtained by the Bruker GLOBAL least-squares orientation matrix refinement procedure, based on the positions of all measured reflections with $I_O > 10\sigma(I_O)$. The space group was confirmed on the base of the analysis of the intensity data by XPREP.[111]

The crystal structures of form 2A, 2B, 2C, 2D and 2L were solved by direct methods using the program SIR2014[98] and refined by means of full-matrix least-squares based on F^2 using the program SHELXL.[99] *OLEX*2[100] was used as GUI.

Crystallographic data and refinement information are reported in Table 3.12. ORTEP diagrams were drawn using *OLEX*2[100] (Figure 3.53).

[111] G. M. Sheldrick (2003) XPREP version 6.14. Bruker-Nonius Inc., Madison, Wisconsin, USA.

Table 3.12 Crystallographic data for crystal form 2A, 2B, 2C, 2D and 2L.

	Form 2A	**Form 2B**	**Form 2C**	**Form 2D**	**Form 2L**
T (K)	100	100	100	100	398
Formula	$C_{30}H_{46}N_6O_{10}$·4.58 O	$C_{30}H_{46}N_6O_{10}$·H_2O	$C_{30}H_{46}N_6O_{10}$	$C_{30}H_{46}N_6O_{10}$	$C_{30}H_{46}N_6O_{10}$
Formula weight	724.06	668.74	650.73	650.73	650.73
System	Triclinic	Triclinic	Monoclinic	Triclinic	Monoclinic
Space group	$P\bar{1}$	$P\bar{1}$	$P2_1/n$	$P\bar{1}$	$P2_1/c$
***a* (Å)**	8.3319(8)	8.363(4)	9.0367(17)	8.577(2)	9.5465(9)
***b* (Å)**	9.5479(10)	9.394(4)	10.6221(18)	9.1796(16)	20.8273(19)
***c* (Å)**	13.312(2)	21.648(10)	18.022(3)	11.532(3)	8.6662(7)
***α* (°)**	94.178(12)	78.362(5)	90	77.088(13)	90
***β* (°)**	104.454(11)	88.664(7)	102.661(4)	89.790(17)	96.573(6)
***γ* (°)**	96.148(9)	83.547(5)	90	68.335(14)	90
***V* (Å^3)**	1014.1(2)	1655.1(13)	1687.9(5)	650.73	1711.8(3)
Z	1	2	2	1	2
***Dx* (g cm^{-3})**	1.186	1.342	1.280	1.319	1.263
λ (Å)	0.71073	0.29520	0.71073	0.71073	0.71073
***μ* (mm^{-1})**	0.095	0.030	0.100	0.100	0.095
F_{000}	385.0	716.0	696.0	348.0	696
R1 (I > 2σI)	0.1257(2023)	0.0731(7288)	0.0606(2516)	0.0597(2839)	0.0981(1303)
$_wR_2$	0.3889(4711)	0.1953(8341)	0.1733(4342)	0.1703(3806)	0.3257(3498)
N. of param.	256	430	209	300	237
N. of reflections	8424	8341	4342	3806	3498
GooF	1.059	1.138	0.916	1.13	1.041
ρ_{min}, ρ_{max} (eÅ^{-3})	-0.55, 0.76	-0.38, 0.71	-0.40, 0.37	-0.33, 0.62	-0.33, 0.29
Restraints	72	-	-	-	58

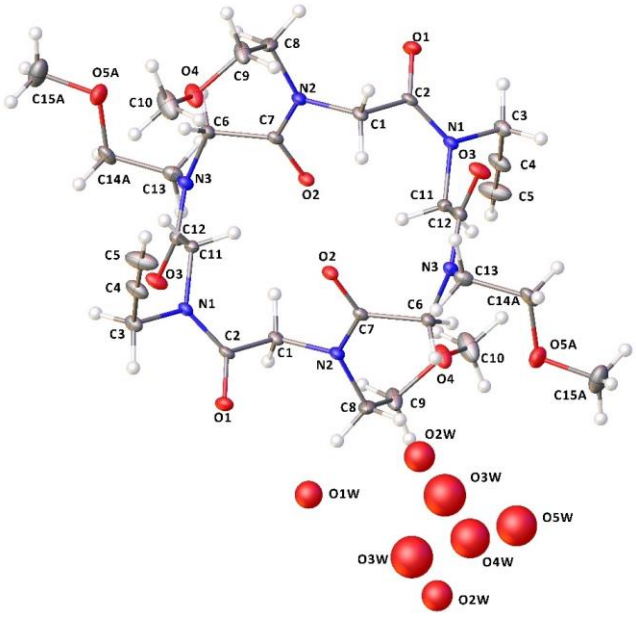
C8
O1
O5A
O4
C9
N2
C2
C15A
C10
C6
C7
C1
N1
C3
O3
C4
C14A
N3
C13
O2
C11
C5
C12
C12
C5
O2
N3
C13
C11
O3
C6
C14A
C4
N1
C7
O5A
C3
C2
C1
N2
O4
C10
C15A
O1
C8
C9
O2W
O3W
O1W
O5W
O3W
O4W
O2W

(a)

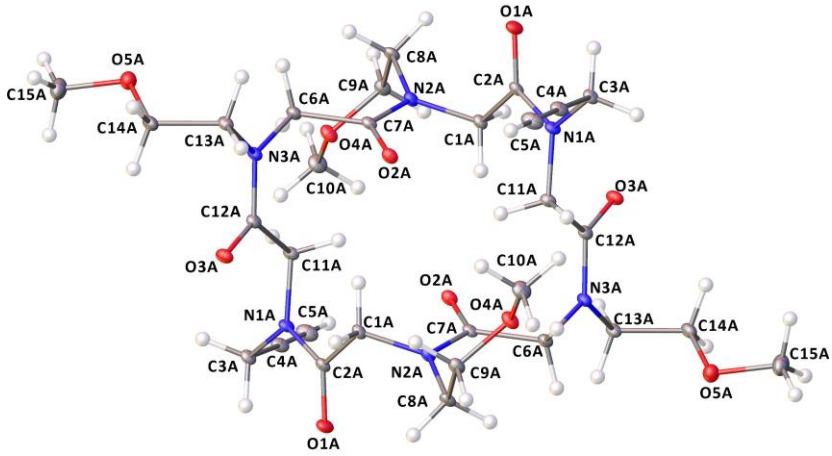
O1A
O5A
C8A
C15A
C9A
N2A
C2A
C4A
C3A
C6A
C14A
C13A
C7A
C1A
C5A
N1A
O4A
N3A
O2A
C10A
C11A
O3A
C12A
C12A
O3A
C11A
C10A
O2A
N3A
O4A
N1A
C5A
C1A
C7A
C13A
C14A
C6A
C15A
C3A
C4A
C2A
N2A
C9A
O5A
C8A
O1A

(b)

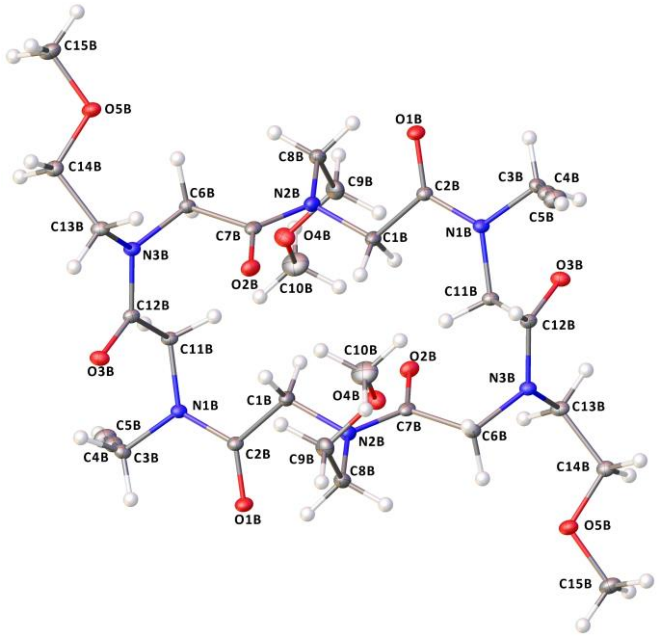
C15B
O5B
C14B
C13B
N3B
C12B
O3B
C11B
N1B
C5B
C4B
C3B
C2B
O1B
C6B
C7B
O2B
C10B
O4B
C1B
N2B
C8B
C9B
O1B
C2B
C3B
C4B
C5B
N1B
C11B
O3B
C12B
N3B
C13B
C14B
O5B
C15B
C10B
O2B
O4B
C1B
C7B
C6B
N2B
C9B
C8B

(c)

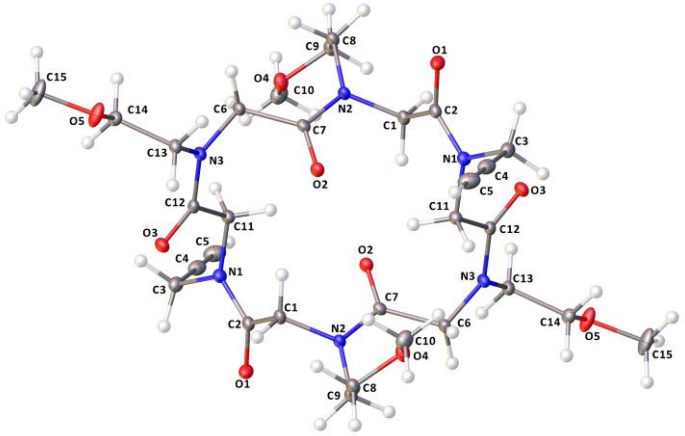
C15
O5
C14
C13
N3
C12
O3
C11
C5
C4
N1
C3
C2
O1
C6
C10
O4
C9
C8
N2
C1
C7
O2
O1
C2
C3
N1
C4
C5
O3
C11
C12
N3
C13
C14
O5
C15
O2
C7
C6
C10
O4
N2
C1
C8
C9

(d)

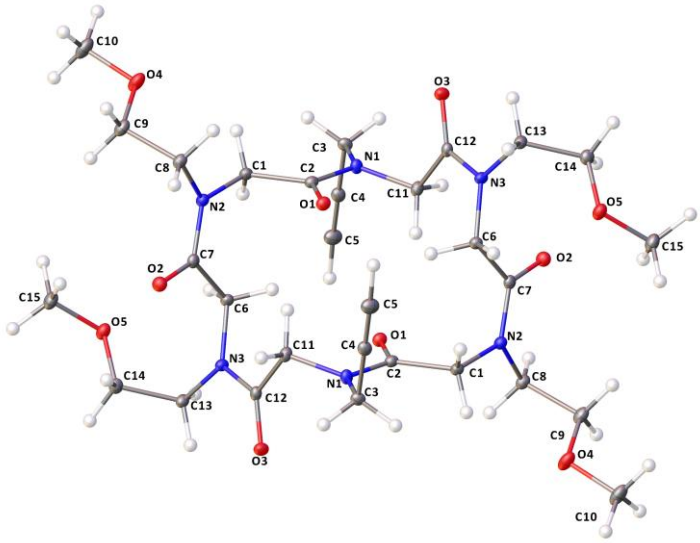

(e)

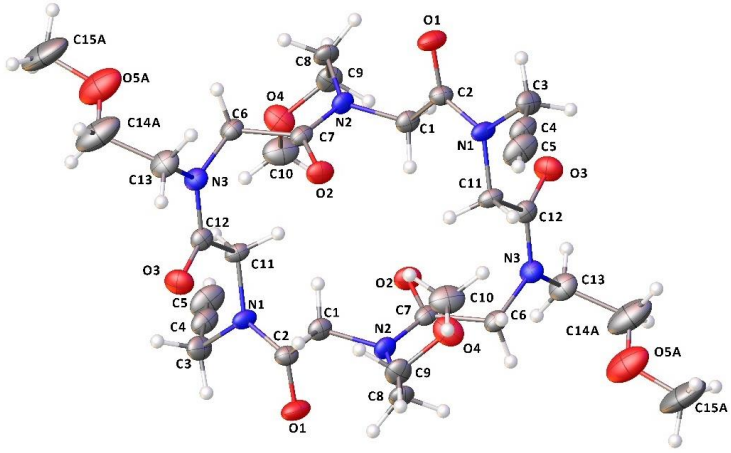

(f)

Figure 3.53 ORTEP diagrams for crystal form 2A (a), 2B type A molecule (b), 2B type B molecules (c), 2C (d), 2D (e), 2L (f). Atom types: C grey, O red, H white, N blue. Ellipsoids are drawn at 20% probability level. Disordered atoms have been omitted for clarity.

3.6.2 Powder diffraction experiment

The variable experiment on powder sample of compound **2** has been performed at the European Synchrotron Radiation Facility (ESRF) in Grenoble at the beamline ID22. A glass capillary of 0.5 mm was filled with powder and analysed using a wavelength of 0.4000669 Å from an insertion device source with a double-crystal Si(111) monochromator and data were collected using the multianalyser stage. The temperature was controlled using an Oxford Cryostream cold nitrogen gas blower. The patterns were collected in a 2θ range from 0.10° to 48° and raw data were rebinned into steps of 0.003° 2θ. The sample was heated up with a rate of 2 K/min from 300 K to 450 K and then cooled down at the same rate to 100 K. During the heating procedure, the powder patterns were collected every 50 K.

Rietveld refinements have been performed using TOPAS V6.

3.6.3 DSC measurements and hot stage microscopy

DSC measurements were performed at the University of Salerno on a TA DSC-Q2000 instrument under a purified N_2 flow (50 mL/min) by heating at a rate of 1 K/min.

Single crystals of form 2A, for a total of 0.3 mg, obtained by $CHCl_3$/iPrOH (2:1) were sealed in an aluminium pan.

Single crystals of form 2B, for a total of 1 mg, obtained by slow evaporation of a solution of $CHCl_3$/iPrOH (2:1) were sealed in an aluminium pan.

Single crystals of form 2C, for a total of 1.4 mg, obtained by kneading compound **2** with ethylene glycol and then dissolving the powder in a solution of $CHCl_3$/iPrOH (2:1) were sealed in an aluminium pan.

Single crystals of form 2D, for a total of 1.45 mg, obtained by slow evaporation of a solution of $CHCl_3$/ H_2O (1:1) were sealed in an aluminium pan.

Hot stage microscopy was performed at the University of Stellenbosch on a hot-stage Linkam DSC600 mounted on an optical microscope Meiji EMZ-8TR equipped with a T98-System controller, a nitrogen liquid cooling pump LNP95 and a water pump ECP. To control the temperature and obtain the images was used the software LinkSys32. The experiment was performed in the temperature range of 303-443 K with a heating rate of 2 K/min. The HSM measurement has been performed by Dr Eleonora Macedi, while the data analysis was performed by me.

CHAPTER IV

Cyclo-[*N*amy$_6$] and *cyclo*-[*N*hex$_6$]

This chapter is dedicated to the description of the results obtained working with *cyclo*-[*N*amy$_6$] (**3**) (Figure 4.1 a) and *cyclo*-[*N*hex$_6$] (Figure 4.1 b) (**4**). In particular, variable temperature single crystal and powder diffraction experiments, computational study of the intermolecular interactions fundamental for the crystal packing and thermal analysis are presented.

We decided to report in one chapter these two compounds since the nature of the side chains is very similar. Indeed, the only difference is related to the length of the alkyl side chains, which differs only for one carbon atom. Interestingly, this small difference has a great impact on their dynamic behaviour in the solid state.

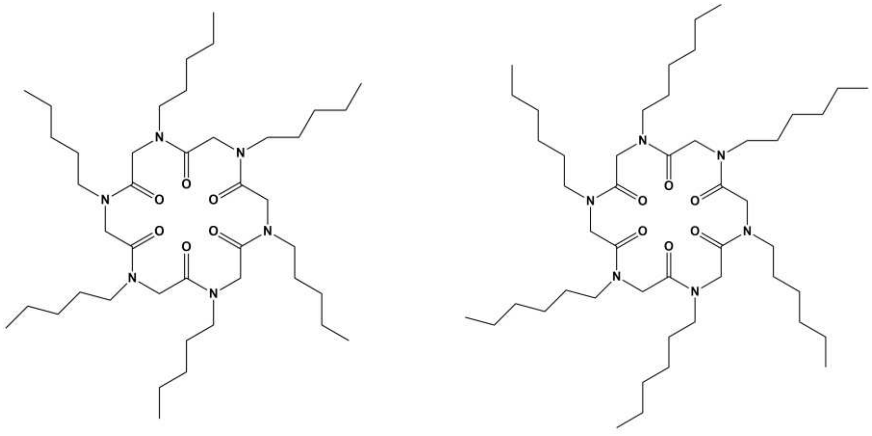

(a) (b)

Figure 4.1 (a) *Cyclo*-[*N*amy$_6$] (**3**). (b) C*yclo*-[*N*hex$_6$] (**4**). *N*amy = *N*-(pentyl)glycine. *N*hex = *N*-(hexyl)glycine.

4.1 Compound 3 and 4

Compound **3** and **4** have been synthesised following the standard procedure: the linear precursor has been synthesized using the sub-monomer approach[54] and then cyclized under high dilution condition with HATU as the coupling agent.

Crystals of compound **3** can be obtained dissolving the cyclic peptoid in hot methanol, obtaining an anhydrous crystal form, form 3A.

This crystal form possesses an inversion centre and a distorted *cctcct* backbone conformation of the peptoid backbone. Moreover, all the side chains point vertically with respect to the macrocycle plane (Figure 4.2 a).

Single crystals of **4** were obtained by slow evaporation of a solution of chloroform/toluene (1:1). This crystal form, form 4A, possesses an inversion centre and a distorted *cctcct* backbone conformation of the peptoid backbone. Also, form 4A is characterized by side chains that point vertically with respect to the macrocycle plane (Figure 4.2 b).

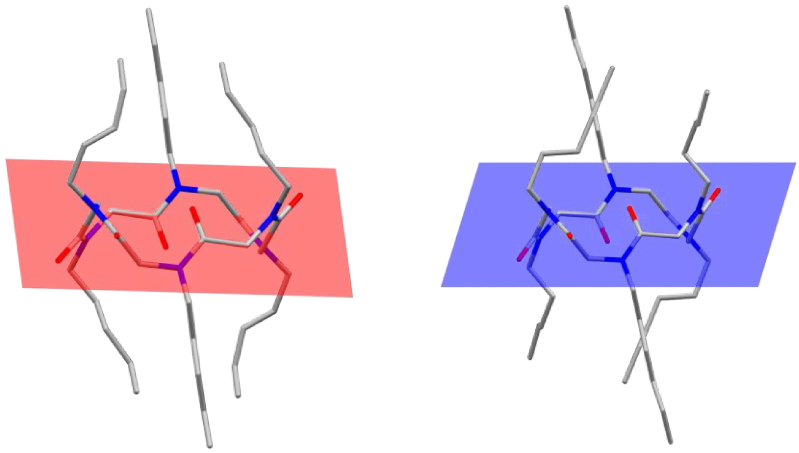

(a) (b)

Figure 4.2 (a) Regression plane of the macrocycle ring of form 3A is shown in red. (b) Regression plane of the macrocycle ring of form 4A molecule is shown in blue. Hydrogen and disordered atoms have been omitted for clarity.

The disposition of the side chains seems to be a particular aspect of cyclic peptoids decorated with long alkyl side chains. A possible explanation is related to the hydrophobic nature of the side chains. Indeed, the solid state assembly of compound **3** and **4** reminds a lipid bilayer wherein the peptoid backbone mimics the hydrophilic region of the bilayer, while the side chains play the role of

the hydrophobic region (Figure 4.3). Thus, we can infer that the crystal packing tends to maximize the interactions of the hydrophobic regions and the best way to do that is by forcing the side chains to point vertically with respect to the macrocycle plane.

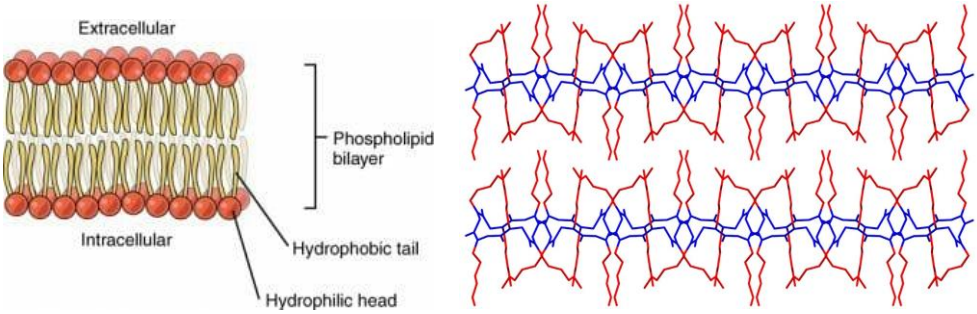

(a) (b)

Figure 4.3 (a) Example of the phospholipid bilayer. In the figure are highlighted the hydrophobic and hydrophilic region. (b) Crystal packing of form 4A. In blue are depicted the cyclic peptoids backbone, in red the side chains. Hydrogen atoms have been omitted for clarity.

The comparison with a phospholipid bilayer it does not seem to be excessive. Indeed, the formation of this type of supramolecular peptoid-based architecture has been already reported in many works published by Zuckermann.[112a,b,c]

The first example of this type of architecture was reported in 2010.[112a] In this paper, Zuckermann and co-workers reported the formation of a two-dimensional crystalline sheet based on peptoids. To obtain the desired architecture, the authors synthesized a polymer characterized by 36 polar, *N*-(2-aminoethyl)glycine (*N*ae) and *N*-(2-carboxyethyl)glycine (*N*ce), and nonpolar, *N*-(phenylethyl)glycine (*N*pe), monomers. The correct succession of the polar and nonpolar residue allowed to obtain different architecture. In particular, the twofold periodic peptoids, (*N*ae-*N*pe)$_{18}$ and (*N*ce-*N*pe)$_{18}$ assembled into a sheet (Figure 4.4). Thanks to different experimental techniques, like X-ray powder diffraction and transmission electron microscopy, it was possible to define the peptoid organization. The authors proposed that the hydrophobic groups point in the interior of the sheet while the opposite charged hydrophilic group are exposed to the surface.

[112] a) K. T. Nam, S. A. Shelby, P. H. Choi, A. B. Marciel, R. Chen, L. Tan, T. K. Chu, R. A. Mesch, B.-C. Lee, M. D. Connolly, C. Kisielowski and R. N. Zuckermann, *Nat. Mater.*, 2010, **9**, 454-460; b) B. Sanii, R. Kudirka, Andrew Cho, Neeraja Venkateswaran, Gloria K. Olivier, Alexander M. Olson, H. Tran, R. M. Harada, L. Tan and R. N. Zuckermann, *J. Am. Chem. Soc.*, 2011, **133**, 20808-20815; c) J. Sun, X. Jiang, R. Lund, K. H. Downing, N. P. Balsara and R. N. Zuckermann, *PNAS*, 2016, **113**, 3954-3959.

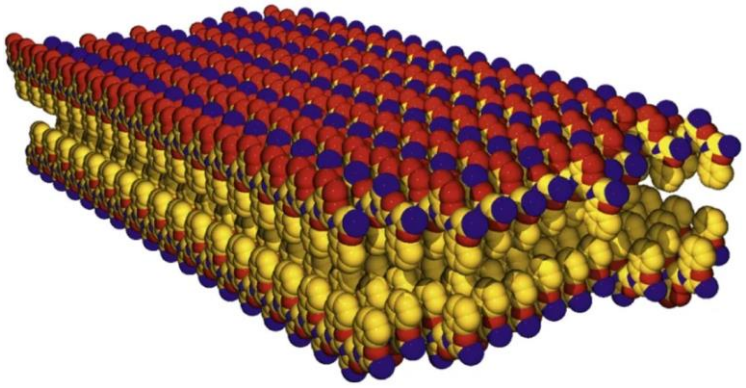

Figure 4.4 Model of peptoid sheet (*N*ae-*N*pe)$_{18}$ and (*N*ce-*N*pe)$_{18}$. Atom types: carbon yellow, nitrogen blue and oxygen red.

More recently, it was reported an extraordinary example of a self-repairing peptoid-based membrane.[113] The authors synthesized a peptoid membrane using a series of amphiphilic peptoids characterized by six polar residues *N*ce and six nonpolar residues, *N*-[2-(4-chlorophenyl)ethyl] glycine ($N_{4\text{-Cl}}$pe). Also in this specific case, the *N*ce group mimic the polar lipid head while $N_{4\text{-Cl}}$pe mimic the hydrophobic tail. The membrane can be easily formed through evaporation of a solution of H_2O/CH_3CN. The membrane-like structure shows the same thickness of lipid bilayer (3.5-4 nm) and the leading cause of this type of organization is related to the hydrophobic interactions. In particular, the peptoids organize in a lipid membrane-like structure characterized by a hydrophobic interior and two polar faces.

These two examples of molecular self-assembly of peptoids remind the solid state arrangement of form 3A and 4A wherein the hydrophobic region (side chains) are hidden between the cyclic peptoid backbone in order to maximize the hydrophobic interactions

4.2 Low temperature X-ray diffraction analysis on crystal form 3A

Crystal form 3A shows high thermal disorder on the *cis* pentyl side chains. It is difficult to define if this type of disorder is due to the thermal movements of the carbon atoms or if we are dealing with the positional disorder.

Regarding the atoms of the *cis* pentyl side chain attached to the nitrogen atom N1, they can occupy two possible positions with refined occupancy factor 0.586(16) and 0.414(16). The same treatment

[113] H. Jin, F. Jiao, M. D. Daily, Y. Chen, F. Yan, Y.-H. Ding, X. Zhang, E. J. Robertson, M. D. Baer and C.-L. Chen, *Nat. Commun.*, 2016, **7**, 12252-12259.

was carried out on the atoms of the *cis* pentyl side chain attached to nitrogen atom N2 with a final refined occupancy of 0.672(8) and 0.328(8).

In Table 4.1 are reported the intermolecular distances (Å), angles (°) and interaction energies (kJ/mol) in the host framework of form 3A.

All the calculations on the crystal packing, the Hirshfeld surface analysis and the energy frameworks analysis were carried on using a cyclic peptoid model without disordered atoms and considering only the side chains whose atoms show the highest occupancy factor value. This decision was necessary since it was not possible to consider the two possible positions of the side chain atoms in the calculation.

As already mentioned in the previous paragraph, all the pentyl side chains point vertically with respect to the macrocycle plane and this disposition determines the formation of a bilayer-like structure. This particular arrangement is characterized by cyclic peptoid molecules that are related to the screw axis parallel to the *b* axis (motif I).

Since the side chains are characterized by only carbon atoms, the strongest interaction is related to backbone-to-backbone contact (Figure 4.5 a). In particular, the atoms involved are the carbonyl oxygen atoms and methylene hydrogen atoms of the backbone (C1-H1B···O3 = 2.35 Å; O3···H1B-C1 = 137.9°; C8-H8B···O1 = 2.46 Å; O1···H8B-C8 = 122.6°).

As we expected, on the Hirshfeld surface (Figure 4.5 b) it is possible to highlight only the red spots related to this type of interactions.

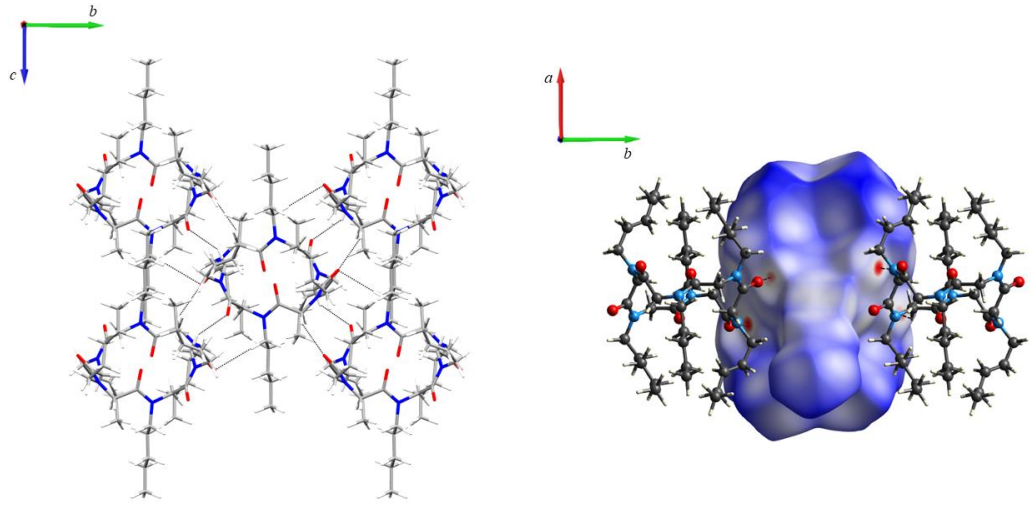

(a) (b)

Figure 4.5 (a) Motif I of the form 3A. (b) Hirshfeld surface mapped with d_{norm} of motif I.

Motif II is characterized by cyclic peptoids aligned along the *c* axis (Figure 4.6 a). In this case, it was not possible to highlight any strong interaction between the macrocycle since the principal interactions are due to the H···H contacts between the side chains hydrogen atoms.

In particular, the principal side chain involved in motif II is the *trans* pentyl side chain. This simple observation allows us to explain why the only side chain not characterized by disorder is the *trans* pentyl side chain. Indeed, the presence of interactions, even if very weak, reduces the atom movements.

In the Hirshfeld surface analysis (Figure 4.6 b) it was not possible to highlight any strong interaction and all the H···H contacts are characterized by white spots.

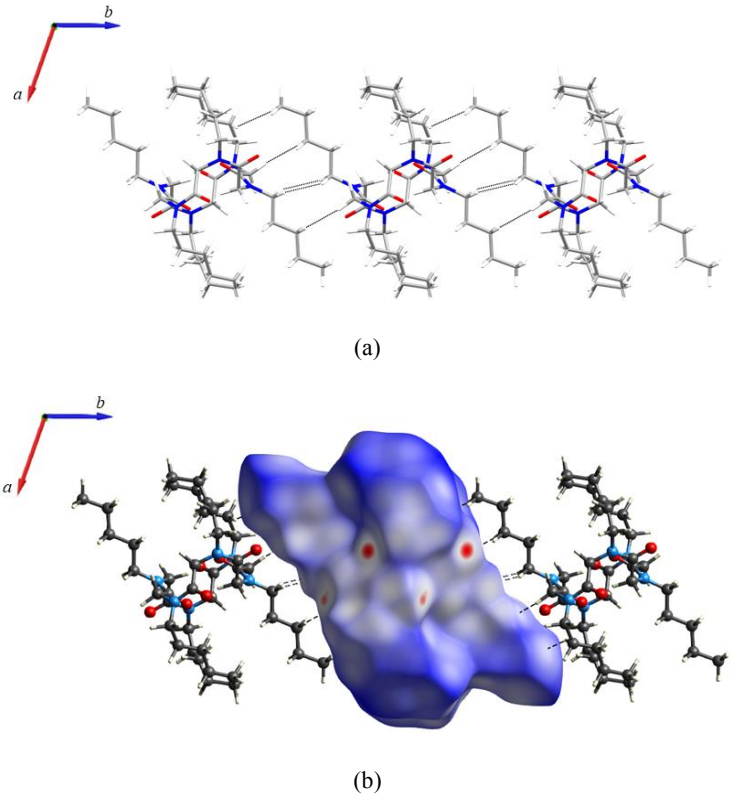

Figure 4.6 (a) Motif II of the form 3A. (b) Hirshfeld surface mapped with d_{norm} of motif II.

In motif III macrocycles interacts by means of H···H contact (Figure 4.7 a). Also in this case, it was not possible to highlight any strong interaction between the macrocycle since the principal interactions are H···H contacts and in the Hirshfeld surface are present only white spots (Figure 4.7 b).

Since motif II and III are characterized by only H···H contacts, the principal energy contribution to these two motifs is the dispersion term as confirmed by the PIXEL calculation reported in Table 4.1.

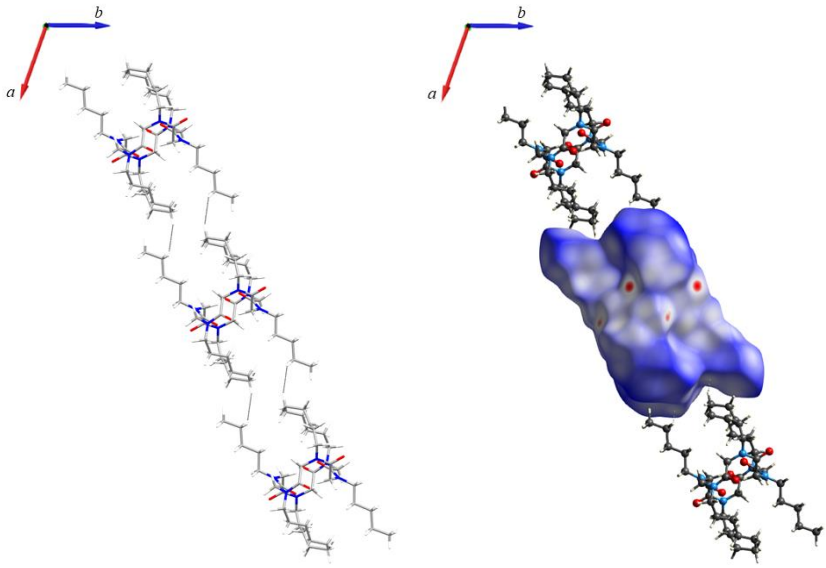

(a) (b)

Figure 4.7 (a) Motif III of the form 3A. (b) Hirshfeld surface mapped with d_{norm} of motif III.

Table 4.1 List of intermolecular distances (Å), angles (°) and interaction energies (kJ/mol) in the framework of form 3A. Energy values are reported in kJ/mol.

Motif	D-H···A	H···A (Å)	D-H···A (°)	Symm. Op.	Centroid Distance (Å)	E_{Coul}	E_{Pol}	E_{Disp}	E_{Rep}	E_{Tot}
I	C1-H1B···O3	2.35	137.9	1-x, -1/2+y, 1/2-z	9.507	-38.3	-15.5	-75.0	47.3	-81.4
	C8-H8B···O1	2.46	122.6	1-x, -1/2+y, 3/2-z						
				1-x, 1/2+y, 1/2-z						
				1-x, 1/2+y, 3/2-z						
II	H···H contacts			x, y, -1+z	11.232	-11.2	-7.5	-49.1	25.8	-42.0
				x, y, 1+z						
III	H···H contacts			-1+x, y, -1+z	15.305	-2.6	-14.4	-30.7	12.6	-22.1
				1+x, y, 1+z						

The crystal packing analysis performed on form 3A shows that cyclic peptoids molecules interact mainly by means of H···H contacts and this observation is confirmed by the intermolecular energy calculation performed by PIXEL that shows that the main contribution to the lattice energy is given by the dispersion energy (Table 4.3). The motif I is characterized by CH···OC interactions involving the backbone oxygen atom. This particular assembly determines the formation of a layer of cyclic peptoids, related by the screw axis, wherein the side chains point all vertical with respect to the macrocycle plane. The *trans* pentyl side chains are directly involved in the definition of motif II and therefore, is the only not disordered side chain.

One of the principal problems that we had to face working with cyclic peptoids with long alkyl side chains is related to the high disorder of the latter.

Since the carbon atoms are all joined by single bonds and do not present any particular movement constraints, they are free to move and the size of the movement is strictly related to the temperature: higher is the temperature, bigger will be the atom movements.

The effect of disorder atoms can be clearly seen also in the X-ray diffraction pattern (Figure 4.8 a,b). Indeed, the atomic motions, due to the thermal vibrations, affect the scattered intensities since the effective volume of the atom appears larger inducing a decrease of the scattering power and this effect increases with the scattering angle.

To eliminate or, at least, reduce this problem, we measured a crystal of compound **3** at 100 K obtaining, with our big surprise, a new crystal form (form 3B).

The measurement 100 K was performed at the Max Planck Institute for solid state research in Stuttgart (Germany).

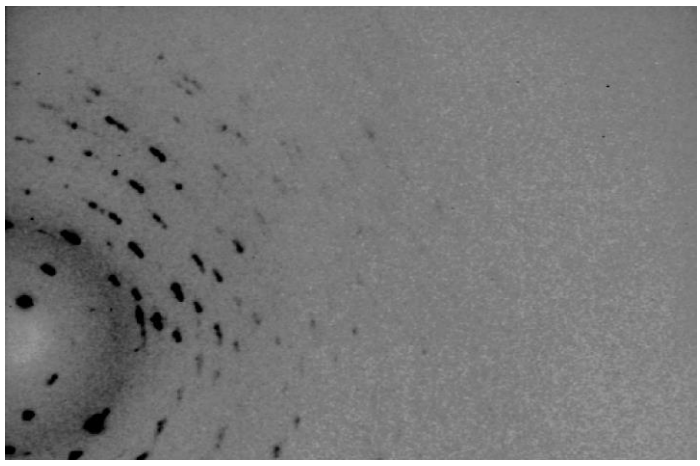

(a)

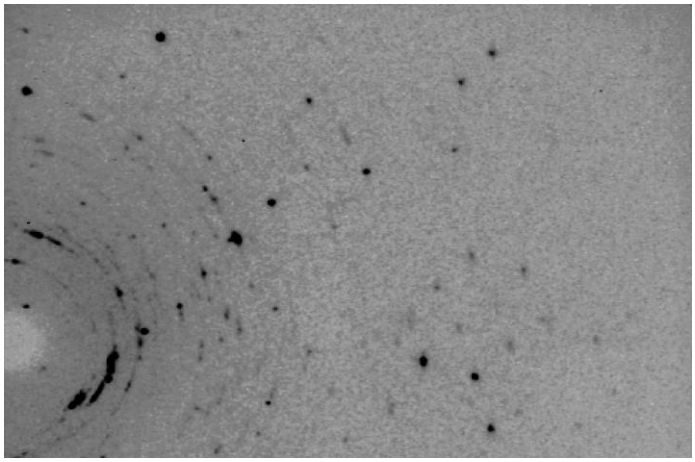

(b)

Figure 4.8 X-ray single crystal pattern obtained at 250 K (a) and 100 K (b). The pattern collected at 100 K contains spots at a higher angle than the pattern collected at 250 K.

Form 3B shows a distorted *cctcct* backbone conformation of the peptoid backbone and all the side chains point vertically with respect to the macrocycle plane. The principal difference between form 3A and 3B is the absence of a molecular inversion centre in form 3B. Indeed, the centre of mass of the cyclic peptoid is not localized on an inversion centre as it happens for form 3A.

After the SCSC transformation, the space group does not change. Regarding the unit cell differences, it is clear that one unit cell axis doubled. Indeed, *b* axis does not change, while *a* and *c* axis are inverted: *c* axis of the form 3A is similar to the *a* axis of form 3B while *c* axis of form 3B is almost doubled with respect to the *a* axis of form 3A (Table 4.7). In order to compare the unit cell volume of the two different crystal forms, we need to halve the volume of form 3B. Considering this aspect, it is evident a decrease in the volume caused by the decrease of the temperature (-6.25%).

The reason for the double *c* axis is related to the lack of the molecular inversion centre. Indeed, taking into account the absence of the inversion centre, in order to respect the periodicity of the crystal considering also the symmetry operation of $P2_1/c$ space group, it is necessary to double the *c* axis with respect to the *a* axis form 3A (Figure 4.9).

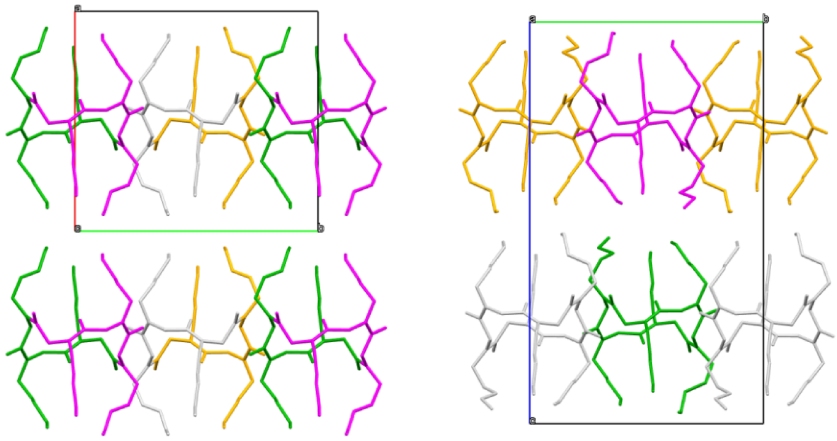

(a) (b)

Figure 4.9 Cyclic peptoids of form 3A (a) and 3B (b) coloured by symmetry operation. The different colours represent a different symmetry operation that generates the depicted molecule. In light grey the identity, in green the screw axis, in orange the inversion centre and in magenta the glide plane. Hydrogen and disordered atoms have been omitted for clarity.

Despite the data collection was performed at 100 K, cyclic peptoid molecules show disorder on two *cis* pentyl side chains. Regarding the atoms of the *cis* pentyl side chain attached to the nitrogen atom N1, they can occupy two possible positions with refined occupancy factor 0.744(9) and 0.256(9). The same treatment was carried out on the atoms of the *cis* pentyl side chain attached to nitrogen atom N2 with the final refined occupancy of 0.863(7) and 0.137(7).

The disordered atoms allow us to explain why the cyclic peptoids are not characterized by a molecular inversion centre. Indeed, if we consider the presence of an ideal inversion centre, the two disordered side chains are related by this symmetry operation but, since they are affected by the different disorder, the inversion centre is forbidden.

In particular, the *cis* pentyl side chain attached to the nitrogen atom N1 shows disorder on the last two carbon atoms of the side chain while in the other disordered *cis* pentyl side chain, the only atom which does not show disorder is the carbon atom attached to the nitrogen atom N4.

The molecular overlay of form 3A and 3B (Figure 4.10) shows that the principal differences are related to the disordered *cis* pentyl side chains. The superimposition was performed without taking into account the disordered atoms and considering only the side chains atoms of form 3A and 3B which show the higher occupancy factor values.

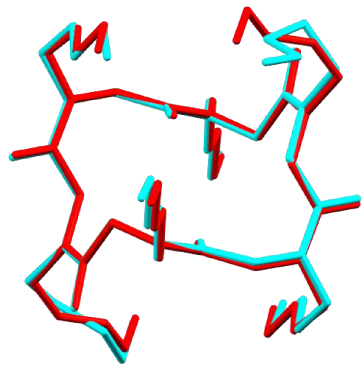

Figure 4.10 Superimposition of the crystal structure of form 3A (red) and form 3B (cyan). RMSD 0.341 Å.

To understand the reason for the transformation it is necessary to carefully analyse the crystal packing of this new crystal form by means of Hirshfeld surface analysis and PIXEL calculations.

In Table 4.2 are reported the intermolecular distances (Å), angles (°) and interaction energies (kJ/mol) in the host framework of form 3B.

The lack of the inversion centre determines small differences in the centroid distances in molecules which are related by symmetry operation. For example, analysing the motifs list in Table 4.2, it can be noted that motif I and II are very similar. Indeed, the molecules in these two motifs are all related by the screw axis but, the absence of the molecular inversion centre determines small differences in centroid distances.

In this thesis, we define different motifs considering the centroid distances and not the symmetry operation, since also a small variation of distance between two molecules can induce the formation of different interactions and, as a consequence, different interaction energy values.

Motif I (Figure 4.11 a) is characterized by backbone-to-backbone interactions involving the carbonyl oxygen atoms and the methylene hydrogen atoms of the backbone (C1-H1B···O3 = 2.36 Å; O3···H1B-C1 = 136.7°; C8-H8B···O4 = 2.35 Å; O4···H8B-C8 = 126.7°). The Hirshfeld surface analysis (Figure 4.11 b) highlights the short contacts between the cyclic peptoid molecules.

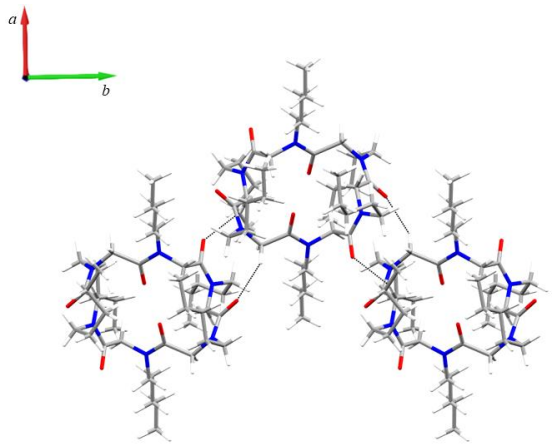

(a)

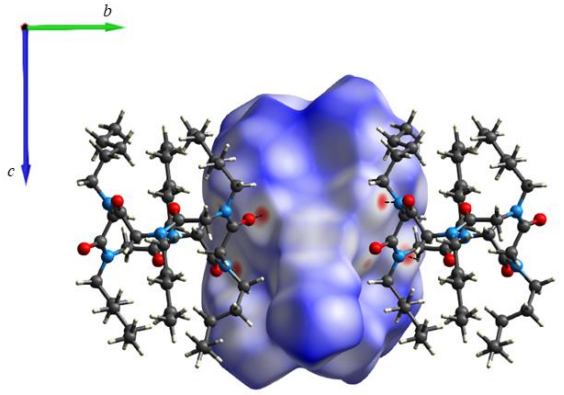

(b)

Figure 4.11 (a) Motif I of the form 3B. (b) Hirshfeld surface mapped with d_{norm} of motif I.

Motif II is very similar to motif I. Indeed, the molecules are related by the same symmetry operation and the only difference is associated with the centroid distances. Motif II (Figure 4.12 a) is characterized by a backbone-to-backbone interaction involving the carbonyl oxygen atoms and the methylene hydrogen atoms of the backbone (C29-H29A···O1 = 2.50 Å; O3···H29A-C29 = 116.7°; C22-H22A···O6 = 2.28 Å; O6···H22A-C22 = 139.9°). The Hirshfeld surface analysis (Figure 4.12 b) highlights the short contacts between the cyclic peptoid molecules.

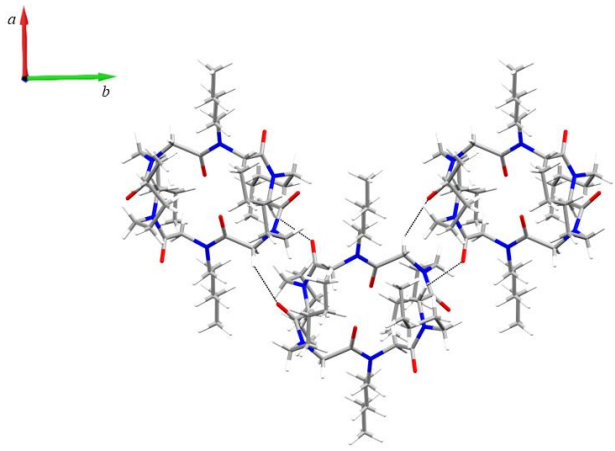

(a)

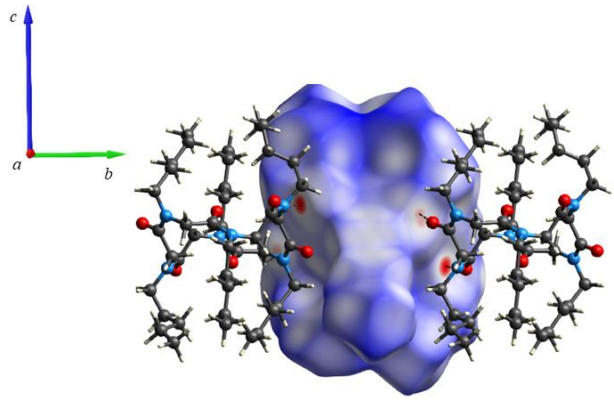

(b)

Figure 4.12 (a) Motif II of the form 3B. (b) Hirshfeld surface mapped with d_{norm} of motif II.

In motif III cyclic peptoid molecules align along the *a* axis by means of H···H contacts (Figure 4.13 a). Also in this case, the principal side chain involved in this type of arrangement is the *trans* pentyl side chain. In the Hirshfeld surface analysis (Figure 4.13 b) it was not possible to highlight any strong interaction and all the H···H contacts are characterized by white spots.

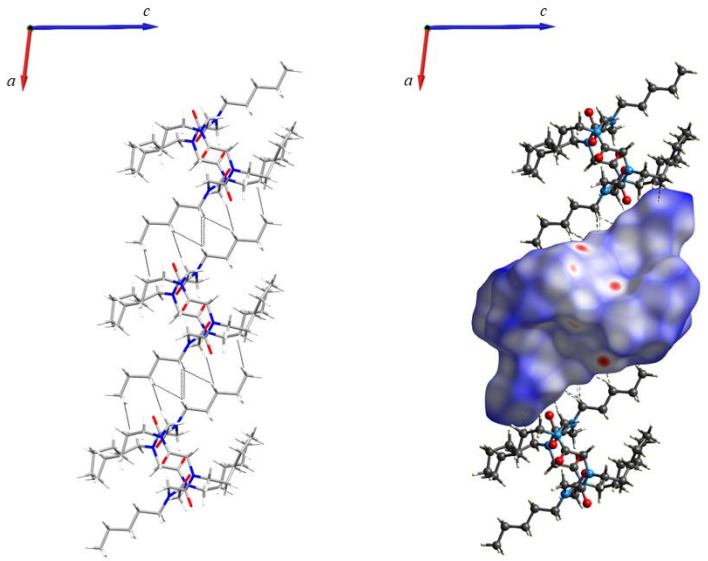

(a) (b)

Figure 4.13 (a) Motif III of the form 3B. (b) Hirshfeld surface mapped with d_{norm} of motif III.

Motif IV is characterized by molecules that align along the *ac* diagonal (Figure 4.14 a). The principal interactions are H···H contacts that involve the *trans* side chain attached to the nitrogen atom N3 and the disordered *cis* pentyl side chains attached to the nitrogen atom N1. In the Hirshfeld surface analysis (Figure 4.14 b) it was not possible to highlight any strong interaction and all the H···H contacts are characterized by white spots.

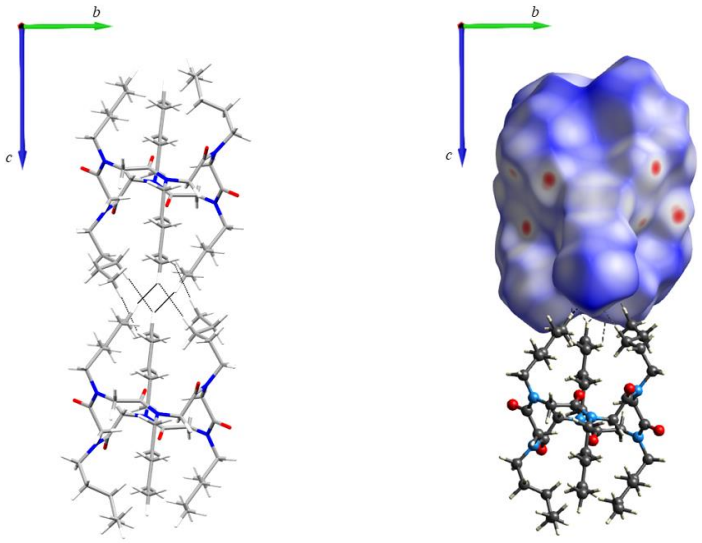

(a) (b)

Figure 4.14 (a) Motif IV of the form 3B. (b) Hirshfeld surface mapped with d_{norm} of motif IV.

Motif V is very similar to motif IV since the cyclic peptoids align along the *ac* diagonal (Figure 4.15 a). The principal interactions are H···H contacts that involve the *trans* side chain attached to the nitrogen atom N6, the *cis* side chain attached to the nitrogen atom N2 and the disordered *cis* pentyl side chains attached to the nitrogen atom N4. In the Hirshfeld surface analysis (Figure 4.15 b) it was not possible to highlight any strong interaction and all the H···H contacts are characterized by white spots.

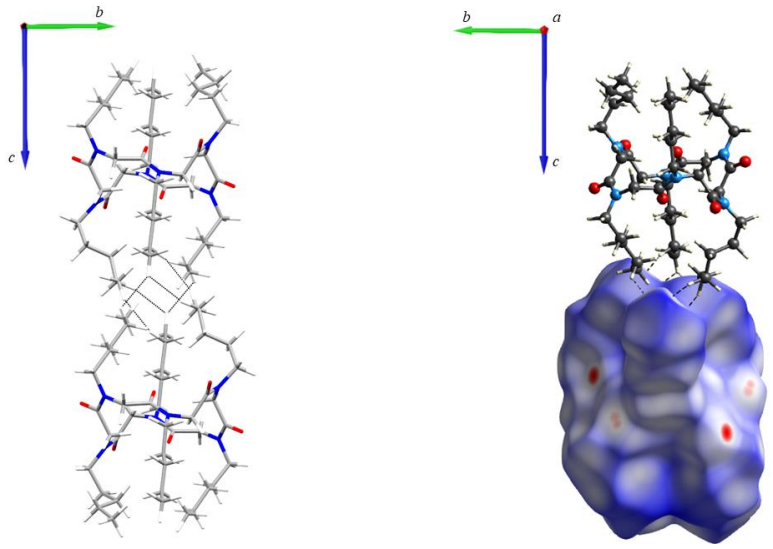

(a) (b)

Figure 4.15 (a) Motif V of the form 3B. (b) Hirshfeld surface mapped with d_{norm} of motif V.

Table 4.2 List of intermolecular distances (Å), angles (°) and interaction energies (kJ/mol) in the framework of form 3B. Energy values are reported in kJ/mol.

Motif	D-H···A	H···A (Å)	D-H···A (°)	Symm. Op.	Centroid Distance (Å)	E_{Coul}	E_{Pol}	E_{Disp}	E_{Rep}	E_{Tot}
I	C1-H1B···O3	2.36	136.7	-x, -1/2+y, 3/2-z	9.448	-49.7	-21.7	-99.2	83.4	-87.2
	C8-H8B···O4	2.35	126.7	-x, 1/2+y, 3/2-z						
II	C29-H29A···O1	2.50	116.7	1-x, -1/2+y, 3/2-z	9.494	-44.0	-19.2	-91.2	67.9	-86.4
	C22-H22A···O6	2.28	139.9	1-x, 1/2+y, 3/2-z						
				x, y, 1+z						
III	H···H contacts			-1+x, y, z	11.309	-13.8	-9.9	-57.0	38.7	-42.0
				1+x, y, z						
IV	H···H contacts			-x, -y, 2-z	14.899	-8.0	-4.4	-44.6	33.8	-23.1
V	H···H contacts			1-x, -y, 1-z	15.058	-9.8	-5.2	-45.9	37.8	-23.0

Considering the symmetry operation necessary to generate the interacting molecules and the centroid distances, it is possible to associate the motifs of form 3A with motifs of form 3B. In

particular, motif I of form 3A can be associated with Motif I and II of form 3B, motif II of form 3A with motif III of form 3B and motif III of form 3A with motif IV and V of form 3B.

This observation clearly demonstrates that there are no big differences between the crystal packing of the two crystal forms but, carefully looking at the energy values associated to each motif, it is clear that the principal differences are related to the intermolecular energy values. Indeed, thanks to the PIXEL calculations, we can with no doubt declare that form 3B shows a more efficient packing with respect to the form 3A.

We can explain this result considering that the cyclic peptoid molecules are closer in crystal form 3B guaranteeing more favourable interactions. Of course, as a consequence of a shorter distance between the cyclic peptoid molecules, the repulsion energy term increases. This can be clearly seen considering the result reported in Table 4.1 and 4.2.

In Table 4.3 are reported the lattice energy values and the packing coefficient for the two crystal forms.

Table 4.3 Coefficient packing, and energy values of the different analysed crystal forms obtained using PIXEL.

Crystal form	Packing coefficient	E_{Coul}	E_{Pol}	E_{Disp}	E_{Rep}	E_{Tot}
Form 3A	0.634	-90.8	-37.6	-244.3	133.5	-239.2
Form 3B	0.690	-118.5	-53.9	-327.1	235.5	-264.1

In conclusion, the difference between the two crystal forms is related to the loss of the molecular inversion centre in form 3B. The shrink of the unit cell volume allows a better crystal packing in the crystal form obtained at 100 K caused mainly by stronger dispersion interactions between the cyclic peptoids molecules. Indeed, despite the increase of the repulsion energy (+76.4%), the dispersion (-33.9%) and Coulomb energy (-30.5%) are more favourable in form 3B.

4.3 Thermal analysis of compound 3

To better characterize the SCSC transformation of crystal form 3A, a DSC analysis was performed.

Starting the measurement at room temperature, the sample was cooled down to 123 K, then heated up to 523 K (Figure 4.16 a) and, finally, cooled down again at room temperature. It is interesting to notice a small exothermic peak during the cooling down at 178 K and a small endothermic peak at

183 K appears during the heating up (Figure 4.16 b). These two peaks can be associated with the reversible SCSC transformation of form 3A.

Moreover, a small endothermic peak appears at 420 K. At 486 K it is possible to appreciate the endothermic peak associated with the melting of the compound. Interestingly, during the come back at room temperature, a recrystallization process appears (457 K).

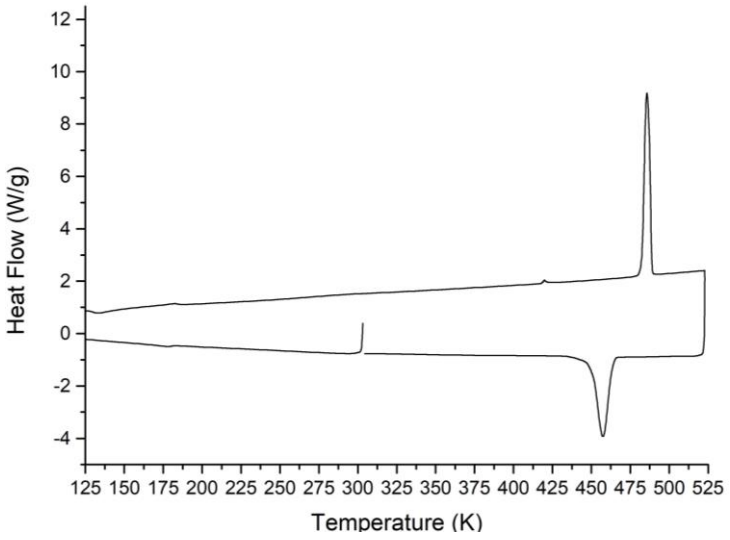

(a)

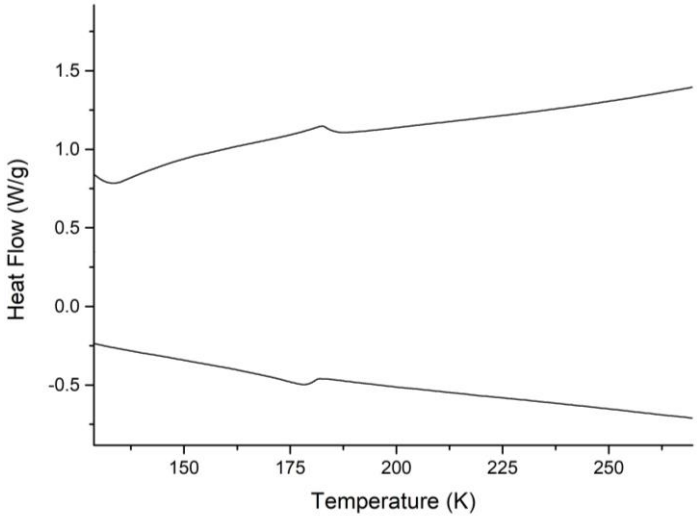

(b)

Figure 4.16 (a) DSC measurement performed on crystals of the form 3A. The plot is reported with exo down. (b) Magnification of the region between the 123 K and 265 K. It is possible to appreciate the two peaks associated with the reversible SCSC transformation.

4.4 Variable temperature X-ray diffraction analysis on compound 4

This crystal form, form 4A, possesses an inversion centre and a distorted *cctcct* backbone conformation of the peptoid backbone. Also form 4A is characterized by side chains that point vertically with respect to the macrocycle plane.

In Table 4.4 are reported the intermolecular distances (Å), angles (°) and interaction energies (kJ/mol) in the host framework of form 4A.

In motif I, cyclic peptoid molecules align in a layer structure wherein the side chains point vertically with respect to the macrocycle plane (Figure 4.17 a). The cyclic peptoids interact by means of backbone-to-backbone CH···OC interactions involving the carbonyl oxygen atoms of the backbone and the methylene hydrogen atoms of the backbone (C9-H9A···O1 = 2.23 Å; O1···H9A-C9 = 146.5°; C17-H17B···O2 = 2.47 Å; O2···H17B-C17 = 114.7°). As we expected, analysing the Hirshfeld surface (Figure 4.17 b), the only red spots on the surface are related to these interactions. Moreover, thanks to the Hirshfeld surface analysis it was possible to identify another CH···OC interaction involving the oxygen atom of the backbone and the methylene hydrogen atom of the *trans* hexyl side chain (C3-H3B···O2 = 2.56 Å; O2···H3B-C3 = 156.0°).

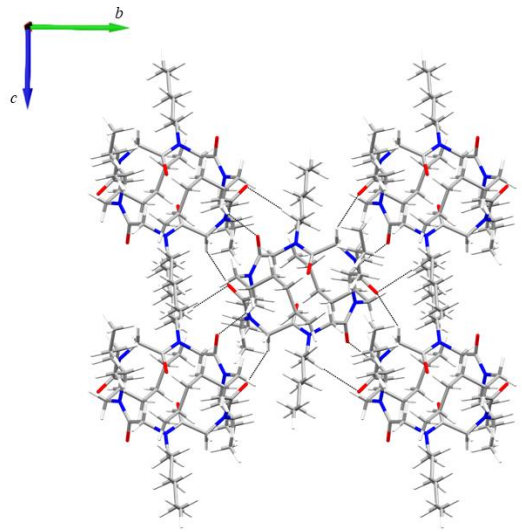

(a)

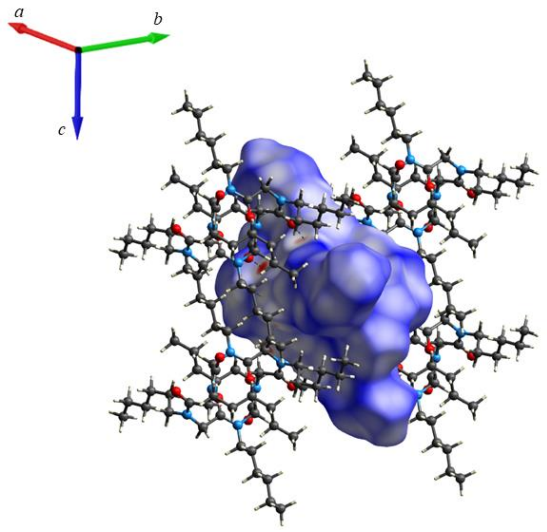

(b)

Figure 4.17 (a) Motif I of the form 4A. (b) Hirshfeld surface mapped with d_{norm} of motif I.

In motif II cyclic peptoids align along the shortest *c* axis by means of H···H contacts (Figure 4.18 a). As we have already demonstrated in the crystal packing of the form 3A and 3B, the *trans* hexyl side chains have a fundamental role in this type of arrangement. Indeed, all the interactions involve this side chain. As we expected, no red spots can be identified on the Hirshfeld surface (Figure 4.18 b).

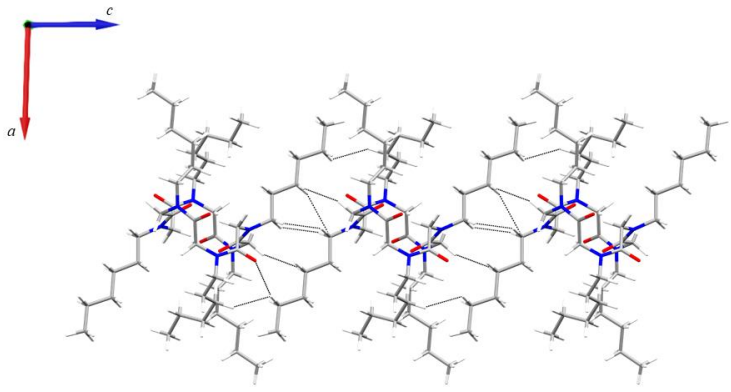

(a)

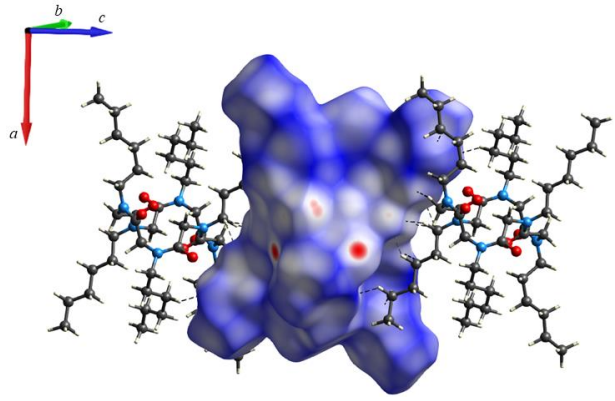

(b)

Figure 4.18 (a) Motif II of the form 4A. (b) Hirshfeld surface mapped with d_{norm} of motif II.

The last motif (motif III) that can be highlight in crystal packing of form 4A is related to the cyclic peptoid molecules that align along the *a* axis (Figure 4.19 a). Also for motif III, it is not possible to highlight any strong interaction, as can be deduced from the Hirshfeld surface analysis (Figure 4.19 b).

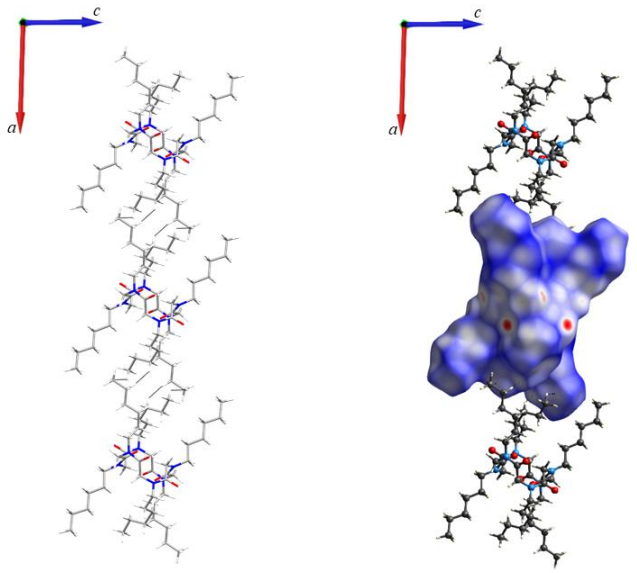

(a) (b)

Figure 4.19 (a) Motif III of the form 4A. (b) Hirshfeld surface mapped with d_{norm} of motif III.

Table 4.4 List of intermolecular distances (Å), angles (°) and interaction energies (kJ/mol) in the framework of form 4A. Energy values are reported in kJ/mol.

Motif	D-H···A	H···A (Å)	D-H···A (°)	Symm. Op.	Centroid Distance (Å)	E_{Coul}	E_{Pol}	E_{Disp}	E_{Rep}	E_{Tot}
I	C9-H9A···O1	2.23	146.5	1-x, -1/2+y, -1/2-z	9.309	-47.1	-19.6	-93.2	71.7	-88.1
	C17-H17B···O2	2.47	114.7							
	C3-H3B···O2	2.56	156.0	1-x, -1/2+y, 1/2-z						
				1-x, 1/2+y, -1/2-z						
				1-x, 1/2+y, 1/2-z						
II	H···H contacts			x, y, -1+z	11.247	-15.9	-11.6	-77.4	47.1	-57.9
				x, y, 1+z						
III	H···H contacts			-1+x, y, z	15.254	-7.4	-2.4	-42.6	19.5	-29.9
				1+x, y, z						

The solid state assembly of form 4A is very similar to the crystal packing of form 3A and 3B. Indeed, it is possible to recognize the same backbone-to-backbone arrangement in motif I, which determines the formation of a layer of cyclic peptoids organized in a sort of bilayer-like arrangement.

Moreover, also in form 4A, the *trans* hexyl side chain has a key role in the crystal packing guaranteeing the formation of the interactions fundamental for motif II.

On crystals of form 4A, a DSC measurement was performed.

Analysing the DSC results (Figure 4.20) it is possible to notice a small endothermic peak at 335 K while the melting occurs at 481 K. After the melting, when the temperature goes down, it is possible to appreciate the presence of an exothermic peak at 427 K indicating a re-crystallization process.

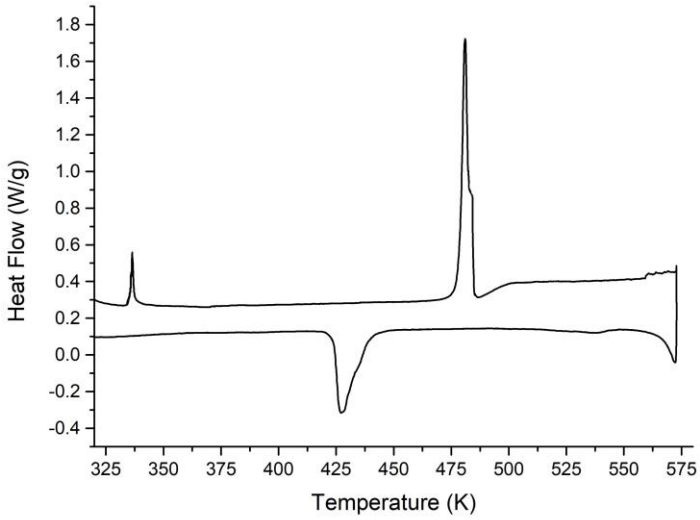

Figure 4.20 DSC measurement performed on crystals of the form 4A. The plot is reported with exo down.

Since crystal form 4A is an anhydrous crystal form, the endothermic peak at 335 K cannot be associated with the loss of solvent but must be associated with a phase transformation. For this reason, a variable temperature SCXRD analysis was performed on a crystal of the form 4A at the Max Planck Institute (MPI) for solid state research.

A first data collection was performed at RT to be sure that the starting phase is the desired one. Then the crystal was heated up to 360 K and measured at this temperature.

Confirming the DSC data, at 360 K we have obtained a new crystal form, form 4B. The unit cell is very similar to the unit cell of form 4A. Of course, it is possible to notice an expansion of the *a, b* axis and the volume due to the higher temperature (Table 4.5). Interestingly, the *c* axis does not change. The main difference is related to the β angle which results to be bigger than the β angle of form 4A.

Table 4.5 Comparison of the unit cell of form 4A and 4B. In parenthesis are reported also the variation in per cent.

Crystal form	***a*** **(Å)**	***b*** **(Å)**	***c*** **(Å)**	***α*** **(°)**	***β*** **(°)**	***γ*** **(°)**	***V*** **(Å^3)**
Form 4A	15.254(5)	14.838(5)	11.247(3)	90	91.957(9)	90	2544.2(14)
Form 4B	16.888(15) (+10.7%)	15.377(14) (+3.6%)	11.247(10) (-)	90	103.204(10) (+12.2%)	90	2843(4) (+11.7%)

Unfortunately, it was not possible to obtain a model of this new crystal form since at 360K temperature the side chains movement is so dramatic that the electron density appears smeared making difficult the precise localization of the carbon atom belonging to the side chain. It was possible to define only the position of all the atoms of the backbone, the *trans* hexyl side chain and the first two carbon atoms of the two *cis* side chains, directly attached to the nitrogen atom of the backbone.

It is interesting that the only side chain that does not show any particular disorder is the *trans* hexyl side chain. The principal reason for this event is related to the importance of the *trans* side chain in the crystal packing (motif II). Indeed, the *trans* hexyl is involved in H···H contacts which ensure the alignment of the cyclic peptoids along the *c* axis. This observation clearly explains why the *c* axis is the only axis that does not change after the SCSC transformation.

Since it was not possible to solve the structure at 360 K, the crystal was cooled down to 100 K and measured at this temperature. With our surprise, we obtained again the form 4A indicating that the SCSC transformation is reversible.

To be able to solve the structure of form 4B, we tried to flash cool a crystal of form 4B in liquid nitrogen. In particular, a crystal of form 4A was heated up to 360 K. At this temperature, we collected a few images in order to obtain the unit cell parameters and confirm the transformation to the form 4B. After this check, the crystal was flash cooled in liquid nitrogen and then mount on the diffractometer at 100 K. With our surprise, the fast cooling procedure was not enough to freeze the form 4B. Indeed, the measurement revealed that we obtained again form 4A.

4.5 Variable temperature powder diffraction experiment on compound 4

On compound **4**, two VT-XRPD experiments were performed. Moreover, since the DSC experiment shows a re-crystallization phenomenon after the melting, we evaluated what happens to the sample after the melting. All the X-ray powder diffraction experiments were performed at MPI.

In the first experiment, a 0.7 mm diameter thin-walled glass capillary was filled with powder of compound **4** obtained after the synthesis procedure. The sample was heated up to 373 K and then was cooled down to 293 K (Figure 4.21 a). In particular, the temperature was increased by steps of 20 K starting from 293 K with a heating rate of 5 K/min and the powder patterns were collected at each temperature step.

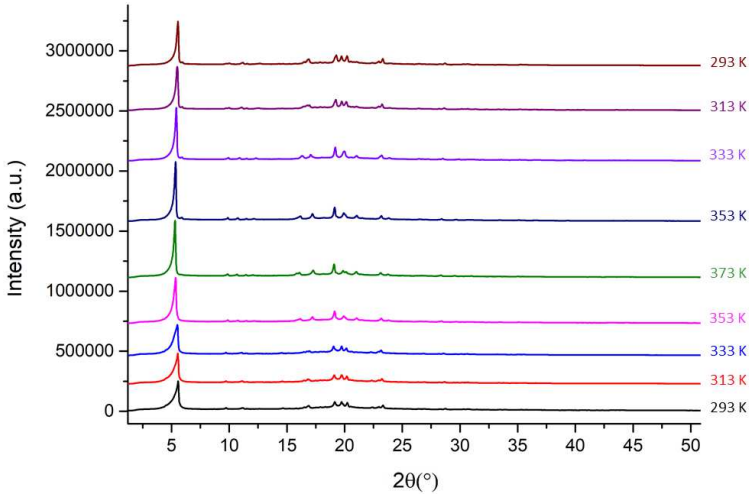

(a)

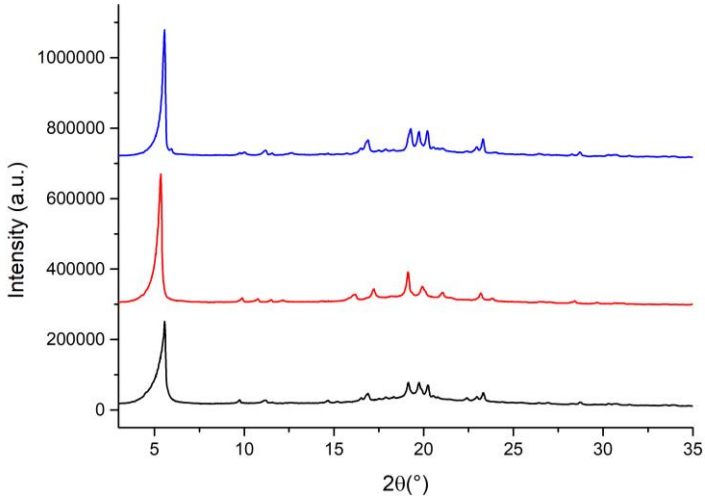

(b)

Figure 4.21 (a) Powder patterns obtained during the variable temperature experiments on compound **4**. (b) Comparison between the powder pattern obtained at 293 K, 353 K and back to 293 K.

As can be seen in Figure 4.21 b, at 353 K we have the transformation of the form 4A to the form 4B. During the cooling procedure, it is possible to obtain again the form 4A.

Considering the results obtained after the DSC, we evaluate also what happens to the sample after the melting temperature, when the sample is cooled down to room temperature (Figure 4.22 a, b).

A glass capillary of 0.7 mm of diameter was filled with a powder of compound **4**. The sample was heated up to 493 K and then cooled down again to room temperature. As can be seen in Figure 4.22 a, it is possible to notice the transformation to the form 4B at 353 K and the melting at 493 K. At 393 K a peak appears at a low angle indicating the re-crystallization process. The pattern obtained at 293 K is different with respect to the starting one.

The powder sample at 293 K, after the melting, is characterized by two phases that were not possible to characterize. A Pawley refinement was performed using the unit cell parameters of form 4A and 4B, but unfortunately, some peaks remain not assigned.

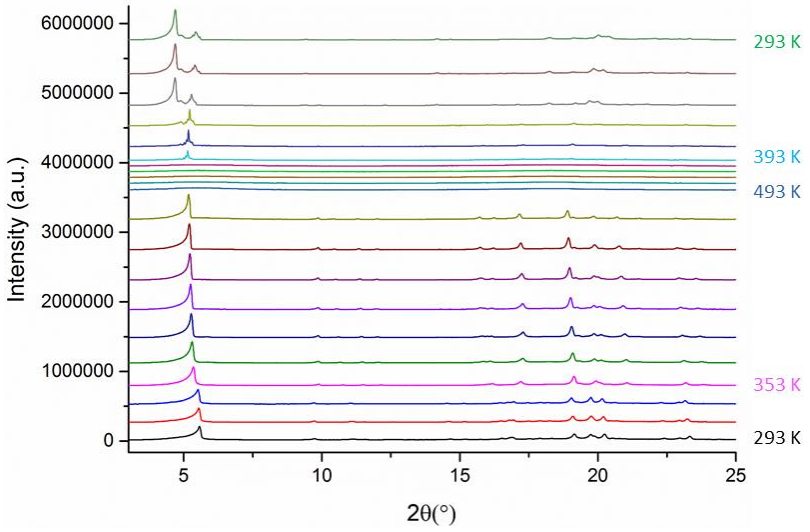

(a)

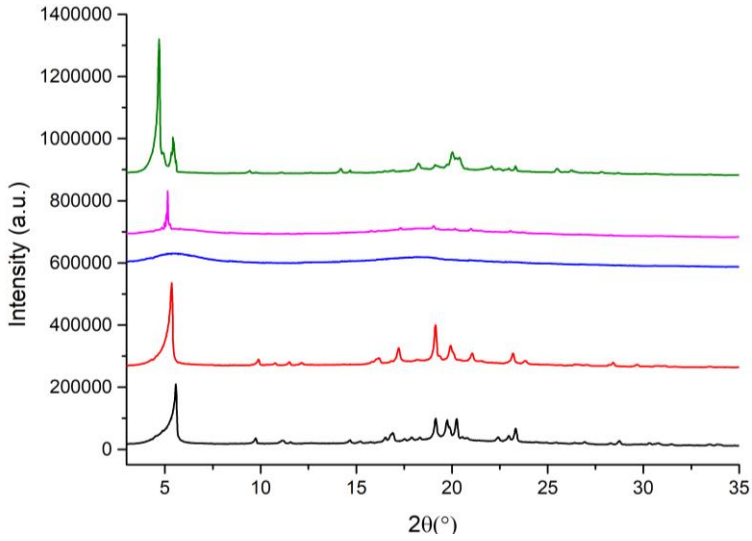

(b)

Figure 4.22 (a) Powder patterns obtained during the variable temperature experiments on compound **4** increasing the temperature until the melting point. For clarity, are indicated only the temperature where it is possible to appreciate changes in the sample. (b) Comparison between the powder pattern obtained at 293 K, 353 K, 493 K, back to 393 and back to 293 K

4.6 Experimental section

4.6.1 Single crystal X-ray data collection, structure solution and refinement

Crystal of form 3A was selected and mounted on a MiTeGen microloop with paratone oil. Data collection were performed at University of Salerno with a Bruker D8 QUEST diffractometer equipped with a PHOTON II detector using Cu*K*α radiation (λ= 1.54178 Å). Data Indexing was performed using APEX3.[108] Data integration and reduction were performed using SAINT.[108] Absorption correction was performed by a multi-scan method in SADABS.[108]

Crystals of form 3B and 4B were selected and mounted on a MiTeGen microloop with paratone oil. Data collections were performed at Max Planck Institute for Solid State Research with a SMART-APEX-I CCD X-ray diffractometer with graphite monochromated Mo*K*α radiation (λ = 0.71073 Å). The reflection intensities were integrated with the SAINT program in the Bruker Suite software

package.[114] Multi-Scan absorption correction was applied using SADABS.[115] The temperature was controlled by means of a Cryostream700^{plus} cooling device produced by the Oxford Cryosystems

Single crystal of form 4A was selected and mounted on a MiTeGen microloop with paratone oil and measured at University of Salerno on a four-circle diffractometer Rigaku AFC7S equipped with a Mercury^2 CCD detector using graphite-monochromated Mo*K*α radiation (λ = 0.71073 Å). Data collection was performed at 100 K using an Oxford Cryosystems Cryostream 700 for temperature control. Data were corrected for Lorentz, polarization and absorption. Data reduction was performed with the crystallographic package CrystalClear.[95]

The crystal structures were solved by direct methods using the program SIR2014[98] and refined by means of full-matrix least-squares based on F^2 using the program SHELXL.[99] *OLEX*2[100] was used as GUI.

Form 3A shows positional disorder on the two cis pentyl side chains. In particular, the carbon atoms can occupy two different positions with refined occupancy of 0.586(16) and 0.414(16) for the atoms of the side chain attached to the nitrogen atom N1, and 0.672(8) and 0.328(8) for the atoms of the side chain attached to the nitrogen atom N2. It was necessary to use restraints on anisotropic displacement parameters to disordered group atoms.

Also form 3B shows positional disorder on two *cis* pentyl side chains. The *cis* pentyl side chain attached to the nitrogen atom N1 shows positional disorder on the two last carbon atoms of the side chains. Their refined occupancy is 0.744(9) and 0.256(9). The *cis* pentyl side chains attached to the nitrogen atom N4 shows positional disorder with refined occupancy factor of 0.863(7) and 0.137(7). In this case, restraints on anisotropic displacement parameters were applied to the disordered group of atoms.

Crystallographic data and refinement information are reported in Table 4.6. ORTEP diagrams were drawn using *OLEX*2[100] (Figure 4.23).

[114] Bruker Suite, Version 2013/1. Bruker AXS Inc., Madison, WI, USA, 2013.
[115] G. M. Sheldrick, SADABS – Bruker AXS area detetctor scaling and absorption correction, version 2008/1; University of Göttingen, Göttingen, Germany, 2008.

Table 4.6 Crystallographic data for crystal form 3A, 3B and 4A.

	Form 3A	**Form 3B**	**Form 4A**
T (K)	296	100	100
Formula	$C_{42}H_{78}N_6O_6$	$C_{42}H_{78}N_6O_6$	$C_{48}H_{90}N_6O_6$
Formula weight	763.10	763.10	847.26
System	Monoclinic	Monoclinic	Monoclinic
Space group	$P\,2_1/c$	$P\,2_1/c$	$P\,2_1/c$
***a* (Å)**	14.6731(11)	11.3089(17)	15.254(5)
***b* (Å)**	15.3415(10)	15.195(2)	14.838(5)
***c* (Å)**	11.2315(8)	26.307(4)	11.247(3)
***α* (°)**	90	90	90
***β* (°)**	108.980(3)	97.4256(18)	91.957(9)
***γ* (°)**	90	90	90
***V* (Å^3)**	2390.8(3)	4482.7(11)	2544.2(14)
Z	2	4	2
***Dx* (g cm^{-3})**	1.060	1.131	1.106
λ (Å)	1.54178	0.71073	0.71073
***μ* (mm^{-1})**	0.560	0.075	0.072
F_{000}	840.0	1680.0	936.0
R1 (I > 2σI)	0.0612(3352)	0.0639(7534)	0.1091(2838)
$_wR_2$	0.2031(4625)	0.1832(9226)	0.2972(5794)
N. of param.	311	552	271
N. of reflections	4625	9226	5794
GooF	1.033	1.054	1.061
ρ_{min}, ρ_{max} (eÅ^{-3})	-0.19, 0.28	-0.32, 0.45	-0.33, 0.30
Restraints	154	23	-

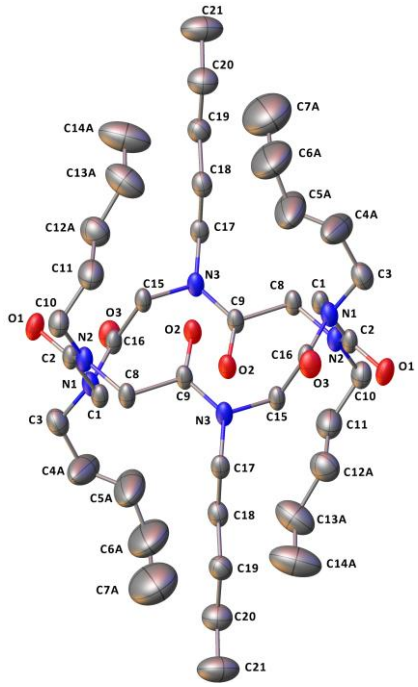
C21
C20
C19
C14A
C7A
C6A
C13A
C18
C5A
C4A
C12A
C17
C11
C15
N3
C8
C1
C3
C10
C9
N1
O1
O3
O2
C16
N2
C2
O2
C16
N2
O1
C8
O3
C10
N1
C9
C15
C11
C3
C1
N3
C12A
C4A
C17
C5A
C18
C13A
C6A
C19
C14A
C7A
C20
C21

(a)

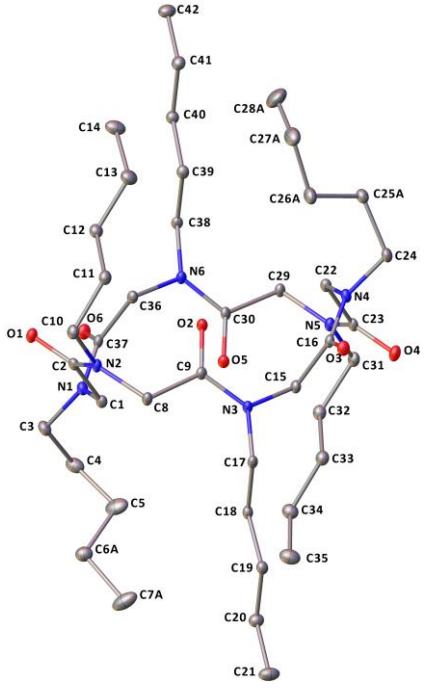
C42
C41
C40
C28A
C27A
C14
C13
C39
C26A
C25A
C12
C38
C24
C11
N6
C29
C22
N4
C10
O6
C36
O2
C30
N5
C23
O1
C37
C16
O4
C2
N2
C9
O5
O3
C31
N1
C1
C8
N3
C15
C3
C32
C4
C17
C33
C5
C18
C34
C6A
C19
C35
C7A
C20
C21

(b)

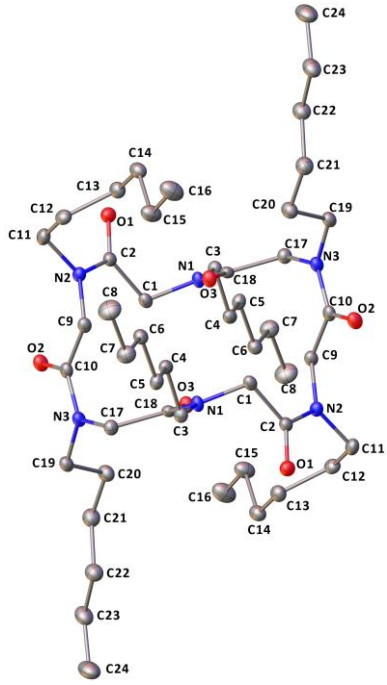

(c)

Figure 4.23 ORTEP diagrams for crystal form 3A (a), 3B and 4A (c). Atom types: C grey, O red, N blue. Ellipsoids are drawn at 20% probability level. Disordered atoms and hydrogen atoms have been omitted for clarity.

4.6.2 Powder diffraction experiment

X-ray powder diffraction experiment was performed at Max Planck Institute for Solid State Research using a Stadi P-Diffraktometer (Stoe), Cu*K*α1 radiation from a primary Ge(111)-Johann-type monochromator and three Mythen 1 K detectors (Dectris). The temperature was controlled by an Oxford Cryostream device (Oxford Cryostream 500).

For the VT-XRPD analysis on compound **4**, the powdered sample was loaded on a 0.7 mm diameter thin-walled glass capillary and heated up with a rate of 5 K/min from 293 K to 373 K increasing the temperature by steps of 20 K and then it was cooled down again to 293 K reducing the temperature by steps of 20 K. At each temperature, a powder diffraction pattern was collected after a delay time of 10 minutes in order to guarantee the thermal equilibration of the sample. Data were collected in a 2θ range from 2.0° to 115.0° measuring the sample for a total scan time of 2 hours.

To evaluate what happens to compound **4** after the melting point, another VT-XRPD analysis was performed. In this specific case, the powder sample was heated up with a rate of 5 K/min from 293 K to 473 K increasing the temperature by steps of 20 K and then cooled down again at 293 K reducing the temperature by steps of 20 K. At each temperature, a powder diffraction pattern was collected after a delay time of 10 minutes in order to guarantee the thermal equilibration of the sample. Data were collected in a 2θ range from 2.0° to 115.0° measuring the sample for a total scan time of 2 hours.

Pawley and Rietveld refinements of X-ray powder diffraction data of compound **3** were performed using TOPAS V6 software.

4.6.3 DSC measurement

DSC measurements were performed at the University of Salerno. The measurement on crystals of form 3A was performed using a TA DSC-Q20 instrument under a purified N_2 flow (50 mL/min), while for crystals of form 4A, the measurement was performed using a TA DSC-Q2000 instrument under a purified N_2 flow (50 mL/min).

Single crystals of form 3A, for a total of 4.5 mg, were sealed in an aluminium pan and cooled down at a rate of 5 K/min until the 123 K. Then the sample was heated up at the same rate until the 523 K and then cooled down again at RT.

Single crystals of form 4A, for a total of 1.0 mg, were sealed in an aluminium pan and heated at a rate of 5 K/min. The cooling down procedure was performed at the same rate.

CHAPTER V

3,3-disubstituted isoindolinone

In this chapter, the results obtained for a 3,3-disubstituted isoindolinone, namely ethyl 2-benzyl-3-oxo-1-(3-oxobutyl)isoindoline-1-carboxylate, are presented (Figure 5.1).

In particular, a phase transformation will be investigated by means of a variable temperature SCXRD analysis, DSC and TGA. Moreover, the intermolecular interaction energies are deeply investigated in order to characterize and understand the reason for the transformation.

Isoindolinones are heterocyclic compounds, characterized by the fusion of a γ-lactam ring with a benzene ring to form a bicyclic nucleus, that is widely diffused in nature and used as a scaffold in many pharmaceutical products.[116]

In details, chiral isoindolinones are the scaffold of bioactive molecules widely used as benzodiazepine-receptor agonists to treat anxiety, [117a,b] atherosclerosis,[118] Alzheimer's disease.[119]

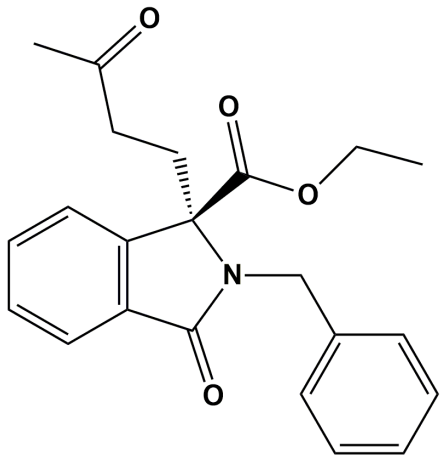

Figure 5.1 Compound **5**.

[116] K. Speck and T. Magauer, *Beilstein J. Org. Chem.*, 2013, **9**, 2048-2078.
[117] a) Z. Hussein, D. J. Mulford, B. A. Bopp and G. R. Granneman, *Br. J. Clin. Pharmacol.*, 1993, **36**, 357-361, b) EP Pat., 1566378, Isoindoline Derivative, 2005.
[118] WO Pat., 2011145022 A1, 2011.
[119] WO Pat., 2003040096 A2, 2003.

5.1 X-ray diffraction analysis and thermal treatment

Two different batches of compound **5** were analysed. In particular, batch 1 contains an enantiomeric excess of one enantiomer with the respect to the other one (e.e. 74%), while batch 2 is a racemic mixture.

The first crystallization trials were performed using batch 1. After several attempts, we were able to obtain single crystals of **5** by slow evaporation of a solution of chloroform/toluene (2:1). The resulting crystal form, form 5A, is a toluene solvate crystal form in space group $P2_1/c$ and the guest molecules are located on an inversion centre. The ratio between the host and guest molecules is 2:1.

Interestingly, the structure shows positional disorder on the two side chains attached to the tetrasubstituted stereocenters (Figure 5.2). Since the only difference between the two side chains is related to the position of the ketone and ester carbonyl groups and their length is similar, the two side chains may switch. In particular, the refined occupancy factors for the two side chains are 0.849(4) and 0.151(4). This phenomenon could be explained considering that the two side chains are very similar and therefore, they can easily exchange their position without altering the crystal packing.

The observed disorder allows two different enantiomers occupy the same position in the unit cell. Thus, the crystal is not a perfect racemic mixture.

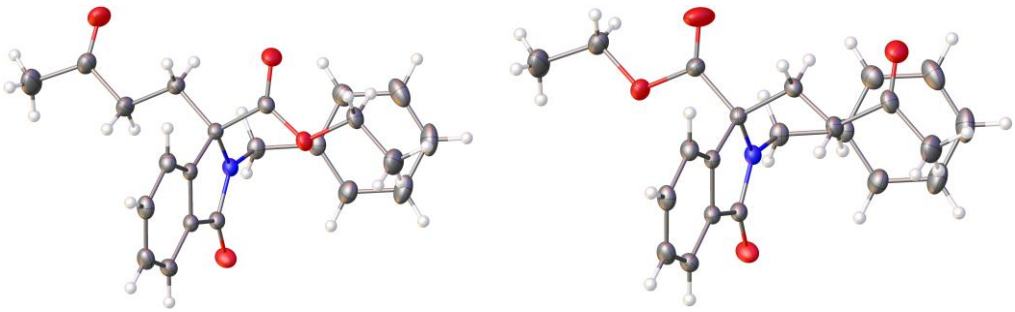

(a) (b)

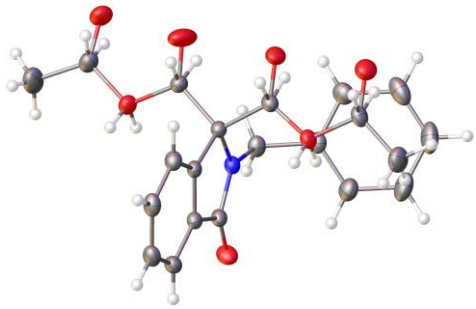

(c)

Figure 5.2 In (a) and (b) is represented compound **5** with no disordered atoms. In (c) is shown the disordered structure.

Also batch 2 gave single crystals of the toluene solvate crystal form in space group $P2_1/c$ in the same conditions. As we expected, the obtained toluene solvate crystal form does not show any disorder for the isoindolinone moiety. This observation clearly indicates that the principal reason for the disordered side chains is related to the enantiomeric excess, which characterizes batch 1.

It is interesting to notice that guest toluene molecules form a layer between host molecules. If we virtually remove the toluene molecules, we obtain an empty structure characterized by voids which occupy 17.9% of unit cell volume (403.36 $Å^3$). This result highlights the importance of toluene molecules in the crystal packing of form 5A.

The crystal packing analysis on form 5A was carried out without considering the disorder for the isoindolinone moiety. Moreover, the toluene molecule lies on an inversion centre and therefore, the methyl group can occupy two different positions with the same probability. For this reason, we decided to consider the toluene molecules as a *p*-xylene since it is not possible to prefer one position with respect to the other one.

In Table 5.1 are reported the intermolecular distances (Å), angles (°) and interaction energies (kJ/mol) in the host framework of form 5A.

In motif I, the molecules align along the *c* axis (Figure 5.3 a) by means of CH···OC interactions which involve the carbonyl oxygen atom of the ester group and the methylene hydrogen atom belonging to the ketone side chain (C13A-H13B···O2A = 2.55 Å; O2A···H13B-C13A = 113.1°) and the hydrogen atom attached to the benzene ring and the carbonyl oxygen atom of the γ-lactam ring (C6-H6···O1 = 2.22 Å; O1···H6-C6 = 174.1°). The interacting molecules are related by the *c* glide plane. In the Hirshfeld surface (Figure 5.3 b), these two contacts are highlighted by two red spots.

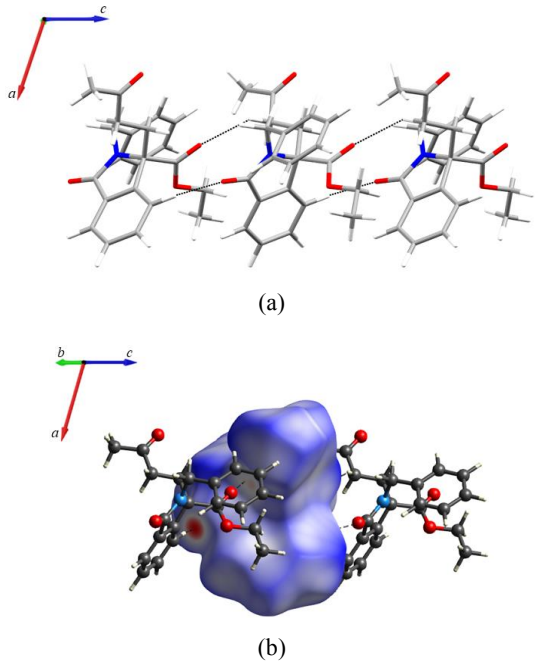

Figure 5.3 (a) Motif I of the form 5A. (b) Hirshfeld surface mapped with d_{norm} of motif I.

In motif II (Figure 5.4 a), molecules related by the screw axis with direction along *b* interact by means of weak C···H and H···H contacts involving the methylene hydrogen atom of the ketone side chain and hydrogen atom of the benzene ring of the isoindolinone scaffold and a weak CH···OC bond, which involves the oxygen atom of the γ-lactam ring and the hydrogen atom of the benzene ring of the isoindolinone scaffold. In this case, no strong interactions can be highlighted with the Hirshfeld surface analysis (Figure 5.4 b).

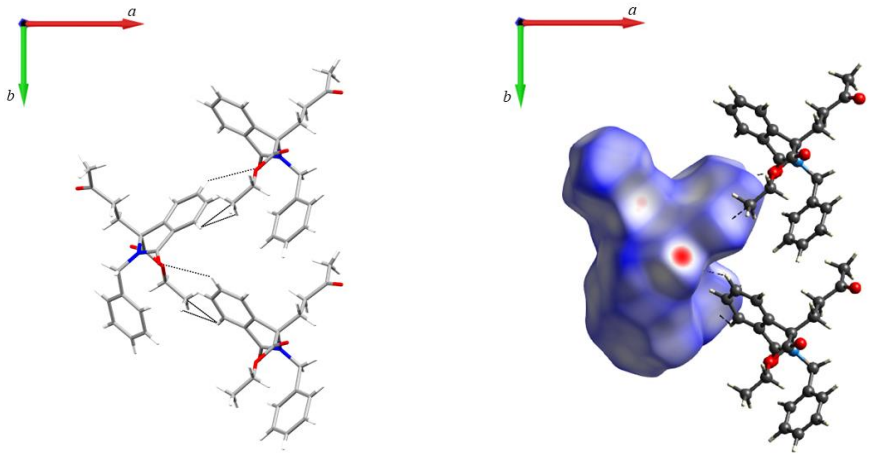

(a) (b)

Figure 5.4 (a) Motif II of the form 5A. (b) Hirshfeld surface mapped with d_{norm} of motif II.

In motif III (Figure 5.5 a) molecules align along the shortest *b* axis interacting by means of H···H and C···H contacts, which mainly involve the benzene ring of the isoindolinone scaffold and the hydrogen atoms of the phenyl group. For this motif also, no strong interaction can be highlighted on the Hirshfeld surface (Figure 5.5 b).

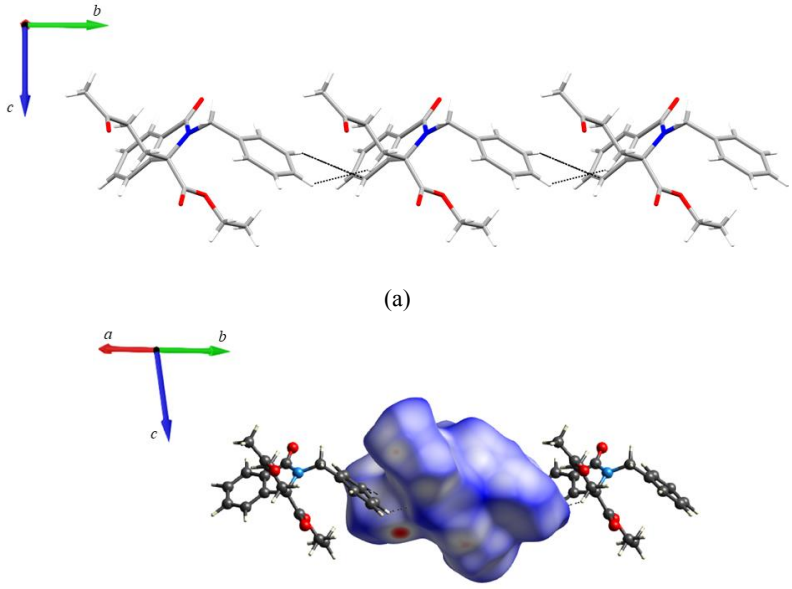

(a)

(b)

Figure 5.5 (a) Motif III of the form 5A. (b) Hirshfeld surface mapped with d_{norm} of motif III.

Concerning the interaction between host and guest molecules, two types of contacts can be highlighted. In motif I-S (Figure 5.6 a,b), the host molecule interacts with toluene by means of C···H and H···H contacts. In motif II-S (Figure 5.7 a,b), host and guest molecules interact by means of two types CH···OC interactions, the former involving the carbonyl oxygen atom of the ketone carbonyl group and the methyl hydrogen atom of the toluene (C4S-H4SB···O4A = 2.47 Å; O4A···H4SB-C4S = 174.2°) and the latter carbonyl oxygen atom of the ketone carbonyl group and the aromatic hydrogen of the toluene (C2S-H2S···O4A = 2.81 Å; O4A··· H2S-C2S = 151.6°). Interestingly, despite motif II-S is characterized by CH···OC interactions which show a good geometry, in PIXEL calculation motif I-S is the motif energetically more favourable.

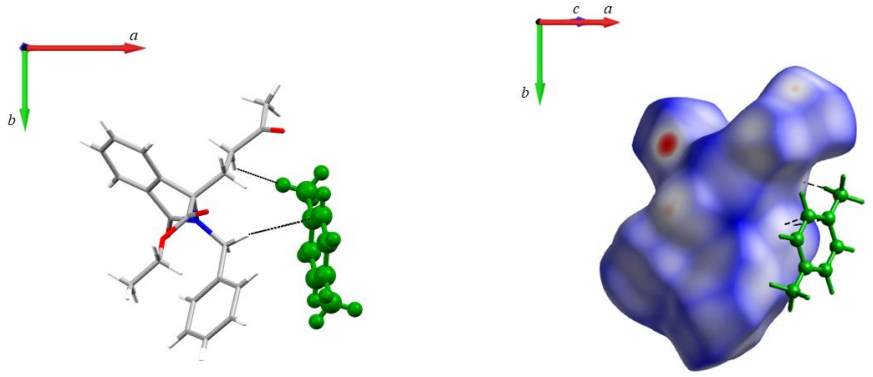

(a) (b)

Figure 5.6 (a) Motif I-S of the form 5A. (b) Hirshfeld surface mapped with d_{norm} of motif I-S.

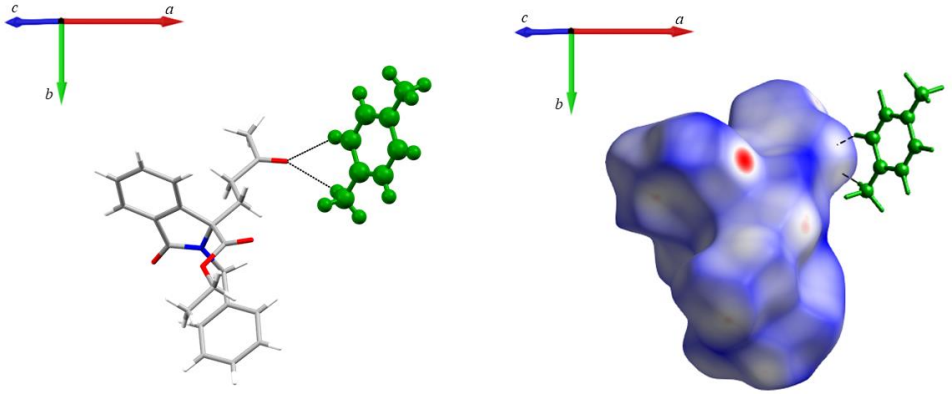

(a) (b)

Figure 5.7 (a) Motif II-S of the form 5A. (b) Hirshfeld surface mapped with d_{norm} of motif II-S.

As can be deduced by the crystal packing analysis and from the data reported in Table 5.1, the molecules in the crystal lattice interact mainly by means of weak H···H and C···H. The only strong interaction is represented by CH···OC interactions, which characterize motif I. The host molecules seem to be fundamental for the crystal packing forming a layer of toluene which interact with isoindolinone molecules by means of different type of contacts (Figure 5.8).

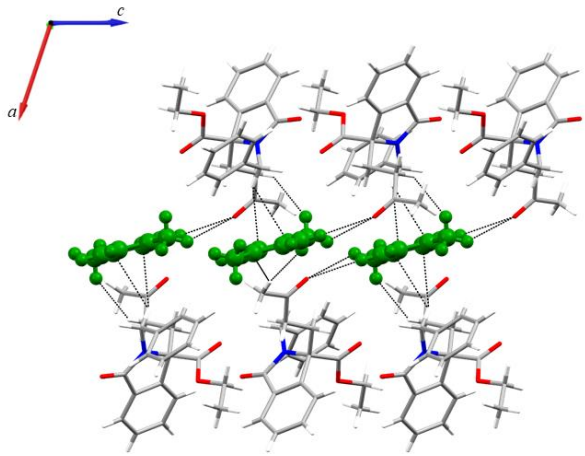

Figure 5.8 Interactions between the host and guest molecules. It is possible to notice the toluene layer parallel to the *bc* plane.

A crystal of form 5A was measured after four days, one week and after three months. Interestingly, after all this time, the crystal does not show any significant difference with respect to the fresh one. Usually, crystals left in the open air for such a long time tend to lose the solvent and therefore, fade. In this case, this event does not happen. This simple observation allows us to further confirm the importance of the guest molecules in the crystal packing.

Moved by curiosity, we decided to heat the crystal to 390 K. We decided to use a temperature slightly higher than the toluene boiling temperature, that is 383 K, to force the loss of solvent molecules.

After the heating procedure, the crystal was measured at room temperature and, surprisingly, we obtained a new crystal form, form 5B, which is a hydrate form.

The differences between form 5A and 5B are related to the loss of toluene molecules, which are replaced by water molecules, while the crystal system changes from monoclinic to orthorhombic and the space group from $P2_1/c$ to *Pccn*.

Table 5.1 List of intermolecular distances (Å), angles (°) and interaction energies (kJ/mol) in the framework of form 5A. Energy values are reported in kJ/mol.

Motif	D-H···A	H···A (Å)	D-H···A (°)	Symm. Op.	Centroid Distance (Å)	E_{Coul}	E_{Pol}	E_{Disp}	E_{Rep}	E_{Tot}
I	C6-H6···O1	2.22	174.1	x, 1/2-y, 1/2+z	6.937	-24.8	-9.8	-42.5	35.5	-41.6
	C13A-H13B···O2A	2.55	113.1	x, 1/2-y, -1/2+z						
II	C···H contacts			1-x, -1/2+y, 1/2-z	9.228	-6.5	-2.4	-23.7	9.3	-23.4
	H···H contacts			1-x, 1/2+y, 1/2-z						
III	C···H contacts			x, -1+y, z	10.408	-4.1	-2.0	-24.2	10.8	-19.5
	H···H contacts			x, 1+y, z						
I-S	C···H contacts			1-x, -1/2+y, 3/2-z	5.261	-8.6	-3.2	-29.9	15.7	-25.9
	H···H contacts			1-x, 1/2+y, 1/2-z						
				1-x, 1/2+y, 3/2-z						
				1-x, -1/2+y, 1/2-z						
II-S	C4S-H4SB···O4A	2.47	174.2	x, y, z	7.618	-7.5	-2.7	-11.3	8.5	-13.1
	C2S-H2S···O4A	2.81	151.6							

The new crystal form shows the presence of water molecules as a guest. During the structure refinement, it was obvious that water molecules possess an occupancy factor less than 1 and therefore, fixed to 0.25 in the final refinement stage. As described in chapter III, also for this water molecules we decided to not refine the occupancy factor and to fix it to a value which not induce an increase of the thermal parameters to a value higher than 0.25. Of course, water molecules come from the atmosphere and, probably, if a crystal of form 5B will be exposed to a high humidity level it will be possible to obtain a hydrate crystal form with water occupancy factor of 1. Unfortunately, it was not possible to perform this hydration experiment.

In the intermolecular energy calculation, we decided to not consider the water molecules mainly for two reasons:

- the occupancy factor is less than 1 and therefore, it seems meaningless to consider the contribution of the water molecules in the crystal packing;

- it was not possible to add hydrogen atoms on the oxygen atom of the water molecule.

In Figure 5.9 is reported a comparison between form 5A and 5B.

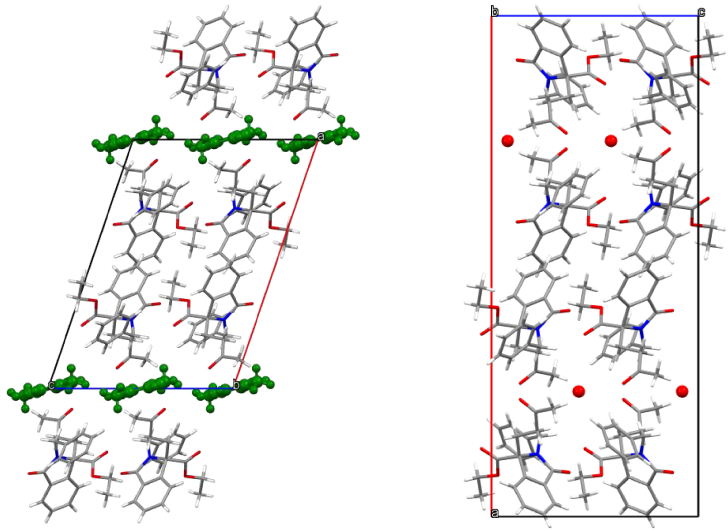

(a) (b)

Figure 5.9 Comparison between the crystal packing of form 5A (a) and 5B (b). The toluene molecules are depicted in ball and stick style and in green.

In Table 5.2 are reported the intermolecular distances (Å), angles (°) and interaction energies (kJ/mol) in the host framework of form 5B.

In motif I, the molecules align along the *c* axis (Figure 5.10 a) by means of CH···OC interactions which involve the carbonyl oxygen atom of the ester group and the methylene hydrogen atom belonging to the ketone side chain (C13A-H13B···O2A = 2.62 Å; O2A···H13B-C13A = 106.5°) and the hydrogen atom attached to the benzene ring and the carbonyl oxygen atom of the γ-lactam ring (C6-H6···O1 = 2.22 Å; O1···H6-C6 = 173.7°). The interacting molecules are related by the glide plane. In the Hirshfeld surface (Figure 5.10 b), these two contacts are highlighted by two red spots.

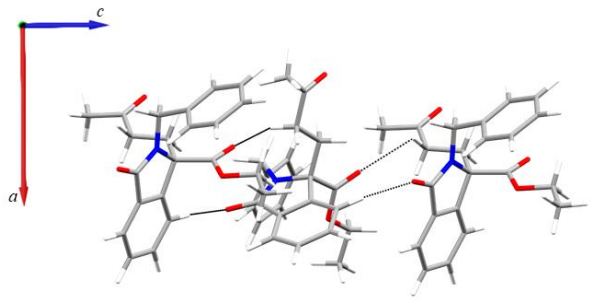

(a)

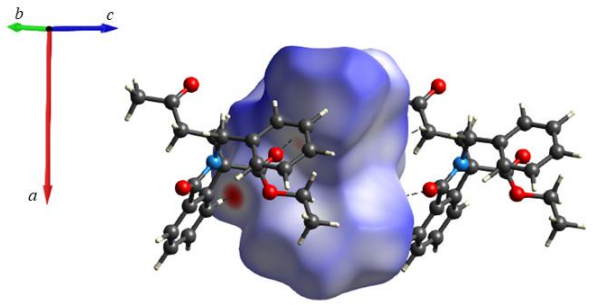

(b)

Figure 5.10 (a) Motif I of the form 5B. (b) Hirshfeld surface mapped with d_{norm} of motif I.

In motif II (Figure 5.11 a) molecules are related by the 2-fold rotation axis with direction [0,0,1]. The molecules interact by means of CH···OC which involve the oxygen atom of the ester carbonyl group and the methylene hydrogen of the phenyl group (C16-H16A···O4A = 2.47 Å; O4A···H16A-C16 = 159.4°) and the oxygen atom of the ester carbonyl group and the hydrogen atom H22 (C22-H22···O4A = 2.55 Å; O4A···H22-C22 = 145.8°). In the Hirshfeld surface analysis (Figure 5.11 b), two small spots indicate the two interactions which characterize motif II.

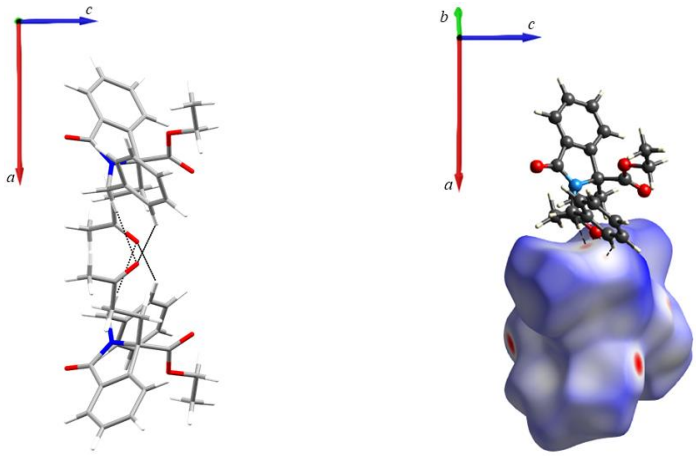

(a) (b)

Figure 5.11 (a) Motif II of the form 5B. (b) Hirshfeld surface mapped with d_{norm} of motif II.

In motif III (Figure 5.12 a), the molecules are related by the screw axis with direction [0,1,0] with screw component [0,1/2,0]. In this case, no strong interaction can be highlighted with the Hirshfeld surface analysis (Figure 5.12 b) and the only interactions are H···H and C···H contacts.

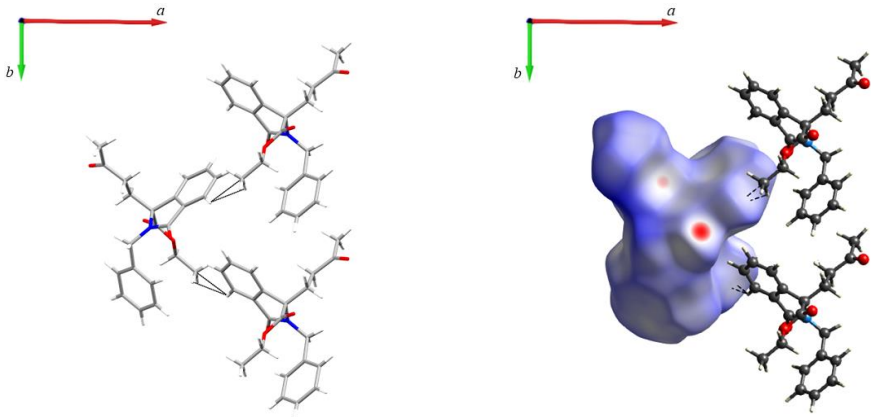

(a) (b)

Figure 5.12 (a) Motif III of the form 5B. (b) Hirshfeld surface mapped with d_{norm} of motif III.

In motif IV (Figure 5.13 a), the molecules align along the shortest *b* axis interacting by means of weak H···H contacts and CH-π interaction between the phenyl group and the benzene group of the insoindolinone scaffold. These interactions are highlighted by white spots in the Hirshfeld surface (Figure 5.13 b).

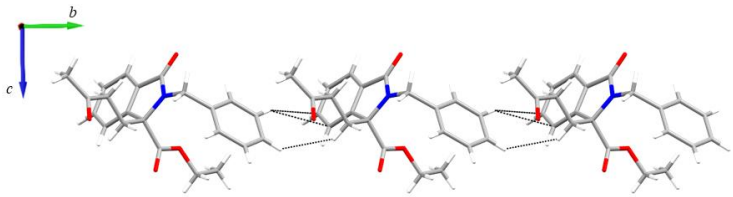

(a)

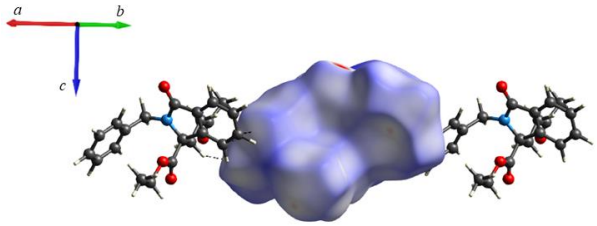

(b)

Figure 5.13 (a) Motif IV of the form 5B. (b) Hirshfeld surface mapped with d_{norm} of motif IV.

Table 5.2 List of intermolecular distances (Å), angles (°) and interaction energies (kJ/mol) in the framework of form 5B. Energy values are reported in kJ/mol.

Motif	D-H···A	H···A (Å)	D-H···A (°)	Symm. Op.	Centroid Distance (Å)	E_{Coul}	E_{Pol}	E_{Disp}	E_{Rep}	E_{Tot}
I	C6-H6···O1	2.22	173.7	x, 3/2-y, -1/2+z	6.942	-26.0	-10.0	-41.1	34.6	-42.6
	C13A-H13B···O2A	2.62	106.5	x, 3/2-y, 1/2+z						
II	C16-H16A···O4A	2.47	159.4	1/2-x, 3/2-y, z	8.515	-20.0	-9.6	-35.3	32.4	-32.4
	C22-H22···O4A	2.55	145.8							
III	H···H contacts			1-x, -1/2+y, 3/2-z	9.265	-6.3	-2.6	-23.9	9.7	-23.0
	C···H contacts			1-x, 1/2+y, 3/2-z						
IV	H···H contacts			x, -1+y, z	10.384	-4.9	-2.4	-24.4	11.4	-20.3
	CH-π interaction			x, 1+y, z						

If we compare the crystal packing of form 5A and 5B, it is evident that there are only a few differences between the two crystal forms (Figure 5.9). Since the unit cell changes from monoclinic to orthorhombic and the β angle becomes equal to 90°, it is possible to notice a shift of isoindolinone molecules with a direction parallel to the *ac* plane. Moreover, considering the new space group

setting (*Pccn*) we must consider a rotation of a row of isoindolinone molecules of 180° along the *a* axis. Analysing the crystal packing of form 5A it was found that the toluene molecules play a fundamental role in the solid state assembly and if we remove them, the formation of new interactions is fundamental to preserve the integrity of the crystal.

In this case, as can be seen in Figure 5.14, the shift and the rotation of the molecules ensure to fill the voids left behind by the toluene molecules and guarantee the formation of new interactions between the isoindolinone molecules (motif II). These contacts should not have been formed without considering these two dramatic events.

If we compare the crystal packing of the two crystal forms, motif II of form 5B is not present in the crystal packing of form 5A. Moreover, we must consider that this type of motif is generated between the isoindolinone molecules that in form 5A were separated by the toluene molecules. Thus, to preserve the integrity of the crystal and establish new interactions, a raw of isoindolinone molecules must rotate and, thanks to this rotation, it is possible to create new interactions that can substitute the interactions that isoindolinone molecules established with the toluene.

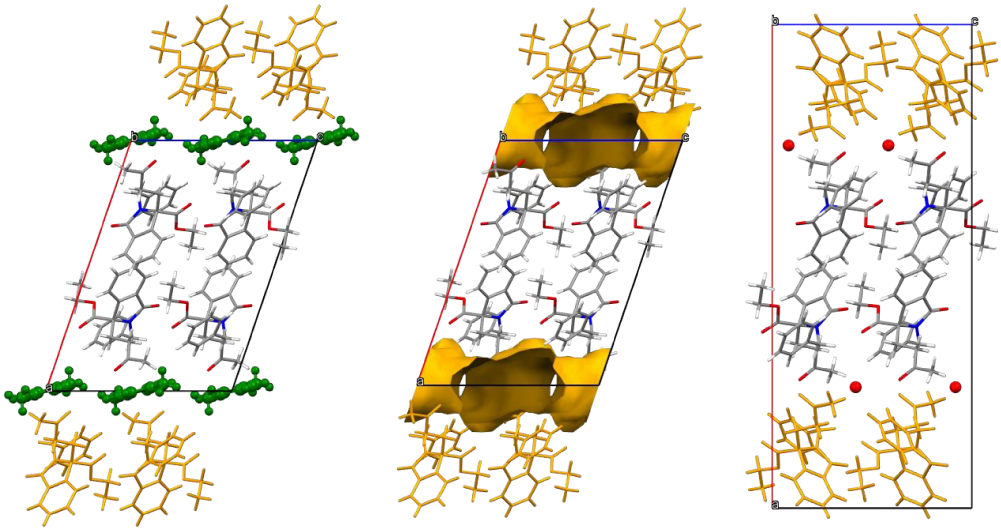

(a) (b) (c)

Figure 5.14 Comparison between the crystal packing of form 5A (a), form 5A with void (b) and form 5B (c). In orange are depicted the molecules which undergo the shift and rotation. In green are depicted the toluene molecules.

We try to reproduce the transformation using crystals obtained with batch 2.

Surprisingly, when we repeated the variable temperature experiment, we were not able to obtain the same thermal behaviour of form 5A. Indeed, when the crystal obtained using batch 2 were heated up to 390 K, they melt.

The different thermal behaviour could be explained considering that crystals obtained with batch 2 do not show disorder in contrast to crystals obtained from batch 1: it is possible that the disorder can guarantee the integrity of the crystal after the removal of toluene molecules and the phase transformation.

5.2 DSC and TGA analysis

Due to the lack of material, all the thermal analysis reported were performed on crystals obtained using compound **5** from batch 2.

The DSC analysis (Figure 5.15) shows two exothermic peaks at 354 K and 365 K that can be associated with the loss of toluene molecules and to the melting. Around 500 K the compound decomposition starts.

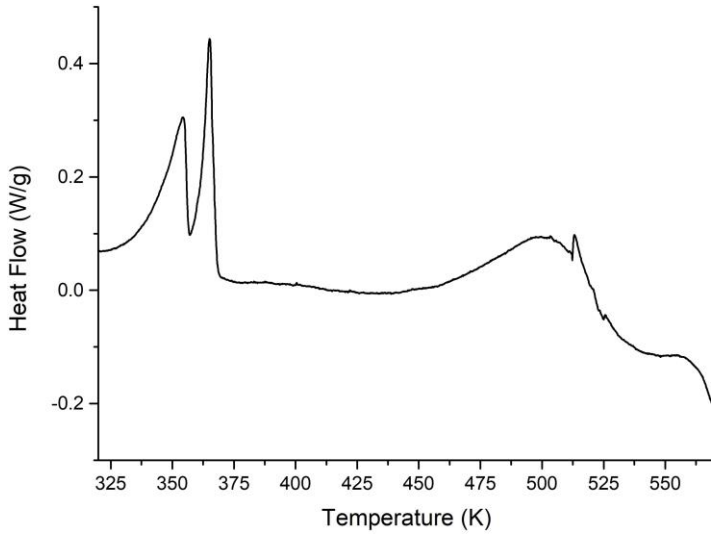

Figure 5.15 DSC measurement performed on crystals of the form 5A. The plot is reported with exo down.

The TGA measurement (Figure 5.16) shows the loss of toluene molecules starting around 320 K and finishing at 360 K. The percentage weight loss is about 11% and it is consistent with the value calculated by considering that in the X-ray crystal structure the host/guest ratio is 2:1.

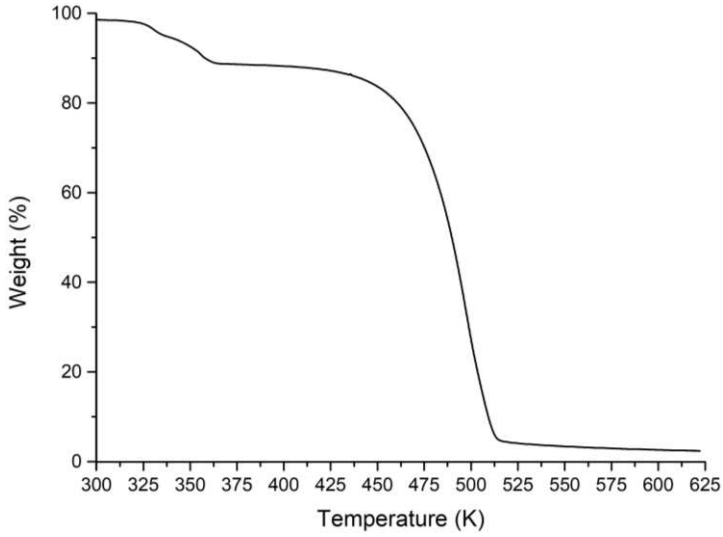

Figure 5.16 TGA analysis on crystals of form 5A. Toluene molecules are released in the temperature range from 310 K to 375 K. The weight loss at 408.46 K is 11%.

5.3 Experimental section

5.3.1 Single crystal X-ray data collection, structure solution and refinement

A crystal of form 5A was selected and mounted on a MiTeGen microloop with paratone oil. Data collection was performed at University of Salerno with a Bruker D8 QUEST diffractometer equipped with a PHOTON II detector using Cu*K*α radiation (λ= 1.54178 Å). Data indexing was performed using APEX3.[108] Data integration and reduction were performed using SAINT.[108] Absorption correction was performed by a multi-scan method in SADABS.[108]

The same crystal measured at room temperature was heated up to 390 K using an Oxford Cryostream cold nitrogen gas blower. After the thermal treatment, a data collection was performed again at room temperature.

In Figure 5.17 is reported the crystal before and after the thermal treatment.

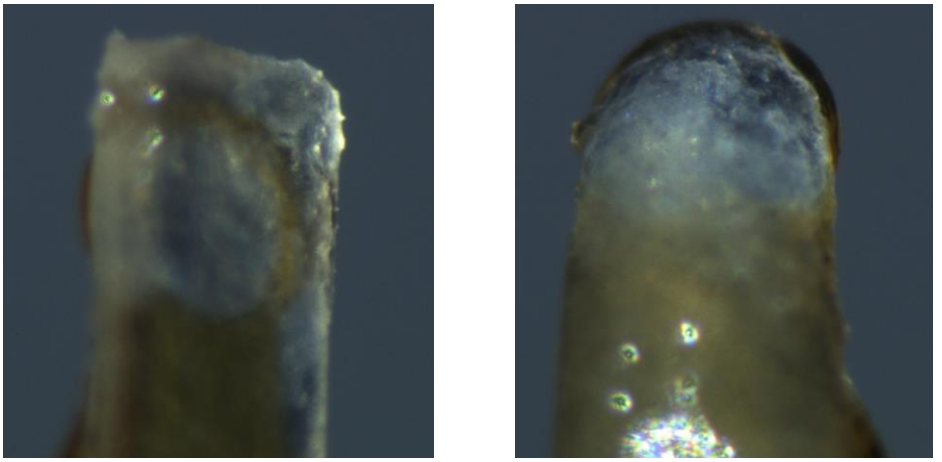

(a) (b)

Figure 5.17 Photo of the crystal taken before (a) and after (b) the thermal treatment at 390 K.

The crystal structures were solved by direct methods using the program SIR2014[98] and refined by means of full-matrix least-squares based on F^2 using the program SHELXL.[99] *OLEX*2[100] was used as GUI.

In both cases, the disordered side chains were treated using EADP and EXYZ SHELXL command. These two commands allow to constraints the position and the anisotropic displacement parameters of different atoms to be the same. In our particular case, since the two side chains can occupy two different positions, we decided to constraints to the same values the coordinates and the anisotropic thermal parameter of the disordered atoms. Moreover, the atom side chains occupancy factors were refined, and final values obtained are 0.849(4) and 0.151(4) in the case of form 5A and 0.860(6) and 0.140(6) for the form 5B. As can be noted, the occupancy factors of the two crystal forms do not change after the thermal treatment.

Crystallographic data and refinement information are reported in Table 5.3. ORTEP diagrams were drawn using *OLEX*2[100] (Figure 5.18).

Table 5.3 Crystallographic data for crystal form 5A and 5B.

	Form 5A	**Form 5B**
T (K)	296	296
Formula	$2(C_{22}H_{23}NO_4) \cdot C_7H_7$	$C_{22}H_{23}NO_4 \cdot 0.13O$
Formula weight	821.95	367.41
System	Monoclinic	Orthorhombic
Space group	$P2_1/c$	*Pccn*
***a* (Å)**	18.056(6)	30.542(8)
***b* (Å)**	10.408(3)	10.384(4)
***c* (Å)**	12.691(3)	12.632(2)
***α* (°)**	90	90
***β* (°)**	108.82(2)	90
***γ* (°)**	90	90
***V* (Å^3)**	2257.5(12)	4006(2)
Z	2	8
***Dx* (g cm^{-3})**	1.209	1.218
λ (Å)	1.54178	1.54178
***μ* (mm^{-1})**	0.655	0.683
F_{000}	874.0	1560.0
R1 (I > 2σI)	0.0629(3922)	0.0947(2997)
$_wR_2$	0.1474(4174)	0.2164(3791)
N. of param.	303	268
N. of reflections	4174	3791
GooF	1.118	1.149
ρ_{min}, ρ_{max} (eÅ^{-3})	-0.20, 0.25	-0.23, 0.23

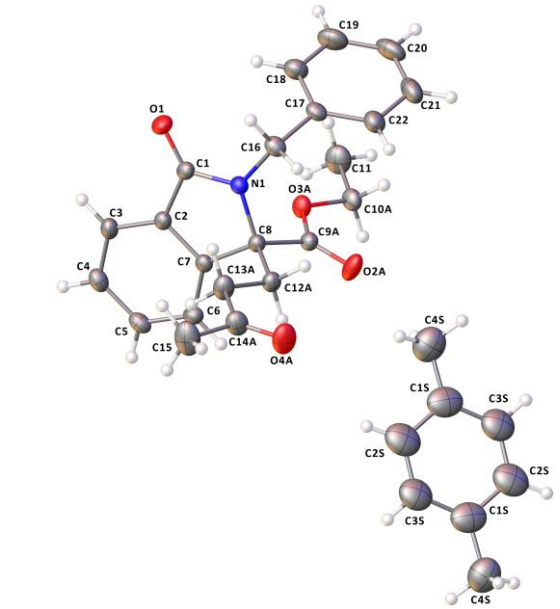

(a)

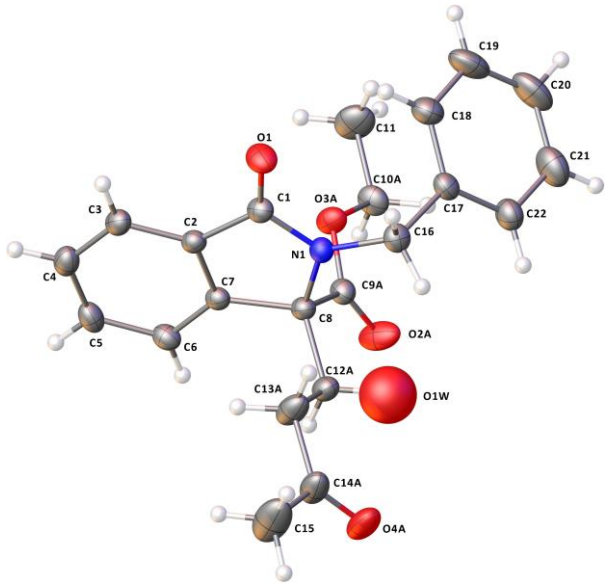

(b)

Figure 5.18 ORTEP diagrams for crystal form 5A (a) and 5B (b). Atom types: C grey, O red, N blue. Ellipsoids are drawn at 20% probability level. Disordered and hydrogen atoms have been omitted for clarity.

5.3.2 DSC and TGA measurements

DSC measurements were performed on a TA DSC-Q2000 instrument under a purified N_2 flow (50 mL/min).

Single crystals, for a total of 1.6 mg, obtained by slow evaporation of a solution of chloroform/toluene (2:1) using compound **5** of batch 2 were sealed in an aluminium pan and heated at a rate of 2 K/min.

TGA measurements were performed on a TA TGA Q500 instrument under a purified N2 flow (50 mL/min) by heating at 2 K/min.

TGA measurement was performed on single crystals of compound **5** from batch 2, for a total of 2.37 mg. The heating rate was of 2 K/min.

CONCLUSION

In this thesis, we have deeply studied the dynamic behaviour of organic molecules in the solid state and how they can respond to external stimuli and adapt to changes mainly by means of X-ray diffraction analysis and computational methods.

In chapter II we have investigated the transformation mechanism and the energetic aspects of an SCSC transformation of an hexacyclic peptoid decorated with four propargyl and two methoxyethyl side chains (compound **1**). In particular, we considered the transformation of an acetonitrile solvate crystal form (form 1A) to an anhydrous crystal form (form 1B) characterized by two independent cyclopeptoids molecules in the asymmetric unit. By studying the energetic aspects of the transformation, it was possible to define that two conformers coexist in the same crystal and to highlight how the conformational change allows the creation of new interactions between the two different conformers guaranteeing the integrity of the crystal. XRPD experiments were also performed on the compound. A VT-XRPD analysis allowed to characterize and determine the structure of a new high temperature crystal form by means of a simulated annealing procedure using data obtained at the Europeans Synchrotron Radiation Facility (ESRF). *In-situ* XRPD allowed to demonstrate, for the first time, that cyclic peptoids are able to adsorb gas like propyne and CO_2 by two different experiments at ESRF and at Max Planck Institute for Solid State Research (MPI). Moreover, thanks to the simulated annealing procedure implemented in TOPAS V6, we were able to localize the guest molecules in the unit cell and to study the main host/guest interactions.

On compound **2** (hexacyclic peptoid decorated with four methoxyethyl and two propargyl side chains), an in-depth crystal packing analysis on four crystal forms was performed. Furthermore, thanks to two different VT-SCXRD experiments, two SCSC transformation were highlighted. In particular, analysing a porous crystal form (form 2A) we have demonstrated that it is possible to remove the water molecules localised inside the channels and inducing an SCSC transformation obtaining a monohydrate crystal form (Form 2B), containing only one water molecule (O1W) which acts as a bridge between the two different conformers. This transformation induces important changes in crystal packing. Indeed, as happened for the transformation of the form 1A to the form 1B, also in this case we have a conformational change, which determines the formation of a new crystal form showing two independent molecules in the asymmetric unit. Moreover, it is possible to force the loss of the bridging water molecule (O1W) thanks to a further thermal treatment inducing a new SCSC transformation and the formation of a new anhydrous crystal form (form 2L). The transformation of

the form 2B to the form 2L is dramatic. Indeed, a rotation of 180° of a row of cyclic peptoids in the crystal is necessary to explain the SCSC transformation. VT-XRPD analysis confirms the dynamic behaviour observed with SCXRD and a new phase transformation and a cis/*trans* isomerization were highlighted.

The fourth chapter is entirely dedicated to the description of the crystal packing of the crystal forms of two cyclic hexapeptoids decorated with alkyl side chains with 5 (compound **3**) and 6 (compound **4**) carbon atoms. Performing a low temperature experiment on crystal form 3A, previously obtained by means of SCXRD analysis at room temperature, we induced an SCSC transformation obtaining a new crystal form (form 3B). The transformation was confirmed also by DSC analysis. Regarding the compound **4**, a thermal analysis on crystal form 4A highlights a transformation when the temperature reaches the 335 K. Thus, a VT-SCXRD analysis was performed in order to study the phenomenon. Thanks to this experiment we were able to obtain a new high temperature phase (form 4B) but, unfortunately, due to the high thermal disorder of the side chains, it was not possible to solve the structure of this new phase. Interestingly, the SCSC transformation is reversible, since crystals of the form 4B flash-cooled in liquid nitrogen and measured at 100 K gave back the form 4A. A VT-XRPD analysis confirms the transformation and highlights a recrystallization process which was already observed in the DSC experiment.

Finally, the last chapter is dedicated to the description of the crystal packing and a phase transformation of a 3,3-disubstituted isoindolinone (compound **5**). The first analysed batch contains an enantiomeric excess of one enantiomer with the respect to the other one (e.e. 74%) and the obtained toluene solvate crystal form (form 5A) shows positional disorder on the two side chains attached to the tetrasubstituted stereocenters. On form 5A, VT-SCXRD analysis was performed determining a transformation to a hydrate crystal form (form 5B). The transformation can be described considering a dramatic change in the crystal packing. Interestingly, no transformation was highlighted performing the same VT-SCXRD experiment on crystals of form 5A, with no disordered atoms, obtained using a second batch with no enantiomeric excess. This observation could be explained considering that the disorder on the stereocenters can help the transformation.

These results highlight that the dynamic behaviour of solid state materials reserves many interesting and sometimes surprising aspects, which deserve to be studied and understood. Recently, many efforts were devoted to the development of molecular machines, but the control of molecular movements in the solid state may foster further and (perhaps) more useful applications.

APPENDIX

A.1 CLP-PIXEL

All the following information about CLP-PIXEL are reported in the papers already cited in this thesis[78a,b,c] and in the software manual freely available on-line.[120]

CLP-PIXEL allows the calculation of the intermolecular potential energies, splitting these energies into three fundamentals contributions: Coulomb-polarization term, dispersion term (London) and repulsion term.

The method is implemented in two forms:

- Atom-atom form, AA-CLP. In the Coulomb-London-Pauli (CLP) assumption the atom-atom potential functions are calculated using a few standard atomic parameters like atomic numbers, atomic polarizability and ionization potentials, and of local atomic point charges from Mulliken population analysis;
- PIXEL form. Intermolecular energies are calculated as numerical integrals over a large number of electron-density units called "pixels". In this case, an *ab initio* molecular orbital calculation is needed in order to prepare the molecular electron density in the form of discrete points on a grid.

The separation of total interactions energies in four terms, Coulombic, polarization, dispersion and repulsion, is very useful. The Coulombic terms are given by the electrostatic interaction among nuclear charges and electron density. Polarization represents the effect of an electrostatic field, produced by the charge distribution of the approaching polarizer molecule, onto a distribution of charges. Dispersion represents secondary mutual polarization due to correlation of electronic motions in the two molecules. Repulsion is the trace of electron spin avoidance. Coulombic term is important for molecules with hydrogen bonds or charged groups, while polarization and dispersion for polarizable molecules.

The main differences between the two methods are related to the formulation of Coulombic terms. Indeed, in CLP are obtained by lattice sums on localized charge parameters and are heavily underestimated. In the PIXEL formulation, they are calculated by a numerical integral equivalent to the standard analytical form and are as accurate as the wavefunction is. Moreover, the PIXELC method can take into account the penetration energy, the part of the Coulombic energy that depends

[120] http://www.angelogavezzotti.it/

on delocalized electrons. Polarization terms are calculated empirically for the AA formulation, or in the linear dipole approximation in PIXEL, where the incoming electric field acts on local polarizabilities and generates a dipole with its associated dipole separation energy. Dispersion terms are simulated in London's inverse sixth power approximation, involving ionization potentials and polarizabilities; repulsion is represented as a modulated function of the electron density overlap.

A.1.1 CLP module

The first step for the CLP-PIXEL calculation is the conversion of the crystallographic information file (.cif) into an ".oih" file which contains the positions of some atomic nuclei in *x*,*y*,*z* coordinates, while the other atoms position are given by a series of indicators which allows the calculation of the explicit *x*,*y*,*z* coordinates. Since the hydrogen bonds are fundamental in crystal energy calculation, during this phase, the hydrogen atoms are normalized at a distance of 1.08 Å for C-H; while for O-H, S-H and N-H the hydrogen bonds are renormalized at a distance from the heavy atom of 1.00, 1.30 and 1.30 Å respectively. This action is necessary since all the force fields are calibrated using such renormalized positions. Then the implicit coordinates in the .oih file, are reported in explicit *x*,*y*,*z* coordinates for all nuclei, including hydrogens.

After the definition of the atomic positions, in CLP module is possible to calculate atomic charge parameters from a Mulliken population analysis on an Extended Huckel wavefunction for the closed shell, neutral molecules. In this case, the resulting charges are related to the relative electronegativities. This step is necessary for CLP module but, it is not needed for PIXEL.

After that, it is possible to perform a calculation with CLP. In particular, a cluster of molecules is defined using the symmetry operations of the space group considering also the value V_{max} that indicates the distance between the reference molecular group (defined by the explicit coordinates) and the surrounding molecular groups. The surrounding molecular groups are included in the lattice energy formation only if the distances between the reference molecular group and the surrounding molecular groups are below V_{max}. The program calculates the lattice energies and separates the intermolecular energies contributions, considering the centroid distances and the symmetry operation, as following (Eq. A1):

$$E(\mathrm{i,j}) = \left\{\frac{1}{(4\pi\varepsilon^{\circ})[F_{\mathrm{Q}}\mathrm{q(i)}][F_{\mathrm{Q}}\mathrm{q(j)}]\mathrm{R(i,j)}^{-1}}\right\} - F_{\mathrm{P}}P(\mathrm{i,j})R(\mathrm{i,j})^{-4} - F_{\mathrm{D}}D(\mathrm{i,j})R(\mathrm{i,j})^{-6} + F_{\mathrm{R}}T(\mathrm{i,j})R(\mathrm{i,j})^{-12} = E(\mathrm{Coul}) - \mathrm{A4}\,R(\mathrm{i,j})^{-4} - \mathrm{A6}\,R(\mathrm{i,j})^{-6} + \mathrm{A12}\,R(\mathrm{i,j})^{-12} \quad \text{A1}$$

where

$$P(\mathrm{i},\mathrm{j}) = \alpha(\mathrm{eff})\ \mathrm{abs}\left(\mathrm{q_i q_j}\right)$$

$$D(\mathrm{i},\mathrm{j}) = \alpha(\mathrm{eff})\ n_\mathrm{i} n_\mathrm{j} \left(I_\mathrm{i} I_\mathrm{j}\right)^{1/2}$$

$$T(\mathrm{i},\mathrm{j}) = (1 + H_\mathrm{Bd} H_\mathrm{Ba})\left(\mathrm{Z_{V,i}} - \mathrm{q_i}\right)\left(\mathrm{Z_{V,j}} - \mathrm{q_j}\right)\left(\mathrm{B_i} B_\mathrm{j}\right)^{1/2}$$

$$\alpha(\mathrm{eff}) = \left\{\left[\alpha_\mathrm{i}\left(\mathrm{Z_{V,i}} - q_\mathrm{i}\right)/\mathrm{Z_{V,i}}\right]\left[\alpha_\mathrm{j}\left(\mathrm{Z_{V,j}} - \mathrm{q_j}\right)/\mathrm{Z_{V,j}}\right]\right\}^{1/2}$$

with q atomic point charges, R atom-atom distances, α atomic polarizabilities, Z_v number of valence electrons, n quantum number of valence orbitals, I atomic ionization potential, B empirical diffuseness parameters and F_Q, F_P, F_D and F_R are general scaling parameters. The B parameters are assigned using carbon = 1 and decreasing the value for more electronegative atoms. The H_{Bd} (hydrogen-bonding donor ability) and H_{Ba} (acceptor ability) parameters are numbers between 0 and ± 1, being negative for acceptors and positive for donors.

If there is only one reference molecular group, the intermolecular potential energy of the molecule in the crystal is (Eq. A2):

$$E(\mathrm{pot},\mathrm{tot}) = \sum_i \sum_j E(\mathrm{i},\mathrm{j})$$

A2

where *i* identifies any atom in the reference molecular group and *j* any atoms in any surrounding molecular group.

If there are n units in the asymmetric unit, E(pot,tot) = E+E'+E"+..., where E is the equivalent of equation (A2) for the packing of the n units all together, and E', E"... are the energies between units 1-2, 1-3...1-n, 2-3, 2-4,...2-n, ... n-n. For example, for three molecules in the asymmetric unit (Eq. A3):

$$E(\mathrm{pot},\mathrm{tot}) = E\ +\ E(1-2) + E(1-3) + E(2-3)$$

A3

A.1.2 PIXEL module

To obtain more reliable results, it is possible to use the PIXEL module. In this case, the only step needed is the creation of the file containing the explicit *x*,*y*,*z* coordinates for all nuclei. Then, a preliminary evaluation of the charge density by quantum chemical methods is necessary.

Considering a molecule (**1**) with nuclei of charge Z_j at points $(j) = [x_j, y_j, z_j]$, ρ_k, derived from quantum mechanical calculation, is the electron density in an elementary volume V_k centred at point $(k) = [x_k, y_k, z_k]$. Each e-pixel has charge $q_k = \rho_k V_k$.

In order to reduce the number of pixels, the distribution is contracted into *n* x *n* x *n* super-pixels, where *n* is the condensation level. Each pixel is assigned to a particular atom in the molecule by assuming *p* as the number of atoms for which the nucleus-pixel distance is smaller than the atomic radius: for $p = 1$, the pixel is assigned to that atom, for $p > 1$, the pixel is assigned to the atom from which the distance is the smallest fraction of the atomic radius and for $p = 0$, the pixel is assigned to the atom whose atomic surface is nearest.

Considering a second molecule **2** with nuclei of charge Z_m at points $(m) = [x_m, y_m, z_m]$, and whose e-pixels of charge $q_i = \rho_i V_i$ are at positions $(i) = [x_i, y_i, z_i]$, the electrostatic potential Φ_i generated by molecule **1** at point (*i*) of the charge density of molecule **2** and that generated by molecule **1** at nucleus *m* of molecule **2**, Φ_m, with the corresponding Coulombic potential energies E_i and E_m, are respectively:

$$\Phi_i = 1/(4\pi\varepsilon_0)\left[\sum_k q_k/R_{ik} + \sum_i Z_i/R_{ij}\right];\ E_i = q_i\Phi_i \qquad \text{A4}$$

$$\Phi_m = 1/(4\pi\varepsilon_0)\left[\sum_k q_k/R_{km} + \sum_i Z_i/R_{jm}\right];\ E_m = Z_m\Phi_m \qquad \text{A5}$$

$$E_{Coul,1-2} = \sum_i E_i + \sum_m E_m \qquad \text{A6}$$

where R_{ln} is the distance between any two centres of pixels or nuclear positions *l* and *n*.

The polarization term is calculated considering ε_i the total electric field applied by surrounding molecules at pixel *i*:

$$E_{Pol,i} = -1/2\mu_i\varepsilon_i = -1/2\alpha_i{\varepsilon_i}^2 \qquad \text{A7}$$

μ_i the dipole induced at pixel *i* and α_i the polarizability at pixel *I*, $\alpha_i = (q_i/Z_{atom})\alpha_{atom}$, where Z_{atom} is the atomic charge and α_{atom} is the polarizability of the atom. The total polarization energy at a molecule is calculated by the sum of the polarization energies at each of its electron density pixels (Eq. A8).

$$E_{Pol,TOT} = \sum E_{Pol,i}$$

A8

Dispersion energies are calculated summing pixel-pixel terms in a London-type expression (Eq. A9):

$$E_{Disp,1-2} = (-3/4)\sum_{i,1}\sum_{j,2} E_{OS}\, f(R)\alpha_i\alpha_j$$

A9

where f(*R*) is (Eq. A10):

$$f(R) = \exp\left[-\left(D/R_{ij} - 1\right)^2\right] \left(\text{for } R_{ij} < D\right)$$

A10

D is an empirical parameter. E_{OS} (oscillator strength) is calculated considering each pixel as a separate oscillator, with an ionization potential I_i, that is a function of the ionization potential I^o of the atom associated to that pixel, and of the distance R_i between the pixel and the nucleus (Eq. A11).

$$E_{OS} = \left(I_i I_j\right)^{1/2};\ I_i = I^O \exp(-\beta R_i)$$

A11

where β is a function of the atom type.

The total charge density overlaps integral between molecules **1** and **2** is calculated over the original uncontracted charge densities and it does not depend on the condensation level. The integration is performed numerically considering all pairs of overlapping charge density elements ρ(i)*ρ(j)*dV, being dV the elementary volume.

The total overlap is subdivided into contributions from pairs of atomic species *m* and *n*, S_{mn}. The expressions are:

$$S_{1-2} = \sum_{\mathrm{i},1} \sum_{\mathrm{j},2} \left[\rho_{\mathrm{i}}(1)\rho_{\mathrm{j}}(2)\right] V = \sum_{\mathrm{m}} \sum_{\mathrm{n}} S_{\mathrm{mn}}$$

A12

$$E_{\mathrm{Rep,mn}} = (K_1 - K_2\, \Delta\chi_{\mathrm{mn}}) S_{\mathrm{mn}}$$

A13

where $\Delta\chi_{mn}$ is the corresponding difference in Pauling electronegativity. K_1 and K_2 are positive disposable parameters.

Finally, the total intermolecular interaction energy is calculated as (Eq. A14):

$$E_{\mathrm{Tot}} = E_{\mathrm{Coul}} + E_{\mathrm{Pol}} + E_{\mathrm{Disp}} + E_{\mathrm{Rep}}$$

A14

In PIXEL method, all the empirical atom parameters are optimized by considering the agreement between the calculated lattice energies and the experimental heats of sublimation, the comparison between the interaction energies between molecular dimers in comparison with *ab initio* calculations and, finally, the agreement between PIXEL and Intermolecular Perturbation Theory.

A.2 Hirshfeld surface

The Hirshfeld surface allows the exploration of the crystal packing and intermolecular interaction in molecular crystals by means of a novel visual manner.[80] In particular, the Hirshfeld surface represents the space occupied by a molecule in the crystal reporting also all the intermolecular interactions.

For each atom in the crystal is possible to define a weight function $w(\mathbf{r})$ (Eq. A15):

$$w_a(r) = \rho_a^{\mathrm{at}}(\boldsymbol{r}) / \sum_{i \in \mathrm{molecule}} \rho_i^{\mathrm{at}}(\boldsymbol{r})$$

A15

where $\rho_i^{\mathrm{at}}(\boldsymbol{r})$ is a spherically averaged Hartree-Fock atomic electron density function centred on a specific nucleus. The electron density of an atomic fragment as (Eq. A16):

$$\rho_a(\boldsymbol{r}) = w_a(\boldsymbol{r}) \rho^{\mathrm{mol}}(\boldsymbol{r})$$

A16

where $\rho^{\mathrm{mol}}(\boldsymbol{r})$ is the molecular electron density.

Since the electron density is localized near the nuclei and decay exponentially, the weight function $w(\mathbf{r})$ is a continuous function which can assume values 1.0 at nucleus and 0 at a distance far from the nucleus.

For a molecule in the crystal, a weight function can be defined as (Eq. A17):

$$w_A(\boldsymbol{r}) = \sum_{i \in \mathrm{molecule}} \rho_i^{\mathrm{at}}(\boldsymbol{r}) \,/\, \sum_{i \in \mathrm{crystal}} \rho_i^{\mathrm{at}}(\boldsymbol{r}) = \rho_{\mathrm{molecule}}(\mathbf{r})/\rho_{\mathrm{crystal}}(\mathbf{r})$$

A17

the numerator is a sum over the atoms in the molecule (promolecule) and the denominator is a sum over the crystal (procrystal). Also in this case, $w_A(\boldsymbol{r})$ is a continuous function with $0 < w_A(\boldsymbol{r}) < 1$. The Hirshfeld surface is obtained when $w_A(\boldsymbol{r}) = 0.5$ and defines the volume where the promolecule electron density dominates the procrystal electron density guaranteeing the maximum proximity of neighbouring molecular volumes.

The Hirshfeld surface is characterized by thousands of points from which it is possible to obtain two fundamental parameters to define the contact distances from every point: d_{e} and d_{i}. In particular, d_{e} is indicated as the distance from a point on the surface to the nearest nucleus outside the surface, d_{i} is indicated as the distance from a point on the surface to the nearest nucleus inside the surface.

With respect to the other molecular visualization based on the atomic radius, the Hirshfeld surface fills 95% of the crystal volume. The voids in the crystal volume (5% of the volume) can be considered as regions where the crystalline electron density is very low. Moreover, the Hirshfeld surface is defined by the molecule itself and the surrounding molecules. Therefore, it contains all the information regarding the intermolecular interactions.

Particularly useful is the description of the Hirshfeld surface considering a unique parameter, d_{norm} that combines both d_{e} and d_{i} distances normalized by the van der Waals (vdW) radius of the atoms involved in the close contact to the surface (Eq. A18).

$$d_{\mathrm{norm}} = \frac{d_{\mathrm{i}} - r_{\mathrm{i}}^{\mathrm{vdW}}}{r_{\mathrm{i}}^{\mathrm{vdW}}} + \frac{d_{\mathrm{e}} - r_{\mathrm{e}}^{\mathrm{vdW}}}{r_{\mathrm{e}}^{\mathrm{vdW}}}$$

A18

From Eq. A20, it is evident that d_{norm} is negative for contacts shorter than the vdW interactions and positive for contacts longer than the vdW interactions. On the Hirshfeld surface the d_{norm} is

represented by red spots, for short contacts, white spots per contacts near to the sum of vDW radii and blue for longer contacts.

As for the CLP-PIXEL calculation, also for the Hirshfeld surface analysis, it is necessary to re-normalize the hydrogen atoms position. Therefore, all the Hirshfeld surface analysis reported in this thesis are performed considering the *X*-H distances from the compilation of Allen *et al*.[84]

A.3 Energy frameworks

Thanks to the Energy frameworks analysis it is possible to better understand the crystal packing combining efficient calculation of intermolecular interaction energy with a graphical representation of their magnitudes. Interaction energies between molecular pairs are represented as cylinders joining the centroids of pairs of molecules, with the cylinder radius proportional to the magnitude of the interaction.

The approach used in CrystalExplorer for the calculation of the intermolecular interaction energies is very similar to Gavezzotti's method.[79b] The total energy is calculated as the sum of the electrostatic, polarization, dispersion and repulsion terms considering a scale factor for every single term (Eq. A19).

$$E_{\mathrm{tot}} = k_{\mathrm{ele}}E_{\mathrm{ele}} + k_{\mathrm{pol}}E_{\mathrm{pol}} + k_{\mathrm{disp}}E_{\mathrm{disp}} + k_{\mathrm{rep}}E_{\mathrm{rep}} \qquad \text{A19}$$

In particular, the E_{ele} (electrostatic energy) can be calculated as (Eq. A20):

$$E_{ele} = \int\int \rho_{\mathrm{A}}(\boldsymbol{r}_{\mathrm{A}})\rho_{\mathrm{B}}(\boldsymbol{r}_{\mathrm{B}})|\boldsymbol{r}_{\mathrm{A}} - \boldsymbol{r}_{\mathrm{B}}|^{-1}\, d\boldsymbol{r}_{\mathrm{A}} d\boldsymbol{r}_{\mathrm{B}} \qquad \text{A20}$$

E_{pol} (polarization energy) is calculated as the sum of the terms of the kind $\frac{1}{2}\alpha F^2$, in which α are isotropic polarizabilities and *F* is the electric field computed at each atomic nucleus resulting from the charge distribution of the other monomer.

E_{disp} (dispersion energy) is given by the Grimme's D2 dispersion correction[121] (Eq. A21)

$$E_{\mathrm{disp}} = s_6 \sum_{i=1}^{N_{\mathrm{at}}-1} \sum_{j=i+1}^{N_{\mathrm{at}}} \frac{C_6^{ij}}{R_{ij}^6} f_{\mathrm{dmp}}(R_{ij})$$

[121] S. Grimme, *J. Comput. Chem.*, 2006, **27**, 1787-1799.

where N_{at} is the number of atoms, C_6^{ij} is the dispersion coefficient for pair ij, s_6 is the scale factor, R_{ij} is an interatomic distance and f_{dmp} is a damping function.

The E_{rep} (exchange-repulsion energy) is calculated between unperturbed charge distributions of the monomers.

The scale factors k_{ele}, *etc*., in Eq. A21 are determined by calibration against quantum mechanical results.